

**Energy Scavenging for Wireless Sensor Nodes
with a Focus on Vibration to Electricity Conversion**

by

Shadrach Joseph Roundy

B.S. (Brigham Young University) 1996

M.S. (University of California, Berkeley) 2000

A dissertation submitted in partial satisfaction of the
requirements for the degree of

Doctor of Philosophy
in

Engineering-Mechanical Engineering
in the

GRADUATE DIVISION

of

THE UNIVERSITY OF CALIFORNIA, BERKELEY

Committee in charge:
Professor Paul K. Wright, Chair
Professor Jan Rabaey
Professor Kristofer S. J. Pister
Professor David A. Dornfeld

Spring 2003

The dissertation of Shadrach Joseph Roundy is approved:

Professor Paul K. Wright, Chair

Date

Professor Jan Rabaey

Date

Professor Kristofer S. J. Pister

Date

Professor David A. Dornfeld

Date

University of California, Berkeley

2003

Energy Scavenging for Wireless Sensor Nodes
with a Focus on Vibration to Electricity Conversion

Copyright 2003

by

Shadrach Joseph Roundy

Abstract

Energy Scavenging for Wireless Sensor Nodes with a Focus on Vibration to Electricity Conversion

by

Shadrach Joseph Roundy

Doctor of Philosophy in Mechanical Engineering

University of California, Berkeley

Professor Paul K. Wright, Chair

The vast reduction in size and power consumption of CMOS circuitry has led to a large research effort based around the vision of ubiquitous networks of wireless communication nodes. As the networks, which are usually designed to run on batteries, increase in number and the devices decrease in size, the replacement of depleted batteries is not practical. Methods of scavenging ambient power for use by low power wireless electronic devices have been explored in an effort to make the wireless nodes and resulting wireless sensor networks indefinitely self-contained. After a broad survey of potential energy scavenging methods, the conversion of ambient vibrations to electricity was chosen as a method for further research.

Converters based on both piezoelectric and electrostatic (capacitive) coupling were pursued. Both types of converters were carefully modeled. Designs were optimized based on the models developed within in total size constraint of 1 cm^3 . Test results from the piezoelectric converters demonstrate power densities of about $200\text{ }\mu\text{W}/\text{cm}^3$ from input vibrations of 2.25 m/s^2 at 120 Hz. Furthermore, test results matched simulated outputs very closely thus verifying the validity of the model as a basis for design. One of

the piezoelectric converters was used to completely power a small wireless sensor device from vibrations similar to those found in common environments.

Electrostatic converters were designed for a category of MEMS processes in which a structural MEMS device is patterned in the top layer of a Silicon on Insulator (SOI) wafer. Simulation results show a maximum power density of $110 \mu\text{W}/\text{cm}^3$ from the same vibration source. Initial electrostatic converter prototypes were fabricated in a SOI MEMS process. Prototypes have been tested and when manually actuated have demonstrated a net electrical power increase due to mechanical work done on the converter. However, a fully functional power generator driven by vibrations has yet to be demonstrated.

Both theory and test results demonstrate that piezoelectric converters are capable of higher power output densities than electrostatic converters. However, because electrostatic converters are more easily implemented in silicon micromachining processes they hold the future potential for complete monolithic integration with silicon based sensors and microelectronics.

Professor Paul K. Wright, Chair

Date

Table of Contents

Chapter 1: Introduction: Overview of the Problem and Potential Sources of Power 1

1.1	Motivation: Wireless Sensor and Actuator Networks	2
1.2	Three Methods of Powering Wireless Sensor Networks	3
1.3	Comparison of Energy Scavenging Technologies	6
1.3.1	<i>Solar Energy</i>	8
1.3.2	<i>Vibrations</i>	9
1.3.3	<i>Acoustic Noise</i>	9
1.3.4	<i>Temperature Variations</i>	9
1.3.5	<i>Passive Human Power</i>	10
1.3.6	<i>Active Human Power</i>	11
1.3.7	<i>Summary of Power Scavenging Sources</i>	11
1.3.8	<i>Conclusions Regarding Power Scavenging Sources</i>	13
1.4	Overview of Vibration-to-Electricity Conversion Research	13

Chapter 2: Characterization of Vibration Sources and Generic Conversion Model 19

2.1	Types of Vibrations Considered	19
2.2	Characteristics of Vibrations Measured	20
2.3	Generic Vibration-to-Electricity Conversion Model	24
2.4	Efficiency of Vibration-to-Electricity Conversion	32

Chapter 3: Comparison of Methods of Converting Vibrations to Electricity..... 36

3.1	Electromagnetic (Inductive) Power Conversion	36
3.2	Electrostatic (Capacitive) Power Conversion	39
3.3	Piezoelectric Power Conversion	41
3.4	Comparison of Energy Density of Converters	45
3.5	Summary of Conversion Mechanisms	47

Chapter 4: Piezoelectric Converter Design, Modeling and Optimization 49

4.1	Basic Design Configuration	49
4.2	Material Selection	52
4.3	Analytical Model for Piezoelectric Generators	55
4.4	Discussion of Analytical Model for Piezoelectric Generators	59
4.5	Initial Prototype and Model Verification	62
4.6	Design Optimization	68

4.7	Analytical Model Adjusted for a Capacitive Load	76
4.8	Discussion of Analytical Model Changes for Capacitive Load.....	83
4.9	Design Optimization for a Capacitive Load	87
4.10	Conclusions.....	92
Chapter 5: Piezoelectric Converter Test Results		95
5.1	Implementation of Optimized Converters	95
5.2	Resistive load tests.....	98
5.3	Discussion of resistive load tests	103
5.4	Capacitive load tests	106
5.5	Discussion of capacitive load test.....	109
5.6	Results from testing with a custom designed RF transceiver	111
5.7	Discussion of results from custom RF transceiver test.....	117
5.8	Results from test of complete wireless sensor node	119
5.9	Discussion of results from complete wireless sensor node.....	126
5.10	Conclusions.....	128
Chapter 6: Case Study: Piezoelectric Converter Design for use in Automobile Tires		129
6.1	Environment inside tires and constraints	129
6.2	Model refinements and analytical expressions	133
6.3	Simulations and design	136
6.4	Experimental results.....	146
6.5	Conclusions.....	154
Chapter 7: Electrostatic Converter Design		156
7.1	Explanation of concept and principle of operation	156
7.2	Electrostatic Conversion Model.....	158
7.3	Exploration of design concepts and device specific models.....	163
7.4	Comparison of design concepts	168
7.5	Design Optimization	176
7.6	Flexure design.....	182
7.6	Discussion of design and conclusion	188
Chapter 8: Fabrication of Capacitive Converters		190
8.1	Choice of process and wafer technology	190

8.2	Basic process flow	191
8.3	Specific processes used.....	193
8.4	Conclusions.....	196
Chapter 9: Capacitive Converter Test Results		198
9.1	Macro-scale prototype and results	198
9.2	Results from fluidic self-assembly process prototypes.....	201
9.3	Results from integrated process prototypes	204
9.4	Results simplified custom process prototypes	214
9.5	Discussion of Results and Conclusions	221
Chapter 10: Conclusions		224
10.1	Justification for focus on vibrations as a power source	224
10.2	Piezoelectric vibration to electricity converters.....	225
10.3	Electrostatic vibration to electricity converters	228
10.4	Summary of conclusions.....	231
10.5	Recommendations for future work	232
References.....		235
Appendix A, Analytical Model of Piezoelectric Generator.....		241
A.1	Geometric terms for bimorph mounted as a cantilever.....	241
A.2	Basic dynamic model of piezoelectric generator	245
A.3	Expressions of interest from basic dynamic model	251
A.4	Alterations to the basic dynamic model.....	254
Appendix B, Analytical Model of In-plane Gap Closing Electrostatic Converter..		260
B.1	Derivation of electrical and geometric expressions	260
B.2	Derivation of mechanical dynamics and electrostatic forces.....	264
B.3	Simulation of the in-plane gap closing converter	268
Appendix C, Development of Solar Powered Wireless Sensor Nodes.....		272
C.1	Photovoltaic cell technologies	272
C.2	Solar Power Circuits	275
C.3	Solar Power Train Results	279
C.4	Discussion of Results.....	284

Acknowledgements

Throughout the course of this research I have had the opportunity to work, collaborate, and interact with a wide range of people. These interactions have been the most rewarding part of my research work. While I cannot possibly thank each of them individually in writing, I wish to acknowledge some that have been particularly helpful and inspiring.

Professor Paul Wright has full-heartedly supported the project from its inception with energy and optimism. His interest in the work, and his material and intellectual support have sustained the project and me personally, for which I am very grateful. I warmly appreciate his genuine interest in me and my family, and his friendship.

Professor Jan Rabaey has graciously acted as a co-advisor on this project. I am extremely thankful for his support and the direction that he has provided to the project from the beginning.

Professors Kris Pister and Seth Sanders have been generous with their time, have provided many important insights, and have aided in the direction of the research. For their support I am grateful.

My colleagues Dan Odell, Mike Montero, Roshan D'Souza, and Kiha Lee have been a tremendous support throughout this work. I am grateful for their lively discussions, their moral support, and friendship.

More recently, it has been a pleasure to work with Dan Steingart and Elizabeth Reilly on this project. Their energetic work and their expertise will undoubtedly lead to great contributions in this area.

I greatly appreciate the help of Brian Otis, who has been generous with his time in helping me understand circuit design issues and in helping with instrumentation.

I appreciate the willing and capable help of both Eric Mellers and Sid Mal, who have helped with many of the implementation details.

My interaction with the many lab mates with whom I have worked has made my time in graduate school a very enjoyable one. At the risk of leaving someone out, I would specifically like to thank Frank Wang, Sung Ahn, V. Sundararajan, Dan Chapman, Ganping Sun, Chuck Smith, Nate Ota, Deb Misra, Palani Kumaresan, Lloyd Lim, Jan Eggert, Duane Kubishta, Sam Lopez, Balaji Kannan, Kenneth Castelino, Ashish Mohole, and Arjun Ghose.

I am ever grateful to my parents for their constant love and confidence in me.

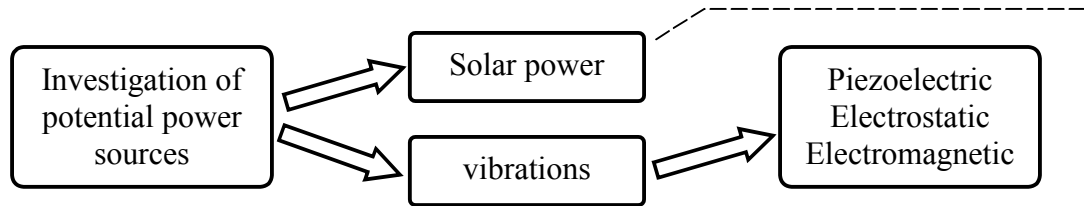
My most heart felt gratitude goes to my wife Michelle. She has been always loving, supportive, and understanding. For her support and partnership I will be always in debt.

Finally, thanks go to my children, Caleb and Seth, who lift my spirits and serve as a continual reminder to me that my research work is not all that important.

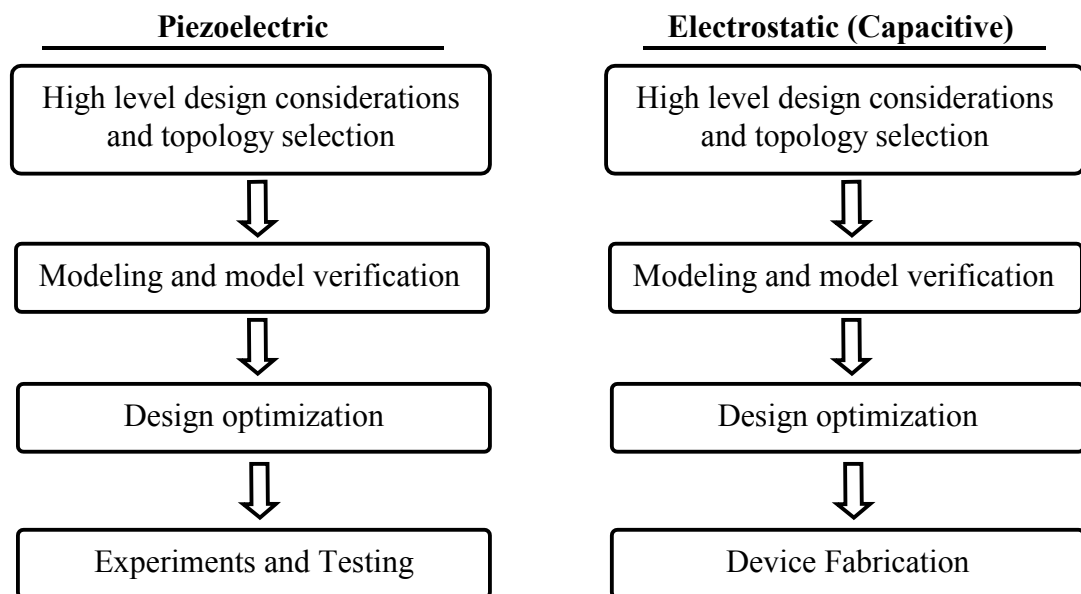
HYPOTHESIS:

Wireless sensor networks can be powered by environmentally scavenged energy.
Specifically, commonly occurring vibrations can power individual nodes.

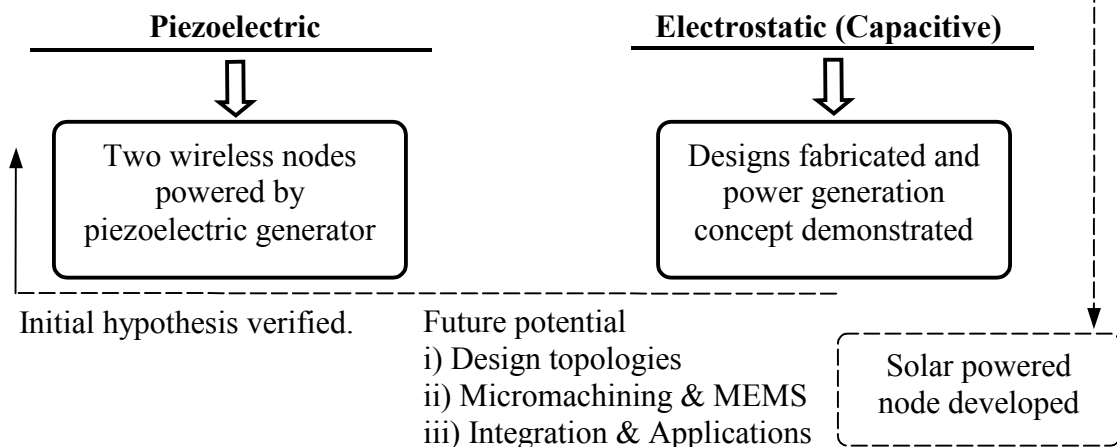
BACKGROUND INVESTIGATIONS AND GENERAL MODELING:



TECHNOLOGY SPECIFIC MODELING, DEVICE DESIGN, AND TESTING:



HYPOTHESIS VERIFICATION:



Chapter 1: Introduction: Overview of the Problem and Potential Sources of Power

1.1 Motivation: Wireless Sensor and Actuator Networks

The past several years have seen an increasing interest in the development of wireless sensor and actuator networks. Such networks could potentially be used for a wide variety of applications. A few possible applications include: monitoring temperature, light, and the location of persons in commercial buildings to control the environment in a more energy efficient manner, sensing harmful chemical agents in high traffic areas, monitoring fatigue crack formation on aircraft, monitoring acceleration and pressure in automobile tires, etc. Indeed, many experts foresee that very low power embedded electronic devices will become a ubiquitous part of our environment, performing functions in applications ranging from entertainment to factory automation (Rabaey *et al* 2000, Gates 2002, Wang *et al* 2002, Hitach mu-Chip 2003).

Advances in IC (Integrated Circuit) manufacturing and low power circuit design and networking techniques (Chandrakasan *et al*, 1998, Davis *et al*, 2001) have reduced the total power requirements of a wireless sensor node to well below 1 milliwatt. Such nodes would form dense ad-hoc networks transmitting data from 1 to 10 meters. In fact, for communication distances over 10 meters, the energy to transmit data rapidly dominates the system (Rabaey *et al* 2002). Therefore, the proposed sensor networks would operate in a multi-hop fashion replacing large transmission distances with multiple low power, low cost nodes.

The problem of powering a large number of nodes in a dense network becomes critical when one considers the prohibitive cost of wiring power to them or replacing batteries. In order for the nodes to be conveniently placed and used they must be small, which places severe limits on their lifetime if powered by a battery meant to last the entire life of the device. State of the art, non-rechargeable lithium batteries can provide up to 800 WH/L (watt hours per liter) or 2880 J/cm³. If an electronic device with a 1 cm³ battery were to consume 100 μ W of power on average (an aggressive goal), the device could last 8000 hours or 333 days, almost a year. Actually, this is a very optimistic estimate as the entire capacity usually cannot be used due to voltage drop. It is worth mentioning that the sensors and electronics of a wireless sensor node will be far smaller than 1 cm³, so, in this case, the battery would dominate the system volume. Clearly, a lifetime of 1 year is far from sufficient. The need to develop alternative methods of power for wireless sensor and actuator nodes is acute.

1.2 Three Methods of Powering Wireless Sensor Networks

There are three possible ways to address the problem of powering the emerging wireless technologies:

1. Improve the energy density of storage systems.
2. Develop novel methods to distribute power to nodes.
3. Develop technologies that enable a node to generate or “scavenge” its own power.

Research to increase the storage density of both rechargeable and primary batteries has been conducted for many years and continues to receive substantial focus (Bomgren 2002, Alessandrini *et al* 2000). The past few years have also seen many efforts to

miniaturize fuel cells which promise several times the energy density of batteries (Kang *et al* 2001, Sim *et al* 2001) Finally, more recent research efforts are underway to develop miniature heat engines that promise similar energy densities to fuel cells, but are capable of far higher maximum power output (Mehra *et al* 2000). While these technologies promise to extend the lifetime of wireless sensor nodes, they cannot extend their lifetime indefinitely.

The most common method (other than wires) of distributing power to embedded electronics is through the use of RF (Radio Frequency) radiation. Many passive electronic devices, such as electronic ID tags and smart cards, are powered by a nearby energy rich source that transmits RF energy to the passive device, which then uses that energy to run its electronics. (Friedman *et al* 1997, Hitach mu-Chip 2003). However, this method is not practical when considering dense networks of wireless nodes because an entire space, such as a room, would need to be flooded with RF radiation to power the nodes. The amount of radiation needed to do this would probably present a health risk and today exceeds FCC (Federal Communications Commission) regulations. As an example, the Location and Monitoring Service (LMS) offered by the FCC operates between 902 and 928 MHz and is used as, but not limited to, a method to automatically identify vehicles (at a toll plaza for example) (FCC 2002). The amount of power transmitted to a node assuming no interference is given by $P_r = P_o \lambda^2 / (4\pi R^2)$ where P_o is the transmitted power, λ is the wavelength of the signal and R is the distance between transmitter and receiver. If a maximum distance of 10 meters and the frequency band of the LMS are assumed, then to power a node consuming 100 μ W, the power transmitter would need to emit 14 watts of RF radiation. In this band the FCC regulations state that

person should not be exposed to more than 0.6 mW/cm^2 (FCC 2002). In the case just described, a person 1 meter away from the power transmitter would be exposed to 0.45 mW/cm^2 , which is just under federal regulations. However, this assumes that there are no reflections between the transmitter and receiver. In a realistic situation, the transmitter would need to far more than 14 watts, which would likely put people in the vicinity at risk. The FCC also has regulations determining how much power can be radiated at certain frequencies indoors. For example, the FCC regulation on ceiling mounted transmitters in the 2.4 – 2.4835 GHz band (the unlicensed industrial, scientific, and medical band) is 1 watt (Evans *et al* 1996), which given the numbers above is far too low to transmit power to sensor nodes throughout a room.

The third method, in which the wireless node generates its own power, has not been explored as fully as the first two. The idea is that a node would convert “ambient” sources of energy in the environment into electricity for use by the electronics. This method has been dubbed “energy scavenging”, because the node is scavenging or harvesting unused ambient energy. Energy scavenging is the most attractive of the three options because the lifetime of the node would only be limited by failure of its own components. *However, it is also potentially the most difficult method to exploit because each use environment will have different forms of ambient energy, and therefore, there is no one solution that will fit all, or even a majority, of applications.* Nevertheless, it was decided to pursue research into energy scavenging techniques because of the attractiveness of completely self-sustaining wireless nodes.

The driving force for energy scavenging is the development of wireless sensor and actuator networks. In particular, this research was conducted as part of a larger project

named PicoRadio (Rabaey *et al*, 2000) that aims to develop a small, flexible wireless platform for ubiquitous wireless data acquisition that minimizes power dissipation. The PicoRadio project researchers have developed some specifications that affect the exploration of energy scavenging techniques that will be used by their devices. The most important specifications for the power system are the total size and average power dissipation of an individual Pico Node (an individual node in the PicoRadio system is referred to here as a Pico Node). The size of a node must be no larger than 1 cm^3 , and the target average power dissipation of a completed node is $100 \text{ }\mu\text{W}$. The power target is particularly aggressive, and it is likely that several generations of prototypes will be necessary to achieve this goal. Therefore, the measure of acceptability of an energy scavenging solution will be its ability to provide $100 \text{ }\mu\text{W}$ of power in less than 1 cm^3 . This does not mean that solutions which do not meet this criterion are not worthy of further exploration, but simply that they will not meet the needs of the PicoRadio project. Thus, the primary *metric* for evaluating power sources used in this research is power per volume, specifically $\mu\text{W}/\text{cm}^3$, with a *target of at least $100 \text{ }\mu\text{W}/\text{cm}^3$* .

1.3 Comparison of Energy Scavenging Technologies

A broad survey of potential energy scavenging methods has been undertaken by the author. The results of this survey are shown in Table 1.1. The table also includes batteries and other energy storage technologies for comparison. The upper (lighter) half of the table contains pure power scavenging sources and thus the amount of power available is not a function of the lifetime of the device. The lower (darker) half of the table contains energy storage technologies in which, because they contain a fixed amount of energy, the power available to the node decreases with increased lifetime. As is the

case with all power values reported in this thesis, power is normalized per cubic centimeter to conform to the constraints of the PicoRadio project. The values in the table are derived from a combination of published studies, experiments performed by the author, theory, and information that is commonly available in data sheets and textbooks. The source of information for each technique is given in the third column. While this comparison is by no means exhaustive, it does provide a broad cross section of potential methods to scavenge energy and energy storage systems. Other potential sources were also considered but deemed to be outside of the application space under consideration or to be unacceptable for some other reason. A brief explanation and evaluation of each source listed in Table 1.1 follows.

		Power Density (μW/cm ³) 1 Year lifetime	Power Density (μW/cm ³) 10 Year lifetime	Source of information
Scavenged Power Sources	Solar (Outdoors)	15,000 - direct sun 150 - cloudy day	15,000 - direct sun 150 - cloudy day	Commonly Available
	Solar (Indoors)	6 - office desk	6 - office desk	Author's Experiment
	Vibrations	200	200	Roundy <i>et al</i> 2002
	Acoustic Noise	0.003 @ 75 Db 0.96 @ 100 Db	0.003 @ 75 Db 0.96 @ 100 Db	Theory
	Daily Temp. Variation	10	10	Theory
	Temperature Gradient	15 @ 10 °C gradient	15 @ 10 °C gradient	Stordeur and Stark 1997
	Shoe Inserts	330	330	Starner 1996 Shenck & Paradiso 2001
Energy reservoirs	Batteries (non-recharg. Lithium)	45	3.5	Commonly Available
	Batteries (rechargeable Lithium)	7	0	Commonly Available
	Hydrocarbon fuel (micro heat engine)	333	33	Mehra et. al. 2000
	Fuel Cells (methanol)	280	28	Commonly Available
	Nuclear Isotopes (uranium)	6x10 ⁶	6x10 ⁵	Commonly Available

Table 1.1: Comparison of energy scavenging and energy storage methods. Note that leakage effects are taken into consideration for batteries.

1.3.1 Solar Energy

Solar energy is abundant outdoors during the daytime. In direct sunlight at midday, the power density of solar radiation on the earth's surface is roughly 100 mW/cm^2 . Silicon solar cells are a mature technology with efficiencies of single crystal silicon cells ranging from 12% to 25%. Thin film polycrystalline, and amorphous silicon solar cells are also commercially available and cost less than single crystal silicon, but also have lower efficiency. As seen in the table, the power available falls off by a factor of about 100 on overcast days. However, if the target application is outdoors and needs to operate primarily during the daytime, solar cells offer an excellent and technologically mature solution. Available solar power indoors, however, is drastically lower than that available outdoors. Measurements taken in normal office lighting show that only several $\mu\text{W/cm}^2$ can be converted by a solar cell, which is not nearly enough for the target application under consideration. Table 1.2 shows results of measurements taken with a single crystal silicon solar cell with an efficiency of 15%. The measurements were taken outside, in normal office lighting, and at varying distances from a 60 watt light bulb. The data clearly show that if the target application is close to a light source, then there is sufficient energy to power a Pico Node, however in ambient office lighting there is not. Furthermore, the power density falls off roughly as $1/d^2$ as would be expected, where d is the distance from the light source.

Conditions	Outside, midday	4 inches from 60 W bulb	15 inches from 60 W bulb	Office lighting
Power ($\mu\text{W/cm}^2$)	14000	5000	567	6.5

Table 1.2: Solar power measurements taken under various lighting conditions.

1.3.2 Vibrations

A combination of theory and experiment shows that about $200 \mu\text{W}/\text{cm}^3$ could be generated from vibrations that might be found in certain building environments. Vibrations were measured on many surfaces inside buildings, and the resulting spectra used to calculate the amount of power that could be generated. A more detailed explanation of this process follows in Chapter 2. However, without discussing the details at this point, it does appear that conversion of vibrations to electricity can be sufficient for the target application in certain indoor environments. Some research has been done on scavenging power from vibrations, however, it tends to be very focused on a single application or technology. Therefore, a more broad look at the issue is warranted (Shearwood and Yates, 1997, Amirtharajah and Chandrakasan, 1998, Meninger *et al* 2001, Glynn-Jones *et al* 2001, Ottman *et al* 2003).

1.3.3 Acoustic Noise

There is far too little power available from acoustic noise to be of use in the scenario being investigated, except for very rare environments with extremely high noise levels. This source has been included in the table however because it often comes up in discussions.

1.3.4 Temperature Variations

Naturally occurring temperature variations can also provide a means by which energy can be scavenged from the environment. Stordeur and Stark (Stordeur and Stark, 1997) have demonstrated a thermoelectric micro-device capable of converting $15 \mu\text{W}/\text{cm}^3$ from a 10°C temperature gradient. While this is promising and, with the

improvement of thermoelectrics, could eventually result in more than $15 \mu\text{W}/\text{cm}^3$, situations in which there is a static 10°C temperature difference within 1 cm^3 are very rare. Alternatively, the natural temperature variation over a 24 hour period might be used to generate electricity. It can be shown with fairly simple calculations, assuming an average variation of 7°C , that an enclosed volume containing an ideal gas could generate an average of $10 \mu\text{W}/\text{cm}^3$. This, however, assumes no losses in the conversion of the power to electricity. In fact some commercially available clocks, such as the Atmos clock, operate on a similar principle. The Atmos clock includes a sealed volume of fluid that undergoes a phase change right around 21°C . As the liquid turns to gas during a normal day's temperature variation, the pressure increases actuating a spring that winds the clock. While this is very interesting, the level of power output is still substantially lower than other possible methods.

1.3.5 Passive Human Power

A significant amount of work has been done on the possibility of scavenging power off the human body for use by wearable electronic devices (Starner 1996, Shenck and Paradiso 2001). The conclusion of studies undertaken at MIT suggests that the most energy rich and most easily exploitable source occurs at the foot during heel strike and in the bending of the ball of the foot. This research has led to the development of the piezoelectric shoe inserts referred to in the table. The power density available from the shoe inserts meets the constraints of the current project. However, wearable computing and communication devices are not the focus of this project. Furthermore, the problem of how to get the energy from a person's foot to other places on the body has not been satisfactorily solved. For an RFID tag or other wireless device worn on the shoe, the

piezoelectric shoe inserts offer a good solution. However, the application space for such devices is extremely limited, and as mentioned, not very applicable to wireless sensor networks.

1.3.6 Active Human Power

The type of human powered systems investigated at MIT could be referred to as passive human powered systems in that the power is scavenged during common activities rather than requiring the user to perform a specific activity to generate power. Human powered systems of this second type, which require the user to perform a specific power generating motion, are common and may be referred to separately as active human powered systems. Examples include standard flashlights that are powered by squeezing a lever and the Freeplay wind-up radios (Economist 1999). Active human powered devices, however, are not very applicable for wireless sensor applications.

1.3.7 Summary of Power Scavenging Sources

Based on this survey, it was decided that solar energy and vibrations offered the most attractive energy scavenging solutions. Both solutions meet the power density requirement in environments that are of interest for wireless sensor networks. The question that must then be asked is: is it preferable to use a high energy density battery that would last the lifetime of the device, or to implement an energy scavenging solution?

Figure 1.1 shows average power available from various battery chemistries (both rechargeable and non-rechargeable) versus lifetime of the device being powered.

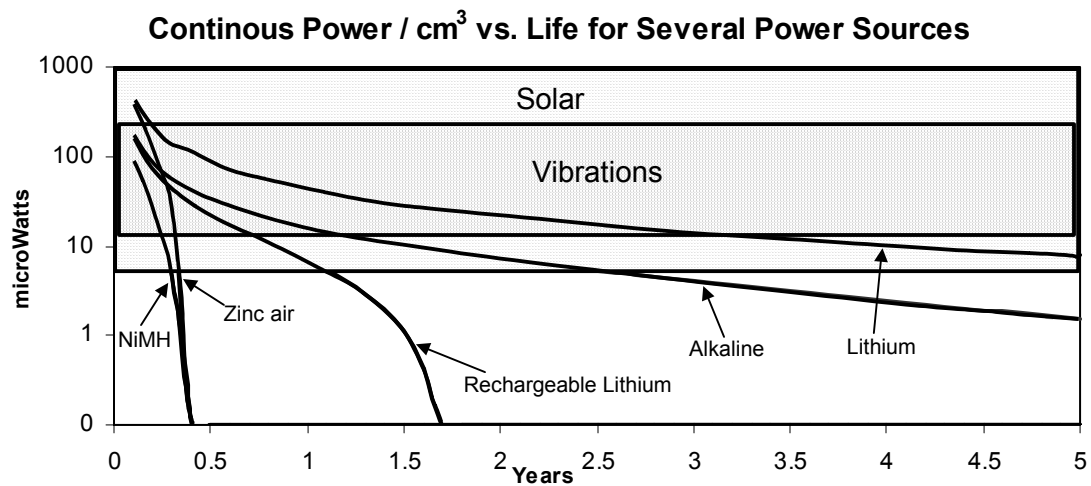


Figure 1.1: Power density versus lifetime for batteries, solar cells, and vibration generators.

The shaded boxes in the figure indicate the range of solar (lightly shaded) and vibration (darkly shaded) power available. Solar and vibration power output are not a function of lifetime. The reason that both solar and vibrations are shown as a box in the graph is that different environmental conditions will result in different power levels. The bottom of the box for solar power indicates the amount of power per square centimeter available in normal office lighting. The top of this box roughly indicates the power available outdoors. Likewise, the area covered by the box for vibrations covers the range of vibration sources under consideration in this study. Some of the battery traces, lithium rechargeable and zinc-air for example, exhibit an inflection point. The reason is that both battery drain and leakage are considered. For longer lifetimes, leakage becomes more dominant for some battery chemistries. The location of the inflection roughly indicates when leakage is becoming the dominant factor in reducing the amount of energy stored in the battery.

The graph indicates that if the desired lifetime of the device is in the range of 1 year or less, battery technology can provide enough energy for the wireless sensor nodes under

consideration (100 μ W average power dissipation). However, if longer lifetimes are needed, as will usually be the case, then other options should be pursued. Also, it seems that for lifetimes of 5 years or more, a battery cannot provide the same level of power that solar cells or vibrations can provide even under poor circumstances. Therefore, battery technology will not meet the constraints of the project, and will not likely meet the constraints of very many wireless sensor node applications.

1.3.8 Conclusions Regarding Power Scavenging Sources

Both solar power and vibration based energy scavenging look promising as methods to scavenge power from the environment. In many cases, perhaps most cases, they are not overlapping solutions because if solar energy is present, it is likely that vibrations are not, and vice versa. It was, therefore, decided to pursue both solar and vibration based solutions for the sensor nodes under development. Solar cells are a mature technology, and one that has been profitably implemented many times in the past. So, while solar power based solutions have been developed for this project (the details are given in Appendix C), the main focus of the research and development effort has been vibration based power generators.

1.4 Overview of Vibration-to-Electricity Conversion Research

Vibration-to-electricity conversion offers the potential for wireless sensor nodes to be self-sustaining in many environments. Low level vibrations occur in many environments including: large commercial buildings, automobiles, aircraft, ships, trains, and industrial environments. Given the wide range of potential applications for vibration based power generation, and given the fact that vibration-to-electricity converters have

been investigated very little, the thorough investigation and development of such converters are merited.

A few groups have previously devoted research effort toward the development of vibration-to-electricity converters. Yates, Williams, and Shearwood (Williams & Yates, 1995, Shearwood & Yates, 1997, Williams *et. al.*, 2001) have modeled and developed an electromagnetic micro-generator. The generator has a footprint of roughly 4mm X 4mm and generated a maximum of 0.3 μW from a vibration source of displacement magnitude 500 nm at 4.4 kHz. Their chief contribution, in addition to the development of the electromagnetic generator, was the development of a generic second order linear model for power conversion. It turns out that this model fits electromagnetic conversion very well, and they showed close agreement between the model and experimental results. The electromagnetic generator was only 1mm thick, and thus the power density of the system was about 10 - 15 $\mu\text{W}/\text{cm}^3$. Interestingly, the authors do not report the output voltage and current of their device, but only the output power. This author's calculations show that the output voltage of the 0.3 μW generator would have been 8 mV which presents a serious problem. Because the power source is an AC power source, in order to be of use by electronics it must first be rectified. In order to rectify an AC voltage source, the voltage must be larger than the forward drop of a diode, which is about 0.5 volts. So, in order to be of use, this power source would need a large linear transformer to convert the AC voltage up by at least a factor of 100 and preferably a factor of 500 to 1000, which is clearly impractical. A second issue is that the vibrations used to drive the device are of magnitude 500 nm, or 380 m/s^2 , at 4.4 kHz. It is exceedingly difficult to find vibrations of this magnitude and frequency in many environments. These vibrations are far more

energy rich than those measured in common building environments, which will be discussed at length in Chapter 2. Finally, there was no attempt in that research at either a qualitative or quantitative comparison of different methods of converting vibrations to electricity. Nevertheless the work of Yates, Williams, and Shearwood is significant in that it represents the first effort to develop micro or meso scale devices that convert vibrations to electricity (meso scale here refers to objects between the macro scale and micro scale, typically objects from a centimeter down to a few millimeters).

A second group has more recently developed an electromagnetic converter and an electrostatic converter. Several publications detail their work (Amirtharajah 1999, Amirtharajah & Chandrakasan 1998, Meninger *et al* 1999, Amirtharajah *et al* 2000, Meninger *et al* 2001). The electromagnetic converter was quite large and designed for vibrations generated by a person walking. (i.e. the person would carry the object in his/her pocket or somewhere else on the body). The device was therefore designed for a vibration magnitude of about 2 cm at about 2 Hz. (Note that these are not steady state vibrations.) Their simulations showed a maximum of 400 μW from this source under idealized circumstances (no mechanical damping or losses). While they report the measured output voltage for the device, they do not report the output power. The maximum measured output voltage was reported as 180 mV, necessitating a 10 to 1 transformer in order to rectify the voltage. The device size was 4cm X 4cm X 10cm, and if it is assumed that 400 μW of power really could be generated, then the power density of the device driven by a human walking would be 2.5 $\mu\text{W}/\text{cm}^3$. Incidentally, they estimated the same power generation from a steady state vibration source driven by machine components (rotating machinery).

The electrostatic converter designed by this same group was designed for a MEMS process using a Silicon on Insulator (SOI). The generator is a standard MEMS comb drive (Tang, Nguyen and Howe, 1989) except that it is used as a generator instead of an actuator. There seems to have been little effort to explore other design topologies. At least, to this author's knowledge, Chandrakasan and colleagues have not been published such an effort. Secondly, there seems to be little recognition of the mechanical dynamics of the system in the design. The authors assume that the generator device will undergo a predetermined level of displacement, but do not show that this level of displacement is possible given a reasonably input vibration source and the dynamics of the system. In fact, this author's own calculations show that for a reasonable input vibration, and the mass of their system, the level of displacement assumed is not practical. Published simulation results for their system predict a power output of 8.6 μW for a device that is 1.5 cm X 0.5 cm X 1 mm from a vibration source at 2.52 kHz (amplitude not specified). However, no actual test results have been published to date.

Amirtharajah *et al* of researchers has also developed power electronics especially suited for electrostatic vibration to electricity converters for extremely low power systems. Additionally, they have developed a low power DSP (Digital Signal Processor) for sensor applications. These are both very significant achievements and contributions. In fact, perhaps it should be pointed out that this group is comprised primarily of circuit designers, and the bulk of the material published about their project reports on the circuit design and implementation, not on the design and implementation of the power converter itself. The research presented in this thesis makes no effort to improve upon or expand

their research in this area. Rather the goal of this work is to explore the design and implementation of the power converter mechanism in great detail.

Very recently a group of researchers has published material on optimal power circuitry design for piezoelectric generators (Ottman *et al* 2003, Ottman *et al* 2002). The focus of this research has been on the optimal design of the power conditioning electronics for a piezoelectric generator driven by vibrations. No effort is made to optimize the design of the piezoelectric generator itself or to design for a particular vibrations source. The maximum power output reported is 18 mW. The footprint area of the piezoelectric converter is 19 cm². The height of the device is not given. Assuming a height of about 5 mm give a power density of 1.86 mW/cm³. The frequency of the driving vibrations is reported as 53.8 Hz, but the magnitude is not reported. The significant contribution of the research is a clear understanding of the issues surrounding the design of the power circuitry specifically optimized for a piezoelectric vibration to electricity converter. Again, the research presented in this dissertation makes no effort to improve on the power electronics design of Ottman *et al*, but rather to explore the design and implementation of the power converter itself.

In order to study vibration to electricity conversion in a thorough manner, the nature of vibrations from potential sources must first be known. Chapter 2 presents the results of a study in which many commonly occurring low level vibrations were measured and characterized. A general conversion model is also presented in chapter 2 allowing a first order prediction of potential power output of a vibration source without specifying the method of power conversion. Chapter 3 will discuss the merits of three different conversion mechanisms: electromagnetic, piezoelectric, and electrostatic. The

development of piezoelectric and electrostatic converters has been pursued in detail. Chapters 4, 5, and 6 present the modeling, design, fabrication, and test results for piezoelectric converters. The development of electrostatic converters is then presented in chapters 7, 8, and 9.

Chapter 2: Characterization of Vibration Sources and Generic Conversion Model

In order to determine how much power can be converted from vibrations, the details of the particular vibration source must be considered. This chapter presents the results of a study undertaken to characterize many commonly occurring, low-level, vibrations. A general vibration to electricity model, provided by Williams and Yates (Williams and Yates 1995), is presented and discussed. The model is non-device specific, and therefore the conversion mechanism (i.e. electromagnetic, electrostatic, or piezoelectric) need not be established for the Williams and Yates model to be used. Power output can be roughly estimated given only the magnitude and frequency of input vibrations, and the overall size (and therefore mass) of the device.

2.1 Types of Vibrations Considered

Although conversion of vibrations to electricity is not generally applicable to all environments, it was desired to target commonly occurring vibrations in typical office buildings, manufacturing and assembly plant environments, and homes in order to maximize the potential applicability of the project. Vibrations from a range of different sources have been measured. A list of the sources measured along with the maximum acceleration magnitude of the vibrations and frequency at which that maximum occurs is shown in Table 2.1. The sources are ordered from greatest acceleration to least. It should be noted that none of the previous work cited in Chapter 1 on converting

vibrations to electricity has attempted to characterize a range of realistic vibration sources.

Vibration Source	Peak Acc. (m/s ²)	Frequency of Peak (Hz)
Base of 5 HP 3-axis machine tool with 36" bed	10	70
Kitchen blender casing	6.4	121
Clothes dryer	3.5	121
Door frame just after door closes	3	125
Small microwave oven	2.25	121
HVAC vents in office building	0.2 – 1.5	60
Wooden deck with people walking	1.3	385
Breadmaker	1.03	121
External windows (size 2 ft X 3 ft) next to a busy street	0.7	100
Notebook computer while CD is being read	0.6	75
Washing Machine	0.5	109
Second story floor of a wood frame office building	0.2	100
Refrigerator	0.1	240

Table 2.1: List of vibration sources with their maximum acceleration magnitude and frequency of peak acceleration.

Additionally, because of interest in embedding self-powered sensors inside automobile tires, acceleration profiles from standard tires have been obtained from the Pirelli tire company (Pirelli, 2002). The “vibrations” exhibited inside tires are significantly different than the other “commonly occurring” sources measured. Therefore, power output estimates and design of devices for this application differ considerably from the standard case. For this reason, these acceleration traces will be considered separately in Chapter 6.

2.2 Characteristics of Vibrations Measured

A few representative vibration spectra are shown in Figure 2.1. In all cases, vibrations were measured with a standard piezoelectric accelerometer. Data were acquired with a National Instruments data acquisition card at a sample rate of 20 kHz. Only the first 500 Hz of the spectra are shown because all phenomena of interest occur

below that frequency. Above 500 Hz, the acceleration magnitude is essentially flat with no harmonic peaks. Measurements were taken in the same environments as the vibration sources with either the vibration source turned off (as in the case of a microwave oven) or with the accelerometer placed nearby on a surface that was not vibrating (as in the case of exterior windows) in order to ensure that vibrations signals were not the result of noise. Figure 2.2 shows measurements taken on the small microwave oven with the oven turned off and on. Note that the baseband of the signal with the microwave “off” is a factor of 10 lower than when “on”. Furthermore, at the critical frequencies of 120 Hz and multiples of 120 Hz there are no peaks in acceleration when the microwave is “off”.

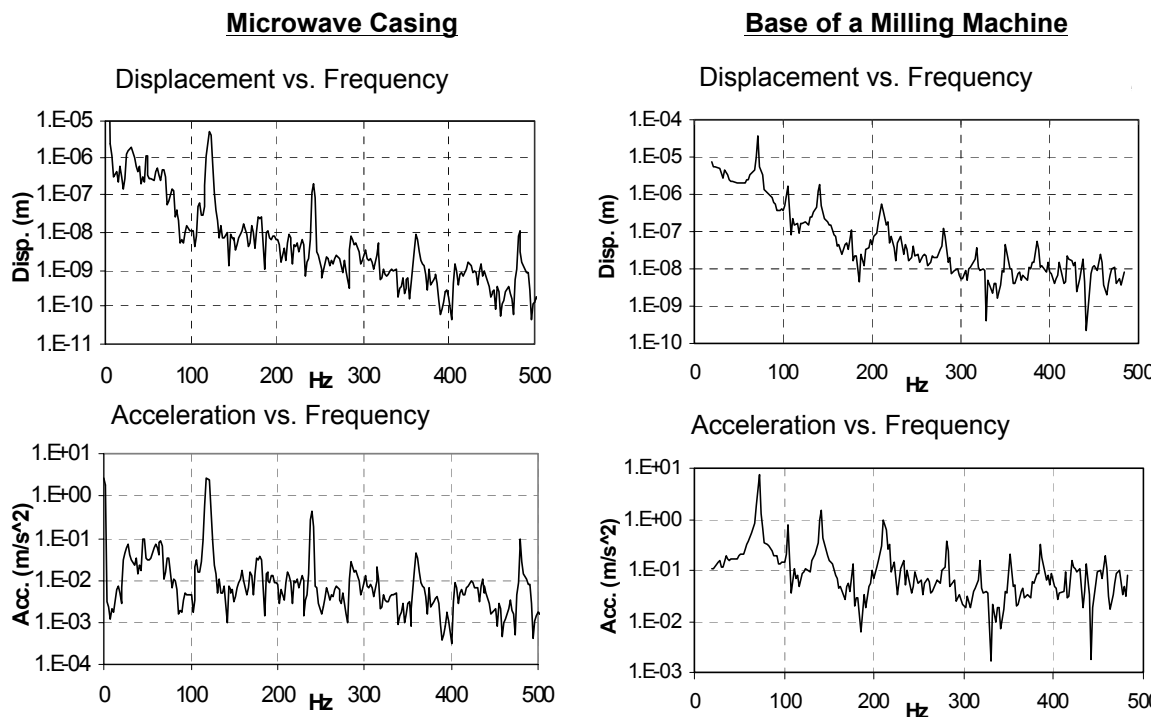


Figure 2.1: Two representative vibration spectra. The top graph shows displacement and the bottom graph shows acceleration.

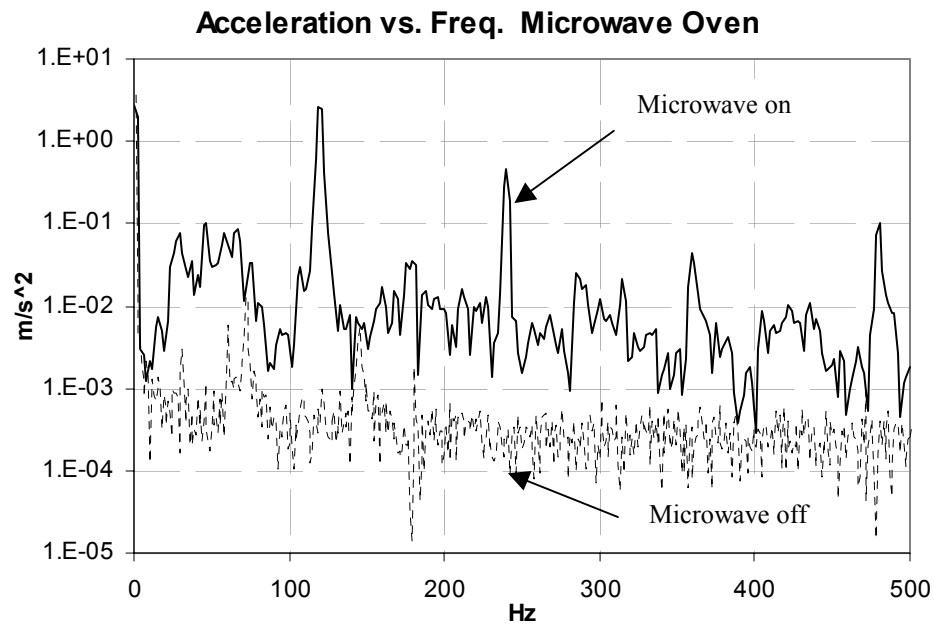


Figure 2.2: Acceleration taken from microwave oven while off and on showing that vibration signal is not attributable to noise.

Vibration spectra are shown only for a small microwave oven and the base of a milling machine, however, other spectra measured but not shown here resemble the microwave and milling machine in several key respects. First, there is a sharp peak in magnitude at a fairly low frequency with a few higher frequency harmonics. This low frequency peak will be referred to as the *fundamental vibration frequency* hereafter. The height and narrowness of the magnitude peaks are an indication that the sources are fairly sinusoidal in character, and that most of the vibration energy is concentrated at a few discrete frequencies. Figure 2.3 shows acceleration vs. time for the microwave oven. The sinusoidal nature of the vibrations can also be seen in this figure. This sharp, low frequency peak is representative of virtually all of the vibrations measured. Second, fundamental vibration frequency for almost all sources is between 70 and 125 Hz. The two exceptions are the wooden deck at 385 Hz and the refrigerator at 240 Hz. This is significant in that it can be difficult to design very small devices to resonate at such low

frequencies. Finally, note that the baseband of the acceleration spectrum is relatively flat with frequency. This means that the position spectrum falls off at approximately $1/\omega^2$ where ω is the circular frequency. Note however that the harmonic acceleration peaks are not constant with frequency. Again, this behavior is common to virtually all of the sources measured.

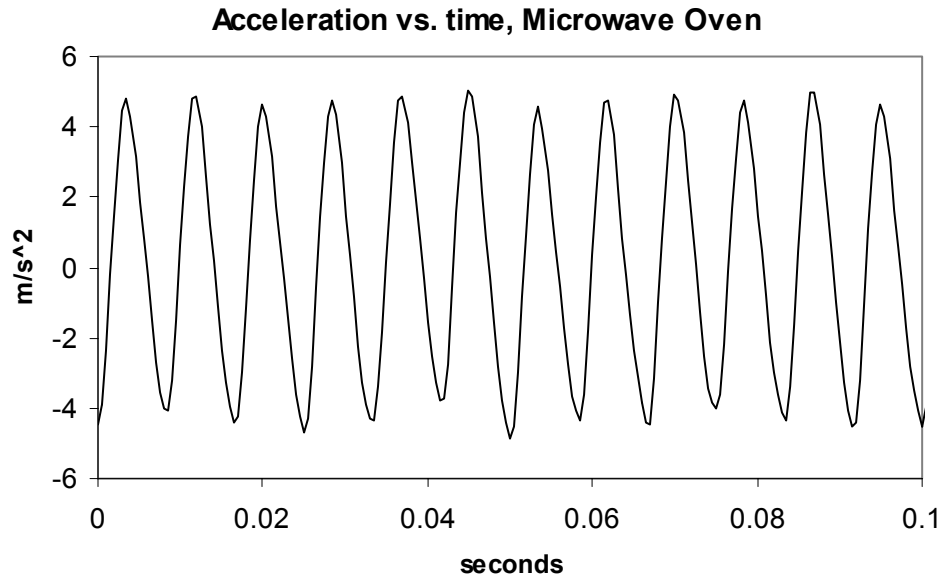


Figure 2.3: Acceleration vs. time for a microwave oven casing showing the sinusoidal nature of the vibrations.

Given the characteristics of the measured vibrations described above, it is reasonable to characterize a vibration source by the acceleration magnitude and frequency of the fundamental vibration mode as is done in Table 2.1. As a final note, the acceleration magnitude of vibrations measured from the casing of a small microwave oven falls about in the middle of all the sources measured. Furthermore, the frequency of the fundamental vibration mode is about 120 Hz, which is very close to that of many sources. For these reasons, the small microwave oven will be taken as a baseline when comparing different conversion techniques or different designs. When power estimates

are reported, it will be assumed that a vibration source of 2.25 m/s^2 at 120 Hz was used unless otherwise stated.

2.3 Generic Vibration-to-Electricity Conversion Model

One can formulate a general model for the conversion of the kinetic energy of a vibrating mass to electrical power based on linear system theory without specifying the mechanism by which the conversion takes place. A simple model based on the schematic in Figure 2.4 has been proposed by Williams and Yates (Williams and Yates, 1995). This model is described by equation 2.1.

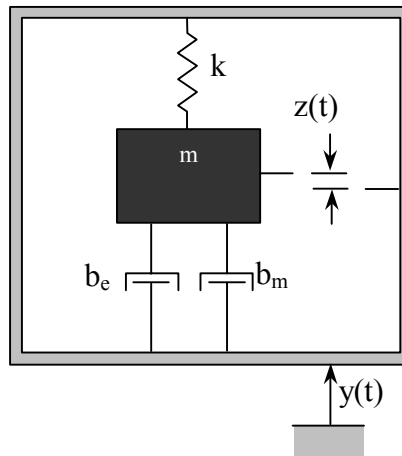


Figure 2.4: Schematic of generic vibration converter

$$m\ddot{z} + (b_e + b_m)\dot{z} + kz = -m\ddot{y} \quad (2.1)$$

where:

z = spring deflection

y = input displacement

m = mass

b_e = electrically induced damping coefficient

b_m = mechanical damping coefficient

k = spring constant

The term b_e represents an electrically induced damping coefficient. The primary idea behind this model is that the conversion of energy from the oscillating mass to electricity (whatever the mechanism is that does this) looks like a linear damper to the mass spring system. This is a fairly accurate model for certain types of electro-magnetic converters like the one analyzed by Williams and Yates. For other types of converters (electrostatic and piezoelectric), this model must be changed somewhat. First, the effect of the electrical system on the mechanical system is not necessarily linear, and it is not necessarily proportional to velocity. Nevertheless, the conversion will always constitute a loss of mechanical kinetic energy, which can broadly be looked at as electrically induced “damping”. Second, the mechanical damping term is not always linear and proportional to velocity. Even if this does not accurately model some types of converters, important conclusions can be made through its analysis, which can be extrapolated to electrostatic and piezoelectric systems.

The power converted to the electrical system is equal to the power removed from the mechanical system by b_e , the electrically induced damping. The electrically induced force is $b_e \dot{z}$. Power is simply the product of force (F) and velocity (v) if both are constants. Where they are not constants, power is given by equation 2.2.

$$P = \int_0^v F dv \quad (2.2)$$

In the present case, $F = b_e \dot{z} = b_e v$. Then equation 2.2 becomes:

$$P = b_e \int_0^v v dv \quad (2.3)$$

The solution of equation 2.3 is very simply $\frac{1}{2} b_e v^2$. Replacing v with the equivalent \dot{z} yields the expression for power in equation 2.4.

$$P = \frac{1}{2} b_e \dot{z}^2 \quad (2.4)$$

A complete analytical expression for power can be derived by solving equation 2.1 for \dot{z} and substituting into equation 2.4. Taking the Laplace transform of equation 2.1 and solving for the variable Z yields the following equation:

$$Z = \frac{-ms^2 Y}{ms^2 + (b_e + b_m)s + k} \quad (2.5)$$

where:

Z = Laplace transform of spring deflection

Y = Laplace transform of input displacement

s = Laplace variable (note: $dz/dt = sZ$)

Replacing the damping coefficients b_e and b_m with the unitless damping ratios ζ_e and ζ_m according to the relationship $b = 2m\zeta\omega_n$, k with ω_n^2 according to the relationship $\omega_n^2 = k/m$, and s with the equivalent $j\omega$ yields the following expression:

$$|Z| = \frac{-\omega^2}{-\omega^2 + 2(\zeta_e + \zeta_m)j\omega\omega_n + \omega_n^2} |Y| \quad (2.6)$$

where:

ω is the frequency of the driving vibrations.

ω_n = natural frequency of the mass spring system.

Recalling that $|\dot{Z}| = j\omega|Z|$ and rearranging terms in equation 2.6 yields the following expression for $|\dot{Z}|$, or the magnitude of \dot{z} .

$$|\dot{Z}| = \frac{-j\omega \left(\frac{\omega}{\omega_n^2} \right)}{2\zeta_T \frac{j\omega}{\omega_n} + 1 - \left(\frac{\omega}{\omega_n} \right)^2} |Y| \quad (2.7)$$

where:

ζ_T = combined damping ratio ($\zeta_T = \zeta_e + \zeta_m$)

Substituting equation 2.7 into 2.4 and rearranging terms results in an analytical expression for the output power as shown below in equation 2.8. Note that the derivation of equation 2.8 shown here depends on the assumption that the vibration source is concentrated at a single driving frequency. In other words, no broadband effects are taken into account. However, this assumption is fairly accurate given the characteristics of the vibration sources measured.

$$|P| = \frac{m\zeta_e\omega_n\omega^2\left(\frac{\omega}{\omega_n}\right)^3 Y^2}{\left(2\zeta_T\frac{\omega}{\omega_n}\right) + \left(1 - \left(\frac{\omega}{\omega_n}\right)^2\right)^2} \quad (2.8)$$

where:

$|P|$ = magnitude of output power

In many cases, the spectrum of the target vibrations is known beforehand. Therefore the device can be designed to resonate at the frequency of the input vibrations. If it is assumed that the resonant frequency of the spring mass system matches the input frequency, equation 2.8 can be reduced to the equivalent expressions in equations 2.9 and 2.10. Situations in which this assumption cannot be made will be discussed more later in this chapter, in Chapter 6, and in Chapter 10 under future work.

$$|P| = \frac{m\zeta_e\omega^3 Y^2}{4\zeta_T^2} \quad (2.9)$$

$$|P| = \frac{m\zeta_e A^2}{4\omega\zeta_T^2} \quad (2.10)$$

where:

A = acceleration magnitude of input vibrations

Equation 2.10 shows that if the acceleration magnitude of the vibration is taken to be a constant, the output power is inversely proportional to frequency. In fact, as shown previously, the acceleration is generally either constant or decreasing with frequency. Therefore, equation 2.10 is probably more useful than equation 2.9. Furthermore, the converter should be designed to resonate at the lowest fundamental frequency in the input spectrum rather than at the higher harmonics. Also note that power is optimized for ζ_m as low as possible, and ζ_e equal to ζ_m . Because ζ_e is generally a function of circuit parameters, one can design in the appropriate ζ_e if ζ_m for the device is known. Finally, power is linearly proportional to mass. Therefore, the converter should have the largest proof mass that is possible while staying within the space constraints. Figure 2.5 shows the results of simulations based on this general model. The input vibrations were based on the measured vibrations from a microwave oven as described above, and the mass was limited by the requirement that the entire system stay within 1 cm³ as detailed in Chapter 1. These same conditions were used for all simulations and tests throughout this dissertation; therefore all power output values can be taken to be *normalized as power per cubic centimeter*. Figure 2.5 shows power out versus electrical and mechanical damping ratio. Note that the values plotted are the logarithm of the actual simulated values. The figure shows that for a given value ζ_m , power is maximized for $\zeta_e = \zeta_m$. However, while there is a large penalty for the case where ζ_m is greater than ζ_e , there is only a small penalty for ζ_e greater than ζ_m . Therefore, a highly damped system will only

slightly under perform a lightly damped system provided that most of the damping is electrically induced (attributable to ζ_e).

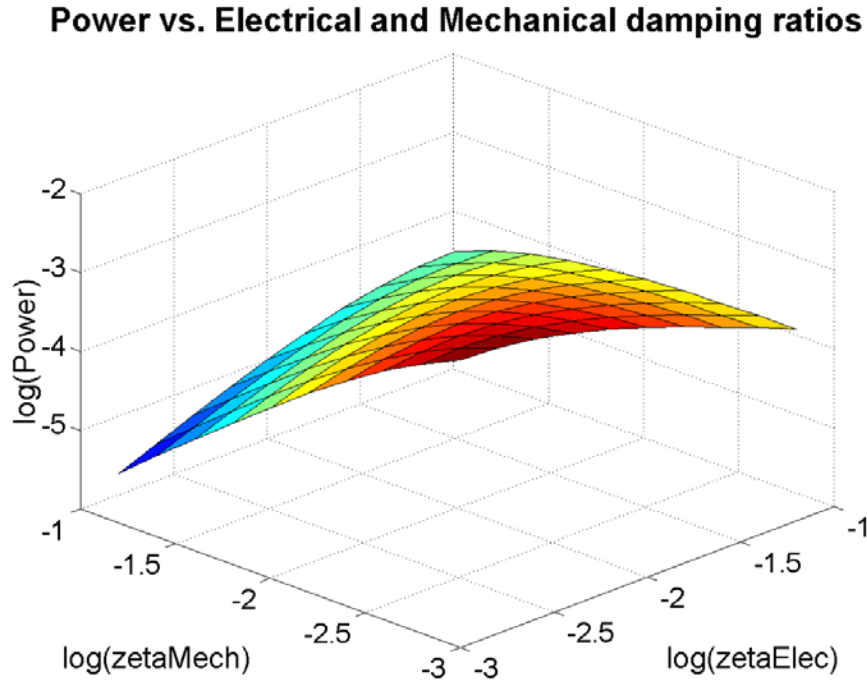


Figure 2.5: Simulated output power vs. mechanical and electrical damping ratios. The logarithms of the actual values are plotted.

Figure 2.5 assumes that the frequency of the driving vibrations exactly matches the natural frequency of the device. Therefore, equation 2.10 is the governing equation for power conversion. However, it is instructive to look at the penalty in terms of power output if the natural frequency of the device does not match the fundamental driving vibrations. Figure 2.6 shows the power output versus frequency assuming that the mechanical and electrically induced damping factors are equal. The natural frequency of the converter for this simulation was 100 Hz, and the frequency of the input vibrations was varied from 10 to 1000 Hz. The figure clearly shows that there is a large penalty even if there is only a small difference between the natural frequency and the frequency

of the input vibrations. While a more lightly damped system has the potential for higher power output, the power output also drops off more quickly as the driving vibrations move away from the natural frequency. Based on measurements from actual devices, mechanical damping ratios of 0.01 to 0.02 are reasonable. Although, the simulation results shown in Figure 2.6 are completely intuitive, they do highlight the critical importance of designing a device to match the frequency of the driving vibrations. This should be considered a primary design consideration when designing for a sinusoidal vibration source.

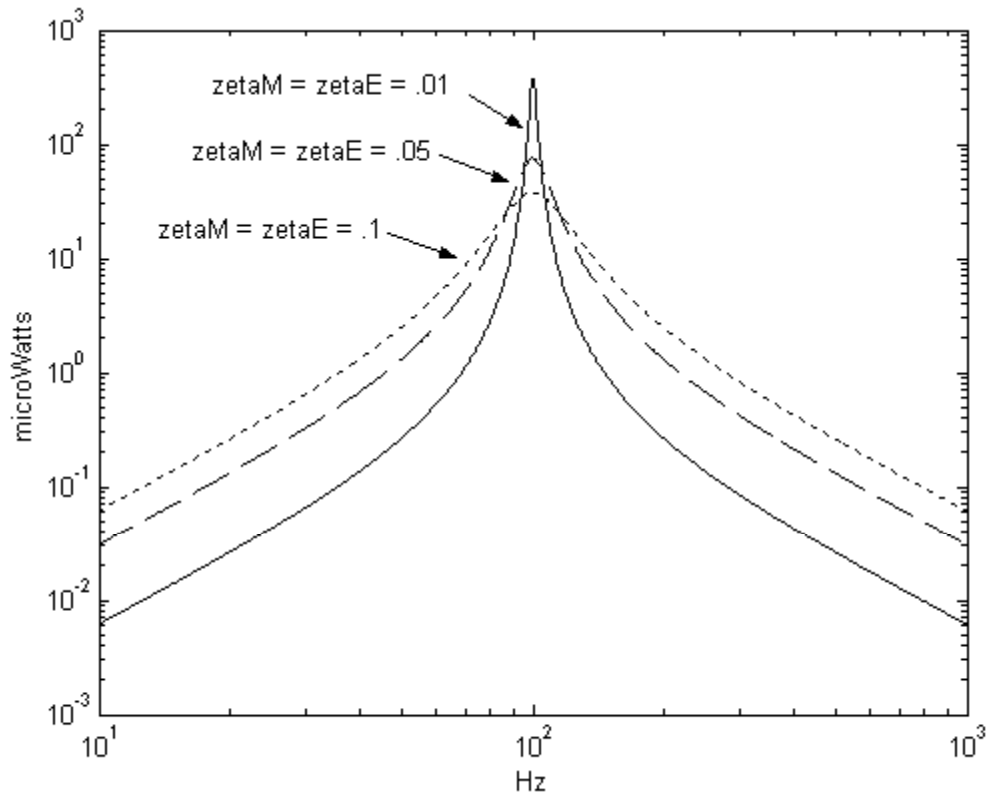


Figure 2.6: Power output vs. frequency for a ζ_m and ζ_e equal to 0.015.

In many cases, such as HVAC ducts in buildings, appliances, manufacturing floors, etc., the frequency of the input vibrations can be measured and does not change much with time. Therefore, the converters can be designed to resonate at the proper frequency,

or can have a one time adjustment done to alter their resonant frequency. However, in other cases, such as inside automobile tires or on aircraft, the frequency of input vibrations changes with time and conditions. In such cases it would be useful to actively tune the resonant frequency of the converter device. Active tuning of the device is a significant topic for future research. More will be said about this topic in Chapter 10. Finally, in some cases the input vibrations are broadband, meaning that they are not concentrated as a few discrete frequencies. The vibration environment inside automobile tires exhibits this type of behavior. A discussion of this case will be presented in Chapter 6.

While the presented generic model is quite simple and neglects the details of converter implementation, it is nonetheless very useful. Because of the simplicity of the mathematics, certain functional relationships are easy to see. While the models for real converters are somewhat more complicated, the following functional relationships are nevertheless still valid.

- The power output is proportional to the square of the acceleration magnitude of the driving vibrations.
- Power is proportional to the proof mass of the converter, which means that scaling down the size of the converter drastically reduces potential for power conversion.
- The equivalent electrically induced damping ratio is designable, and the power output is optimized when it is equal to the mechanical damping ratio.
- For a given acceleration input, power output is inversely proportional to frequency. (This assumes that the magnitude of displacement is achievable)

since as frequency goes down, the displacement of the proof mass will increase.)

- Finally, it is critical that the natural frequency of the conversion device closely matches the fundamental vibration frequency of the driving vibrations.

2.4 Efficiency of Vibration-to-Electricity Conversion

The definition of the conversion efficiency is not as simple as might be expected. Generally, for an arbitrary electrical or mechanical system, the efficiency would be defined as the ratio of power output to power input. For vibration to electricity converters the power output is simple to define, however, the input power is not quite so simple. For a given vibrating mass, its instantaneous power can be defined as the product of the inertial force it exerts and its velocity. Equation 2.11 shows this relationship where $m\ddot{y}$ is the inertial force term and \dot{y} is the velocity (y is the displacement term).

$$P = m\ddot{y}\dot{y} \quad (2.11)$$

The mass could be taken to be the proof mass of the conversion device. (It does not make sense to use the mass of the vibrating source, a machine tool base or large window for example, because it could be enormous. The conversion is limited by the size of the converter.) The displacement term, y , cannot be the displacement of the driving vibrations because the proof mass will actually undergo larger displacements than the driving vibrations. Using the displacement of the driving vibrations would therefore underestimate the input power and yield efficiencies greater than 1.

Likewise, using the theoretical displacement of the proof mass neglecting damping as the displacement term y in equation 2.11 is not very useful. The displacement of the proof mass (z) is given by $z = Qy$ where Q is the quality factor and y is the displacement

of the input vibrations. The quality factor is the ratio of output displacement of a resonant system to input or excitation displacement. In mathematical terms, the quality factor is defined as $Q = 1/(2\zeta_T)$ for linear systems where ζ_T is the total damping ratio as described earlier. If the damping (or losses) were zero, then both the displacement of the proof mass and the force exerted by the vibration source on the converter would be infinite. The input power would also then be infinite resulting in an erroneous efficiency of zero.

The most appropriate approach is to define the input power in terms of the mechanical damping ratio, which represents pure loss. The input power would then be the product of inertial force of the proof mass and its velocity under the situation where there is no electrically induced damping. The input power is then a function of the mechanical damping ratio (ζ_m). The output power is the maximum output power as defined by equation 2.10, or by more accurate models and simulations in specific cases. It is assumed that the electrically induced damping ratio (ζ_e) can be arbitrarily chosen by setting circuit parameters. An efficiency curve can then be calculated that defines efficiency as a function of the mechanical damping ratio. Such a curve is shown in Figure 2.7.

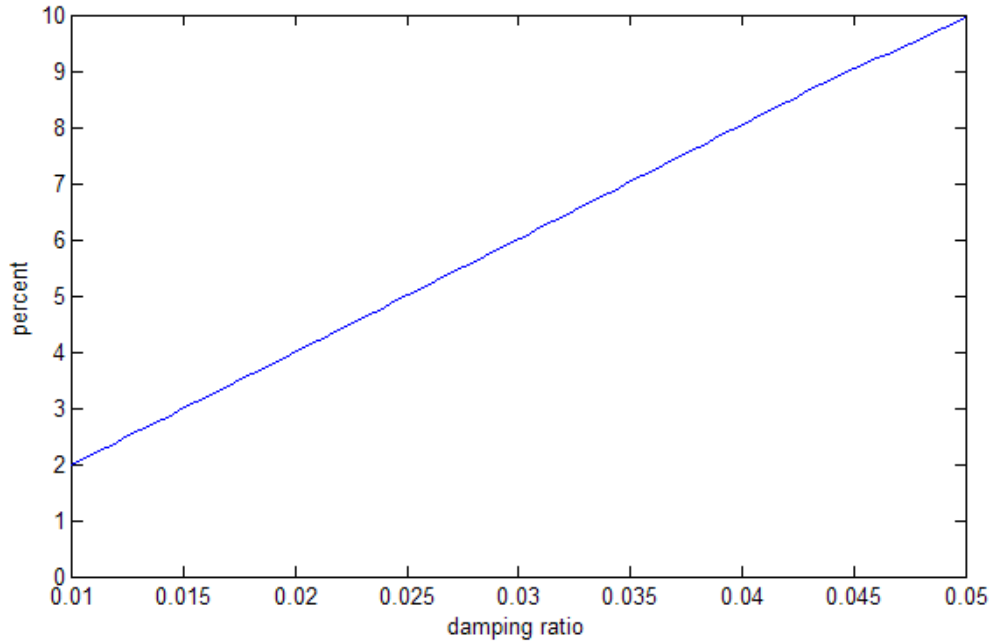


Figure 2.7: Conversion efficiency versus mechanical damping ratio.

The figure points out one of the difficulties in using efficiency as a metric for comparison, which is that the efficiency increases as the damping ratio increases. However, this does not mean that the output power increases with increased damping. As the mechanical damping ratio goes up, the input power goes down, and so while the ratio of output to input power increases, the actual output power decreases. This point is illustrated by Figure 2.8, which shows output power versus mechanical damping ratio. Because of this non-intuitive relationship between damping and efficiency, it is more meaningful to characterize energy conversion devices in terms of power density, defined as power per volume or $\mu\text{W}/\text{cm}^3$, rather than by efficiency. Throughout this thesis, devices will generally be compared by their potential power density given a standard input vibration source rather than by their efficiency. Nevertheless, for a given mechanical damping ratio, efficiency as defined and described above could be useful in comparing converters of different types.

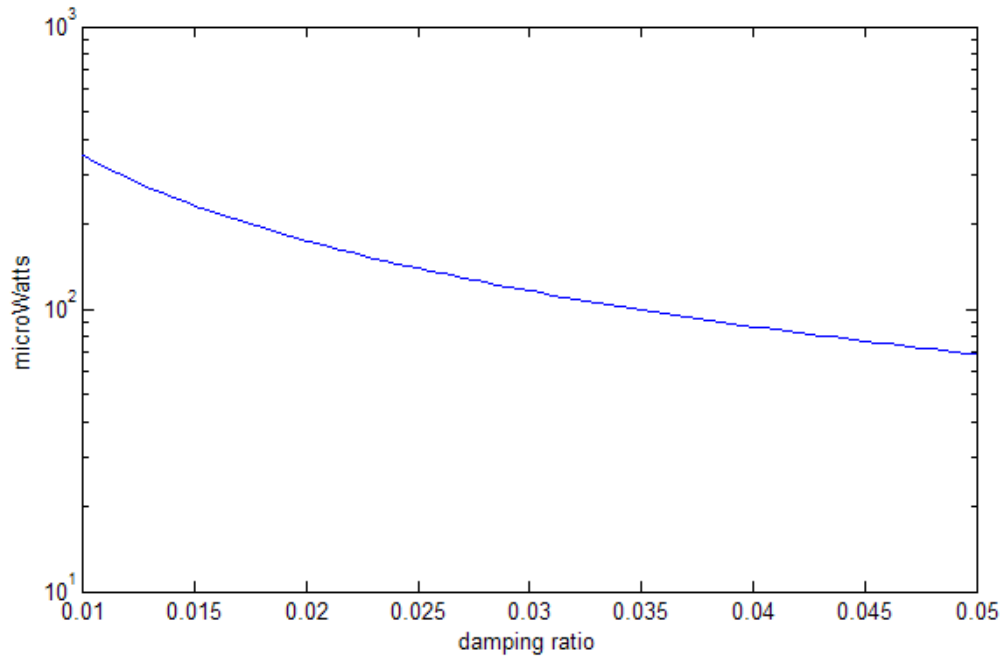


Figure 2.8: Simulated Power output versus mechanical damping ratio.

There exists perhaps a better way to define “input” power when comparing converters of different technologies. For a given mechanical damping ratio, the “input” power could be defined as the maximum possible power conversion as defined by equation 2.10, that is the power output predicted by the technology independent model presented in this chapter. Efficiency for a given device can then be defined as the actual output power divided by the maximum possible output power for the same mechanical damping ratio. This definition of efficiency is perhaps the most useful in comparing devices from different technologies.

Chapter 3: Comparison of Methods of Converting Vibrations to Electricity

There are three methods typically used to convert mechanical motion to an electrical signal. They are: electromagnetic (inductive), electrostatic (capacitive), and piezoelectric. These three methods are all commonly used for inertial sensors as well as for actuators. Conversion of energy intended as a power source rather than a sensor signal will use the same methods, however, the design criteria are significantly different, and therefore the suitability of each method should be re-evaluated in terms of its potential for energy conversion on the meso and micro scale. This chapter will provide an initial, primarily qualitative, comparison of these three methods. The comparison will be used as a basis to identify the areas that merit further detailed analysis.

3.1 Electromagnetic (Inductive) Power Conversion

Electromagnetic power conversion results from the relative motion of an electrical conductor in a magnetic field. Typically the conductor is wound in a coil to make an inductor. The relative motion between the coil and magnetic field cause a current to flow in the coil. A device that employs this type of conversion, taken from Amirtharajah and Chandrakasan (Amirtharajah & Chandrakasan, 1998) is shown in Figure 3.1.

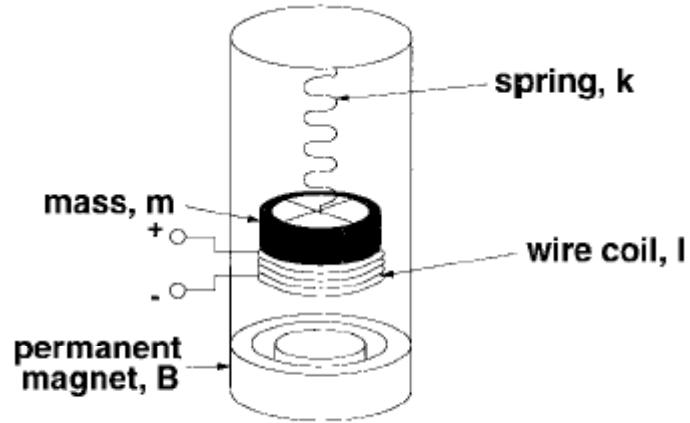


Figure 3.1: Electromagnetic conversion device from Amirtharajah and Chandrakasan, 1998.

The voltage on the coil is determined by Faraday's Law given in equation 3.1.

$$\mathcal{E} = -\frac{d\Phi_B}{dt} \quad (3.1)$$

where:

\mathcal{E} is the induced emf

Φ_B is the magnetic flux

In the simple case of a coil moving through a perpendicular magnetic field (as shown in Figure 3.1) of constant strength, the maximum open circuit voltage across the coil is given by equation 3.2.

$$V_{oc} = NBl \frac{dy}{dt} \quad (3.2)$$

where:

N is the number of turns in the coil

B is the strength of the magnetic field

l is the length of one coil ($2\pi r$)

y is the distance the coil moves through the magnetic field

Using the baseline vibrations of 2.25 m/s^2 at 120 Hz, assuming the maximum device size is 1cm^3 , and making a few assumptions about the strength of the magnetic

field and fabrication of the coil, it can easily be shown that output voltages above 100 mV are highly improbable. Table 3.1 shows open circuit voltages under various assumptions. It should be noted that the assumptions under which 124 mV could be produced are exceptionally optimistic, and frankly, it is highly unlikely that they could be achieved. In fact, the estimate of 15 to 30 mV is far more realistic given today's technology. These low voltages present a serious problem. These would be AC voltages that need to be rectified in order to be used as a power source for electronics. In order to rectify the voltages, they would have to be transformed up to the range of two to several volts necessitating a transformer with a conversion ratio on the order of 100. It would be problematic to implement such a transformer in the volume of 1cm^3 . To do so would seriously reduce the size of the proof mass that could be designed into the system, thus reducing the potential for power conversion.

Minimum line and space for coil fabrication (μm)	1	1	0.5	0.25
Strength of magnetic field (Tesla)	0.5	1	1	1
Open circuit voltage produced (mV)	<i>15.5</i>	<i>31</i>	<i>62</i>	<i>124</i>

Table 3.1: Estimates of open circuit voltage for an inductive generator.

There are a couple of significant strengths to electromagnetic implementation. First, no separate voltage source is needed to get the process started as in electrostatic conversion. Second, the system can be easily designed without the necessity of mechanical contact between any parts, which improves reliability and reduces mechanical damping. In theory, this type of converter could be designed to have very little mechanical damping.

Two research groups (Williams *et. al.*, 2001, Amirtharajah & Chandrakasan, 1998) have developed electromagnetic converters. The reasons that the results of these two projects are not completely applicable to the current project have been explained in

Chapter 1. To summarize, the device developed by Williams *et. al.*, produces voltages far too low to be of use for the current project, and the device is designed to be driven by vibrations an order of magnitude higher in frequency than those under consideration. The device built and tested by Amirtharajah and Chandrakasan is significantly larger than the upper bound of 1cm^3 currently under consideration, and the fabrication method is not scalable down to the sizes under consideration. While Williams *et. al.* built and tested a microfabricated device, it is difficult to integrate this type of device with standard microelectronics. For one thing, a strong magnet has to be manually attached to the device. Additionally, just how much this magnet and its motion would affect electronics in extremely close proximity is an open question.

3.2 Electrostatic (Capacitive) Power Conversion

Electrostatic generation consists of two conductors separated by a dielectric (i.e. a capacitor), which move relative to one another. As the conductors move the energy stored in the capacitor changes, thus providing the mechanism for mechanical to electrical energy conversion.

A simple rectangular parallel plate capacitor will be used to illustrate the principle of electrostatic energy conversion. The voltage across the capacitor is given by equation 3.3.

$$V = \frac{Qd}{\epsilon_0 lw} \quad (3.3)$$

Where:

Q is charge on the capacitor

d is the gap or distance between plates

l is the length of the plate

w is the length of the plate

ϵ_0 is the dielectric constant of free space

Note that the capacitance is given by $C = \epsilon_0 lw/d$. If the charge is held constant, the voltage can be increased by reducing the capacitance, which can be accomplished either by increasing d , or reducing l or w . If the voltage is held constant, the charge can be increased by reducing d , or increasing l or w . In either case, the energy stored on the capacitor, which is given by equation 3.4, increases. An excellent discussion of charge constrained conversion versus voltage constrained conversion is given by Meninger *et al* (Meninger *et al*, 2001). The converter, then, exists of a capacitive structure, which when driven by vibrations, changes its capacitance.

$$E = \frac{1}{2}QV = \frac{1}{2}CV^2 = \frac{Q^2}{2C} \quad (3.4)$$

The primary disadvantage of electrostatic converters is that they require a separate voltage source to initiate the conversion process because the capacitor must be charged up to an initial voltage for the conversion process to start. Another disadvantage is that for many design configurations mechanical limit stops must be included to ensure that the capacitor electrodes do not come into contact and short the circuit. The resulting mechanical contact could cause reliability problems as well as increase the amount of mechanical damping.

Perhaps the most significant advantage of electrostatic converters is their potential for integration with microelectronics. Silicon micromachined electrostatic transducers are the backbone of MEMS technology. MEMS transducers use processes very similar to microelectronics. Therefore, because of the process compatibility, it is easier to integrate electrostatic converters based on MEMS technology than either electromagnetic or piezoelectric converters. Another advantage is that, unlike electromagnetic converters,

appropriate voltages for microelectronics, on the order of two to several volts, can be directly generated. The modeling and design of electrostatic converters will be presented in detail in Chapter 7. The fabrication and testing of electrostatic vibration based generators will be presented in Chapters 8 and 9.

3.3 Piezoelectric Power Conversion

Piezoelectric materials are materials that physically deform in the presence of an electric field, or conversely, produce an electrical charge when mechanically deformed. This effect is due to the spontaneous separation of charge within certain crystal structures under the right conditions producing an electric dipole. At the present time, polycrystalline ceramic is the most common piezoelectric material. Polycrystalline ceramic is composed of randomly oriented minute crystallites. Each crystallite is further divided into tiny “domains”, or regions having similar dipole arrangements. Initially the polar domains are oriented randomly, resulting in a lack of macroscopic piezoelectric behavior. During manufacturing, the material is subjected to a large electrical field (on the order of 2kV/mm), which orients the polar domains in the direction of the external electrical field. The result is that the material now exhibits macroscopic piezoelectricity. If a voltage is applied in the same direction as the dipoles (the direction of the poling electric field), the material elongates in that direction. The opposite effect is also present, specifically if a mechanical strain is produced in the direction of the dipoles, a charge separation across the material (which is a dielectric) occurs, producing a voltage. A more detailed description of the piezoelectric effect is beyond the scope of this thesis. For a more detailed description the reader is referred to Ikeda (Ikeda 1990).

The constitutive equations for a piezoelectric material are given in equations 3.5 and 3.6.¹

$$\delta = \sigma/Y + dE \quad (3.5)$$

$$D = \epsilon E + d\sigma \quad (3.6)$$

where:

δ is mechanical strain

σ is mechanical stress

Y is the modulus of elasticity (Young's Modulus)

d is the piezoelectric strain coefficient

E is the electric field

D is the electrical displacement (charge density)

ϵ is the dielectric constant of the piezoelectric material

Without the piezoelectric coupling term, dE, equation 3.5 is simply Hooke's Law.

Likewise, without the coupling term, d σ , equation 3.6 is simply the dielectric equation, or a form of Gauss' law for electricity. The piezoelectric coupling provides the medium for energy conversion. The electric field across the material affects its mechanics, and the stress in the material affects its dielectric properties.

¹ Different nomenclature conventions are used in the literature when dealing with piezoelectric systems. Perhaps the most common is the convention used by Tzou (Tzou 1993) in which T is used as the stress variable defined as stress induced by mechanical strain and piezoelectric affects. (Note that Tzou uses σ as the stress induced only by mechanical strain.) S is used as the strain variable, s is the compliance (the inverse of elastic constant), ϵ is the dielectric constant, d is the piezoelectric strain constant, E is the electric field, and D is the electrical displacement. Furthermore, in the fully general case, each of these variables is a tensor. While this is the convention most commonly used, it seems overly burdensome for use in the current context, which is quite simple in terms of mechanics. The less common convention used by Schmidt (Schmidt, 1986) is deemed more useful for the current analysis. The primary changes from the convention used by Tzou are as follows: δ is used as strain, σ is used as stress, and Y is the elastic constant (Young's modulus). Furthermore, it is assumed that the mechanics take place along a single axis, and therefore, each variable or constant is treated as a single scalar quantity rather than a tensor. The correct value of each constant, and interpretation of each variable are determined by the specifics of the device under consideration. This convention has been used in equations 3.5 – 3.7 and will be used throughout. As a final note, it is sometimes confusing to mechanical engineers to use Y instead of E for the elastic modulus, and δ instead of ϵ for strain. However, as both E and ϵ have other meanings in the context of piezoelectric materials, other variable names must be used. The most suitable convention has therefore been chosen.

A circuit representation of a piezoelectric element is shown in Figure 3.2. The source voltage is simply defined as the open circuit voltage resulting from equation 3.6. (The open circuit condition means that the electrical displacement (D) is zero.) The expression for the open circuit voltage is given by equation 3.7.

$$V_{OC} = \frac{-dt}{\varepsilon} \sigma \quad (3.7)$$

where:

t is the thickness of the piezoelectric material.

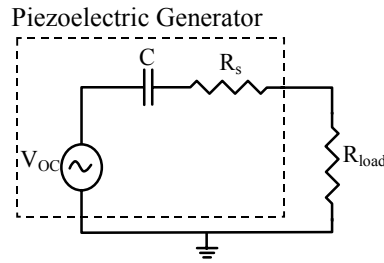


Figure 3.2: Circuit representation of a piezoelectric element.

If the piezoelectric material undergoes a periodic or sinusoidal stress due to external vibrations, an AC open circuit voltage defined by equation 3.7 can be measured across the material. If a simple resistive load is attached to the piezoelectric generator as shown in Figure 3.2, an AC voltage (V_{load}) will appear across the load. The average power delivered to load is then simply $P = V_{load}^2 / 2R_{load}$. In reality, a simple resistor is not a very useful load. The voltage should be rectified and conditioned by power electronics. However, the circuit shown in Figure 3.2 gives an easy and useful calculation of power generation.

It is commonly assumed that piezoelectric devices provide high voltages and low currents (Amirtharajah 1999). However, the voltage and current levels really depend on the physical implementation and the particular electrical load circuit used. In reality, it is quite easy to design a system that produces voltages and currents in the useful range.

Modeling and experiments performed by the author show that voltages in the range of two to several volts and currents on the order of tens to hundreds of microAmps are easily obtainable. Therefore, like electrostatic converters, one of the advantages of piezoelectric conversion is the direct generation of appropriate voltages.

A second advantage is that no separate voltage source is needed to initiate the conversion process. Additionally, there is generally no need for mechanical limit stops. (There are certain cases where limit stops are important, however, as will be covered in more detail in chapter 6, this situation is uncommon.) Therefore, in principle, these devices can be designed to exhibit very little mechanical damping. Electromagnetic converters share these same advantages. It may, therefore, be said that piezoelectric converters combine most of the advantages of both electromagnetic and electrostatic converters.

The single disadvantage up to this point of piezoelectric conversion is the difficulty of implementation on the micro-scale and integration with microelectronics. While it is true that piezoelectric thin films can be integrated into MEMS processing (Lee and White, 1995), the piezoelectric coupling is greatly reduced (Verardi *et al*, 1997). Therefore, the potential for integration with microelectronics is less than that for electrostatic converters. The design and modeling of piezoelectric converters will be covered in more detail in Chapter 4. Chapter 5 presents test results from prototype electrostatic converters including a complete wireless sensor node powered by a piezoelectric converter.

3.4 Comparison of Energy Density of Converters

A very useful comparison of the three methods can be made by considering the energy density inherent to each type of transducer. First consider piezoelectric transducers. If an open circuit load situation is assumed, the constitutive relationship given in equation 3.6 reduces to the expression in equation 3.8.

$$d\sigma = -\epsilon E \quad (3.8)$$

The energy density of a dielectric material may be expressed as $\frac{1}{2}\epsilon E^2$. (Note that the units here are J/m³.) Multiplying each side of equation 3.8 by $\frac{1}{2}E$ (or its equivalent $d\sigma/2\epsilon$) yields the expression in equation 3.9. Equation 3.9 gives energy density both in terms of the electrical state of the material (E) and the mechanical state of the material (σ). If the yield strength of the material (σ_y) is substituted for σ , then the maximum possible energy density is given by $\sigma_y^2 d^2 / 2\epsilon$. The piezoelectric coupling coefficient (k) is related to the strain coefficient (d) by the expression in equation 3.10. If k is used rather than d , the expression for maximum energy density is $\sigma_y^2 k^2 / 2Y$. This may be a more intuitive form because the coupling coefficient is often used as a measure of the quality of a piezoelectric material. A coupling coefficient of 1 implies perfect coupling between the mechanical and electrical domains. Substituting in physical data for a common piezoelectric material (PZT-5H), yields a result of 35.4 mJ/cm³. The more expensive and less common single crystal piezoelectric material, PZN-PT, yields 335 mJ/cm³. As a practical number, assuming the properties of PZT-5H and a factor of safety of 2, the maximum energy density would be 17.7 mJ/cm³.

$$\epsilon E^2 = \frac{\sigma^2 d^2}{\epsilon} \quad (3.9)$$

$$d = k \sqrt{\epsilon/Y} \quad (3.10)$$

The energy density of a capacitive device is $\frac{1}{2}\epsilon E^2$. In the case of an electrostatic variable capacitor, the dielectric constant used is that of free space (ϵ_0). What, then, should the maximum allowable electric field for the calculation be? Maluf (Maluf 2000) arbitrarily uses 5 MV/m, which of course corresponds to 5 volts over a 1 μm gap. This seems too low for an estimation of maximum energy density. The maximum electric field that gas can withstand is given by Paschen's curve. At atmospheric pressure in air, the minimum voltage of Paschen's curve, which would correspond to the maximum electric field allowable, corresponds to 100 MV/m or 100 volts over a 1 μm gap. If 100 MV/m is used as a maximum electric field, the resulting energy density is 44 mJ/cm³, or a little more than PZT-5H. However, if a more realistic 30 volts over a 1 μm gap is assumed (or 30 MV/m), the resulting energy density would be 4 mJ/cm³.

The maximum energy density of an electromagnetic actuator (or sensor) is $\frac{1}{2}B^2/\mu_0$ where B is the magnetic field, and μ_0 is the magnetic permeability. The magnetic permeability of free space is 1.26×10^{-6} H/m. Maluf uses 0.1 Tesla as a maximum value for magnetic field, which seems quite reasonable. The resulting energy density is 4 mJ/cm³. If an extremely high value of 1 Tesla is used as a maximum magnetic field, the resulting energy density would be 400 mJ/cm³. Table 3.2 summarizes the maximum energy density for all three types of converters.

Type	Governing Equation	Practical Maximum	Theoretical Maximum
Piezoelectric	$u = \frac{\sigma_y^2 k^2}{2Y}$	17.7 mJ/cm ³	335 mJ/cm ³
Electrostatic	$u = \frac{1}{2} \epsilon E^2$	4 mJ/cm ³	44 mJ/cm ³
Electromagnetic	$u = \frac{B^2}{2\mu_0}$	4 mJ/cm ³	400 mJ/cm ³

Table 3.2: Summary of maximum energy density of three types of transducers.

3.5 Summary of Conversion Mechanisms

The above discussion has been a primarily qualitative comparison of the three methods of power conversion. The purpose of performing this comparison is to serve as a basis for narrowing the range of design possibilities before performing detailed analysis, design, and optimization. The primary advantages and disadvantages of each type of converter based on this comparison are summarized in Table 3.3. It is believed that information summarized in Table 3.3 is sufficient to rule out electromagnetic converters as a suitable possibility implementation. While electromagnetic converters may be useful for larger systems, or systems exhibiting vibrations of far greater acceleration magnitude than those under consideration, they are not suitable in the context under consideration. Piezoelectric converters exhibit all of the advantages of electromagnetic converters while additionally directly providing useful voltages and exhibiting higher practical energy densities. Furthermore, the only disadvantage of piezoelectric converters is also common to electromagnetic converters. Therefore, there is no advantage of electromagnetic over piezoelectric conversion.

Type	Advantages	Disadvantages
Piezoelectric	<ol style="list-style-type: none"> 1. No separate voltage source. 2. Voltages of 2 to 10 volts. 3. No mechanical stops. 4. Highest energy density. 	<ol style="list-style-type: none"> 1. Microfabrication processes are not compatible with standard CMOS processes and piezo thin films have poor coupling.
Electrostatic	<ol style="list-style-type: none"> 1. Easier to integrate with electronics and microsystems 2. Voltages of 2 to 10 volts. 	<ol style="list-style-type: none"> 1. Separate voltage source needed. 2. Mechanical stops needed.
Electromagnetic	<ol style="list-style-type: none"> 1. No separate voltage source. 2. No mechanical stops. 	<ol style="list-style-type: none"> 1. Max. voltage of 0.1 volts. 2. Difficult to integrate with electronics and microsystems.

Table 3.2: Summary of the comparison of the three conversion mechanisms.

Because piezoelectric and electrostatic converters each have unique advantages, a detailed study of these two types has been performed. The following chapters will discuss in detail the analysis, design, optimization, fabrication, and testing of piezoelectric converters (Chapters 4 – 6) and electrostatic converters (Chapters 7 – 9).

Chapter 4: Piezoelectric Converter Design, Modeling and Optimization

A qualitative comparison of electrostatic, electromagnetic, and piezoelectric converters was presented in chapter 3. Chapter 4 will consider the modeling, design, and optimization of piezoelectric converters. Basic design configurations will first be discussed and evaluated. Models are then developed and validated. These models are then used as a basis for optimization.

4.1 Basic Design Configuration

The piezoelectric constitutive equations were presented as equations 3.5 and 3.6 in the previous chapter. They will be repeated here as equations 4.1 and 4.2 for convenience.

$$\delta = \sigma/Y + dE \quad (4.1)$$

$$D = \epsilon E + d\sigma \quad (4.2)$$

where:

δ is mechanical strain

σ is mechanical stress

Y is the modulus of elasticity (Young's Modulus)

d is the piezoelectric strain coefficient

E is the electric field

D is the electrical displacement (charge density)

ϵ is the dielectric constant of the piezoelectric material

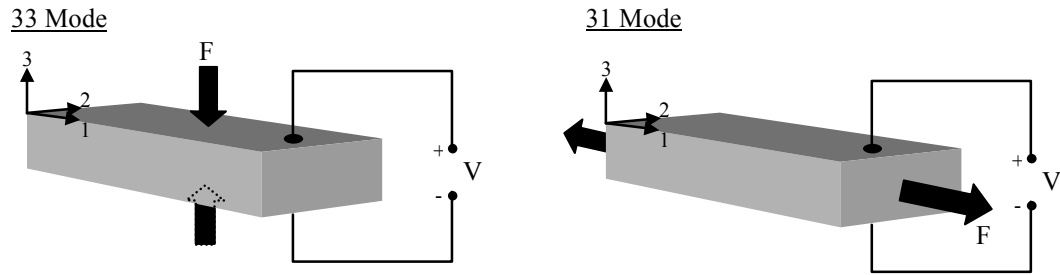


Figure 4.1: Illustration of 33 mode and 31 mode operation of piezoelectric material.

Figure 4.1 illustrates the two different modes in which piezoelectric material is generally used. The x, y, and z axes are labeled 1, 2, and 3. Typically, piezoelectric material is used in the 33 mode, meaning that both the voltage and stress act in the 3 direction. However, the material can also be operated in the 31 mode, meaning that the voltage acts in the 3 direction (i.e. the material is poled in the 3 direction), and the mechanical stress / strain acts in the 1 direction. Operation in 31 mode leads to the use of thin bending elements in which a large strain in the 1 direction is developed due to bending. The most common type of 31 elements are bimorphs, in which two separate sheets are bonded together, sometimes with a center shim in between them. As the element bends, the top layer of the element is in tension and bottom layer is in compression or vice versa. Therefore, if each layer is poled in the same direction and electrodes are wired properly, the current produced by each layer will add. For obvious reasons, this is termed parallel poling. Conversely, if the layers are poled in opposite directions, the voltages add. This is termed series poling. Bending elements with multiple layers (more than two), can also be made and internal electrodes provide the proper wiring between layers. In all cases, the potential for power conversion is the same. In theory, the poling and number of layers only affects the voltage to current ratio.

Figure 4.2 illustrates the operation of a piezoelectric bimorph mounted as a cantilever beam and poled for series operation.

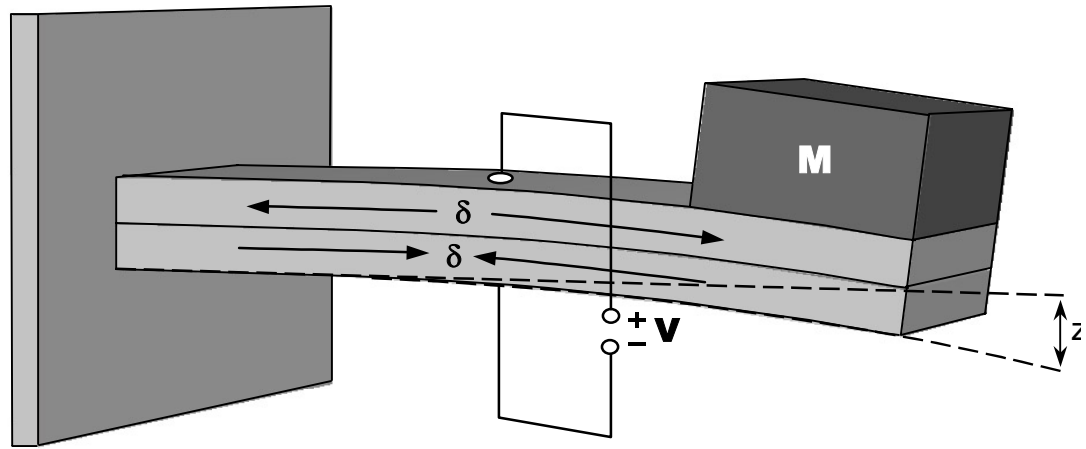


Figure 4.2: Operation of a piezoelectric bimorph.

Although the electrical/mechanical coupling for 31 mode is lower than for 33 mode, there is a key advantage to operating in 31 mode. The system is much more compliant, therefore larger strains can be produced with smaller input forces. Also, the resonant frequency is much lower. An immense mass would be required in order to design a piezoelectric converter operating in 33 mode with a resonant frequency somewhere around 120 Hz. Therefore, the use of bending elements operating in 31 mode is essential in this case.

A bending element could be mounted in many ways to produce a generator. A cantilever beam configuration with a mass placed on the free end (see Figure 4.2) has been chosen for two reasons. First, the cantilever mounting results in the lowest stiffness for a given size, and even with the use of bending elements it is difficult to design for operation at about 120 Hz in less than 1 cm³. Second, for a given force input, the cantilever configuration results in the highest average strain for a given force input.

Because the converted power is closely related to the average strain in the bender, a cantilever mounting is preferred. Note that an improvement on the simple cantilever of uniform width can be obtained varying the width of the beam. The width of the beam can be varied such that the strain along the length of the beam is the same as the strain at the fixed end, resulting in a larger average strain. This approach could result in a maximum potential average strain equal to double the average strain for the fixed width cantilever beam. The derivation of average strain for different beam-mounts, and for a beam with varying width is given in Appendix A. For the purposes of model development, a beam of uniform width is assumed in order to keep the mathematics more manageable and because benders of uniform width are easily obtainable which makes validation of the model easier. The model developed does not lose generality from the assumption of a uniform width beam. The important relationships for design that emanate from the analytical model hold equally well if a beam of non-uniform width is used.

4.2 Material Selection

Many piezoelectric materials are available. In comparing different materials a few fundamental material properties are important. The piezoelectric strain coefficient (d) relates strain to electric field. The coupling coefficient (k) is an indication of the material's ability to convert mechanical energy to electrical energy or vice versa. It is functionally related to the strain coefficient by equation 4.3.

$$k = \sqrt{\frac{Y}{\epsilon}} d \quad (4.3)$$

Clearly, materials with larger strain and coupling coefficients have a higher potential for energy conversion. The strain and coupling coefficients are different in 33 mode than in

31 mode, and are generally much higher in 33 mode. However, for reasons already explained, it is preferable in this case to design elements that operate in 31 mode. Two other material properties in equation 4.3 are also important. They are the dielectric constant (ϵ) and the elastic, or Young's, modulus (Y). A higher dielectric constant is generally preferable because it lowers the source impedance of the generator, and piezoelectric materials often have high impedance resulting in higher voltage and lower current output. The elastic modulus primarily affects the stiffness of the bender. Generally, the other material properties are more important for power conversion, and the system can be designed around the stiffness. Finally, the tensile strength of the material is very important. As mentioned earlier, the power output is related to the average strain developed. In certain cases, the design will be limited by the maximum strain that a bender can withstand. In these cases, a material with a higher tensile strength would be preferable.

Property	Units	PZT	PVDF	PZN-PT
Strain coefficient (d_{31})	10^{-12} m/v	320	20	950
Strain coefficient (d_{33})	10^{-12} m/v	650	30	2000
Coupling coefficient (k_{31})	CV/Nm	0.44	0.11	0.5
Coupling coefficient (k_{33})	CV/Nm	0.75	0.16	0.91
Dielectric constant	ϵ/ϵ_0	3800	12	4500
Elastic modulus	10^{10} N/m ²	5.0	0.3	0.83
Tensile strength	10^7 N/m ²	2.0	5.2	8.3

Table 4.1: Comparison of promising piezoelectric materials

Table 4.1 shows a few of the most promising piezoelectric materials and their key properties (Starner 1996, Park and Shrout, 1997, Piezo Systems Inc, 1998). Strain and coupling coefficient values are given for both 33 and 31 modes. In other locations the

subscripts have been omitted for simplicity, and it is assumed that the 31 mode coefficients apply. PZT (lead zirconate titanate) is probably the most commonly used piezoelectric material at the current time because of its good piezoelectric properties. PZT is a polycrystalline ceramic that, while exhibiting excellent piezoelectric coefficients, is rather brittle. There are several versions or recipes of PZT available that all have similar but slightly different properties. The specific material used here is the commonly available PSI-5H4E (Piezo Systems Inc., 1998). This same material is used for simulation, prototyping, and testing. PVDF is a piezoelectric polymer (Schmidt, 1986) that is attractive for some applications. While some of its properties are far inferior to PZT, it may be attractive in certain applications because of its higher tensile strength and lower stiffness, and because it is not brittle like ceramics. PZN-PT (Lead Zinc Niobate – Lead Titanate) is a single crystal piezoelectric material much like PZT (Park and Shrout, 1997). It has excellent properties, however, it has just become available commercially only very recently (TRS Ceramics, 2002). It is very expensive and only very small crystals can currently be produced. Because large flat elements would be needed for generators, it is not currently viable, but would be very attractive in the future. Based on this comparison of piezoelectric materials, PZT has been chosen as the primary material for further development. However, generators based on PVDF have also been modeled and optimized for comparison. As will be shown later, PZT generators are capable of higher power output than PVDF and therefore prototypes for testing have been built using PZT.

4.3 Analytical Model for Piezoelectric Generators

Assuming this basic configuration (a bender mounted as a cantilever with a mass on the end), an analytic model can be developed based on beam theory and equations 4.1 and 4.2. A convenient method of modeling piezoelectric elements is to model both the mechanical and electrical portions of the piezoelectric system as circuit elements. The piezoelectric coupling is then modeled as a transformer (Flynn and Sanders 2002). The effective number of turns (n^*) for the transformer is explained below using equations 4.5 and 4.6. Figure 4.3 shows the circuit model of the piezoelectric element.

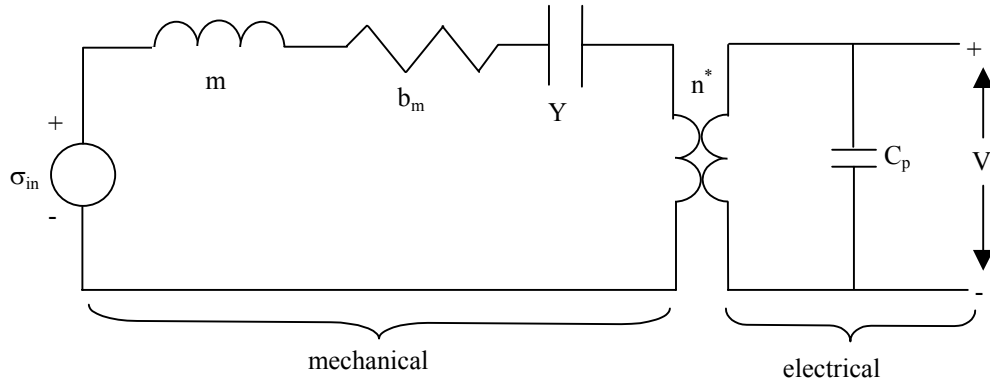


Figure 4.3: Circuit Representation of Piezoelectric Bimorph

The across variable (variable acting across an element) on the electrical side is voltage (V) and the through variable (variable acting through an element) is current (i) (Rosenberg and Karnopp, 1983). The across variable on the mechanical side is stress (σ) and the through variable is strain (δ). It is easier to use stress and strain as variables rather than force and tip displacement because the piezoelectric constant, d , relates to stress and strain. As will be shown later, strain becomes the state variable rather than the more commonly used displacement in the equations of motion. The mass attached to the end of the cantilever beam is shown as an inductor. The damper is shown as a resistor. It

should be noted that the units of the coefficient b_m in this model are Ns/m^3 rather than the conventional Ns/m . In other words, b_m relates stress to strain rate rather than force to velocity. The stiffness term, Y , relating stress to strain is shown as a capacitor. C_p is the capacitance of the bimorph. The vibration input is shown as a stress generator (σ_{in}), which comes from the input acceleration \ddot{y} . The relationship between the input vibrations (\ddot{y}) and an equivalent stress input is:

$$\sigma_{in} = \frac{m}{b^{**}} \ddot{y} \quad (4.4)$$

where:

b^{**} = geometric constant relating average bending stress to force at the beam's end

The transformer relates stress (σ) to electric field (E) at zero strain, or electrical displacement (D) to strain (δ) at zero electric field. So the equations for the transformer follow directly from equations 4.1 and 4.2, and are:

$$\sigma = -dYE \quad (4.5)$$

$$D = -dY\delta \quad (4.6)$$

The equivalent turns ratio (n^*) for the transformer is then $-dY$.

Once the circuit has been defined and the relationship between the physical beam and the circuit elements on the “mechanical” side of the circuit has been specified, system equations can be developed using Kirchhoff's Voltage Law (KVL) and Kirchhoff's Current Law (KCL). Appendix A contains a full derivation of the system equations. Only the resulting model, shown in equations 4.7 and 4.8, is presented here.

$$\ddot{\delta} = \frac{-k_{sp}}{m} \delta - \frac{b_m b^{**}}{m} \dot{\delta} + \frac{k_{sp} d}{m t_c} V + b^* \ddot{y} \quad (4.7)$$

$$\dot{V} = \frac{-Y d t_c}{\epsilon} \dot{\delta} \quad (4.8)$$

where:

V = voltage at the output

t_c = thickness of a single layer of the piezoelectric material

k_{sp} = equivalent spring constant of cantilever beam

b^* = geometric constant relating average strain to displacement at the beam's end

Note that no electrical load has been applied to the system. The right side of Figure 4.3 is an open circuit, and so no power is actually transferred in this case. It is instructive to consider the case in which a simple resistor is used as the load. This results in the circuit model shown in Figure 4.4. The resulting change in the system equations is only minor, and is shown in equations 4.9 and 4.10.

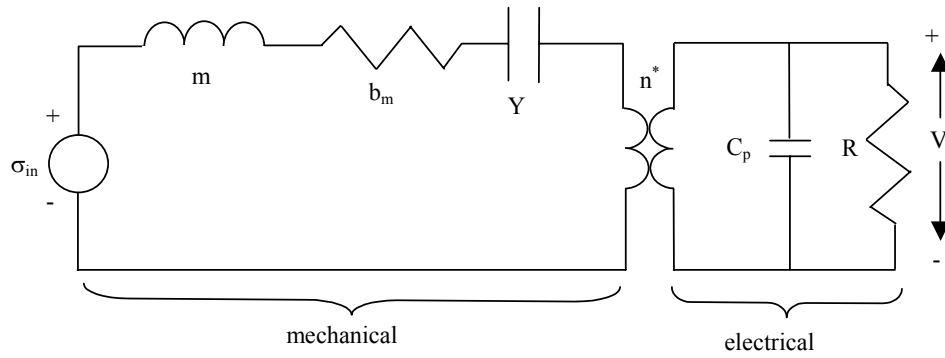


Figure 4.4: Circuit model of piezoelectric bimorph with resistive load

$$\ddot{\delta} = \frac{-k_{sp}}{m} \delta - \frac{b_m b^{**}}{m} \dot{\delta} + \frac{k_{sp} d}{m t_c} V + b^* \ddot{y} \quad (4.9)$$

$$\dot{V} = \frac{-Y d t_c}{\epsilon} \dot{\delta} - \frac{1}{R C_p} V \quad (4.10)$$

where:

R = load resistance

C_p = capacitance of the piezoelectric bender

This model is similar in many respects to the general second order model discussed in Chapter 2 and given in equation 2.1. Although this model is 3rd order, it is linear, and

equation 4.9 is in the same basic form as equation 2.1. The electrical coupling term,

$\frac{k_{sp} dn}{mt_c} V$, in equation 4.9 can be used to find the equivalent linear damping ratio, ζ_e ,

which represents the electrically induced damping that was the basis of power conversion for the generic model of Chapter 2. The equivalent electrically induced damping ratio is given by the expression in equation 4.11. (Again, see Appendix A for a full derivation of equation 4.11.)

$$\zeta_e = \frac{\omega k^2}{2\sqrt{\omega^2 + 1/(RC)^2}} \quad (4.11)$$

where:

k = piezoelectric coupling coefficient. (See equation 4.3 for relationship between coupling coefficient and strain coefficient (d)).

By proper selection of the load resistance (R), ζ_e will be equal to the mechanical damping ratio ζ . The optimal value of R can be found in two ways. The first is to simply equate the expression in equation 4.11 with the mechanical damping ratio, ζ , and solve for R . Alternatively, if it is assumed that the frequency of the input vibrations (ω) is equal to the undamped natural frequency of the device (ω_n), an analytical expression for power transferred to the load can be obtained. This expression is given in equation 4.12. The optimal value of R can then be found by differentiating equation 4.12 with respect to R , and solving for R . In either case, the expression in equation 4.13 is found to give the optimal load resistance. Note that if there were no piezoelectric coupling (i.e. the coupling coefficient $k = 0$), the optimal load resistance would just be $1/\omega C$, which is obvious by inspection of the circuit in Figure 4.4.

$$P = \frac{1}{\omega^2} \frac{RC^2 \left(\frac{Y_c dt_c b^*}{\varepsilon} \right)^2}{(4\zeta^2 + k^4)(RC\omega)^2 + 4\zeta k^2(RC\omega) + 2\zeta^2} A_{in}^2 \quad (4.12)$$

$$R_{opt} = \frac{1}{\omega C} \frac{2\zeta}{\sqrt{4\zeta^2 + k^4}} \quad (4.13)$$

where:

A_{in} = acceleration magnitude of input vibrations

4.4 Discussion of Analytical Model for Piezoelectric Generators

Because of the close similarity of the model for the piezoelectric generator to the generic conversion model presented in Chapter 2, the conclusions drawn for the generic model also hold for the piezoelectric case.

1. The output power is proportional to the proof mass. This is not immediately obvious from the expression for power in equation 4.12. However, for a given frequency, if the mass increases other variables in equation 4.12 also change increasing the predicted power output. For example, if the mass increases, either the thickness or the width of the beam must go up to maintain the same resonant frequency. If the thickness increases, both t_c and b^* will increase, thus raising the predicted power out. If the width increases, C increases, again resulting in a higher predicted output power.
2. The power output is proportional to the square of the acceleration magnitude of the driving vibrations. This follows directly from equation 4.12.

3. There is an equivalent electrically induced damping ratio, ζ_e , and the power output is maximized when that damping ratio is equal to the mechanical damping ζ in the system. Furthermore, as shown in Figure 2.5, it is better for ζ_e to be larger than ζ , rather than smaller than ζ . As shown in equation 4.11, ζ_e is a function of R , and can therefore be controlled by the selection of the load resistance. Figure 4.5 shows the simulated power output for vs. load resistance, and Figure 4.6 shows the same simulated power output vs. the equivalent electrically induced damping factor. The mechanical damping ratio for these two simulations was 0.02. These two figures clearly demonstrate the above conclusion. In reality, the load will not be as simple as a resistor. However, the load will remove kinetic energy from the vibrating beam-mass system, and so act as electrically induced damping. Some circuit parameters can such that the power transfer to the load is maximized even with more complicated load circuitry.

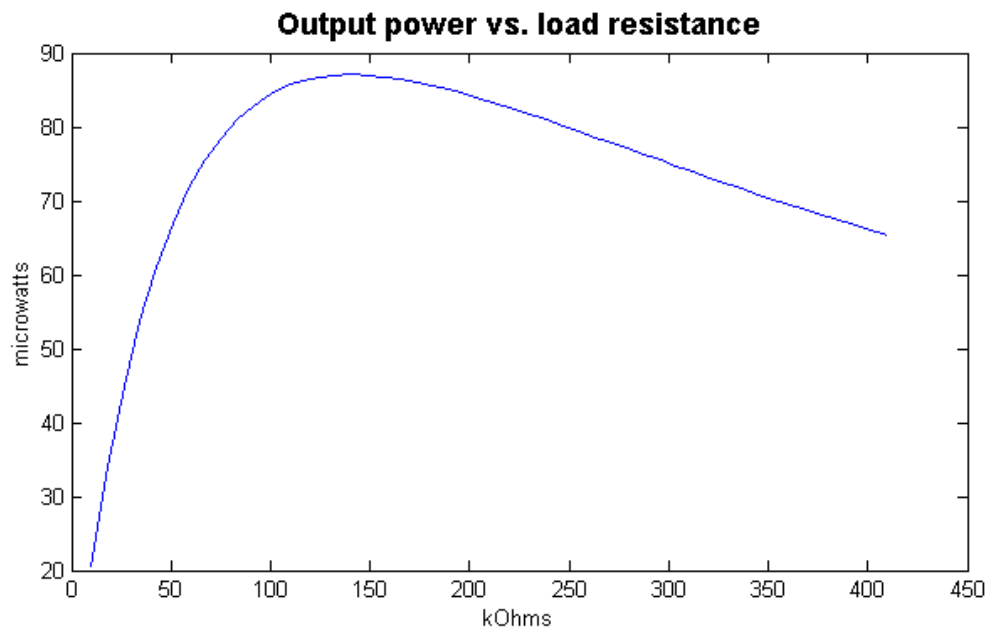


Figure 4.5: Simulated output power vs. load resistance

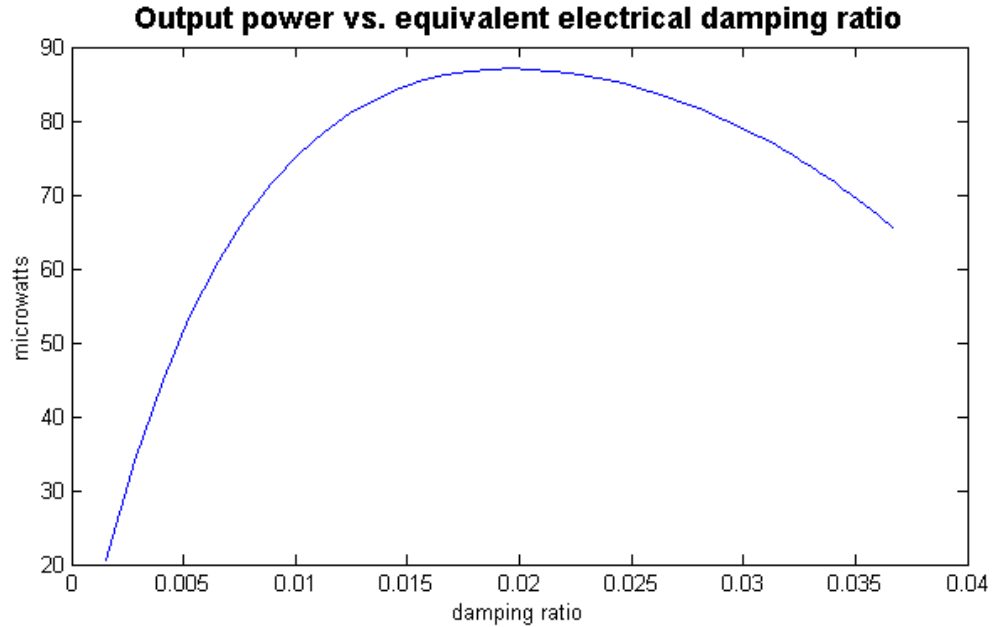


Figure 4.6: Simulated output power vs. equivalent electrical damping ratio

4. The power output is inversely related to the frequency. Again, this follows from equation 4.12. It should be noted, that as the frequency of the system goes down, the displacement of the proof mass goes up. Depending on how the lower frequency was achieved (i.e. longer beam, thinner beam, increased mass, etc.) the increased displacement may be accompanied by increased strain. There is a limit to how much strain can be supported by the material, and so in some cases, the power output may be limited by the fracture strain of the piezoelectric material. This will be discussed in more detail later in Chapter 6.
5. Finally, equation 4.12 assumes that the frequency of the driving vibrations is equivalent to the natural frequency of the generator device. It is critical that these two frequencies match as closely as possible. The relationship

demonstrated in Figure 2.6, that the output power falls off dramatically as the driving frequency diverges from the natural frequency, also holds in the present case.

In reality it is not all that useful to design a generator to power a resistor, the value of which is chosen to optimize power transfer from the generator to the resistor. In practice the generator would be used in conjunction with a rectifier to charge up a storage capacitor, which feeds into a voltage regulator or DC-DC converter. This circuit configuration is shown later in Figure 4.14, and the implications for power conversion are discussed in more detail in section 4.7. However, at this point it should be noted that all of the above conclusions still hold for the real circuit. *The primary difference is that the equivalent electrically induced damping is no longer a function of a load resistance, but of other parameters, some of which are designable.*

4.5 Initial Prototype and Model Verification

A bimorph made of lead zirconate titanate (PZT) with a steel center shim was used as a prototype to verify the model in equations 4.9 and 4.10. The bimorph, with attached mass (made from a relatively dense alloy of tin and bismuth) and fixture, is shown in Figure 4.7.

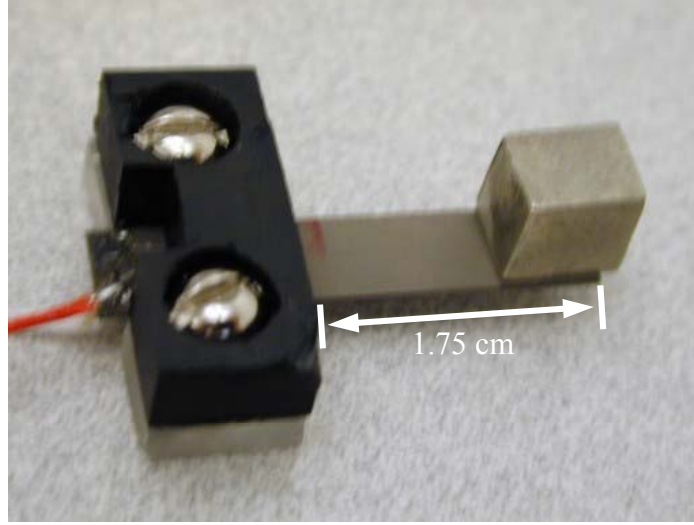


Figure 4.7: Piezoelectric (PZT) generator prototype.

The total volume of the bimorph and mass is approximately 1 cm^3 . The converter was driven with vibrations at 120 Hz with an acceleration magnitude of 2.25 m/s^2 . Again, these vibrations are roughly equivalent to those measured on a small microwave oven. The beam length and mass were chosen so that the system's natural frequency matched the driving frequency. The mechanical damping ratio, ζ , was measured as 0.015, and the piezoelectric coupling coefficient, k_{31} , was measured to be 0.12. The damping ratio was measured by applying an impulse to the system, and then measuring output. An example of the resulting damped oscillations is shown in Figure 4.8. The magnitude of oscillations is measured at two separate points, n periods apart. The damping ratio can then be calculated as a function of the log decrement of the two magnitudes, and the number of periods as shown in equation 4.14 (James *et. al.*, 1994).

$$\zeta = \frac{1}{2\pi n} \ln \left(\frac{x_1}{x_2} \right) \quad (4.14)$$

where:

x_1 is the magnitude at one point of the damped oscillation

x_2 is the magnitude of the damped oscillation n periods later

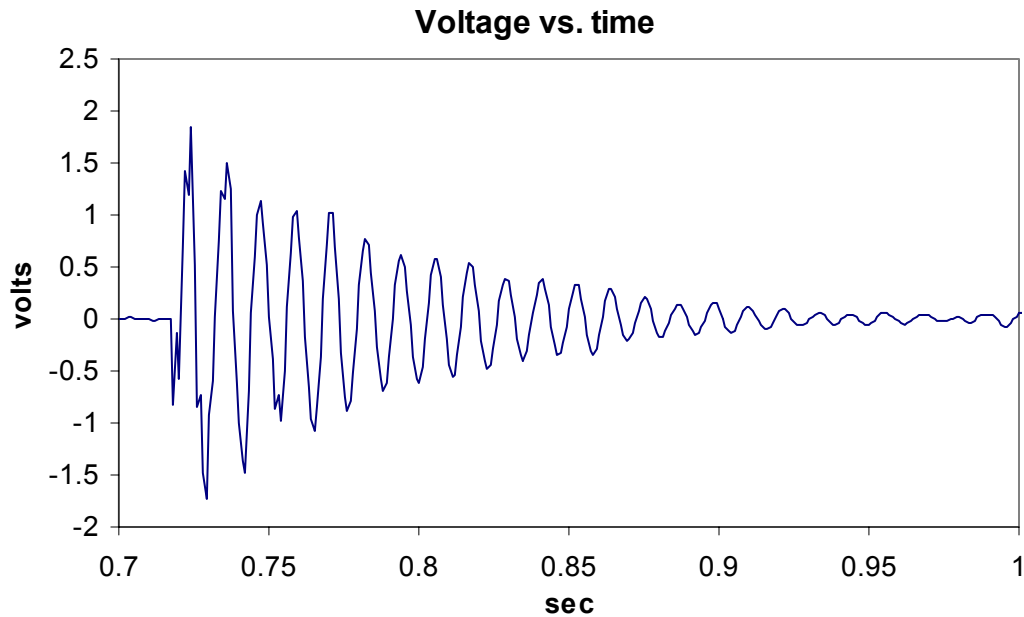


Figure 4.8: Damped oscillation from a force impulse to a piezoelectric generator

Several measurements were taken. The mean value of these measurements was 0.014 and the standard deviation was 0.0057. The coupling coefficient was measured by attaching a strain gauge to the base of the bender as shown in Figure 4.9. The bender was then excited, and the voltage output from both the strain gauge and the piezoelectric bender was measured. The average stress in the area on which the strain gauge is attached (see Figure 4.9) is easily calculated from the output of the strain gauge. The average stress for the whole beam is then calculated based on the average stress in the area on which the strain gauge was attached and the geometry of the beam. Likewise the electric field (E) generated in the bender is easily calculated from the measured voltage and the thickness of the bender. The coupling coefficient can then be calculated from the average stress and electric field by the piezoelectric relationship shown in equation 4.15 (Piezo Systems Inc., 1998). The published coupling coefficient for the particular material used is 0.32. Because of the bonding between layers and a metal center shim, the

published data from the manufacturer says to expect a working coupling coefficient of 0.75 times that of the published value (or 0.24) when using benders. However, the average measured value by the method just explained was 0.12, or about half of what it should be. The measured value for the coupling coefficient has been used in simulations rather than the published value, which has resulted in much better agreement between the model and experiments. Other material properties were taken from published data (Piezo Systems Inc., 1998).

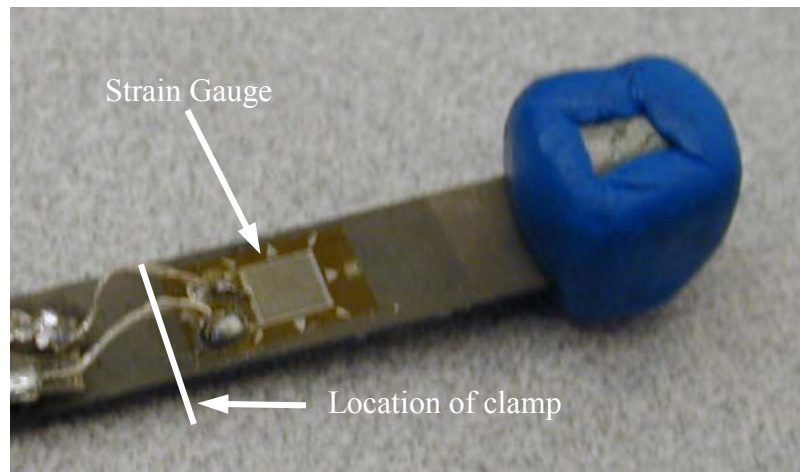


Figure 4.9: Piezoelectric bender with strain gauge attached in order to measure coupling the coupling coefficient

$$k = \frac{E\sqrt{Y\varepsilon}}{\sigma_{ave}} \quad (4.15)$$

The prototype piezoelectric generator shown in Figure 4.7 was mounted to the vibration exciter as shown in Figure 4.10. The prototype was then driven with vibrations of 2.25 m/s^2 at 120 Hz.



Figure 10: First piezoelectric prototype mounted to the vibrometer for testing

The output was measured using a range of different load resistances. The measured and simulated output power versus load resistance is plotted in Figure 4.11. The measured and simulated voltage across the resistor is shown in Figure 4.12. The good agreement between experiments and simulations verifies that the model shown in equations 4.9 and 4.10 is sufficiently accurate to use for design and optimization purposes. Furthermore, the models can be used to obtain relatively accurate estimates of power generation.

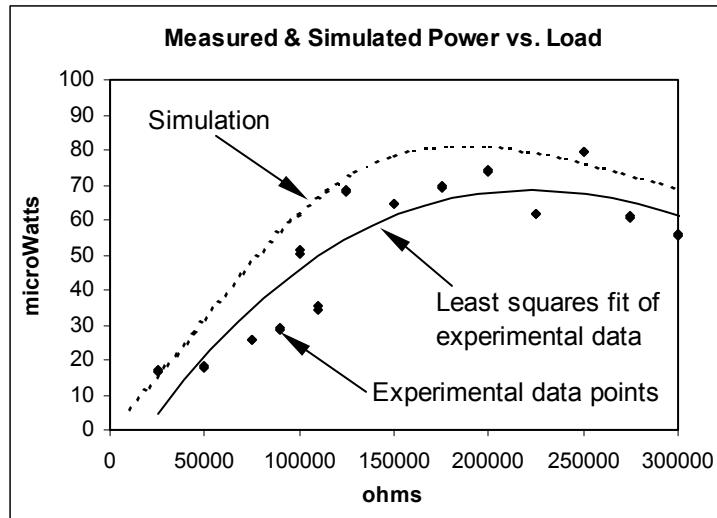


Figure 4.11: Measured and simulated output power versus resistive load.

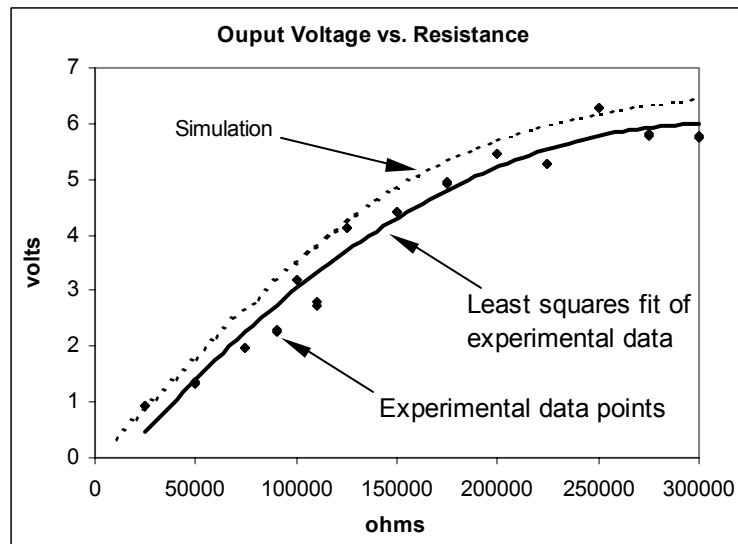


Figure 4.12: Measured and simulated output voltage versus resistive load

If a bimorph poled for parallel operation was used instead, the optimal load resistance would be cut by a factor of 4, the output voltage would be cut in half, and the output current would increase by a factor of 2. In either case, the output voltage is within the right order of magnitude.

4.6 Design Optimization

Having defined the basic design concept, and developed and validated a model to predict the power output of that design concept, a formal mathematical optimization can be performed in order to choose dimensions and design parameters.

The objective function for the optimization is the analytical expression for power shown equation 4.12. The output of a dynamic simulation could be, and has been, used as the “objective function”. However if the driving vibrations are concentrated at a single frequency and are sinusoidal in nature, then the output of the dynamic simulation matches equation 4.12 exactly. The variables over which the design can be optimized are shown in Table 4.2.

Variables	Description
l_m	Length of the mass
h_m	Height of the mass
w_m	Width of the mass
l_b	Length of the cantilever beam
w_b	Width of the cantilever beam
l_e	Length of the electrode on the beam surface
t_p	Thickness of piezoelectric layer
t_{sh}	Thickness of the center shim
R_{load}	Load resistance

Table 4.2: Design variables for optimization

It should perhaps be noted that the piezoelectric material is not conductive. Charge can be collected from the surface and transported to the load only if the surface is covered by a conductive electrode. Portions of the surface that are not covered by an electrode act as a simple mechanical element, but do not contribute to the electrical power generation.

For this reason the length of the beam and the length of the electrode are separate variables that do not necessarily have the same value.

Other parameters, such as bender capacitance and the proof mass are determined by these design variables with a few assumptions. First, it is assumed that a more dense material for the proof mass will always be preferable to a less dense material. This follows from the linear relationship between mass and power output, and the fact that the designs will generally be constrained by volume, not weight. Tungsten is the most dense commonly used material at 19 g/cm^3 . Rhenium is actually slightly more dense, but is quite rare and extremely expensive. Other more dense materials are not commonly available and/or radioactive. Because of its extremely high hardness, tungsten is difficult to work with. Typically tungsten/nickel alloys are used which have densities around 17 g/cm^3 . A 90% tungsten, 6% nickel, 4% copper alloy with a density of 17 g/cm^3 was assumed as the material for the proof mass for optimization purposes. Second, the baseline input vibrations of 2.25 m/s^2 at 120 Hz were used for optimization. The optimal design will, of course, be one with a resonant frequency at or very near 120 Hz. The optimization routine could be repeated for any particular vibration input magnitude and frequency, and would yield different design parameters. Third, it is assumed that only one piezoelectric layer is used on each side of the bender (this is typically referred to as a bimorph). More layers could be used; however this does not impact the output power. The overall thickness of the piezoelectric material affects the output power, and the number of layers adding up to that thickness changes the voltage to current output ratio and the optimal load resistance, but not the output power. Therefore, a single layer was assumed, and the actual design can incorporate more layers to give the appropriate

voltage and current outputs. Finally, two separate optimizations were performed for two different materials, PZT and PVDF. As discussed previously, these two materials represent the most attractive commercially available materials.

The optimization problem can then be formulated as shown in Figure 4.13. There are three nonlinear constraints, and one linear constraint. The linear constraint, $l_e - l_b - l_m \leq 0$, results from the fact that it is physically impossible for the electrode length to be longer than the sum of the beam and mass lengths. The first two non-linear constraints, $(l_b + l_m)w_m h_m < 1\text{cm}^3$ and $(l_b + l_m)w_b h_m \leq 1\text{cm}^3$, represent overall volume constraints. As mentioned previously, the goal in this context is to design a vibration converter using a space of 1cm^3 or less. Finally, the maximum strain cannot exceed the yield strain of the piezoelectric material, which leads to the third non-linear constraint. The average strain is one of the state variables of the dynamic simulation, and the maximum strain can be easily calculated from the average strain and the beam geometry. Although strain is not a direct function of the design parameters, it can nevertheless be used as a non-linear optimization constraint.

<p>Maximize: $P = f(l_m, h_m, w_m, l_b, w_b, l_e, t_p, t_{sh}, R_{load})$</p> <p>Subject to:</p> $(l_b + l_m)w_m h_m \leq 1\text{cm}^3$ $(l_b + l_m)w_b h_m \leq 1\text{cm}^3$ $l_e - l_b - l_m \leq 0$ $l_m, h_m, w_m, l_b, w_b, l_e, t_p, t_{sh}, R_{load} \geq 0$

Figure 4.13: Formulation of optimization problem

The optimization problem represented in Figure 4.13 was solved using the nonlinear constrained optimization function in the optimization toolbox in Matlab. Matlab uses the Sequential Quadratic Programming (SQP) method to solve nonlinear

constrained optimization problems (Schittowski, 1985). The design that results from the optimization routine (using PZT as the piezoelectric material) is an extremely long, narrow bender with a narrow, tall proof mass. The exact design parameters that result are shown in Table 4.3.

Variables	Optimized Value
l_m	5 cm
h_m	1 cm
w_m	1.8 mm
l_b	6.3 mm
w_b	1.8 mm
l_e	6.3 mm
t_p	0.321 mm
t_{sh}	0.256 mm
R_{load}	463 k Ω
P_{out}	1.7 mW

Table 4.3: Optimal design parameters and predicted power output.

This design is clearly not practical. In addition to its awkward aspect ratio, it has a very high electrical impedance. Therefore practical limits need to be placed on some of the design variables. These limits can be represented as additional linear constraints. The variables to which the limits should be applied, and the precise values of the limits will depend on the application space of the converter and available materials. Table 4.4 shows one practical set of limits, the resulting design parameters, and simulated output power. Table 4.5 shows another set of limits with resulting design parameters and output power. PZT was used for the optimizations of both Table 4.4 and 4.5. Because the supplier (Piezo Systems Inc.) used by the author for PZT bimorphs only carries two thicknesses, the optimization routine was limited to 0.139 mm and 0.278 mm. Likewise,

the supplier only carries elements with center shim thickness of 0.102 mm. It will be noticed that the differences between the design shown in Table 4.4 and that shown in Table 4.5 is that the total length limit is relaxed to 3 cm for the latter the thicker of the two available benders was used. Assuming that any thickness could be purchased, results in the optimal design parameters and power output shown in Table 4.6.

Variables	Optimized Value	Range Allowed
l_m	8.5 mm	$l_m + l_b < 1.5$ cm
h_m	7.7 mm	$h_m \leq 7.7$ mm
w_m	6.7 mm	All, subject to total volume constraint
l_b	6.5 mm	$l_m + l_b < 1.5$ cm
w_b	3 mm	All, subject to total volume constraint
l_e	6.5 mm	All, subject to above constraint
t_p	0.139 mm	$t_p = 0.139$ mm
t_{sh}	0.102 mm	$t_{sh} = 0.1016$
R_{load}	200 k Ω	All greater than zero
P_{out}	215 μ W	

Table 4.4: Optimal design parameters and output power for one reasonable set of parameter constraints.

Variables	Optimized Value	Range Allowed
l_m	17.3 mm	$l_m + l_b < 3$ cm
h_m	7.7 mm	$h_m \leq 7.7$ mm
w_m	3.6 mm	All, subject to total volume constraint
l_b	10.7 mm	$l_m + l_b < 3$ cm
w_b	3.2 mm	All, subject to total volume constraint
l_e	10.7 mm	All, subject to above constraint
t_p	0.278 mm	$t_p = 0.278$ mm
t_{sh}	0.102 mm	$t_{sh} = 0.1016$
R_{load}	151 k Ω	All greater than zero
P_{out}	380 μ W	

Table 4.5: Optimal design parameters and output power for a second reasonable set of parameter constraints.

Variables	Optimized Value	Range Allowed
l_m	2.56 cm	$l_m + l_b < 3 \text{ cm}$
h_m	7.7 mm	$h_m \leq 7.7 \text{ mm}$
w_m	3.3 mm	All, subject to total volume constraint
l_b	4.4 mm	$l_m + l_b < 3 \text{ cm}$
w_b	3.3 mm	All, subject to total volume constraint
l_e	4.4 mm	All, subject to above constraint
t_p	0.149 mm	All
t_{sh}	0.120 mm	All
R_{load}	170 k Ω	All greater than zero
P_{out}	975 μW	

Table 4.6: Optimal design and power output if piezo-ceramic thickness other than those available from the supplier are used.

A coupling coefficient of 0.18 and a damping ratio of 0.02 were used for optimization purposes based on the measured values as described earlier. Measurements were taken with PZT-5H with a brass shim instead of the PZT-5A with a steel shim as used for the first prototype. Also, the clamp was decreased in size. These two changes account for the higher coupling coefficient (0.18 compared to 0.12 previously) and the higher damping ratios (0.02 compared to 0.014) used in the optimizations. It should be noted that all tests were performed with benders that have center shims made of metal (either steel or brass). The metal center shim adds strength to the bender and makes it much easier to cut and solder because of the brittleness of the piezoelectric ceramic. However, the presence of a center shim reduces the effective coupling coefficient (Piezo Systems Inc., 1998) by about 25%. If this published value is correct, improved power output could be obtained by using a bender without a center shim. However, the

reliability of such a bender would be greatly reduced. Because of the reliability issues, it has been decided to use benders with a center shim for the purposes of this study.

A separate set of optimizations was performed using PVDF as the piezoelectric material. The published coupling coefficient of PVDF is 0.106, but the effective value in a laminate is about 75% of that number, or 0.08. (Starner, 1996). However, its yield strain is far greater than that of PZT (0.02 for PVDF compared with 0.0014 for PZT). The design resulting from an unconstrained optimization is a very short, very wide design. This would naturally be expected because PVDF is so much more compliant than PZT. Again, practical limitations must be put on the design space. Tables 4.7 and 4.8 show two sets of reasonable limits on design variables with the resulting optimal designs and output parameters. The power output is somewhat lower than that for the PZT benders due to the greatly reduced coupling coefficient of PVDF. Also, the impedance of the designs is significantly higher due to the drastically reduced dielectric constant of PVDF. However, the optimization routine assumes that the bender is constructed of a single layer of piezoelectric material on each side. In reality, each side of the bender could consist of multiple layers wired in parallel, which would significantly reduce the impedance of the generator. However, it is generally the case that a PZT design will have lower impedance than a PVDF design.

Variables	Optimized Value	Range Allowed
l_m	7 mm	All, subject to total volume constraint
h_m	7.7 mm	$h_m \leq 7.7$ mm
w_m	10 mm	$w_m \leq 10$ mm
l_b	3 mm	$l_b \geq 3$ mm
w_b	10 mm	$w_b \leq 10$ mm
l_e	3 mm	$l_e \geq 3$ mm
t_p	0.178 mm	All
t_{sh}	0 mm	All
R_{load}	27.6 M Ω	All greater than zero
P_{out}	181 μ W	

Table 4.7: Optimal design parameters and power output for a PVDF design with one set of reasonable constraints.

Variables	Optimized Value	Range Allowed
l_m	4.6 mm	All, subject to total volume constraint
h_m	7.7 mm	$h_m \leq 7.7$ mm
w_m	15 mm	$w_m \leq 15$ mm
l_b	2.1 mm	$l_b \geq 3$ mm
w_b	15 mm	$w_b \leq 15$ mm
l_e	2.1 mm	$l_e \geq 3$ mm
t_p	0.117 mm	All
t_{sh}	0 mm	All
R_{load}	23.6 M Ω	All greater than zero
P_{out}	211 μ W	

Table 4.8: Optimal design parameters and power output for a PVDF design with a second reasonable set of constraints

Although the power output is lower, there are some potential benefits to pursuing a design using PVDF. First, PVDF has greater reliability because it is not a brittle material. If the yield strength of the PVDF is exceeded, it will not crack and it will continue to

function fairly well. If the yield strength of PZT is exceeded, it will crack and will lose most of its power conversion capability. Secondly, PVDF is much less expensive than PZT. So, if cost is the driving factor, and sufficient energy can be obtained with PVDF, it may be preferable.

As mentioned, the above optimizations were performed assuming a two layer bimorph (a single layer on each side of the center shim), and that the layers are arranged in series. No constraint was applied to the output voltage. In fact all of the optimal designs result in a fairly large (around 20 volts) output voltage. However, the desired output voltage can be tailored by adjusting the number of layers, while keeping the total piezo thickness constant. As mentioned previously, dividing the piezoelectric material into multiple layers wired in parallel does not affect the output power; it only affects the voltage to current ratio. Therefore, the above optimizations can easily be applied to multi-layer benders with lower output voltages.

4.7 Analytical Model Adjusted for a Capacitive Load

The above analysis and optimization is based on a simple resistive load. This is not a very realistic approximation of a real electrical load. In reality, the electrical system would look something like the circuit shown in Figure 4.14. The mechanical representation for the piezoelectric bender is not shown in Figure 4.14, but is exactly the same as in Figures 4.3 and 4.4.

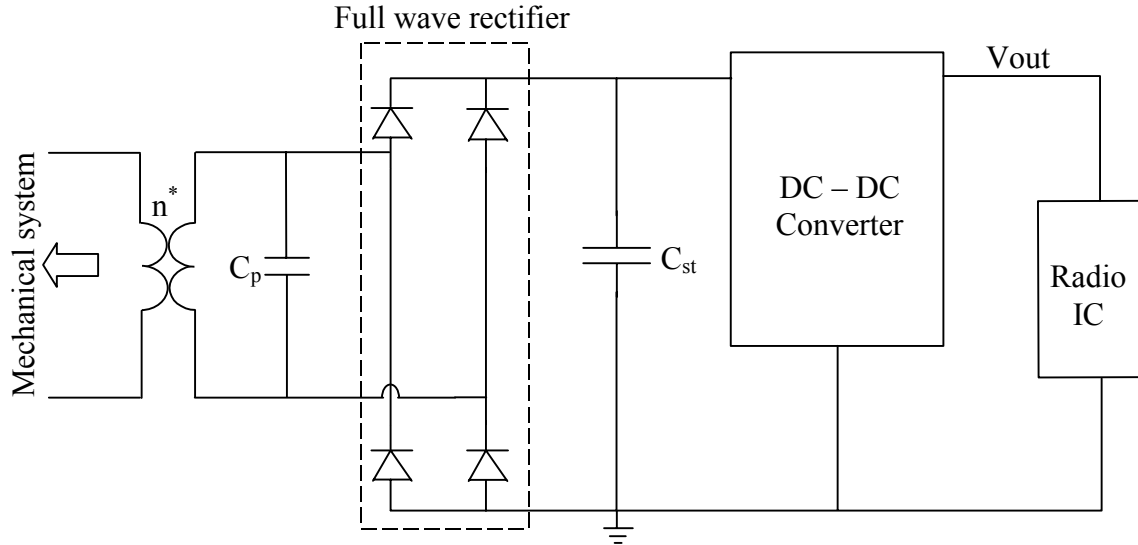


Figure 4.14: Piezoelectric generator with power circuitry for a piezoelectric generator. Mechanical portion of piezoelectric generator is not shown.

The piezoelectric bender charges up a large energy storage capacitor (C_{st}) through a full wave rectifier. The large capacitor acts as an energy buffer between the input from the piezoelectric generator the output to the integrated circuit (IC). In wireless systems, the IC will typically turn on for a short period of time and receive and transmit data, and then turn back off, or go into a sleep mode (Rabaey *et al*, 2000). In the sleep mode it will dissipate very little power. In the “on” (or transmit) state, it will dissipate far more power than can be generated by the piezoelectric bender. So, during the “on” state, the voltage across the storage capacitor will fall, and during the sleep state, the voltage on the storage capacitor will increase. The IC will typically operate at very low duty cycles, around 1%. A DC-DC converter is needed so that the varying voltage across C_{st} can be converted to a steady DC voltage for the IC. The system should be designed such that the average input power is at least as great as the average output power.

A large capacitor is chosen as the means of energy storage rather than a rechargeable battery for two primary reasons. First, a capacitor can be charged up by any

method. In this case, it will be slowly charged up by pulses of current from the piezoelectric generator. Rechargeable batteries perform better when a specific charge-up profile is followed. While the specific charge-up profile is different for each battery chemistry, it is generally preferable to charge the battery up quickly with relatively large currents. In particular, lithium-ion batteries perform better when charged at constant current. This type of charge-up profile is simply not possible using a vibration generator unless sophisticated battery charging circuitry is used. However, the use of such circuits would greatly increase the power dissipation of the system, and therefore is not practical. The second reason is that rechargeable batteries have a relatively short shelf life. Therefore, after 1 to 2 years of operation the batteries would need to be replaced. Capacitors, on the other hand, have a virtually infinite lifetime. While it is true that batteries have a higher energy density than capacitors, the new “super” capacitors (Raible and Michel, 1998, National Research Council, 1997) have significantly improved energy density that is more than adequate for the current application. Rechargeable lithium-ion batteries have a maximum energy density of about 1000 J/cm^3 . In practice, commercial batteries range from about $100 - 700 \text{ J/cm}^3$. Super capacitors have energy densities ranging from about 10 to 90 J/cm^3 , which is about a factor of 10 lower than rechargeable batteries. However, even 5 joules of power would keep a node using an average of $100 \text{ } \mu\text{W}$ alive for over 10 hours with no power input.

About 99% of the time, the IC is in sleep mode and drawing very little current, the DC-DC converter may be shut down during sleep mode as well, therefore, the vibration converter is basically just charging up the storage capacitor. A simplified circuit representation for this case is shown in Figure 4.15. This representation is useful in that

it is simple enough to develop an analytical model from which design criteria may be taken.

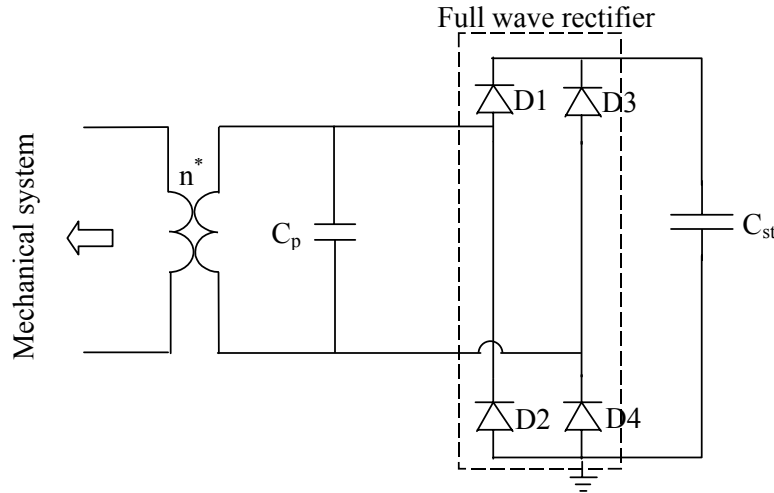


Figure 4.15: Simplified circuit used to analyze the charging of the storage capacitor.

There are potential three states in which the circuit shown in Figure 4.15 can operate. An ideal diode model is used in order to simplify the analysis. The assumption of ideal diodes does not change the basic functionality of the circuit. The ideal diode model assumes that the offset voltage of the diodes is zero, that the on resistance is zero, and that there is no reverse leakage. As V increases and reaches V_{st} , diodes D1 and D4 will turn on, diodes D2 and D3 will be off. This situation will be referred to as **stage 1**. As V decreases and reaches $-V_{st}$, then diodes D2 and D3 will conduct, and D1 and D4 will be off. This is referred to as **stage 2**. Finally if V is greater than $-V_{st}$ and less than V_{st} , all four diodes will be off. This is referred to as **stage 3**. Note that in stage 1, V_{st} and V are equal (assuming ideal diodes), and in stage 2, V_{st} is equal to $-V$. In any of the three stages, the first of the system equations is unchanged. This equation is given above as equation 4.7 and repeated here as equation 4.15.

$$\ddot{\delta} = \frac{-k_{xp}}{m}\delta - \frac{b_m b^{**}}{m}\dot{\delta} + \frac{k_{sp}d}{mt_c}V + b^*\ddot{y} \quad (4.15)$$

In stage 3, the circuit situation is the same as that shown Figure 4.3, and so the second of the two system equations is the same as that given above as equation 4.8 and repeated here as equation 4.16. The equivalent circuit representation for stage 1 is shown in Figure 4.16. Stage 2 results in the same circuit representation except that the polarity of V needs to be changed. The second of the two system equations for both stage 1 and stage 2 is given in equation 4.17. So, the system model is given by equations 4.15 and 4.17 for stages 1 and 2, and equations 4.15 and 4.16 for stage 3.

$$\dot{V} = \frac{-Ydt_c}{\varepsilon}\dot{\delta} \quad (4.16)$$

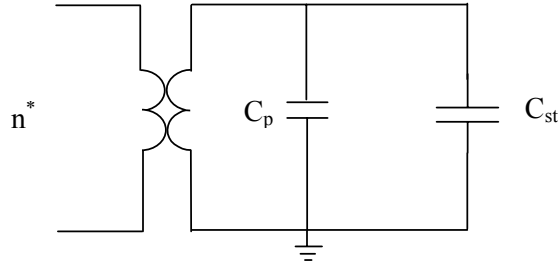


Figure 4.16: Equivalent circuit representation for stage 1, diodes D1 and D4 conducting.

$$\dot{V} = \frac{-YdA}{C+C_{st}}\dot{\delta} \quad (4.17)$$

where:

A is the area covered by the electrode on the piezoelectric bender

If a few simplifying assumptions are made, a closed form solution can be found that will provide some design intuition. In particular, it can be seen how a capacitive load circuit changes design criteria as compared to a resistive load. As with previous calculations, it is assumed that the input vibrations are a sinusoid of fixed frequency and

amplitude. The second assumption that needs to be made is that the level of strain in the piezoelectric material is also a sinusoid of fixed amplitude and frequency. In other words, it is assumed that the voltage on the storage capacitor (C_{st}) does not affect the magnitude of the strain in the bender. This is not completely true according to the equations of motion. The voltage on C_{st} affects the level of apparent damping, and therefore will affect the magnitude of the strain in the bender. However, because the apparent damping only changes a little, the affect on the strain is not dramatic. As will be shown, this assumption results in only small deviations between the closed form analytical solution, and a full dynamic simulation.

A new variable, V_s , can then be defined, which is the voltage that would result across the piezoelectric bender if there were no electrical load (i.e. the open circuit voltage). The circuit for this situation is shown in Figure 4.3. Following from equation 4.8, V_s can then be given by equation 4.18. Given the assumption that the strain in the bender is a sinusoid of constant magnitude and frequency, a circuit representation for stage 1 (diodes D1 and D4 conducting) that is equivalent to the representation shown in Figure 4.16 is shown in Figure 4.17. V_s is given by $V_s(t) = V_s \sin(\omega t)$. Note that the variable V in Figure 4.16 is the same variable as V is equations 4.15 through 4.17.

$$V_s = \frac{-Ydt_c}{n\epsilon} \delta \quad (4.18)$$

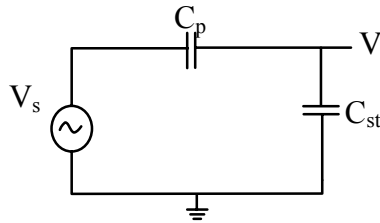


Figure 4.16: Equivalent circuit representation for stage 1, diodes D1 and D4 conducting.

During each half cycle of the sinusoid a certain amount of charge is transferred to C_{st} , causing the voltage on C_{st} to rise. This amount of charge, ΔQ , is given by equation 4.19.

$$\Delta Q = \int_{t_1}^{t_2} i dt = \int_{t_1}^{t_2} C_p \frac{d(V_s - V)}{dt} dt \quad (4.19)$$

where:

- t_1 is the time at which diodes D1 and D4 turn on. The point at which the circuit enters stage 1.
- t_2 is the time at which diodes D1 and D4 turn off. The point at which the circuit leaves stage 1 and enters stage 3. This is also the point at which V_s reaches its maximum point.

For simplicity, $V(t_2)$ will be referred to as V_2 , and $V(t_1)$ as V_1 . ΔQ can then also be given by $\Delta Q = C_{st}(V_2 - V_1)$. The increase in energy per half cycle is given by equation 4.20. Realizing the power transferred is just $2 \cdot f \cdot \Delta E$, where f is the frequency of the input vibrations, then power can be given by the expression in equation 4.21, which is a function of V_1 and V_s rather than V_1 and V_2 . Thus, all of the terms in the expression for power as shown in equation 4.21 are known at the start of each half cycle. See Appendix A for a detailed derivation of the power expression.

$$\Delta E = \frac{1}{2} (Q_2 V_2 - Q_1 V_1) = \frac{1}{2} C_{st} (V_2^2 - V_1^2) \quad (4.20)$$

$$P = \frac{\omega C_{st}}{2\pi (C_{st} + C_p)^2} \{ C_p^2 V_s^2 + 2C_{st} C_p V_s V_1 - C_p V_1^2 (2C_{st} + C_p) \} \quad (4.21)$$

4.8 Discussion of Analytical Model Changes for Capacitive Load

Equation 4.21 has been arranged such that V_2 has been replaced by V_s and other constants. V_s is a function of the magnitude of the input vibrations, material properties, and the geometry of the design. The only variable in equation 4.21 that will change during the operation of the generator and load circuit is V_1 . We can see therefore that the power transfer to the storage capacitor during a given half cycle is a function of V_1 , the voltage on the storage capacitor at the beginning of the half cycle. Figure 4.17 shows the power transferred to the storage capacitor as a function of time. The design parameters used for the simulation are those shown in Table 4.4. A storage capacitor of 1 μF was used. This compares to a piezo device capacitance of 9.4 nF. Two traces are shown. The solid line shows the result of a dynamic simulation, and the dashed line is calculated from equation 4.21. It will be noticed that the assumptions stated above do in fact alter the output power, but the agreement between the simulation and analytical solution are close enough to use the analytical solution to generate some design intuition. Figure 4.18 shows the power output as a function of V_1 . It can clearly be seen from Figure 4.18 and less clearly from equation 4.21 that there is an optimal operating voltage. For this particular simulation, the maximum value of V (the value of V_s) when C_{st} is completely charged up is 21 volts. The optimal value of V_1 in this case is 10 or 11 volts depending on whether the analytical solution or the simulation is used. In general, the optimal operating point will be near half of the maximum voltage, V_s . In fact, if equation 4.21 is differentiated with respect to V_1 and solved for the optimal V_1 , the resulting expression for the optimal value of V_1 is:

$$V_{1opt} = \frac{C_{st}}{2C_{st} + C_p} V_s \quad (4.22)$$

Because C_{st} will naturally be much larger than C_p , V_{1opt} is very closely equal to half V_s .

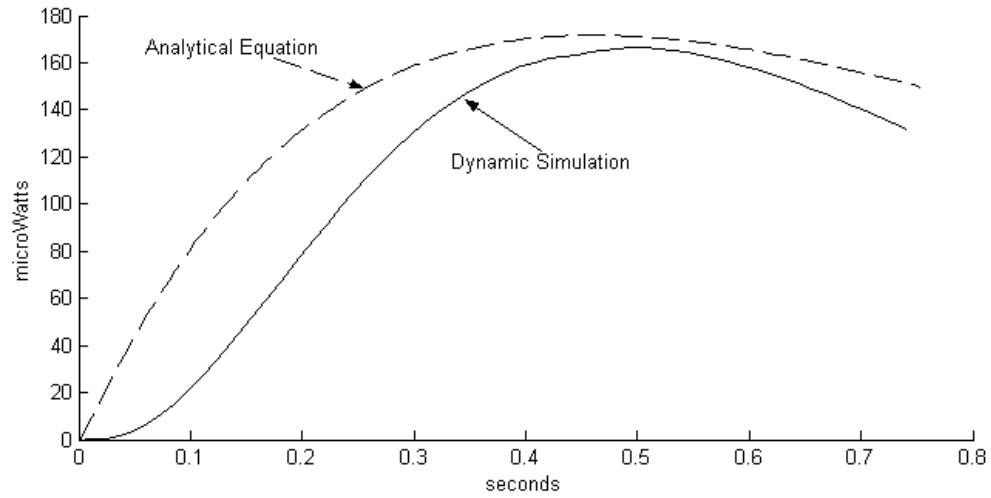


Figure 4.17: Simulated and analytically calculated power output vs. time. Storage capacitance is $1 \mu\text{F}$.

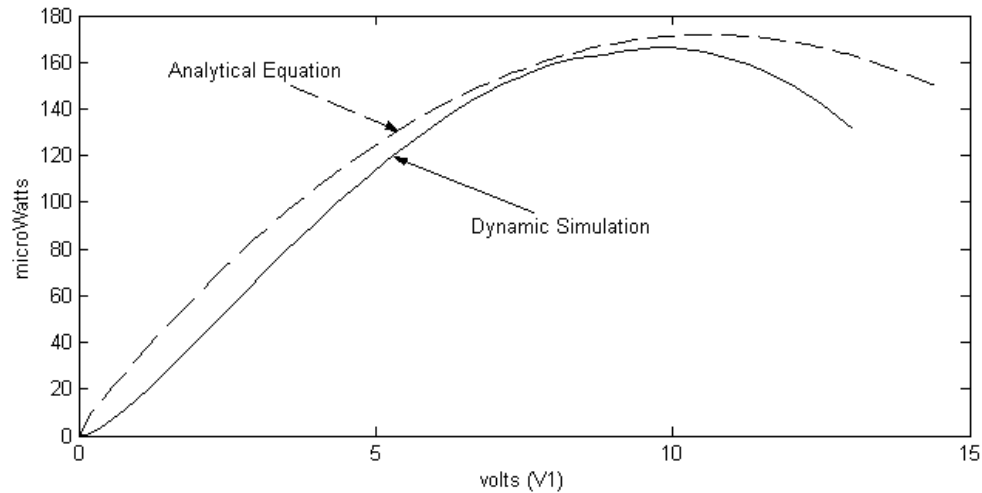


Figure 4.18: Simulated and analytically calculated power output vs. V_1 , the voltage across the storage capacitor at the moment that the diodes turn on in a given half cycle. Storage capacitance is $1 \mu\text{F}$.

A few different considerations will dictate the selection of the value of the storage capacitor. First, the capacitor has to be large enough to source the necessary current to the load when it turns on without dropping the input voltage to the DC-DC converter below an acceptable value. Second, in many instances, it will be desirable to store as much energy as possible. In this case, super capacitors that can have capacitances in

excess of 1 F/cm^3 , would seem to be a good choice. The volume constraints of the entire system should also be taken into account when selecting the capacitor. In addition to all of these considerations, equation 4.21 indicates the level of power transfer is related to value of the storage capacitance. Figure 4.19 shows the maximum power transfer as a function of the storage capacitance. The power for each value of C_{st} was calculated as the maximum power transfer with respect to V_1 , or the highest point on the graph shown in Figure 4.18. The design parameters and input for the generator are the same as those used in Figure 4.17 and 4.18. As the value of C_p in this simulation is 9.4 nF , it is clear that power transfer is best when C_{st} is at least many times larger than C_p . If C_{st} is about a factor of 100 or more greater than C_p , the value of C_{st} has very little affect on the power transfer. Therefore, C_{st} should be as large as possible subject to the volume constraints of the system.

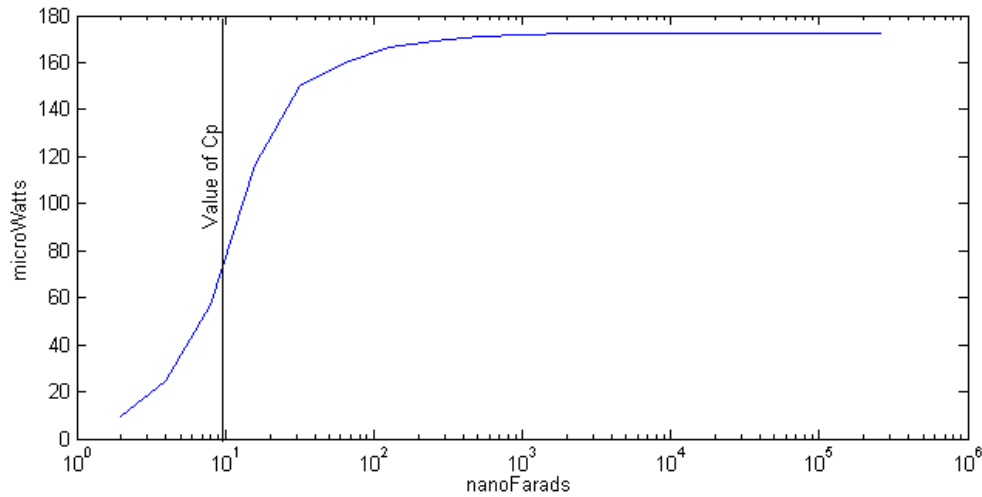


Figure 4.19: Power transfer to storage capacitor (C_{st}) as a function of the capacitance of C_{st} .

Clearly the capacitance of the piezo generator will also have an affect on the power transfer. This is clearly evident from equation 4.21. However, one cannot change the capacitance of the generator without changing other design parameters that will affect

both the relationship between the strain and V_s , and the relationship between the input vibrations and average strain. Equation 4.21 indicates that all other things being constant, the power output is higher for a higher value of C_p (assuming that C_{st} is larger than C_p). However, it is difficult to see how this translates into the selection of design parameters for the bender because a change in design parameters will also affect V_s . A full optimization incorporating all design variables will be discussed in the following section. As will be shown, simply increasing C_p by creating more, thinner layers in the bender while keeping the same overall geometry (a multilayer bender) does not increase the power output.

The model developed for a capacitive load will serve as the basis for design parameter optimization. In addition, however, it provides some engineering intuition into how the system should be designed. First, C_{st} should be chosen to be as large as possible within the volume and cost constraints of the system. Also, the entire system should be designed such that the voltage on the storage capacitor during operation does not drop below about half the maximum voltage generated by the piezoelectric bender. If the voltage is allowed to drop below this value, the power transfer to the storage capacitor is significantly reduced. At the very least, this would require that the storage capacitor be large enough that during a typical transmit cycle its voltage does not drop by more than about 25% of the maximum voltage generated by the generator (V_s). Ideally, however, the load circuitry would adjust its duty cycle and possibly its operation in other ways depending on the voltage across the storage capacitor.

4.9 Design Optimization for a Capacitive Load

In the same manner as was done for the generator connected to a resistive load, a formal mathematical optimization can be performed in order to choose optimal dimensions for a generator with a capacitive load. Because the model for output power is different, the resulting model will not be exactly the same as that for the resistive load. As discussed, there is no load resistance to affect the power transfer, and the load capacitance does not affect the power transferred in the same way as the load resistance.

The variables over which the design can be optimized are exactly the same as shown above in Table 4.2 except that the load resistance (R_{Load}) is removed from the optimization. The storage capacitance (C_{st}) could be included as an optimization variable, but this seems pointless since, as was shown in the previous section, a larger C_{st} will always result in more power output. However, as long as C_{st} is about a factor of 100 greater than the capacitance of the bender, the value of C_{st} has very little affect on the power transfer. The optimization is performed with the same input vibrations of 2.25 m/s^2 at 120 Hz representing a sort of mean value for those vibrations measured. The same assumptions regarding mass, the bimorph configuration, and materials (PZT and PVDF) made earlier also apply to the optimizations for a capacitive load.

Using a $C_{st} = 1 \mu\text{F}$, the results of a dynamic simulation of equations 4.14 – 4.16 can be used as the “objective function” for the Matlab optimization routines. The power transfer varies as a function of time, or more precisely as a function of the ratio between current and maximum voltages across the storage capacitor. It was decided that the most relevant value to use for a basis of optimization is the maximum power output (the

highest point on the curve shown in Figure 4.17). As before, the only constraints on the optimization are those on the overall size, electrode length, and maximum strain.

The optimizations were performed using the material properties for PZT. The optimal design value variables and power output are shown in Table 4.9.

Variables	Optimized Value
l_m	5 cm
h_m	1 cm
w_m	1.7 mm
l_b	8.4 mm
w_b	1.7 mm
l_e	8.4 mm
t_p	0.352 mm
t_{sh}	0.281 mm
P_{out}	1.4 mW

Table 4.9: Optimal design parameters and output power for capacitive load case using a storage capacitance of $1\mu\text{F}$.

As was the case with the resistive load the optimization results in an impractical design. The aspect ratio is awkward, and would not likely result in a very robust structure. Interestingly, the optimal design parameters are not far removed from those for the resistive load case. Additional constraints need to be added in order for a practical design to result. The specific constraints depend on the specific application. Optimization results for two additional sets of reasonable constraints are shown in Tables 4.10 and 4.11. The constraints in Table 4.10 correspond to those shown in Table 4.4 for the resistive load case. The design was optimized such that the total length could not exceed 1.5 cm, and the thickness of the bender was constrained to that which is available from the supplier used (Piezo Systems Inc.). Table 4.11 corresponds to Table 4.6 for the

resistive load case. The total length constraint is increased to 3 cm, and it is assumed that benders of any thickness could be purchased or manufactured.

Variables	Optimized Value	Range Allowed
l_m	7.0 mm	$l_m + l_b < 1.5$ cm
h_m	7.7 mm	$h_m \leq 7.7$ mm
w_m	6.7 mm	All, subject to total volume constraint
l_b	8.0 mm	$l_m + l_b < 1.5$ cm
w_b	3 mm	All, subject to total volume constraint
l_e	7.7 mm	All, subject to above constraint
t_p	0.139 mm	$t_p = 0.139$ mm
t_{sh}	0.102 mm	$t_{sh} = 0.1016$
P_{out}	125 μ W	

Table 4.10: Optimal design parameters and output power for capacitive load of 1 μ F incorporating one reasonable set of parameter constraints.

Variables	Optimized Value	Range Allowed
l_m	24.5 mm	$l_m + l_b < 3$ cm
h_m	7.7 mm	$h_m \leq 7.7$ mm
w_m	3.3 mm	All, subject to total volume constraint
l_b	5.5 mm	$l_m + l_b < 3$ cm
w_b	3.3 mm	All, subject to total volume constraint
l_e	5.5 mm	All, subject to above constraint
t_p	0.149 mm	All
t_{sh}	0.120 mm	All
P_{out}	695 μ W	

Table 4.11: Optimal design parameters and output power for a second reasonable set of parameter constraints. Load was 1 μ F.

The basic results for the capacitive load case closely follow the resistive load case. The optimal design variables vary somewhat between the two cases, but are not

dramatically different. The power transfer is somewhat higher for a pure resistive load. Additionally, in both cases, the high cost of adding extra geometry constraints can be seen. Simply opening up the length constraint and allowing for any bender thickness increases the power output by several times for both resistive and capacitive loads.

As with the resistive load case, the optimization was performed assuming a simple layer bimorph. No constraint was placed on the voltages generated. It was mentioned before, that the bender could be designed with an appropriate number of layers to generate the desired voltage to current ratio without affecting the output power. The fact that the number of layers does not affect the power output, but only the voltage to current ratio is more intuitive for the case of the resistive load because the impedance of the load was being changed to match the impedance of the bender. However, in the current case, the load impedance is not being changed, and so one may intuitively think that using a multilayer bender with the same geometry would increase (or at least affect) the power transfer because it decreases the impedance of the bender. This, however, is not the case, as long as the storage capacitance is much greater (about a factor of 100) than the bender capacitance. The desired operating voltage across the storage capacitor can then be designed if the magnitude of the input vibrations is roughly known by specifying the number of layers in the optimal design. Figure 4.20 shows the power output versus time for the design shown in Table 4.10 for 1, 2, and 4 layer benders. Notice that the maximum power output does not change, but the voltage at which the maximum power output occurs changes. Figure 4.21 shows the voltage across the storage capacitor from the same simulation. Notice that for the benders with more layers, the voltage at which

maximum power transfer occurs is reached more quickly, but that voltage is lower. A storage capacitance of $4\text{ }\mu\text{F}$ was used in these simulations.

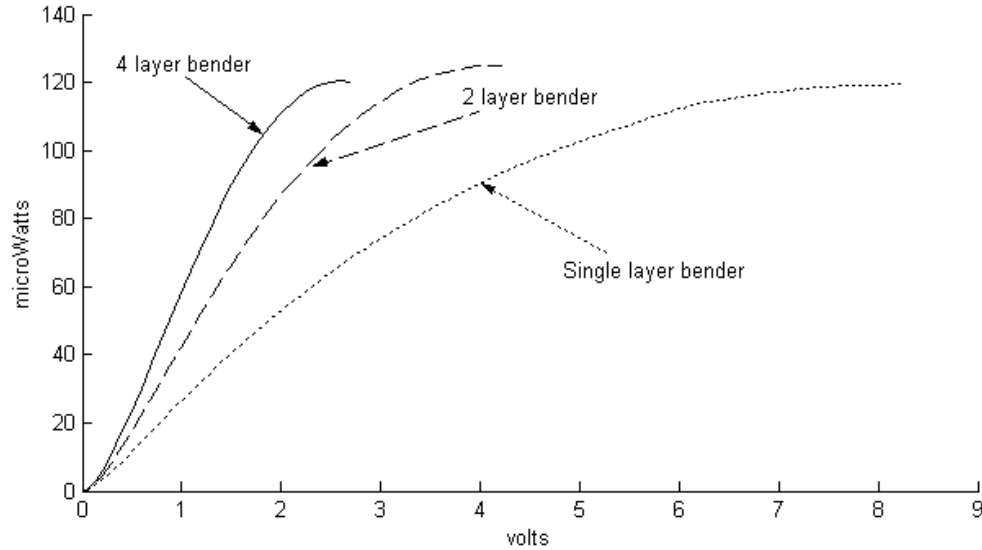


Figure 4.20: Power transferred vs. voltage across the storage capacitor for the same design incorporating different numbers of layers in the piezoelectric bender.

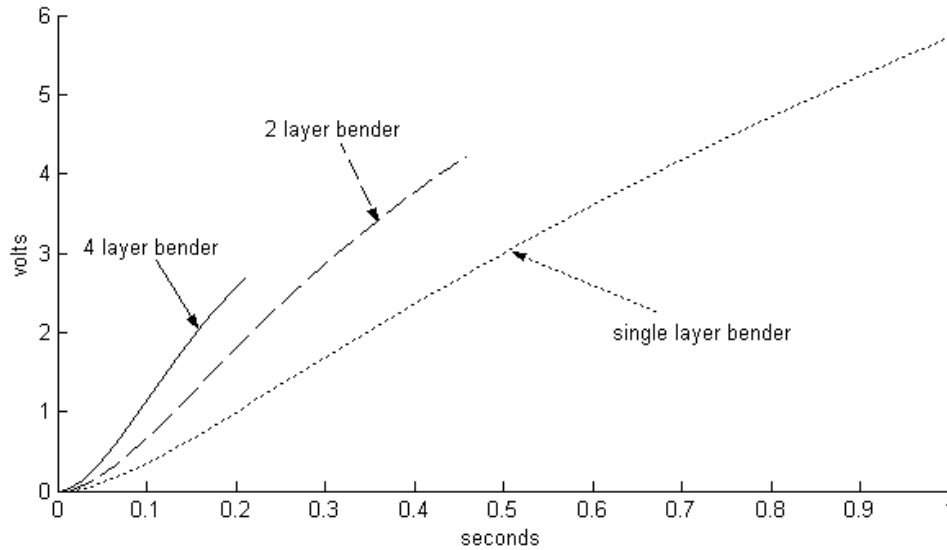


Figure 4.21: Voltage across storage capacitor vs. time for the same design incorporating different numbers of layers in the piezoelectric bender.

As a final note regarding the operating voltage, one could of course incorporate the operating voltage as a constraint in the optimization routine. This may be necessary if

only benders of a pre-specified thickness were available. Doing so, however, will further reduce the optimal power output because the design space will be further constrained. As is evident from the optimal designs shown with varying constraints, the sensitivity of the power output to many of the constraints is quite high. Thus reducing the design space has a large affect on the power output.

4.10 Conclusions

Because of the high stiffness of piezoelectric materials and the low frequency of most potential vibration sources, a piezoelectric bender has been chosen as the basic device on which to base the design and modeling of a piezoelectric generator. A bender (or bimorph) has the advantage that it can easily be designed with lower stiffness so that higher strains can be generated with a given force input. Many piezoelectric materials are available for use. Lead zirconate titanate (PZT) is the most commonly used piezoelectric ceramic and has very good properties. It has been chosen as the primary material on which to base designs and power estimates. A piezoelectric polymer, PVDF, is also considered because of its higher yield strain and better fatigue characteristics.

A detailed model has been developed and validated with a preliminary prototype device. This model has then been used as a basis for design optimization. Optimal designs generated with the two different materials mentioned and different electrical loading situations exhibit power densities on the order of hundreds of microwatts per cubic centimeter from input vibrations of 2.25 m/s^2 at about 120 Hz. A summary of the power output from each of the several designs presented in the chapter is shown in Table 4.12. The electrical loading conditions, material, and design constraints used for each design are also shown in the table. Note that all designs were constrained be less than 1

cm^3 in total volume and constrained such that the maximum strain experienced did not exceed the yield strain of the material.

Design Table	Power	Load	Material	Optimization Constraints
Table 4.4	215 μW	Res., 200 $\text{k}\Omega$	PZT-5H	$l < 1.5 \text{ cm}$, $t_p = 0.139 \text{ mm}$
Table 4.5	380 μW	Res., 151 $\text{k}\Omega$	PZT-5H	$l < 3 \text{ cm}$, $t_p = 0.278 \text{ mm}$
Table 4.6	975 μW	Res., 170 $\text{k}\Omega$	PZT-5H	$l < 3 \text{ cm}$, no constraint on t_p
Table 4.7	181 μW	Res., 26.7 $\text{M}\Omega$	PVDF	$l > 3 \text{ mm}$, $w_m < 1 \text{ cm}$
Table 4.8	211 μW	Res., 23.6 $\text{M}\Omega$	PVDF	$l > 3 \text{ mm}$, $w_m < 1.5 \text{ cm}$
Table 4.10	125 μW	Cap., 1 μF	PZT-5H	$l < 1.5 \text{ cm}$, $t_p = 0.139 \text{ mm}$
Table 4.11	695 μW	Cap., 1 μF	PZT-5H	$l < 3 \text{ cm}$, no constraint on t_p

Table 4.12: Summary of power output from the designs presented in this chapter.

The power available from PZT designs considerably exceeds that available from PVDF designs ($695 \mu\text{W}/\text{cm}^3$ compared to $211 \mu\text{W}/\text{cm}^3$). Also, optimal designs generated with a resistive load are capable of generating a little more power than those generated with a capacitive load ($975 \mu\text{W}/\text{cm}^3$ compared to $695 \mu\text{W}/\text{cm}^3$). However, while the model for the resistive load is useful in roughly predicting power output, validating the models, and gaining design intuition, it is not very useful in terms of practical applications. Therefore, the power output values predicted for capacitive load circuits are considered more useful and realistic.

Given the discussion presented in this chapter and previous chapters, the following simple design sequence emerges:

- Define and design the characteristics of the load (most likely a wireless sensor of some sort). Define such things as the voltage, standby current, transmit or “on” current, average power dissipation, minimum duty cycle, is duty cycle adjustable depending on energy available, etc.
- Define the characteristics of the input vibrations. What is their average magnitude and frequency? Is the frequency and magnitude consistent over time, etc.?

- Estimate the power potential from the vibrations using the generic power expression given in equation 2.5. Determine how much volume, or mass, is necessary to supply the power needed for the load. Is vibration conversion feasible? If so, proceed.
- Choose or design a suitable DC-DC converter or voltage regulator for the application and full wave rectifier.
- Choose the storage capacitor (or rechargeable battery) based on system and load constraints. These constraints will include, but are not limited to, volume, cost, maximum current draw, and maximum acceptable voltage drop during transmit or “on” state.
- Run the optimization routine described above with the chosen storage capacitor (or rechargeable battery). Evaluate the resulting design to see if the power generation is adequate.
- Choose the number of layers in the bender in order to get an acceptable operating voltage range as input to the DC-DC converter.
- Evaluate bender capacitance and storage capacitance. Is storage capacitance at least a factor of 100 greater than bender capacitance? If not, re-evaluate choice of storage capacitance.

Chapter 5: Piezoelectric Converter Test Results

A model to predict the output of piezoelectric generators was developed and discussed in the previous chapter. This model was validated with a prototype to ensure its accuracy and suitability of for use as a basis for design optimization. Optimal designs were generated and discussed. Actual converters were designed and built based on these optimizations. This chapter will discuss the implementation of these converters and present test results showing the improvement of the optimal designs. The converters have been used to power small wireless sensor devices, and results from such tests will also be presented.

5.1 Implementation of Optimized Converters

As explained in the previous chapter, the design of optimized prototypes is still constrained to materials that are commonly available. Because only a few prototypes were built, it was not feasible to ask a manufacturer to fabricate benders to our specifications. Therefore, the design was limited to benders that are available off-the-shelf. Piezo Systems Inc. carries a number of such benders that meet the specifications for this project quite well. It is quite easy to cut the benders to any size, however, the thickness of the ceramic layers is determined by what the manufacturer carries. The best commonly available bimorphs found were PZT PSI-5H4E with a brass center shim of thickness 0.1016 mm. Each of the two piezoelectric ceramic layers has a thickness of 0.1397 mm for a total bender thickness of 0.381 mm. It was also decided to use a bimorph poled for parallel operation so that the output voltages would remain in the 3 to 10 volt range.

The total volume of the device was constrained to 1cm^3 . Because the power output is proportional to the mass of the system, a very dense material should be used for the proof mass. As explained previously, a tungsten alloy (90% tungsten, 6% nickel, 4% copper) was chosen as the material for the proof mass.

The construction of the test devices was rather simple. A base was machined from plastic. The electrodes were etched off from the bender where the mass was to be attached. Remember that, as shown in chapter 4, the optimal electrode length is generally equal to, or very close to the beam length up to the point where the mass is attached. The electrodes on the benders purchased were made of nickel and were easily etched off with common copper PC board etchant. Because the bimorphs used for these designs were poled in parallel, the center shim needed to be electrically contacted. In order to achieve this, a small slot was milled near the base of the beam (see Figure 5.1 below). The slot was just wide enough to solder a wire to the center shim. Two other wire leads were then soldered to the electrodes on either side of the bimorph. The proof mass was attached to the end of the bender using super glue. Two methods of attaching the bender to the plastic base were used: the bender was either clamped down or attached with super glue. Both methods of attachment are shown in Figure 5.1. The generator in Figure 5.1 has the dimensions given in Table 4.4. Damping ratios were measured using the same procedure as outlined in Chapter 4 for the clamped beams and the beams attached with super glue. The average damping ratio for the clamped beam tests was 0.025 with a standard deviation of 0.0098, and the average damping ratio for the glued beam tests was 0.031 with a standard deviation of 0.014.

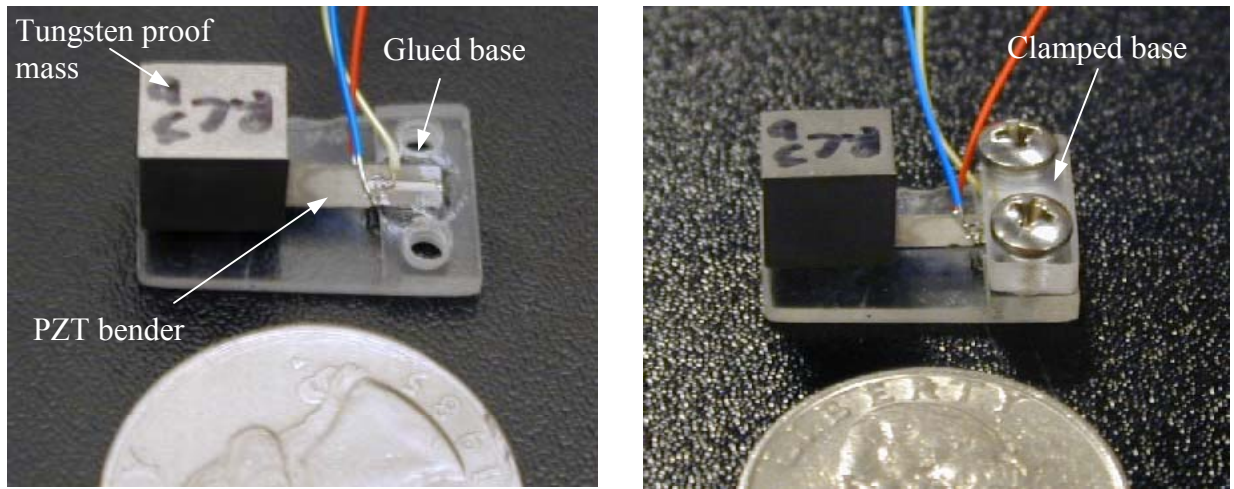


Figure 5.1: Piezoelectric test generators. The left picture shows bimorph held down with super glue, the right picture shows the bimorph held down with a clamp.

A few different designs incorporating different sets of constraints were built and tested. The two designs shown previously in Tables 4.4 and 4.5 were chosen as solutions incorporating a reasonable set of constraints. The primary difference between the two designs is in the geometric length constraint. For the design shown in Table 4.4, a maximum total length of 1.5 cm was used as a practical constraint in the optimization routine. This design will be referred to as **Design 1**, and is shown above in Figure 5.1. The design shown in Table 4.5 was limited to a total length of 3 cm. This design will be referred to as **Design 2**. Designs 1 and 2 are shown in Figure 5.2. In reality, the total length constraint will be determined by the specific application. The total volume constraint for each design was 1 cm^3 , and all other constraints were the same as explained in Chapter 4.

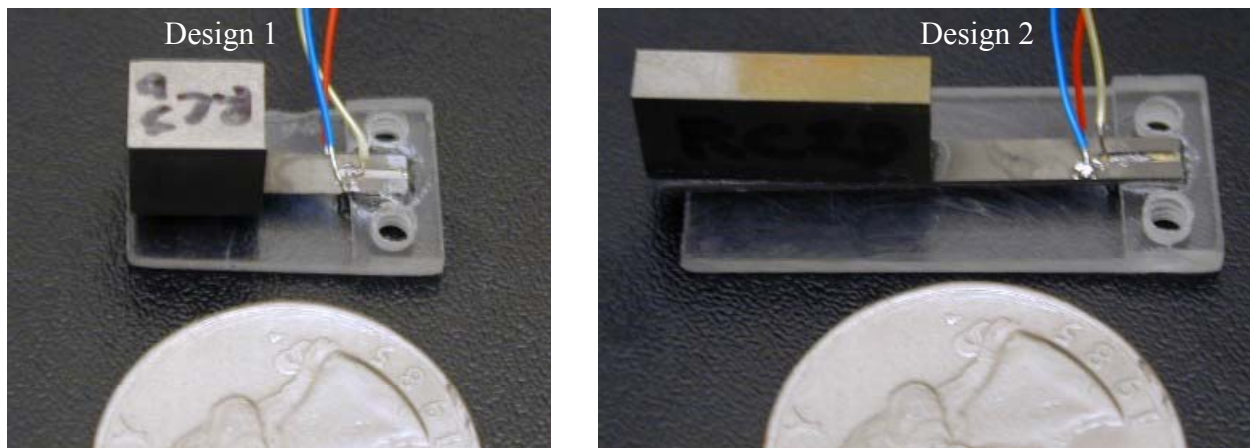


Figure 5.2: Two test generators built to two different sets of optimized dimensions. Design 1 is on the left and Design 2 is on the right.

5.2 Resistive load tests

The generators were mounted on a small vibrometer as shown in Figure 5.3. The base of the generator was mounted using double sided tape. Although not a tremendously rigid attachment method, the double-sided tape has a flat frequency response within the range of interest. Because the driving vibrations of interest are low frequency (120 Hz), only frequencies up to 500 Hz were measured. The frequency response of an accelerometer mounted with tape from 0 to 500 Hz is shown in Figure 5.4.



Figure 5.3: Vibrometer with test generator mounted.

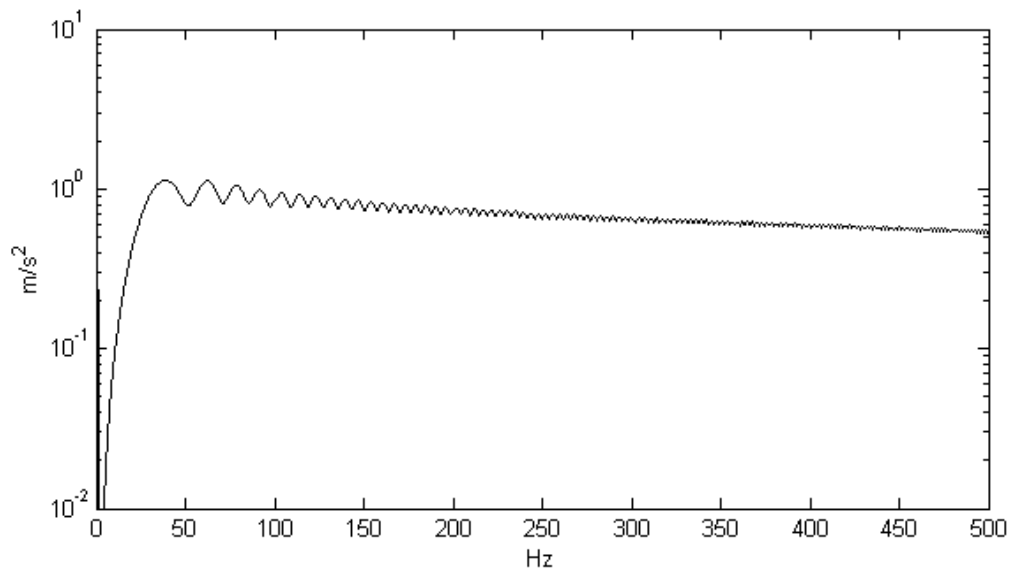


Figure 5.4: Frequency response of an accelerometer mounted with tape to the vibrometer. Response is flat showing that tape has no affect up to 500 Hz.

The vibrometer was calibrated before each set of tests performed. The accelerometer was used to calibrate the vibrometer outputs 0.1 volts per g (9.81 m/s^2). An amplifier with a gain of 10 was used with the accelerometer to output 1 volt per g.

There are then 3 inputs to the amplifier that can affect the acceleration output. The vibrometer is actuated by producing a sine wave (or some other waveform) from a signal generator (Agilent 33120A), using the waveform as the input to a power amplifier (Labworks PA-138), and connecting the output of the power amplifier to the input of the vibrometer (Labworks ET-126). The magnitude and frequency of the source waveform, and the gain of the power amplifier all affect the acceleration of acceleration generated by the vibrometer. The magnitude of the source waveform was kept constant at 1 volt rms. Only the frequency and gain on the power amplifier were used to produce the desired vibrations. The vibrometer was calibrated for each set of tests done. The results of the calibration done for one set of tests are shown in Figure 5.5. The points shown are averages of three measurements taken at three different frequencies and three different gains within the range of interest. Three calibration curves are shown, one for each gain. The equations from the quadratic curve fits are shown on the figure. Note the nonlinear relationship between acceleration and frequency. Other calibrations performed, resulted in similar data.

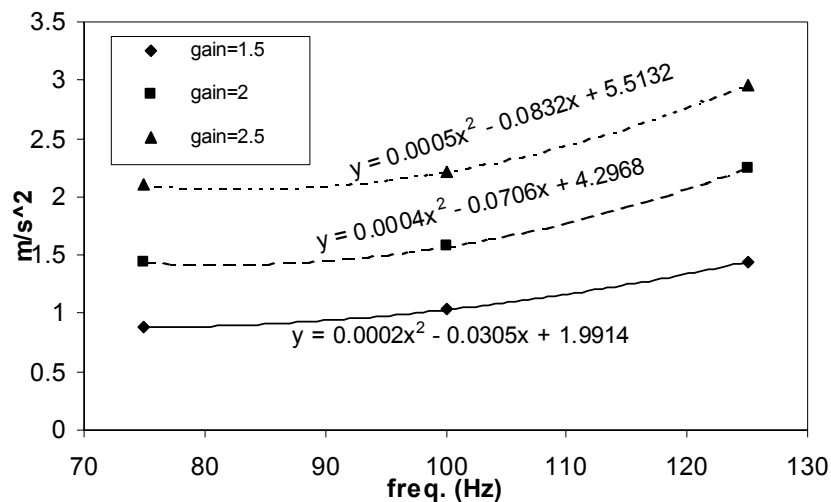


Figure 5.5: Acceleration vs. frequency output of the vibrometer for three different power amplifier gains.

The piezoelectric generator was terminated with a resistor and the voltage across the resistor was measured. The voltage signal was first passed through a unity gain buffer to decouple the capacitance of the data acquisition system from the generator. The test circuit is shown in Figure 5.6. A National Instruments data acquisition card (DAQCard-AI-16XE-50) capable of acquiring 20,000 samples per second was used in conjunction with LabView software to acquire the data.

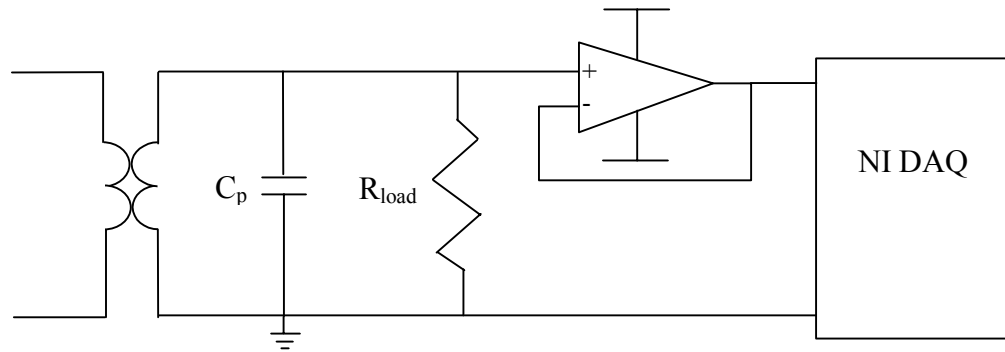


Figure 5.6: Measurement circuit for resistive load tests.

The output power and peak voltage versus load resistance for Design 1 is shown in Figure 5.7. The natural frequency of the generator was measured, and then the input to the vibrometer was set to the natural frequency. The input magnitude of the vibrations was 2.25 m/s^2 . For Design 1 the measured natural frequency was 85 Hz. The power and voltage output versus load resistance for Design 2 are shown in Figure 5.8. Again the natural frequency was measured and found to be 60 Hz. The simulated data shown in both figures was calculated with a damping ratio of 0.025 and an effective coupling coefficient (k_{31}) of 0.18.

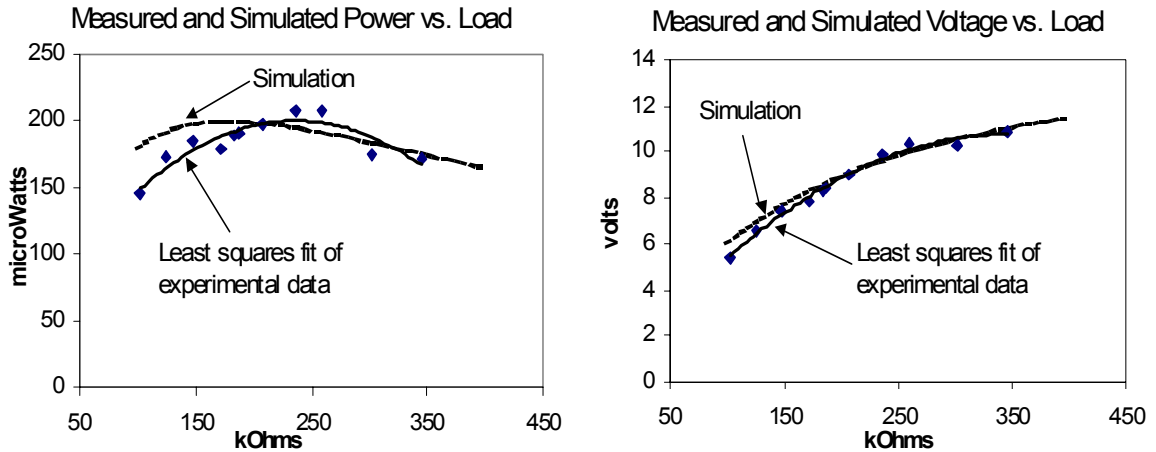


Figure 5.7: Measured and simulated output power and peak voltage versus load resistance for Design 1.

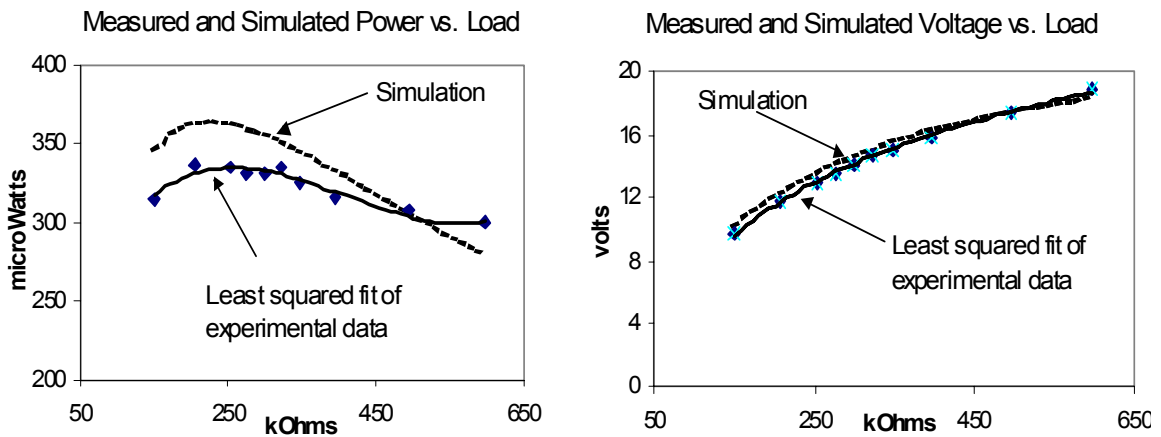


Figure 5.8: Measured and simulated output power and voltage versus load resistance for Design 2.

As discussed previously, it is essential for maximal power output that the natural frequency of the generator match the frequency of the input vibrations. Figure 5.9 shows the measured power output versus drive frequency for Design 1. Figure 5.10 shows the measured power output versus drive frequency for Design 2. It appears from the graphs that Design 2 is more sensitive to variations in the drive frequency than Design 1. The most reasonable explanation for this is that the overall damping for Design 2 is lower, and therefore the quality factor is higher.

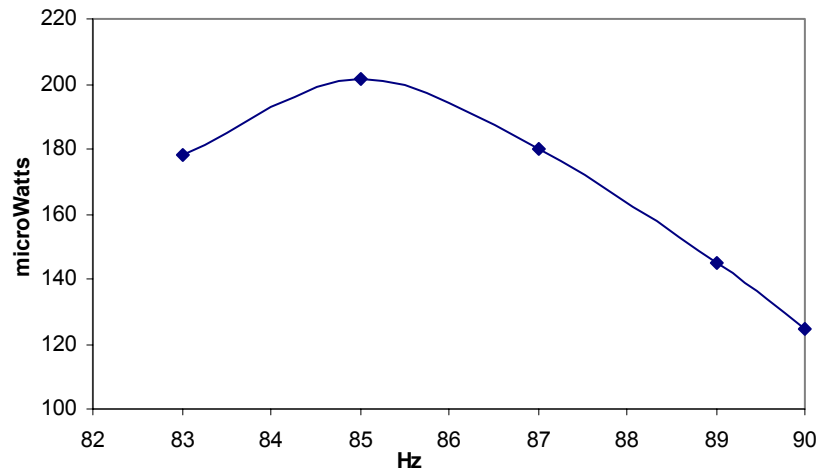


Figure 5.9: Measured power output versus drive frequency for Design 1.

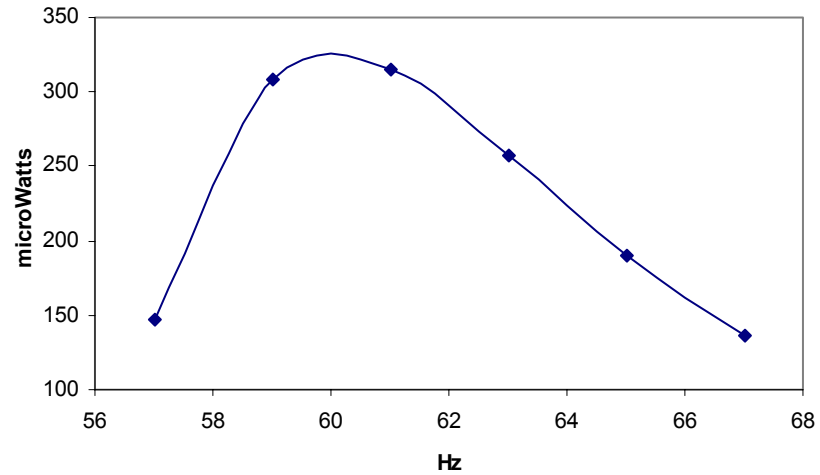


Figure 5.10: Measured power output versus drive frequency for Design 2.

5.3 Discussion of resistive load tests

The maximum power output and peak voltage values match the simulations rather well. The optimized designs are driving the piezoelectric material harder (closer to its fracture strain). Furthermore, the designs are smaller, and therefore the unaccounted for effect of the clamp may be more significant. Given these two considerations, one may expect that the simulations would not match experiments as well. While there is a greater discrepancy than previously observed, the experimental data still fits quite well. The

maximum power output observed from Design 2 was 335 μW compared with a maximum simulated value of 365 μW . The maximum power output observed from Design 1 was 207 μW compared to a maximum simulated value of 200 μW . Furthermore, the data points were tightly grouped around a fitted line that shows the same trend as the simulations.

Note that the maximum simulated power outputs in Figures 5.7 and 5.8 do not exactly match those in Tables 4.4 and 4.5. The maximum power output shown in Figure 5.7 is 200 μW compared to 215 μW for Table 4.4. The maximum power in Figure 5.8 is 365 μW compared to 380 μW for Table 4.5. The primary reason is that a damping ratio of 0.025 was used for the simulations shown in Figures 5.7 and 5.8 compared with a ratio of 0.02 used for the optimization routine. Also, the measured natural frequencies are lower than the designed natural frequencies. The measured natural frequencies were used in the simulations shown Figures 5.7 and 5.8. The higher damping ratios will tend to decrease the power output, and the lower frequencies will tend to increase the power output. The net effect was that the simulated values shown in Figures 5.7 and 5.8 are a little lower than those shown in Tables 4.4 and 4.5

There was a very large mismatch between the designed and measured natural frequency. It should first be mentioned that the parts were actually designed for 100 Hz rather than 120 Hz. A constraint was placed on the natural frequency as part of the optimization routine. However, in order that the optimization would converge more quickly and reliably, a range of 100 Hz to 130 Hz was allowed. In both cases (Design 1 and Design 2) the dimensions generated by the optimization routine resulted in natural frequencies of 100 Hz, as would be expected. After construction, the beam length of

Design 2 was measured as 11.3 mm compared to the designed value of 10.7 mm. The measured beam length of Design 1 was 6.5 mm as designed. Finally, the clamp is assumed to be perfectly rigid which is a poor assumption as will be discussed in more detail in the following chapter. The result is that the natural frequency was much lower than the designed value for both designs, and more particularly for Design 2.

A value of 0.18 was used for the coupling coefficient (k_{31}) in both the optimizations shown in Tables 4.4 and 4.5 and the simulations shown in Figures 5.7 and 5.8. The published value of k_{31} for PZT-5H is 0.44. The coupling coefficient was measured for a prototype made of PZT-5A as described in section 4.5. The published k_{31} for PZT-5A is 0.32, and the measured effective value for the bender was 0.12, or 0.375 times the published value. Taking this same ratio, and applying it to the PZT-5H benders, results in an effective coupling coefficient of 0.165. It was found, however, that a slightly higher value of 0.18 results in better matching between calculated and measured output. This coincides with a comment from the manufacturer that the benders with the brass center shim should have slightly better coupling than those with a steel center shim.

There are many similarities between the model developed in chapter 4 for the piezoelectric generator and the generic power conversion model developed in chapter 2, particularly when a simple resistive load is used. If the measured mass, natural frequency, and damping ratio are used as input to the generic model, a quick comparison can be made. Using the values measured from Design 1, the generic model predicts a maximum power output of 239 μW compared to a measured value of 197 μW and a simulated value of 195 μW . Using the values from Design 2, the generic model predicts

a maximum power output of 394 μW compared to a measured value of 335 μW and a simulated value of 365 μW .

5.4 Capacitive load tests

The same two prototypes were connected to a capacitive load circuit and driven on the vibrometer. The voltage across the load capacitor was measured and compared to simulated values. The test circuit used is shown in Figure 5.11. The generators were driven at their natural frequency with an acceleration magnitude of 2.25 m/s^2 as before. Figure 5.12 shows the measured and simulated voltage across a 1.6 μF load capacitor and the simulated and measured power transfer to the load capacitor versus time from the testing of Design 1. Figure 5.13 shows the same plots with a 3.3 μF load capacitor. Figures 5.14 and 5.15 show the measured and simulated voltage and power transfer for Design 2 using 3.3 and 5.5 μF load capacitors. In actual operation a storage capacitor much larger than 1.6 to 5.5 μF would be used. However, smaller capacitors were used for these tests because of the very long simulation times required if much larger capacitors (i.e. super capacitors) are used. As explained in chapter 4, the size of the storage capacitor does not have an effect on the level of power transfer as long as the storage capacitance is two to three orders of magnitude greater than the capacitance of the device. The measured capacitance of each of the two devices tested was about 9 nF, or about 200 to 700 times smaller than the storage capacitors used.

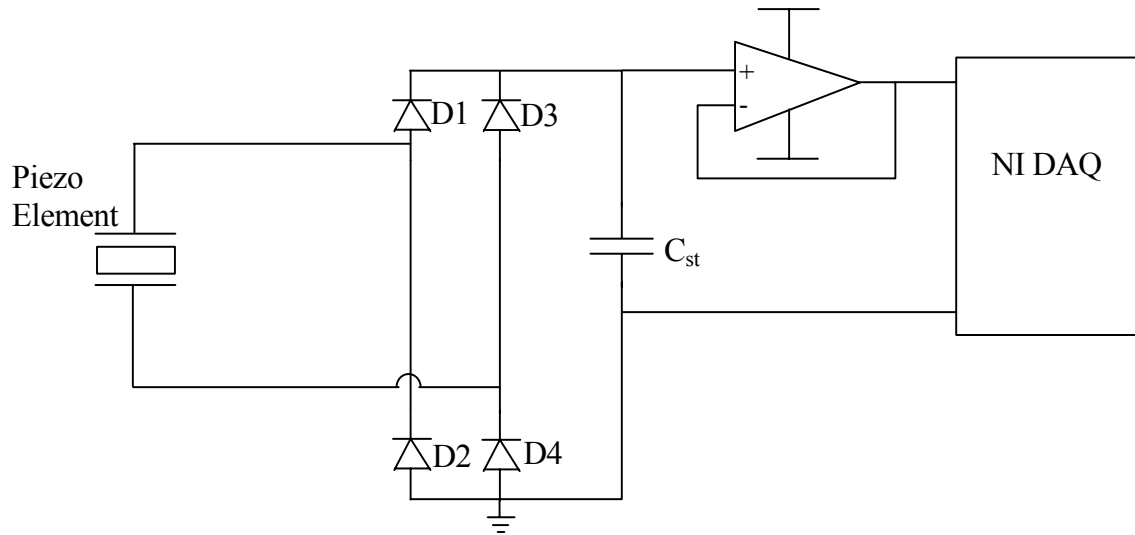


Figure 5.11: Measurement circuit for capacitive load tests.

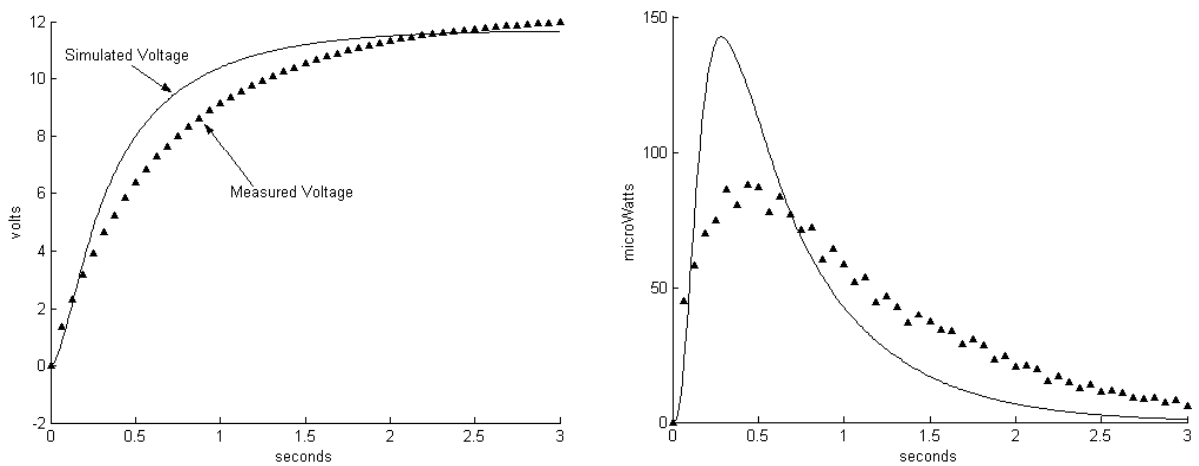


Figure 5.12: Measured and simulated voltage across a 1.6 μF storage capacitor versus time for Design 1 (left). Measured and simulated power transfer to the load capacitor versus time (right).

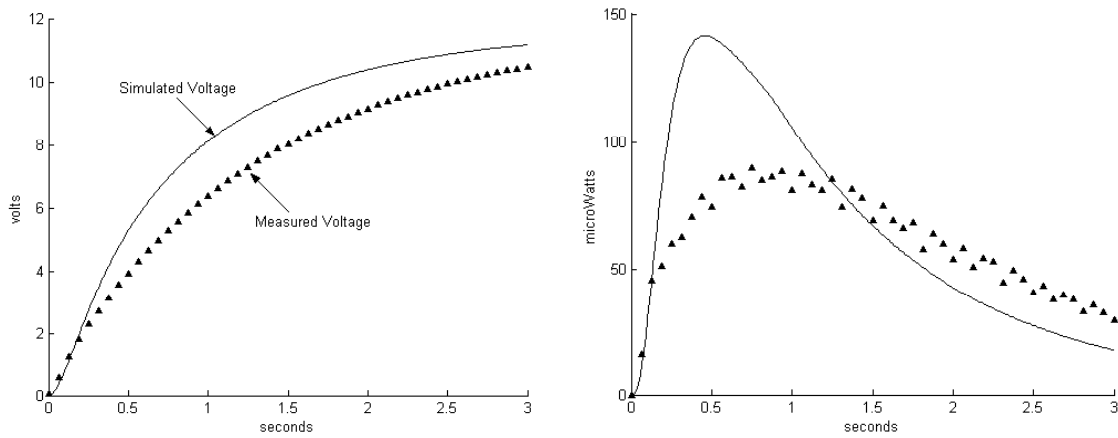


Figure 5.13: Measured and simulated voltage across a 3.3 μF storage capacitor versus time for Design 1 (left). Measured and simulated power transfer to the load capacitor versus time (right).

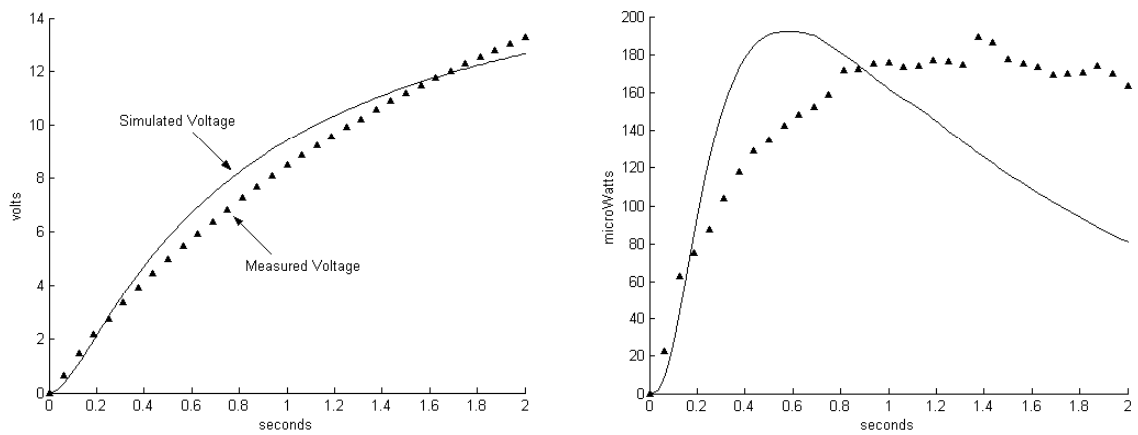


Figure 5.14: Measured and simulated voltage across a 3.3 μF storage capacitor versus time for Design 2 (left). Measured and simulated power transfer to the load capacitor versus time (right).

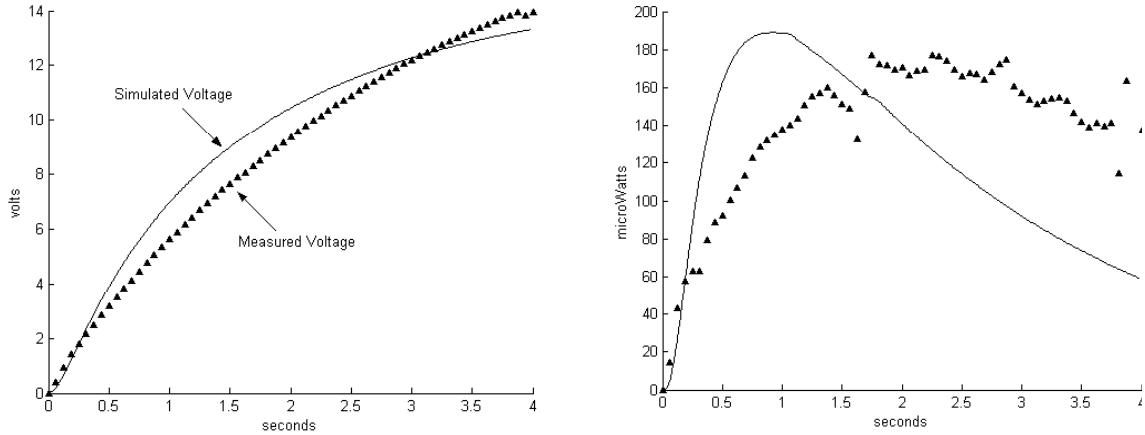


Figure 5.15: Measured and simulated voltage across a 5.5 μ F storage capacitor versus time for Design 2 (left). Measured and simulated power transfer to the load capacitor versus time (right).

5.5 Discussion of capacitive load test

There is good agreement between the simulated and measured voltage versus time curves with the exception that in the voltage range of 5 to 10 volts the two curves temporarily deviate from one another. Incidentally, the 5 to 10 volt range corresponds to about 0.5 to 0.8 times the open circuit voltage of the piezo generator. The power transferred to the storage capacitor is a function of $V \cdot dV/dt$ where V is the voltage across the storage capacitor. Therefore, the differences in magnitude and slope between the voltage curves become magnified on the power versus time curves. It will be remembered that the simulations assumed ideal diodes. In reality the voltage drop across the diodes depends on the amount of current flowing through the diodes. As the voltage across the storage capacitor approaches the open circuit voltage, this current is very small. However, at lower voltages, the current is larger, resulting in a larger voltage drop. It is the author's opinion that the unmodeled effect of the diodes is primarily

responsible for the discrepancies between the simulated and measured voltage and power versus time curves. While the ideal diode assumption undoubtedly causes some error, it does not change the essential design criteria or the validity of the essential parts of the model.

It should also be noted that the maximum measured voltage for Design 2 actually exceeds the simulated values. The result is that the maximum measured power is still very slightly lower than the maximum simulated power, and the measured power transfer reaches its maximum value later time than the simulated power. The best explanation of this result seems to be that, as explained, the diodes account for the lower slope. However, the actual strain developed in the bender is higher than the simulated value, which would result in a higher final, or maximum, voltage. Just why the maximum measured voltage is higher than the simulated value is not exactly known, however it is not uncommon for the measured voltage to be higher than calculated values for piezoelectric sensors due to changes in boundary conditions (Moulson and Herbert, 1997).

The storage capacitance does not seem to affect the measured power output. The maximum power output is about 90 μW for Design 1 for each of the two storage capacitors, and about 180 μW for Design 2 for each of the two storage capacitors. Previous calculations have shown that as long as the storage capacitance is 2 to 3 orders of magnitude larger than the device capacitance, its value does not affect the power transfer. This result is verified by the experimental measurements.

The measured power output is significantly lower for the capacitive load than for the resistive load. The first reason for this is that the devices built and tested were

optimized for a resistive load, not for a capacitive load. However, as can be seen from the optimizations performed in Chapter 4, the best achievable power transfer is still lower for a capacitive load than for a resistive load even if the design is optimized for a capacitive load.

5.6 Results from testing with a custom designed RF transceiver

The generator labeled as Design 2 in Figure 5.2 was used to power a custom designed, low power transceiver. A schematic of the power circuit used in conjunction with the generator is shown in Figure 5.16. Actual part numbers used are labeled on the schematic where appropriate. The physical implementation of the circuit is shown in Figure 5.17. The piezoelectric converter was attached to the vibrometer shown in Figure 5.3 and driven by vibrations at 60 Hz of 2.25 m/s^2 .

The low power transceiver was designed by Otis and Rabaey (Otis and Rabaey, 2002). A block diagram of the receiver and transmitter is shown in Figure 5.18 and the physical transceiver is shown in Figure 5.19. A close-up of one of the custom designed IC's is also shown in the figure. The radio transmits at 1.9 GHz and consumes 10 mA at 1.2 volts. In the test results shown in this section, the transmitter was turned on and broadcast a pure tone. No meaningful information was transmitted. The purpose was to verify the proper functionality of the generator, power circuit, and transmitter, and therefore a simple pure tone was sufficient for the test.

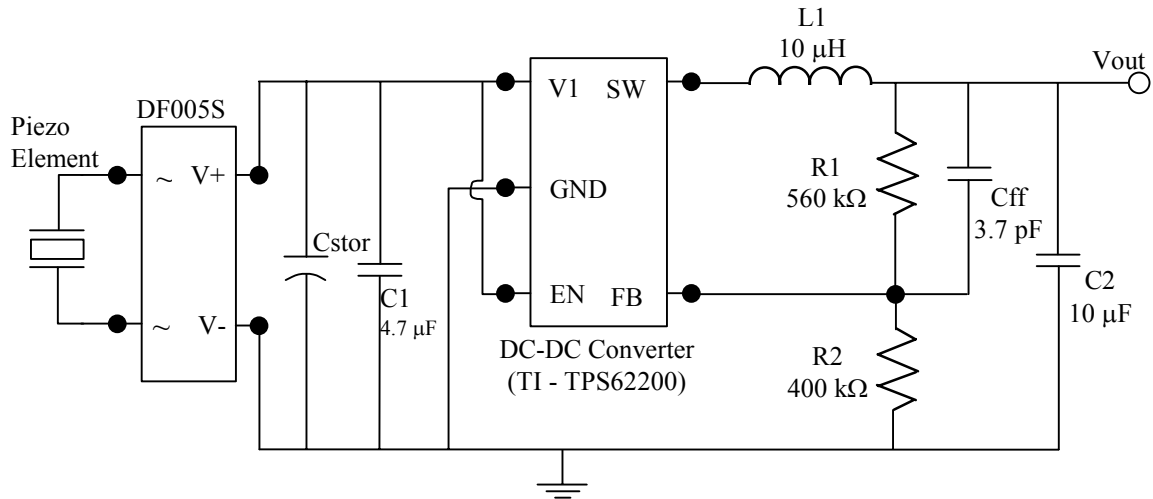


Figure 5.16: Schematic of power circuit. V1 is the input voltage to the DC-DC converter, SW is the switching or output pin, GND is the ground pin, EN is the enable pin, FB is the feedback pin that sets the output voltage.

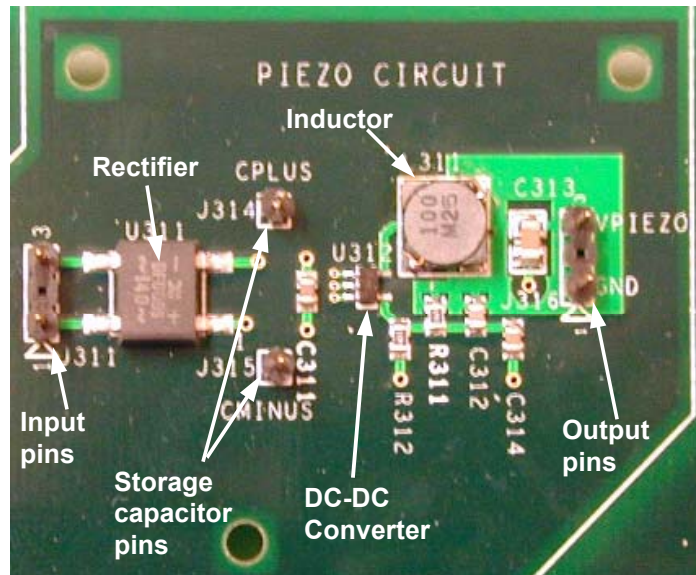


Figure 5.17: Implementation of power circuit.

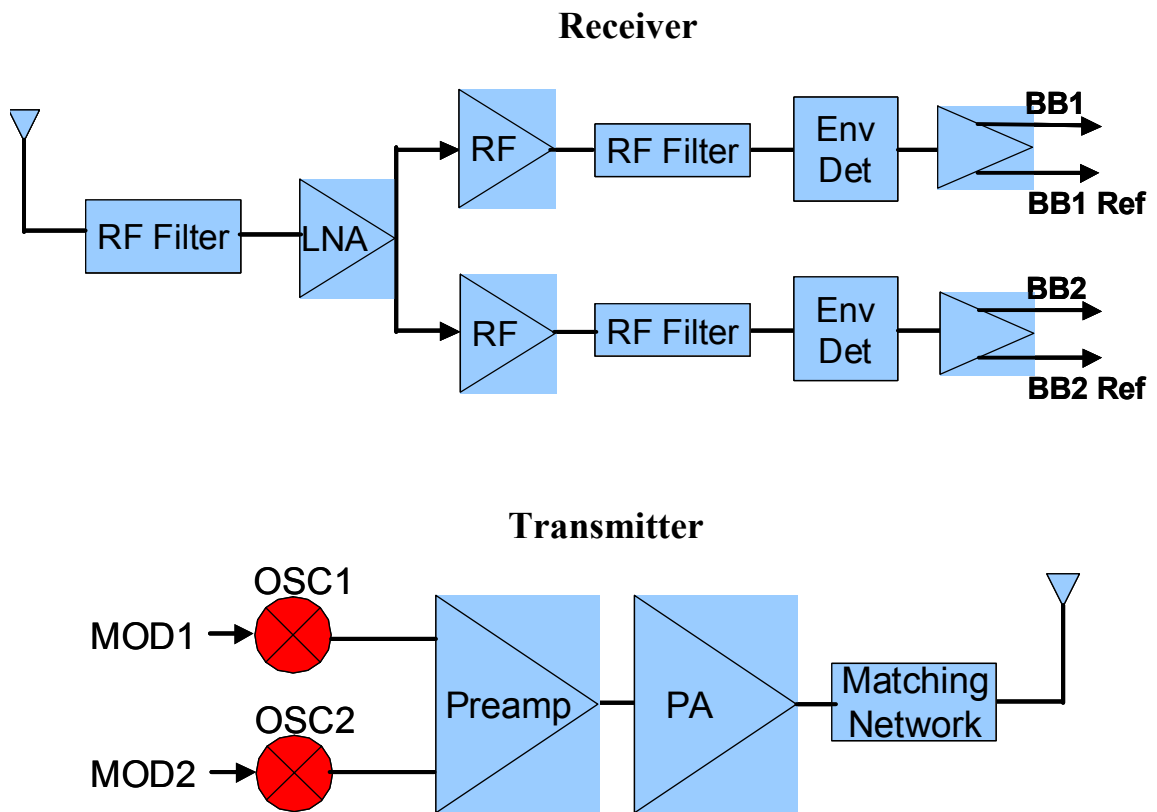


Figure 5.18: Block diagram of receiver and transmitter designed by Otis and Rabaey.

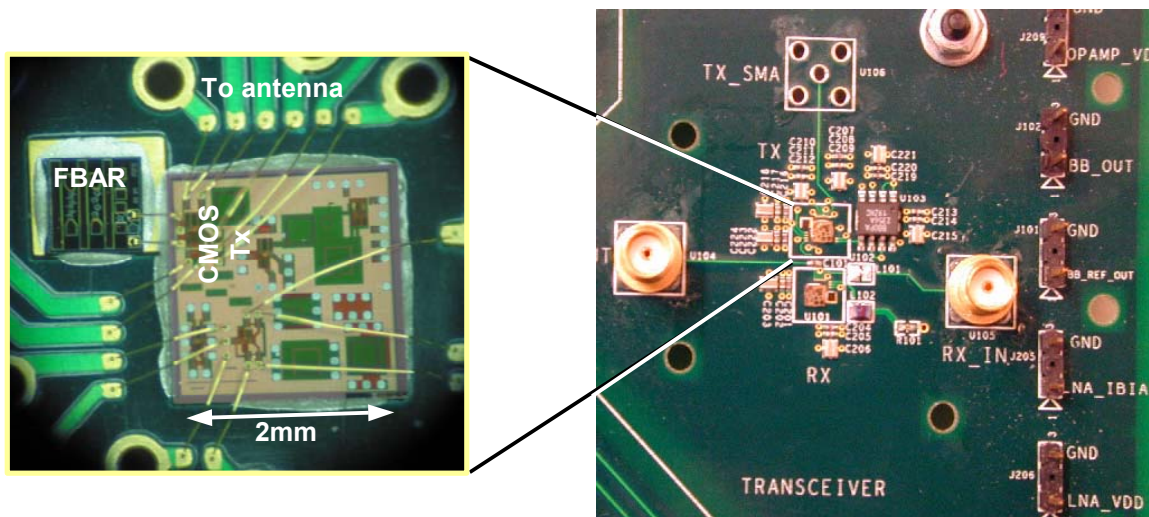


Figure 5.19: Custom radio transceiver designed by Otis and Rabaey with close-up of one of the custom chips.

As described earlier, the proposed method of operation of a wireless sensor node is that the radio transmitter and receiver will operate in bursts, being turned off most of the time. The projected duty cycle, the “on” time divided by the total time or $DC = \frac{t_{on}}{t_{total}}$, is typically less than 1% (Rabaey *et al*, 2000). During the “off” time, the input capacitor to the DC-DC regulator charges up. During the “on” time, this capacitor is discharged as the power dissipation exceeds the input power. The supportable duty cycle is then given, more or less, by the ratio of input power from the generator to power dissipation when the radio is on. Figure 5.20 shows the results of a test done with a 200 μ F input capacitor. In reality, a larger super capacitor on the order of 1 F would probably be used, however the 200 μ F capacitor was convenient for the test because it is easier to see the charge / discharge cycle on the input capacitor.

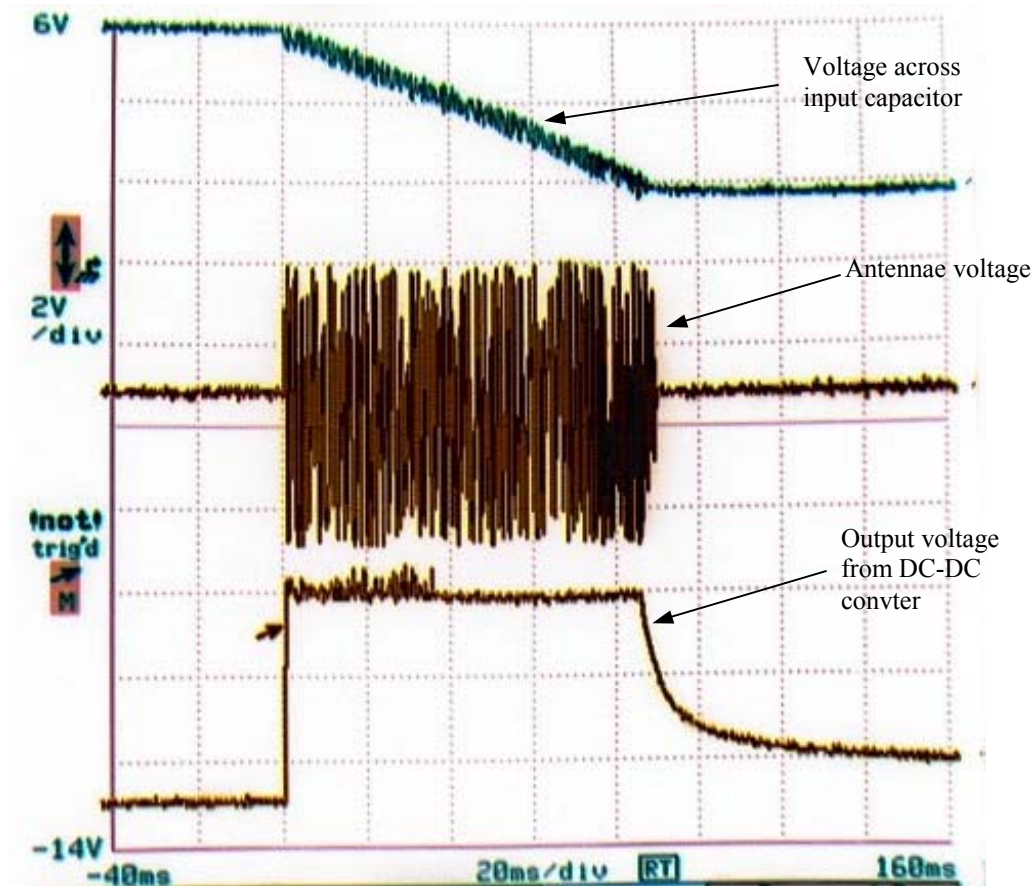


Figure 5.20: Test results showing voltage across 200 mF input capacitor, antennae signal and output of regulator.

The top trace in Figure 5.20 shows the voltage across the input capacitor versus time. Data was acquired for 200 mSec. Although the short time scale makes it difficult to see, the voltage is ramping up at the beginning and end of the trace. The section where the voltage is ramping down is obviously the portion of time for which the radio was on. In this particular case, the switch was closed connecting the input capacitor to the rest of the system and left closed until the voltage across the capacitor fell so far that the DC-DC converter was no longer able to regulate its output. The second trace shows the voltage signal sent out the antennae. In this case a simple pure tone is being transmitted. The transmission frequency is 1.9 GHz. Because of the long time scale (relative to a 1.9 GHz signal) shown, the details of the transmission output cannot be seen. Figure 5.21 shows

the frequency spectrum of the transmission signal. Finally the bottom trace shows the output voltage from the DC-DC converter. The voltage is initially zero, when the radio turns on it jumps to 1.2 volts, and when the input falls too low, the output falls off on a first order decay down to about 0.25 volts.

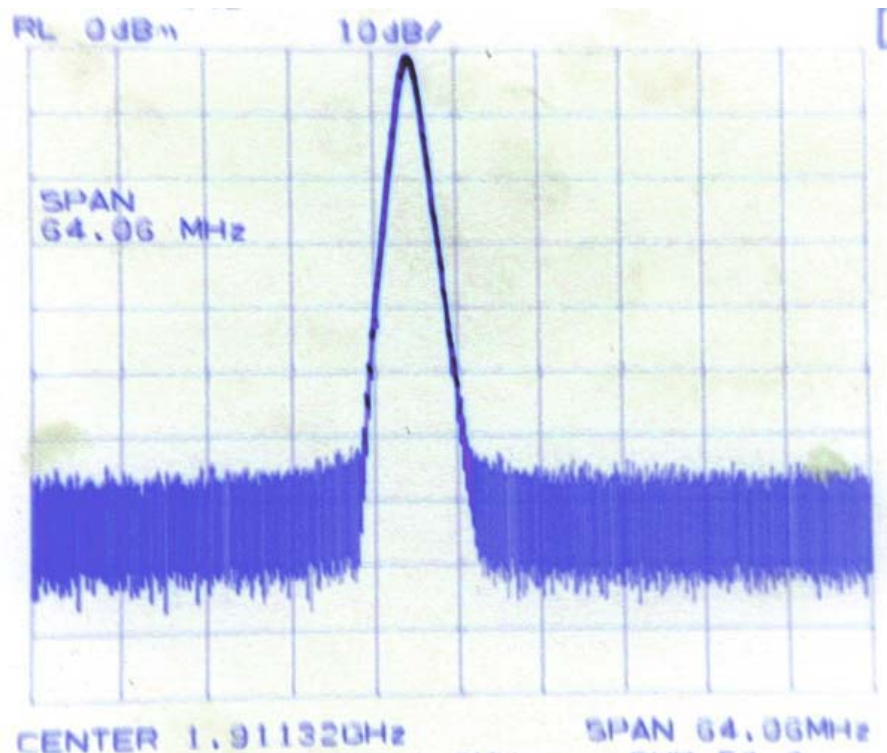


Figure 5.21: Frequency spectrum of transmission signal (centered at 1.9 GHz).

Because of the short time scale (relative to the charging time of the input capacitor) of Figure 5.20 it is difficult to tell how fast the input capacitor is being charged. Figure 5.22 shows the voltage across the 200 μF input capacitor. The load is turned off and the input vibrations are the same as for the test shown in Figure 5.20, namely 2.25 m/s^2 at 60 Hz. Note that it takes about 8.5 seconds to charge from 2 volts to 6 volts. Figure 5.20 showed that it takes about 85 milliseconds for the radio to discharge the input capacitor from 6 volts back down to about 2 volts. Therefore, the supportable duty cycle using this

particular generator, vibration source, and radio is 8.5 seconds divided by 0.085 seconds, or 1%.

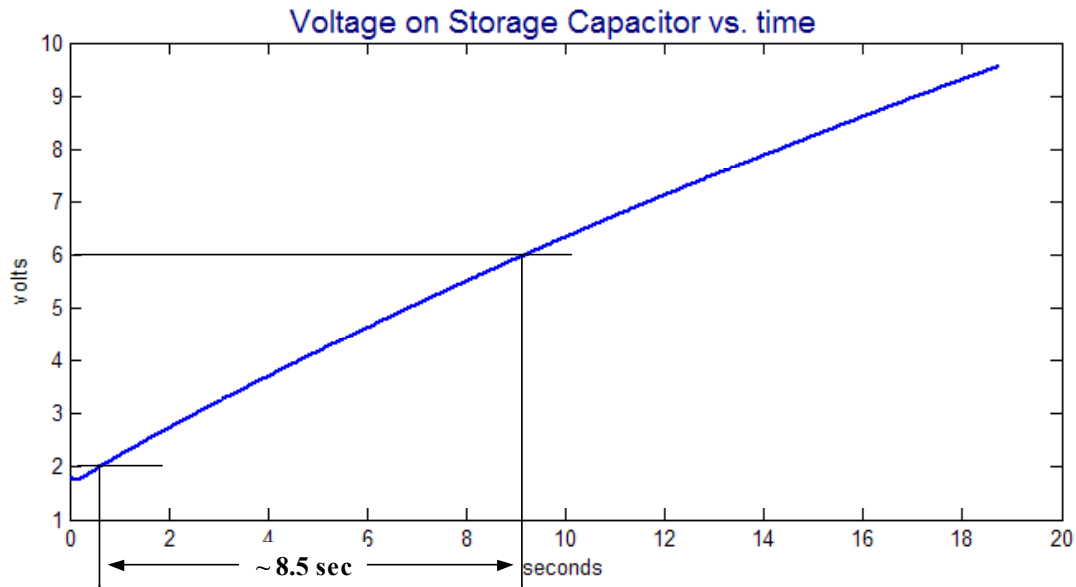


Figure 5.22: Voltage across 200 μF input capacitor as it charges up from a vibration source of 2.25 m/s^2 at 60 Hz.

5.7 Discussion of results from custom RF transceiver test

The tests to power Otis and Rabaey's transceiver were very successful in that enough power was delivered to be able to support a duty cycle of about 1%, which is the upper end of the projected duty cycle of the entire system. Also, the power delivered was of high enough quality for the transmitter to produce a good, clean signal out. That being said, it should be remembered that while the radio is the highest power portion of an entire sensor node, it does not account for all of the power usage.

The efficiency of the power circuit may be roughly estimated as follows. The power delivered to the radio was 12 mW (10 mA at 1.2 volts) when on, and zero when off. Therefore, the average power delivered to the load is 120 μW . The quiescent current

of the DC-DC converter used is about 20 μA . The average input voltage to the DC-DC converter is about 4 volts in this case. So, the quiescent current of the DC-DC converter dissipates about 80 μW of power when on. However, note that the DC-DC converter is off when the radio is off, and the quiescent current in the “off” state is only 1 μA . So, the average power dissipation due to quiescent current is 4.76 μW or roughly 5 μW . Additionally, according to the data sheet, the DC-DC converter is about 90% efficient when on, resulting in an additional average power loss of 12 μW . Finally the diodes in the full wave rectifier account for about a 0.6 volt drop. At an average input voltage of 4 volts, this represents a 13% loss in power. Other power losses, such as current through the feedback resistors, are considered negligible. The average power delivered to the input capacitor is then $120 + 5 + 12 = 137 \mu\text{W}$. This represents 87% of the power produced (13% is lost in the rectifier diodes), which then must be 157 μW . The total efficiency of the power circuit would then be 76%, which isn’t bad. However, the full wave rectifier represents more than half the power lost. This could possibly be improved. A little more active circuitry could attempt to ensure that the voltage across the input capacitor remains more or less at the optimal voltage for power transfer from the piezo generator. This could improve the effective produced power above 157 μW . For this particular generator, the best voltage for power transfer is about 8 volts, which would have the additional benefit of reducing the power loss in the rectifier by one half. However, the power lost in the DC-DC converter due to quiescent current would double. Finally, a DC-DC converter designed specifically for this power train would likely be more efficient overall than the off-the-shelf chip used for this test.

One observation is that the input voltage to the DC-DC converter (across the input capacitor) is very noisy. This is due to the high frequency switching of the DC-DC converter and the relatively high input impedance. In actual operation a super capacitor of approximately 1 Farad would likely be used which would decrease the input impedance and reduce this noise. The output voltage from the DC-DC converter is also quite noisy. This could partially be due to the high input impedance. However, the transceiver still operated well with the relatively noisy power signal. Again, a power circuit designed for higher input impedance may also help reduce this noise.

5.8 Results from test of complete wireless sensor node

The previous two sections have described the operation of a custom designed RF transceiver. However, the transceiver was not incorporated into a complete functioning wireless sensor node. The power dissipation of currently available wireless sensor nodes is too high to be powered by a vibration to electricity converter of size 1 cm^3 or less under vibrations of about 2.25 m/s^2 . It is likely that the average power consumption of general purpose wireless sensor nodes will soon fall to levels at which they can be powered by a 1 cm^3 converter from the baseline vibration source used in this study. At present, however, the power consumption is still a factor of 5 to 10 too high. Nevertheless, it is desirable to build and test a complete system to demonstrate feasibility.

Two options are possible. The generators already built could be driven with vibrations of higher amplitude, or a larger generator could be built and driven with low-level vibrations. The latter option was pursued because larger amplitude vibrations run the risk of exceeding the fracture strain of the devices already designed and built. An additional consideration is that driving the generator with vibrations of higher amplitude

will increase the open circuit voltage produced by the generator, which means that the best operating voltage at the input to the DC-DC converter will be higher. Using the generator labeled as Design 2, the resulting input voltage would be about 12 volts. Such a large difference between the input and output voltage greatly limits the number of commercial DC-DC converters that can be used.

A larger generator was designed and built. This generator is shown in Figure 5.23 and will be referred to as Design 3. The size of the generator is about 3 cm by 2 cm by 0.8 cm, or 6 times larger than Design 2. The proof mass is 52.2 grams or 6.4 times larger than Design 2. The generator was used to power the small general purpose, programmable wireless sensor node shown in Figure 5.24 (Warneke *et al* 2001)².

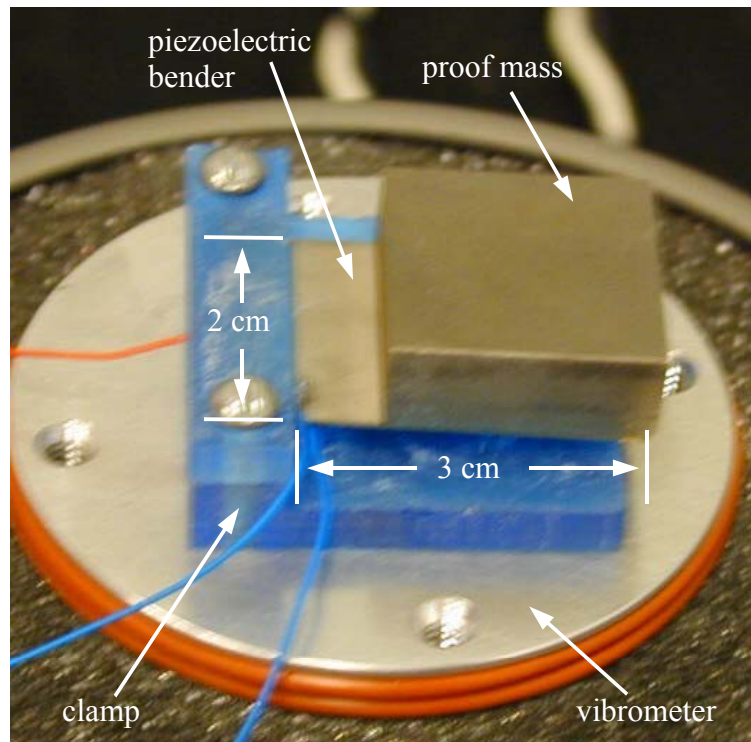


Figure 5.23: Larger generator built to power a complete wireless sensor node.

² The wireless sensor node shown in Figure 5.24 was developed by a group of researchers at UC Berkeley. It is generally referred to as the “Mica Mote”. The same group has since developed another, smaller wireless sensor node referred to as a “Dot Mote”, which has about the same footprint of the US quarter with a thickness of about 1cm. Both the “Mica Mote” and “Dot Mote” are now manufactured by Crossbow Technology, Inc. Additionally, very similar wireless nodes are now manufactured and sold by Dust Inc.

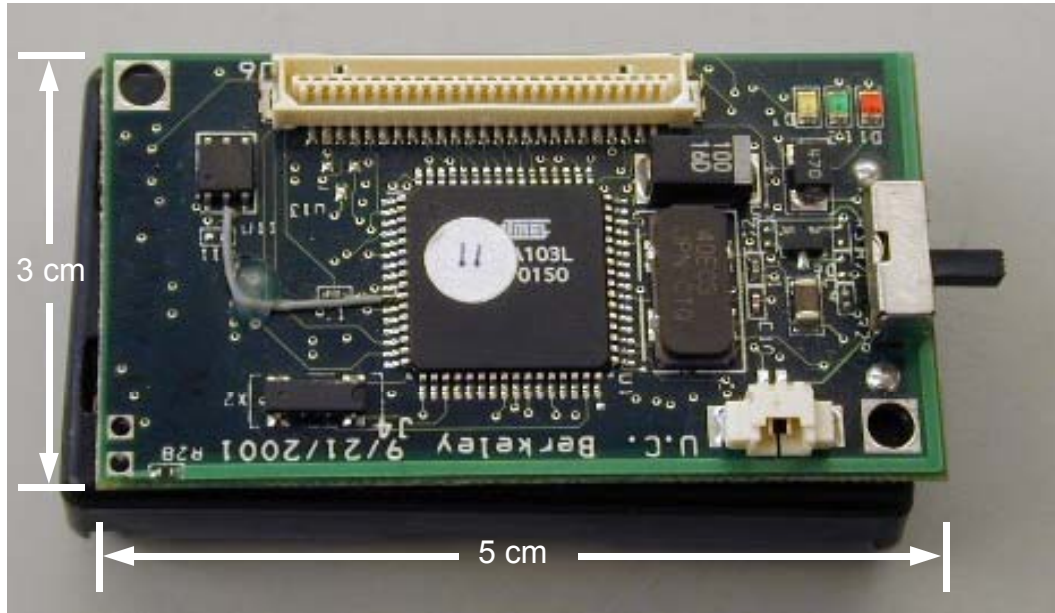


Figure 5.24: Complete programmable wireless sensor node.

The generator was designed to have roughly the same open circuit voltage as Design 2, but to output much more current. It was to be designed to run at 120 Hz, however, due to two factors, the actual resonant frequency is only 40 Hz. The first factor is that the clamp is more compliant than accounted for. The second factor is that the material of the wrong thickness was used in constructing the device resulting in lower stiffness and higher capacitance. The device capacitance was measured as 171 nF. The device was driven with accelerations of 2.25 m/s^2 (as in previous tests) at 40 Hz. The power output versus load resistance is shown in Figure 5.25 for the case when the generator is terminated with a simple resistor. Note that the maximum power is $1700 \text{ }\mu\text{W}$ and occurs at a load resistance of $18 \text{ k}\Omega$.

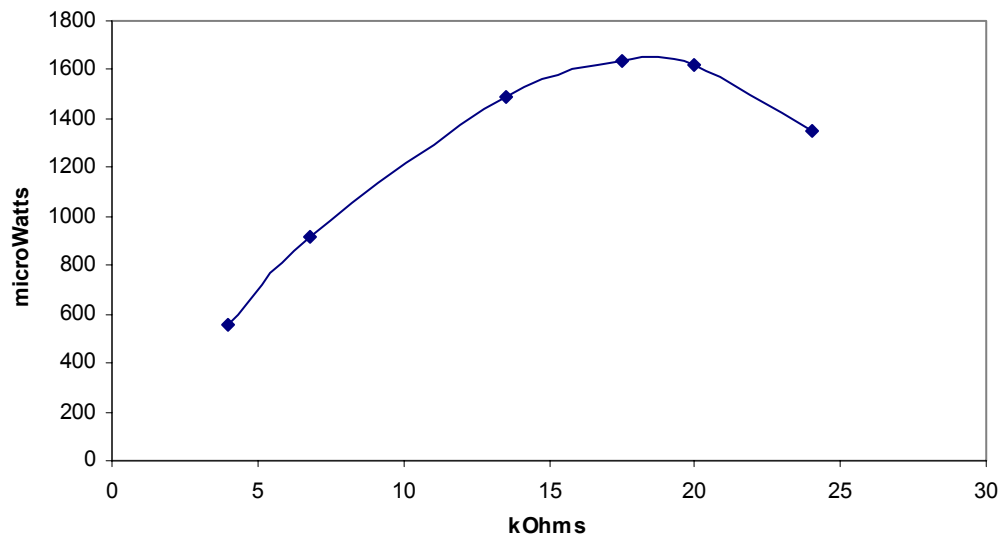


Figure 5.25: Power vs. load resistance for the generator labeled Design 3.

The same power circuit shown in Figure 5.17 was used to connect the generator to the wireless sensor node with two small alterations. The feedback resistors for the DC-DC converter were altered to output the 3 volts needed by the sensor node rather than the 1.2 volts used in the previous test. Secondly, an input capacitor of 10 mF was used rather than 200 μ F because of the greater power production and dissipation. Again, in real operation a super capacitor of about 1 F would be used, but this size capacitor makes it difficult to see the voltage variations that correlate to system operation. Figure 5.26 shows the charge-up of the 10 mF input capacitor without the load connected. Figure 5.27 shows the power transfer from the converter to the input capacitor versus time. As can be seen, when the voltage across the capacitor reaches an appropriate voltage (about 0.5 times the open circuit voltage) the power transfer is about 700 μ W.

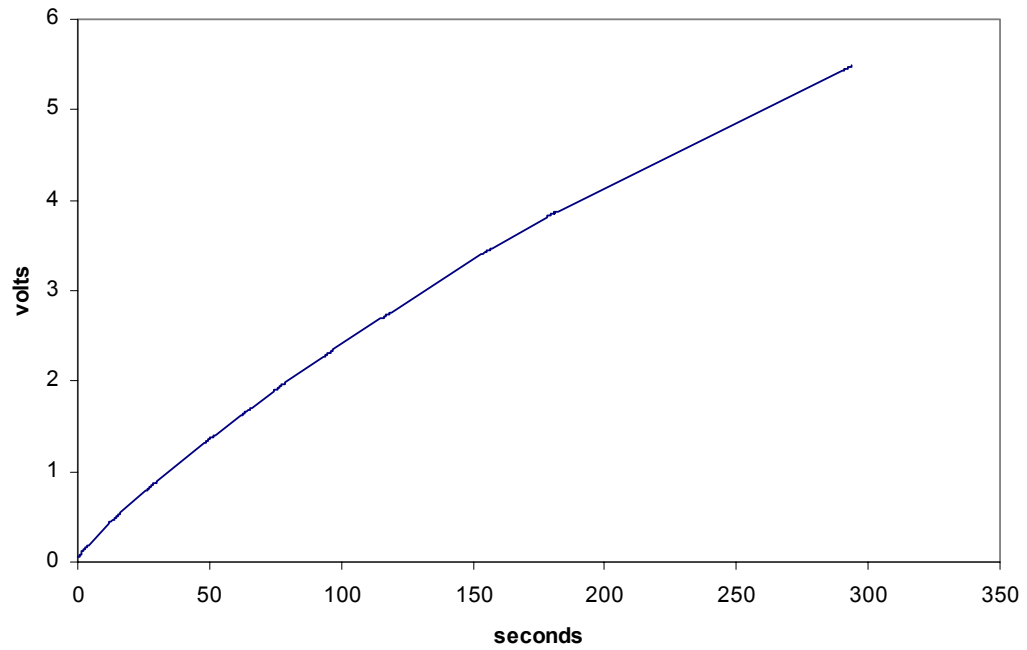


Figure 5.26: Voltage across the 10 mF input capacitor versus time with load disconnected.

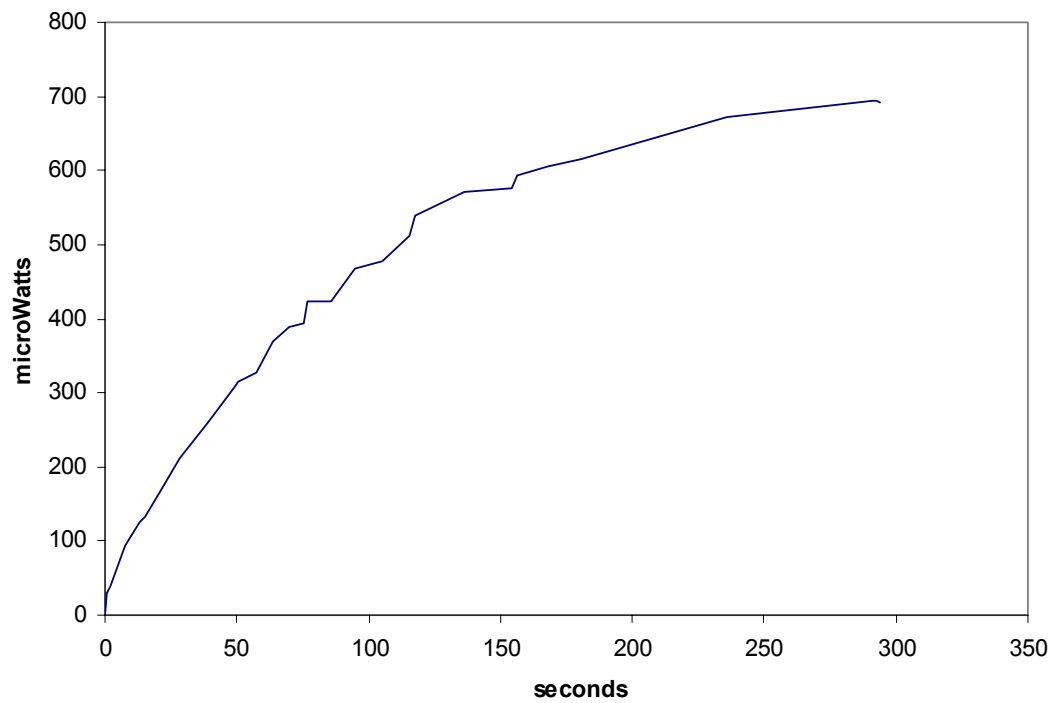


Figure 5.27: Power transfer to the 10 mF input capacitor versus time with load disconnected.

A program that measures one of the sensor inputs 10 times per second and transmits the reading was written and downloaded to the wireless sensor node shown in Figure 5.24. Each transmitted packet contains only one sensor reading. The node accepts analog sensor inputs from 0 to 3 volts. The voltage across the input capacitor was divided by 4 with a resistive divider and wired to the sensor input. The voltage across the input capacitor was also directly measured with a data acquisition system for comparison. Because the power consumption of the node is far greater than 700 μW , a switch was placed in between the input capacitor and DC-DC converter in order to turn the system on and off in the same manner done previously. Figure 5.28 shows both the directly measured voltage across the input capacitor and the transmitted voltage multiplied by 4. Figure 5.29 shows the calculated power consumption of the wireless sensor node. The power consumption was calculated from the voltage profile across the input capacitor. The power out of the capacitor is simply $P_{\text{out}} = V_{\text{in}} * I_{\text{out}} = -C_{\text{in}} V_{\text{in}} dV_{\text{in}}/dt$. Subtracting the power dissipation of the DC-DC converter, the power lost through resistive dividers, and the power transferred to into the input capacitor from the generator, the result is the power dissipation of the wireless sensor node as shown in Figure 5.29.

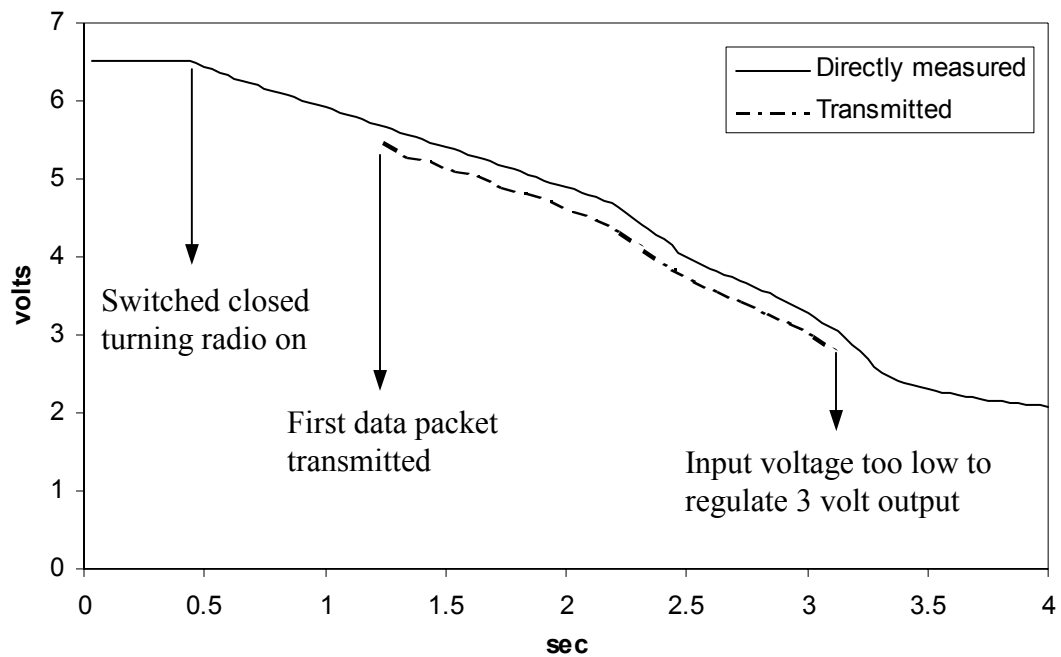


Figure 5.28: Directly measured and transmitted input voltage versus time.

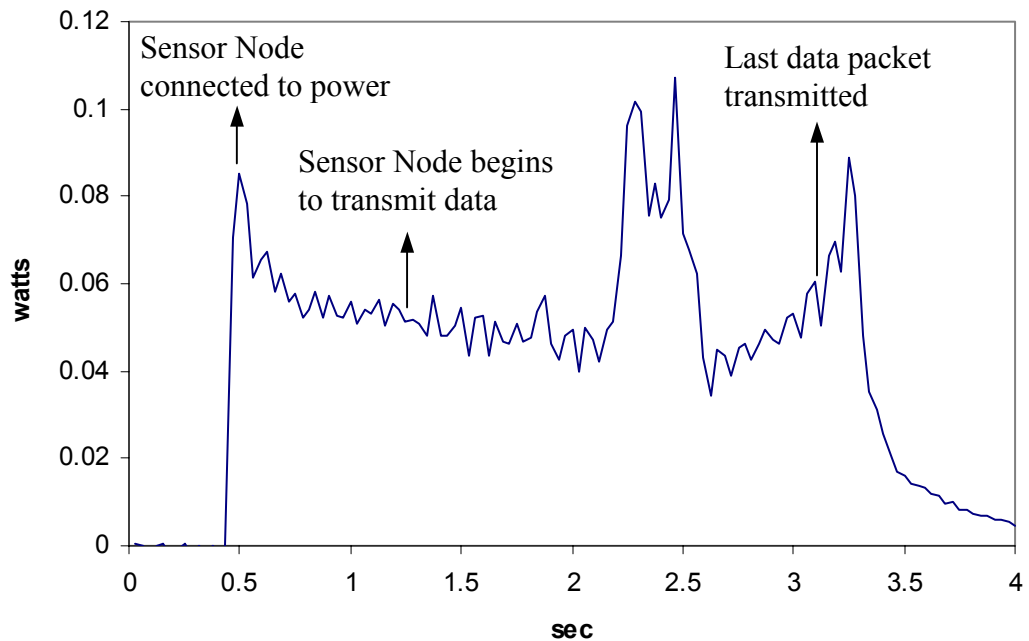


Figure 5.29: Power dissipation versus time of the wireless sensor node.

5.9 Discussion of results from complete wireless sensor node

The generator was designed for a 0.02 inch thick bender. The bender actually used was 0.015 inches thick. Because the resonant frequency is proportional to the thickness cubed, the resulting resonant frequency should be $(.015/.02)^3$ or 0.42 times the designed frequency. This would result in a resonant frequency of 50 Hz. The remaining discrepancy is due to compliance of the clamp. While the input vibrations are not exactly the same as those used for Design 2, they are close enough to provide a reasonably good comparison. Remembering that Design 3 (the larger design) is about 6 times larger than Design 2 (the mass is actually 6.4 times that of Design 2), the power output of Design 3 should be about 6 times greater. The maximum power through a resistive load for Design 3 is 1700 μW compared to 335 μW for Design 2 resulting in a power output ratio of 5.1. Further investigation would be necessary to determine why the power ratio does not track exactly with the mass ratio. However, a 20% percent discrepancy is not unexpected and does not significantly contradict the fact that power output is proportional to mass.

The voltage profiles shown in Figure 5.28 indicate an offset of about 0.25 volts between the directly measured voltage and the transmitted voltage. It is possible that the voltage divider across the input capacitor was not exactly a $\frac{1}{4}$ divider due to parallel resistances. It is also possible that the voltage results from the acquisition of the signal by the wireless sensor node. In either case, the reason is not particularly important for this test. The purpose was to demonstrate a fully functional system, which the test does effectively. A second observation is that the wireless sensor node takes about 0.75 seconds to start up and begin acquiring and transmitting data. In actual operation a hard switch would not be used to shut the node down. The node could be programmed to go

into a very low power sleep mode and turn on at some predetermined duty cycle. However, the implementation of such a program is beyond the scope of this test.

An approximate supportable duty cycle can be calculated based on the data shown in Figures 5.26 and 5.28. Figure 5.26 shows that the generator charges the input capacitor from 3 volts to 5 volts in 130 seconds. Figure 5.28 demonstrates that it takes the sensor node about 1.3 seconds to dissipate through this same range (5 volts back down to 3 volts). Therefore, the supportable duty cycle is about 1% for this system. More intelligent power circuitry that would attempt to maintain the input voltage at its optimal value would considerably improve the supportable duty cycle.

In the same manner that was done for the previous test reported, the approximate efficiency of the system can be quickly estimated. In this case the power delivered to the wireless sensor node ranges from 50 mW to 100 mW with an average value of about 60 mW. At a duty cycle of 1% the average power consumption of the node would be 600 μ W (assuming that power dissipation is zero when “off”). Just as described previously in section 5.7 the power dissipation in the DC-DC converter due to quiescent current is about 5 μ W. The converter is roughly 90% efficient when on, resulting in an additional average power loss of 60 μ W. Finally the diodes account for account for about a 10.7% loss in power due to voltage drop. (The average voltage across the input capacitor is about 5 volts for this example.) Current through feedback resistors is considered negligible. The average power delivered to the input capacitor is then $600 + 5 + 60 = 665$ μ W. This represents 89.3% of the power produced, which then must be 745 μ W. The total efficiency of the power circuit would then be 80.6%. Again, over half of the power

loss is due to the rectification diodes. The efficiency of the circuit could be improved in exactly the same manner as described in section 5.7.

5.10 Conclusions

Four basic sets of tests have been performed with three different piezoelectric vibration-to-electricity converters. Two 1cm^3 converters were tested using a simple resistive load to characterize the maximum power generation. Secondly, the two converters were tested with a purely capacitive load to characterize the power transfer in a more realistic situation. One of the converters was then used to power a custom design radio transceiver that consumes 12 mW when on. Finally, a third, larger converter was built and used to power a complete wireless sensor node that draws approximately 60 mW when on. The conclusions from these tests are summarized below.

- The maximum demonstrated power density from a vibration source of 2.25 m/s^2 at 60 Hz is $335\text{ }\mu\text{W/cm}^3$.
- The maximum measured power transfer to a capacitive load is $180\text{ }\mu\text{W/cm}^3$, or a little over half the power dissipated by a purely resistive load.
- A 1 cm^3 generator has been successfully used to power a custom design RF transceiver. The generator can sustain about a 1% duty cycle for this transceiver.
- A larger, 6 cm^3 , generator has been built and used to test a complete programmable wireless sensor node. The sustainable duty cycle was 1%.
- The efficiency of the power circuitry used is approximately 75% - 80%. Significant improvement can be made on the design of the power electronics.

Chapter 6: Case Study: Piezoelectric Converter Design for use in Automobile Tires

Experimental results for some piezoelectric converter designs optimized within a volume constraint of 1 cm^3 and for use with steady state sinusoidal vibrations were presented in the previous chapter. Results from the operation of a wireless sensor node powered by one of these converters were also shown. This chapter will utilize the models and principles already developed to explore the design of a converter for a very different type of environment, an automobile tire. It is desirable to embed wireless sensor nodes inside automobile tires in order to send real time data to the car and improve the safety and performance of the vehicle. Using vibrations to generate the power for these wireless sensor nodes has been suggested. This chapter will discuss the different assumptions that apply, how these assumptions affect the models and the potential power output, and finally demonstrate a converter capable of powering a wireless sensor node embedded inside a tire.

6.1 Environment inside tires and constraints

Up to this point, only low level steady state vibrations have been considered as a driving source for vibration to electricity converters. Based on numerous measurements, it has been concluded that most commonly occurring low level vibrations are sinusoidal in nature and have an fundamental frequencies between about 75 and 200 Hz. Furthermore, the acceleration magnitude ranges from below 1 m/s^2 to a maximum of about 10 m/s^2 (or 0.1 to 1 g). By contrast, the accelerations experienced in an automobile

tire can exceed 1000 m/s^2 . Furthermore, the acceleration profiles do not match steady state sinusoidal vibrations very well. An example of the radial acceleration inside a tire is shown in Figure 6.1. The car, in this particular case, was traveling at 100 Km/hr. This data is provided by the Pirelli tire company, and is reproduced here with their permission. The same data is shown in the frequency domain in Figure 6.2.

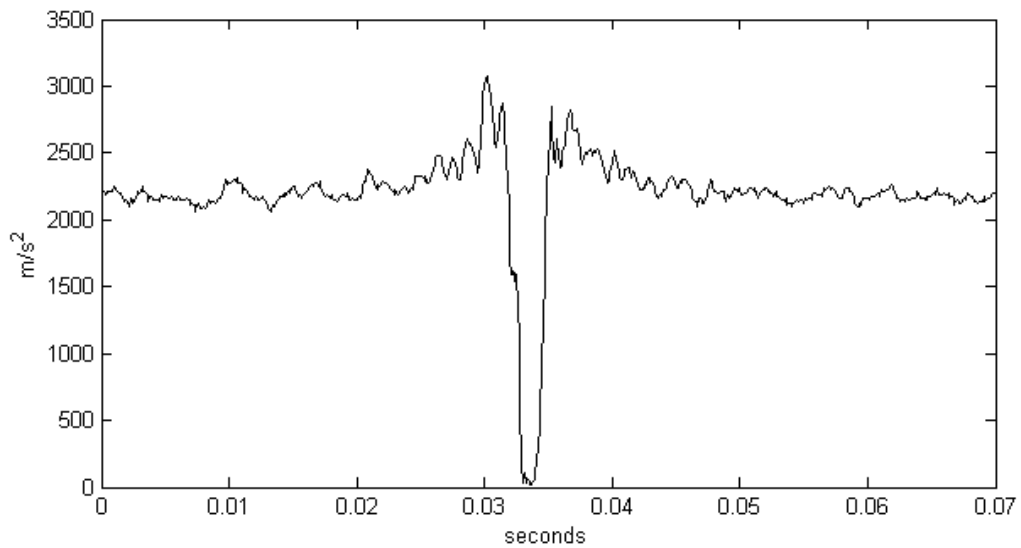


Figure 6.1: Radial acceleration vs. time from a tire traveling at 100 km/hr. Data for one revolution shown.

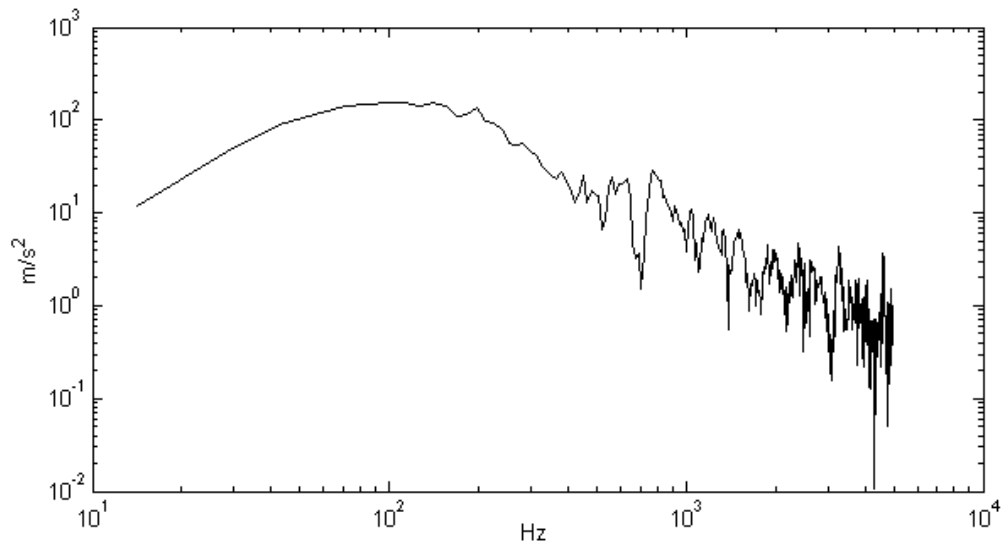


Figure 6.2: Radial acceleration vs. frequency from a tire traveling at 100 km/hr.

As a point on a tire moves around, it is subject to an almost constant centripetal acceleration. This is seen as the more or less horizontal line at about 2200 m/s^2 in Figure 6.1. When that point on the tire comes into contact with the ground, the centripetal acceleration goes to zero for the short time that the point is translating along the surface of the ground. The result is a very sharp inverse spike in acceleration. There are many subtle details about this acceleration profile that relate to the tire's interaction with the road, but discussion of these is beyond the scope of this dissertation. As is seen from Figure 6.2, there is no longer a dominant peak in acceleration magnitude at a specific frequency. The acceleration is distributed over a band of frequencies with some smaller high frequency spikes. It should also be noted that the dominant frequency band is dependant both on the speed of the car and the nature of the surface, as are the higher frequency spikes. This dramatically affects the design of converter because there is no longer a dominant driving frequency to which the natural frequency of the bender should be matched. Furthermore, the extremely large accelerations will affect the design. Limit stops will need to be introduced to prevent the piezo ceramic from exceeding its fracture strain. Furthermore, the robustness of the design and clamp becomes a key factor. The challenge is no longer to try to maximize the amount of strain developed in the bender, but to prevent it from breaking while still generating as much power as possible given the yield strain of the material and the volume constraints.

The size constraint for this application is more demanding than previously considered. The entire size of the device should not exceed $5\text{mm} \times 5\text{mm} \times 5\text{mm}$. The high curvature of the tire at the point where the tire comes into contact with the ground dictates this small size constraint. In theory, this would cut the maximum potential power

density by a factor of 8. Remember however, that the input vibrations are far more energetic than previously considered. An additional consideration is that because of the smaller size and smaller mass, the resulting resonant frequencies of converters will be much higher.

There is a certain amount of information that must be acquired and transmitted for each tire revolution. Therefore, the critical energy consumption target is the number of joules required to acquire and transmit this information per tire revolution. The level of power consumption will then depend on the speed of the car. At faster speeds, the information must be transmitted more frequently, and therefore the average power consumption is higher. A simple equation to estimate the power needed to acquire the necessary sensor readings (accelerometer readings in this case) and transmit information calculated from the sensor readings with the target wireless system is given in equation 6.1 (Doherty *et al*, 2001)

$$E_{rev} = n_{samples} * n_{axes} * 50 pJ + (n_{bits} + 10) * 10 nJ \quad (6.1)$$

where:

- $n_{samples}$ is the number of data samples to acquire per revolution
- n_{axes} is the number of axes for which data is acquired
- n_{bits} is the number of bits that must be transmitted

According to the specifications from the tire manufacturer, 100 samples per revolution per axis must be acquired, and 5 bytes per axis per revolution must be transmitted (or 120 bits per revolution). The resulting minimum energy per revolution required then is 1.3 $\mu J/rev$.

6.2 Model refinements and analytical expressions

A few model refinements were made in order to accurately model the system. The previously developed model assumed a perfectly rigid cantilever mounting. As was discussed earlier this resulted in the measured natural frequencies being a little lower than the predicted values. However, the overall model was still able to predict the power output quite well. The clamped (or glued) mounting is, of course, not perfectly rigid. A better model for the mounting of the clamped or glued beam is the pin-pin model shown in Figure 6.3. The beam is modeled with two pin constraints, one at the end of the beam, and a second at the point where the clamp meets the beam. The resulting changes to the dynamic model are minimal, and are detailed in Appendix A. It should be noted that the incorporation of the pin-pin model is more important for smaller generators where a greater proportion of the bender is in the clamp. The rigid cantilever mounting model results in a greater discrepancy in terms of both predicted natural frequency and power output for the smaller converters than for the larger converters. The pin-pin mounting model results in a lower predicted natural frequency. It was found that the measured natural frequency matched the predicted natural frequency with the pin-pin model to within less than 1%. Secondly, the pin-pin model results in a more realistic stress profile along the length of the beam. The result is a significantly better match between experimental and simulated data for the smaller converters.

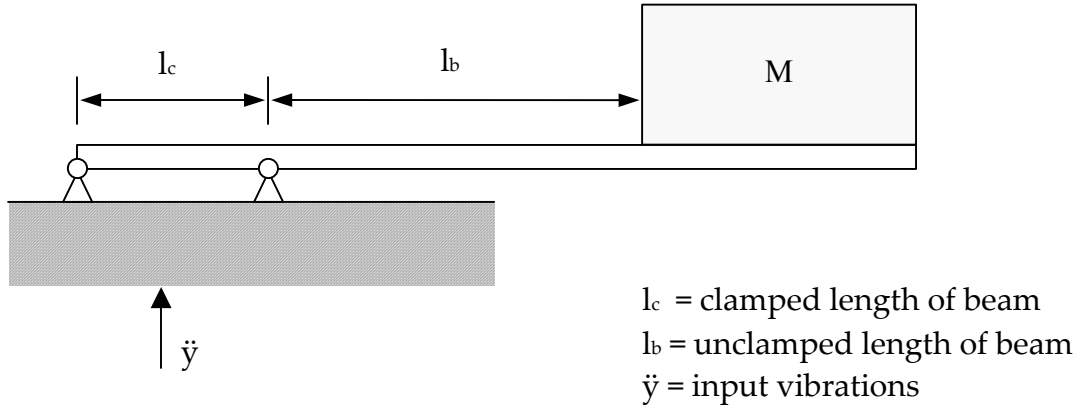


Figure 6.3: Illustration of pin-pin mounting model for piezoelectric generator.

A second model change is the incorporation of limit stops. Because the input accelerations are so large, the resulting strain would far exceed the fracture strain of the ceramic in some cases. Limit stops must be placed such that the displacement of the proof mass is stopped when the maximum strain in the bender is at some fraction of the yield strain. The limit stops need to be incorporated into the simulation. A reasonable coefficient of restitution of 0.5 between the proof mass the stop is assumed.

The analytical power solutions presented in Chapter 4 no longer apply because of the limit stops. Making a few simplifying assumptions, analytical expressions can be developed that give some insight into how the limit stops affect power generation, and how the design variables affect power generation with the existence of limit stops. It is first assumed that the input vibrations are sinusoidal and fixed at a specific frequency. This is not really the case, but makes an analytical expression possible that gives valid insight. Second, it is assumed that the proof mass does in fact hit the limit stop on each cycle. Then the amplitude of the oscillating strain is fixed by the limit stops. Again, this assumption simplifies the reality of the situation, but is nevertheless useful. Finally it is assumed that the generator is terminated with a resistor. The circuit equation of the

system (the second of the two equations in the system model given in chapter 4 as equation 4.10) is given here as equation 6.2.

$$\dot{V} = \frac{-Ydt_c}{n\varepsilon} \dot{\delta} - \frac{1}{RC_p} V \quad (6.2)$$

The term $\dot{\delta}$ is now a fixed quantity dependent only on the placement of the limit stops and natural frequency of the generator. The voltage signal across the load capacitor can then be solved, and is given by the expression in equation 6.3.

$$|V| = \frac{-d_{31}Yt}{n\varepsilon} \frac{\omega RC}{(\omega RC)^2 + 1} |\dot{\delta}| \quad (6.3)$$

where: ω is the frequency of the input vibrations

The power transferred to the load is given simply as $P = V^2/R$. If it assumed that R is related to the capacitance as $R = k/\omega C$ where k is some constant, then an analytical expression for power can be obtained as shown in equation 6.4.

$$|P| = \frac{(d_{31}Y)^2}{\varepsilon} \left(\frac{k}{k^2 + 1} \right)^2 \omega l w t \quad (6.4)$$

where: l is the length of the electrode on the cantilever
 w is the width of the cantilever beam
 t is the total thickness of the piezoelectric material

While the expression for power given in equation 6.4 will not give a very accurate estimate of output power for the device embedded inside a tire, the trends highlighted by the expression are valid, and so it does give some insight into the design of the generator for the strain limited case. Based on equation 6.4, the goal should be to maximize the product of l , w , and t . If the generator is being designed such that its natural frequency matches the frequency of the input vibrations then maximizing this product will result in a long skinny design. For a given electrode area ($l*w$), a long skinny design will result in

a thicker bender than a shorter wider design. Note that the optimization algorithm for the non-strain limited case also resulted in a long skinny design. Simulation results will be shown in the following section that demonstrate how the product of l , w , and t affect the power generation.

The same trends hold true if the model is adjusted for a capacitive load. In the case of the capacitive load, the maximum voltage that is reached across the storage capacitor (in the fully charged state) is given by equation 6.5. δ_{\max} is the maximum strain allowed by virtue of limit stops.

$$V_{\max} = \frac{-d_{31}Yt}{n\epsilon} \delta_{\max} \quad (6.5)$$

If it is assumed that C_{st} is much greater than C_p ($C_{st} + C_p \approx C_{st}$), then the rate at which the voltage across the storage capacitor increases is given by equation 6.6. In order to maximize the power transfer to the storage capacitor both the maximum voltage and the rate of increase should be maximized. As is the case with the resistive load in a strain limited situation, the optimal design should try to maximize both $l*w$ and t . Again this results in a long skinny design.

$$\dot{V} \approx \frac{-d_{31}YA}{C_{st}} \dot{\delta} \quad (6.6)$$

6.3 Simulations and design

Simulations have been performed in order to verify the conclusions drawn in the previous section. Figure 6.4 shows the average strain and voltage versus time from a simulation using a resistive load. The effect of the limit stops is clearly evident on the strain versus time plot. Figure 6.5 shows the simulated energy per revolution using a

resistive load for three different designs, all of which have the same resonant frequency, proof mass, device capacitance, and overall size. The $l \cdot w \cdot t$ product, however, is different for the three designs. It can be seen that, as discussed in the previous section, the energy per turn increases with an increasing $l \cdot w \cdot t$ product for all three car velocities simulated. However, the increase is very small, indicating that within the stringent volume constraints, design parameter optimization can only marginally improve the power output.

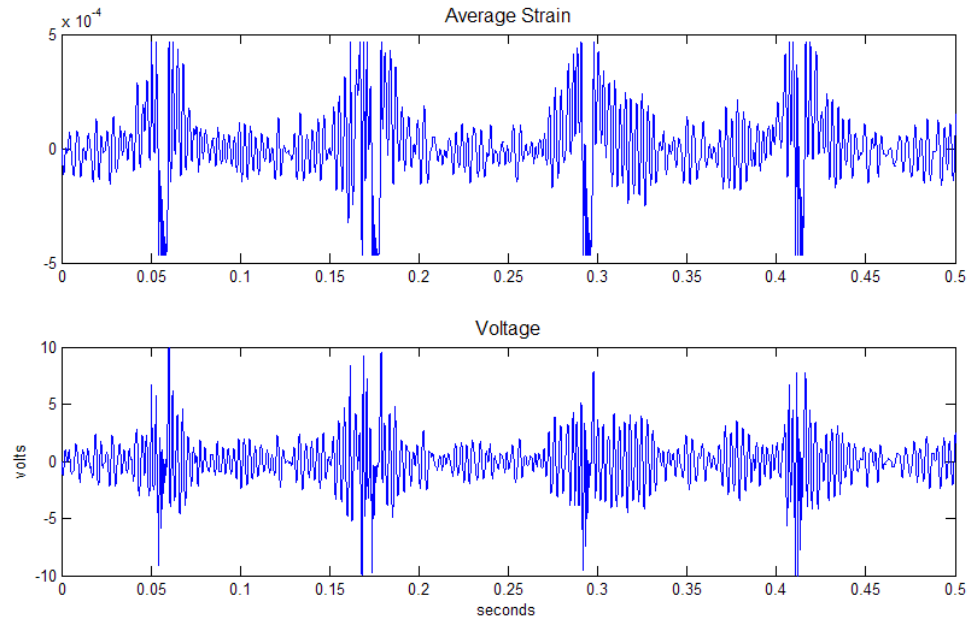


Figure 6.4: Average strain (top) and output voltage (bottom) versus time for a simulation using a small bender design with a resistive load of 300 k Ω .

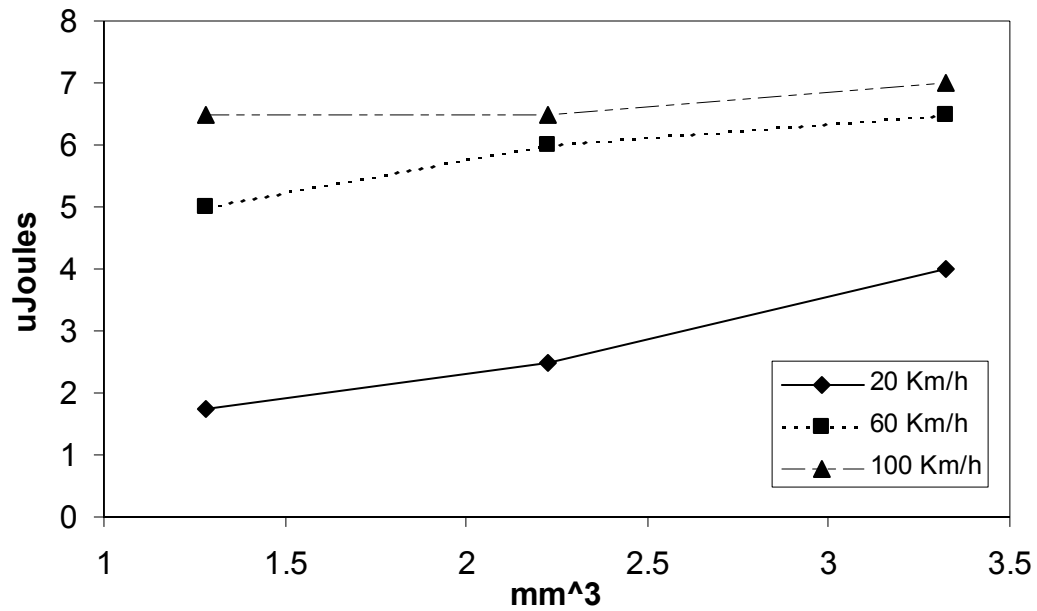


Figure 6.5: Energy per revolution versus the $l*w*t$ product. Three designs are shown with $l*w*t$ equal to 1.3, 2.2, and 3.3 mm³ simulated at three different car velocities.

Simulations were also performed on the same three designs with a capacitive load of 1μF. Figure 6.6 shows the energy per revolution transferred to the storage capacitor for the same three car velocities. Again, the energy per revolution generally increases as the $l*w*t$ product increases. There is a slight decrease at the highest velocity, however, it is believed that this is an anomaly and due to some abnormalities in the acceleration data used as input at 100 km/hr. In the case of the capacitive load, the dependence on the $l*w*t$ product is more pronounced. For purposes of comparison, Figure 6.7 shows the power transferred to the storage capacitor for each of the three designs at 60 km/hr. Note that the volume of this device is approximately 5mm X 5mm X 5mm, so in order to get power per cubic centimeter for comparison with data presented previously, the output power would need to be multiplied by 8.

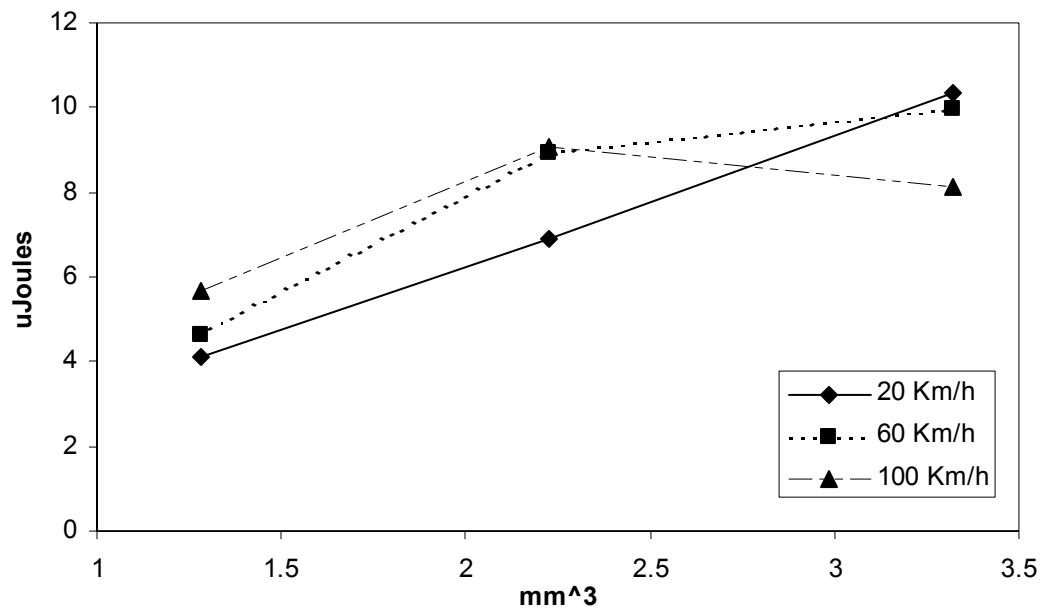


Figure 6.6: Energy per revolution versus the $l \cdot w \cdot t$ product with a capacitive load of $1\mu\text{F}$. Three designs are shown with $l \cdot w \cdot t$ equal to 1.3, 2.2, and 3.3 mm³ simulated at three different car velocities.

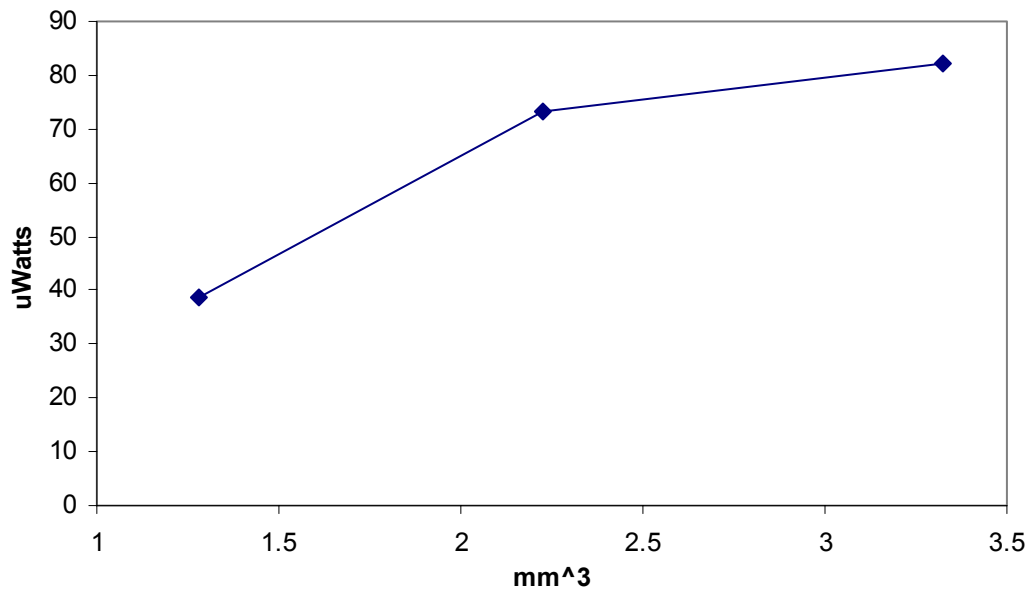


Figure 6.7: Power transferred to a capacitive load of 1mF versus the $l \cdot w \cdot t$ product for three different designs.

Because the input vibrations are no longer concentrated at a single frequency, the generator cannot be designed to be a resonant system in the same way as done previously.

As shown above in Figure 6.2, the input vibrations are distributed over a band of frequencies. It is however, generally the case that most of the power is below about 200 Hz. However, this fact changes one of the key design criteria, which was to design the natural frequency of the generator to match the frequency of the driving vibrations. Some basis must therefore be developed on which to base the design of the natural frequency of the generator. Figure 6.8 shows the energy per revolution versus resonant frequency. Three different designs were simulated at three different car velocities. The three designs had different resonant frequencies, but the mass, device capacitance, $l \cdot w \cdot t$ product, and volume are constant.

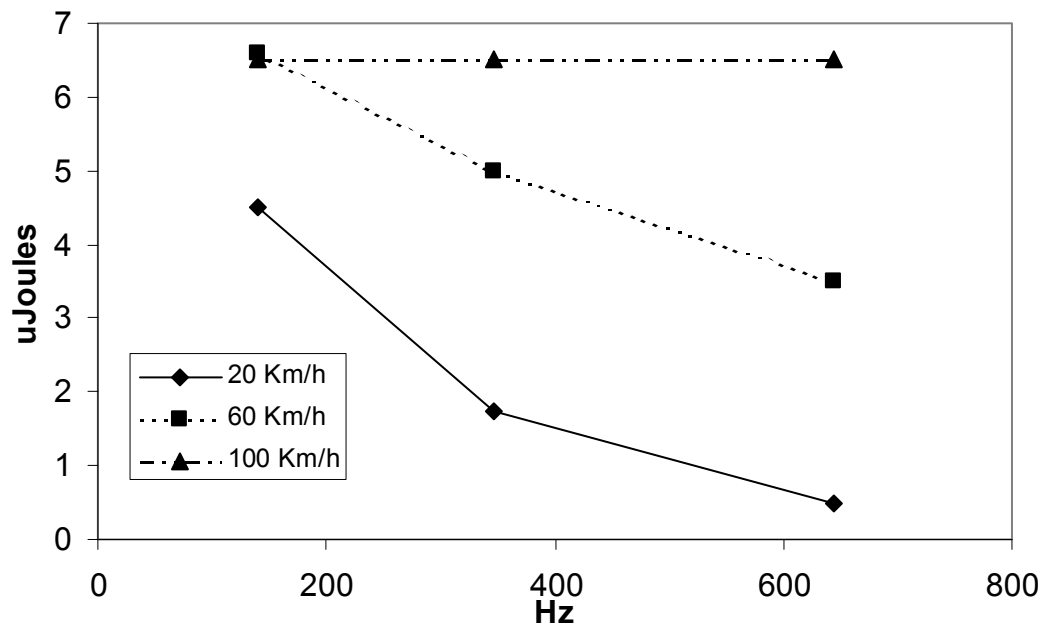


Figure 6.8: Energy per revolution versus natural frequency. Three different designs shown with resonant frequencies of 145, 345, and 645 Hz.

It is interesting that the resonant frequency has a greater effect at lower speeds. One possible reason for this is that the frequency spectrum of the input vibrations is more concentrated at low frequencies for slower car velocities. However, the more likely explanation is that the higher frequency designs are stiff enough that they don't reach the

limit stops at lower car velocities. At higher speeds all designs reach the limit stops, and so the output power is not very dependent on the resonant frequency. However, at lower speeds, the more compliant designs develop more strain in the piezoelectric material, and therefore produce more energy per revolution. Because a generator needs to provide enough power to run the electronics at all speeds down to 20 km/hr, it is desirable to design for as low a natural frequency as is practical. Again, this design reasoning argues for a long skinny generator.

The requirement that the generator must function correctly from 20 km/hr all the way up to 140 km/hr causes severe reliability issues. In order to maximize robustness, one would want to design the cantilever such that it would just reach the limit stops under the most harsh input (140 km/hr). Although the resulting design would be robust, it would also be very stiff and would not generate the required power at lower speeds. The problem with a more compliant design is, of course, that at high car speeds, the proof mass collides with the limit stops while it is still moving at a very high velocity. The result is that large impact forces are imparted to the limit stops and casing, and that shock waves are propagated down the cantilever beam. The design of an appropriate casing and limit stops for a compliant bender is not a trivial project. This project is being undertaken, but will not be reported here.

Because of the stringent volume constraint the size of the proof mass is considerably reduced. In order to maximize the proof mass, the geometry shown in Figure 6.9 was adopted. This design more effectively uses the available volume. The resulting proof mass using the tungsten alloy previously described is about 0.7 grams.

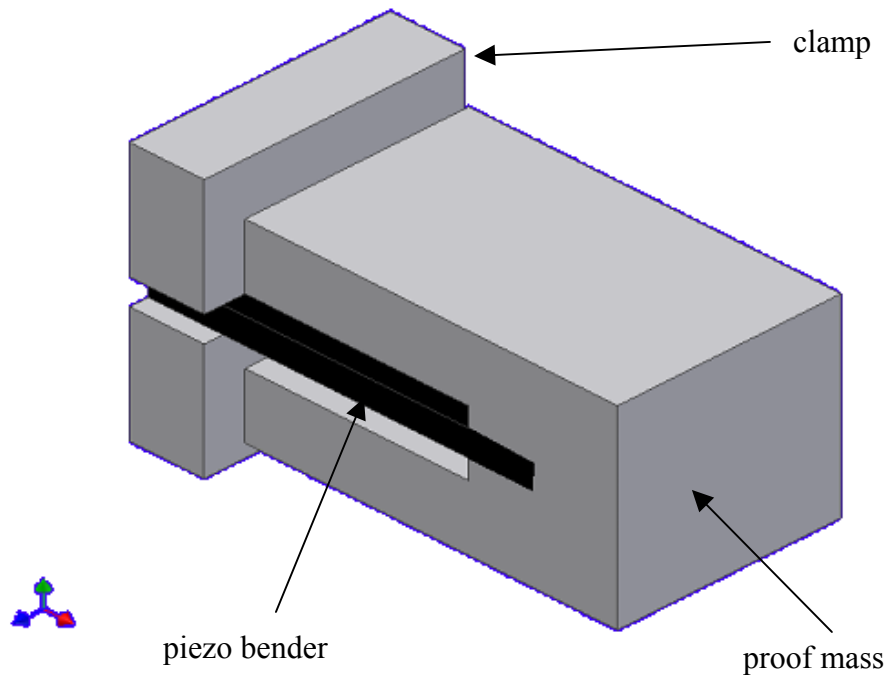


Figure 6.9: Proof mass, bender, and clamp for small generator designed to embedded inside automobile tires.

One possible concern is that the rotational inertia of the proof mass may affect the dynamics of the generator. It is conceivable that, if the rotational inertial of the proof mass was large enough, it would more or less just translate up and down, and the beam would bend in more of an ‘S’ shape. This is illustrated in Figure 6.10. Calculations show that the rotational inertial is an order of magnitude below the value at which it would have a significant effect. The ratio of the moment generated at the end of the beam to the torque generated by the inertia of the mass is given in equation 6.7. Within the volume constraints of this project, this ratio ends up to be within the range of 15 to 35. Therefore, the rotational inertia will not significantly affect the dynamics of the bender. This is further verified by the fact that the simulations match measured data very closely as will be shown in the next section.

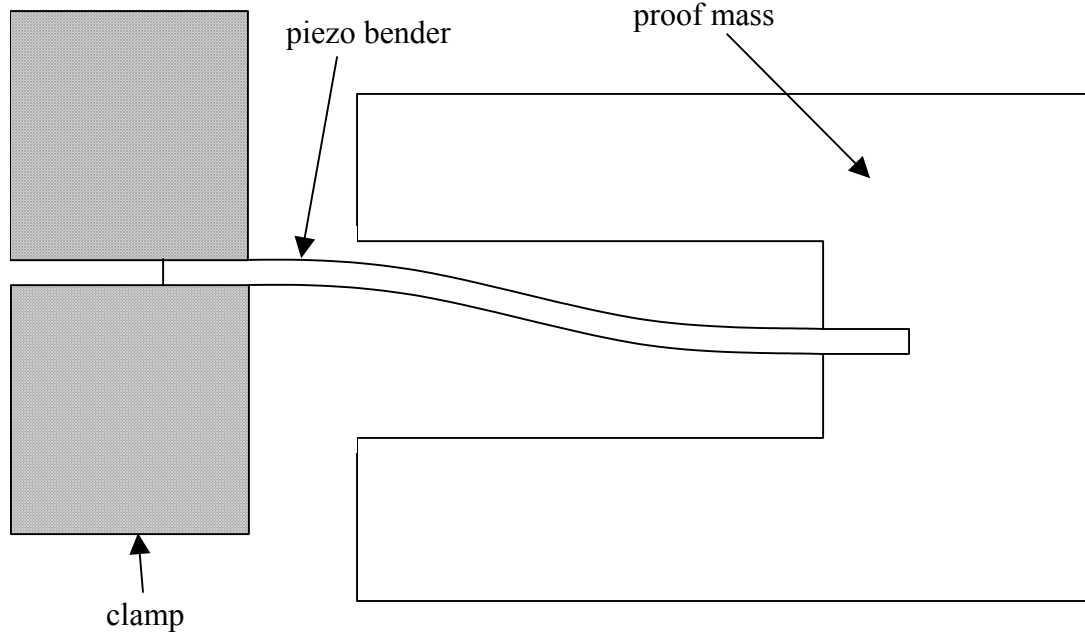


Figure 6.10: Schematic of generator showing the potential affect of the rotational inertia on the bending of the beam.

$$\frac{M}{T} = \frac{2YI_b}{l_b \omega^2 I_m} \quad (6.7)$$

where: M is the moment generated at the end of the beam
T is the torque generated by the rotational inertia of the mass
Y is Young's modulus for the piezoelectric ceramic
 I_b is the moment of inertia for the bender
 l_b is the length of the beam
 I_m is the mass moment of inertia of the proof mass

It is difficult to effectively run the optimization algorithm using a dynamic simulation as the objective function when limit stops are involved because the resulting response surface has discontinuities. The optimization algorithm cannot calculate derivatives at discontinuities in the response surface, so the algorithm either fails to converge or results in a clearly sub-optimal design. Using some engineering judgment and the results derived from analytical expressions in conjunction with the optimization

algorithm, one can come up with a close to optimal design. There is of course no guarantee that the design is truly optimal, but it will be close. Using this procedure, the design parameters listed in Table 6.1 are proposed as a good design for a generator that will be embedded inside an automobile tire.

Variables	Optimized Value
l_m	4 cm
h_m	3.5 cm
w_m	3.5 mm
l_b	4.0 mm
w_b	3.2 mm
l_e	4.0 mm
t_p	0.05 mm
t_{sh}	0.1 mm
mass	0.7 g

Table 6.1: Optimal design parameters for a generator to be embedded inside a tire.

The design was constrained to a total length of 5mm. Figures 6.11 – 6.13 show the simulated energy generated per turn for three different car velocities. Each “hump” is one revolution of the tire. The energy is reset to zero after each revolution. The resulting energy is different from each revolution because the input acceleration profile is slightly different for each succeeding turn of the tire. However, the figures show that at 20 km/hr the average energy generation is about $2\mu\text{J/rev}$, and about $5\mu\text{J/rev}$ and $6\mu\text{J/rev}$ for 60 km/hr and 100 km/hr respectively. This level of power generation is just barely enough to power the wireless sensor at slow speeds, but should be more than adequate at higher speeds. As a final note, simulated energy results shown above in Figures 6.5 – 6.8 are in some instances higher than those reported here because those designs were not limited to a total length of 5mm.

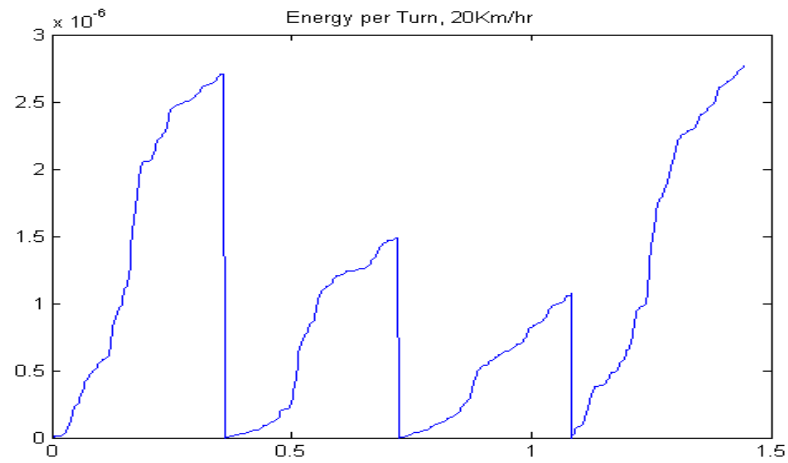


Figure 6.11: Energy per revolution (Joules) versus time (sec.) at 20 km/hr. Data for 4 tire revolutions is shown.

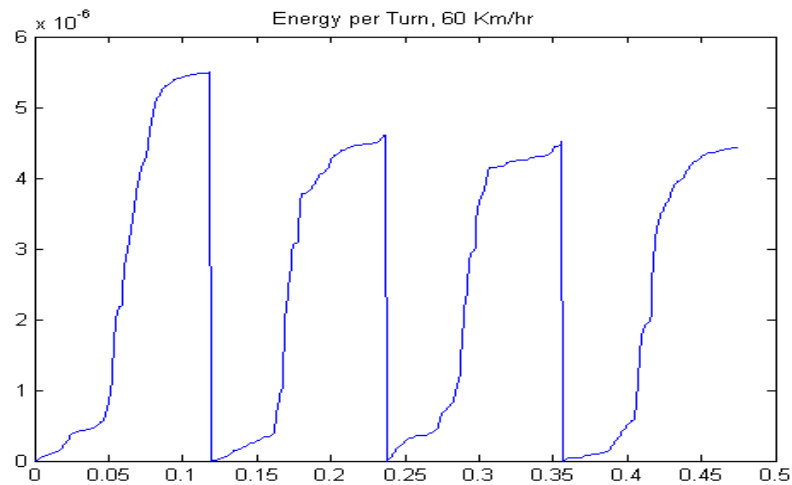


Figure 6.12: Energy per revolution (Joules) versus time (sec.) at 60 km/hr. Data for 4 tire revolutions is shown.

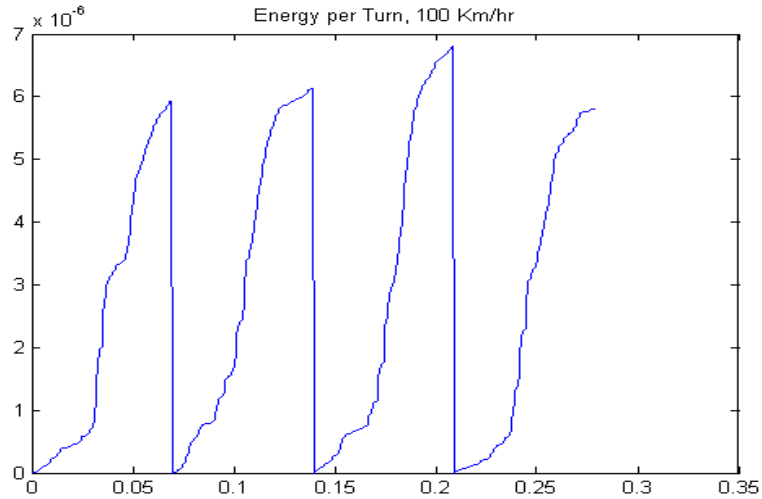


Figure 6.13: Energy per revolution (Joules) versus time (sec.) at 100 km/hr. Data for 4 tire revolutions is shown.

6.4 Experimental results

An unpackaged prototype was first built and tested. A photograph of the prototype is shown in Figure 6.14: The dimensions of this prototype do not exactly match those in Table 6.1 because of the common problem that we can only obtain benders in standard thicknesses. Therefore the thickness of the piezo layer used is 0.1397 mm (t_p) and the thickness of the shim is 0.1016 mm (t_{sh}). All other dimensions are as stated in Table 6.1.

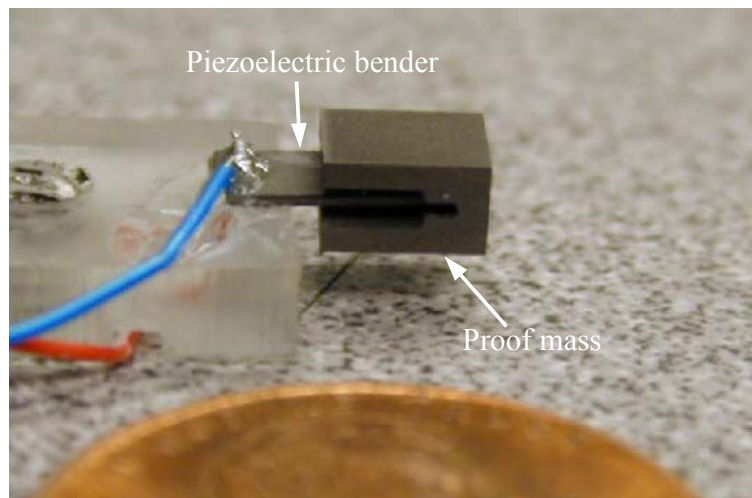


Figure 6.14: Unpackaged generator prototype.

It is very difficult to actually test a generator inside a tire and get meaningful results. Therefore the generator was tested on a vibrometer. The vibrometer hardware used is not capable of duplicating the acceleration traces from actual tire measurements. Therefore a square wave input was used to try to simulate the critical qualities of the real acceleration traces. It should also be noted that the vibrometer used is not capable of producing accelerations as large in magnitude as those experienced inside a tire at high speeds. An example of the acceleration output from the vibrometer with a square wave input at 50 Hz is shown in Figure 6.15. The frequency spectrum of the same data is shown in Figure 6.16.

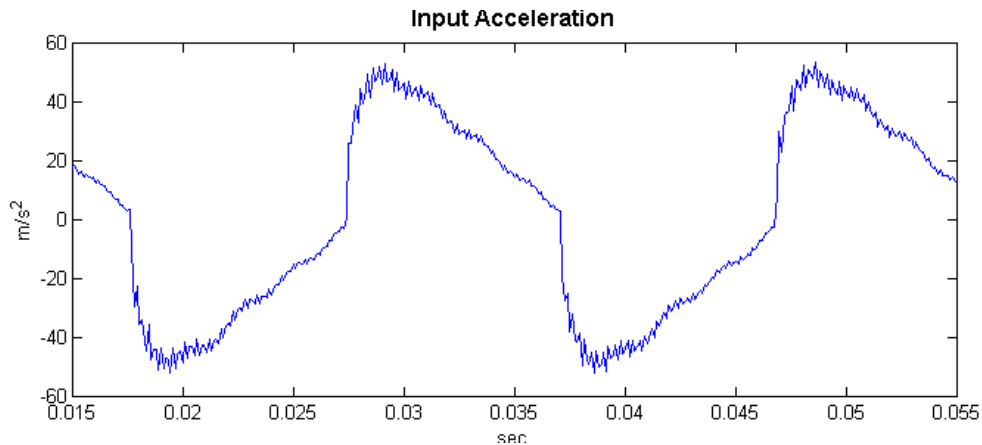


Figure 6.15: Acceleration versus time measured from the vibrometer with a square wave input from the signal generator.

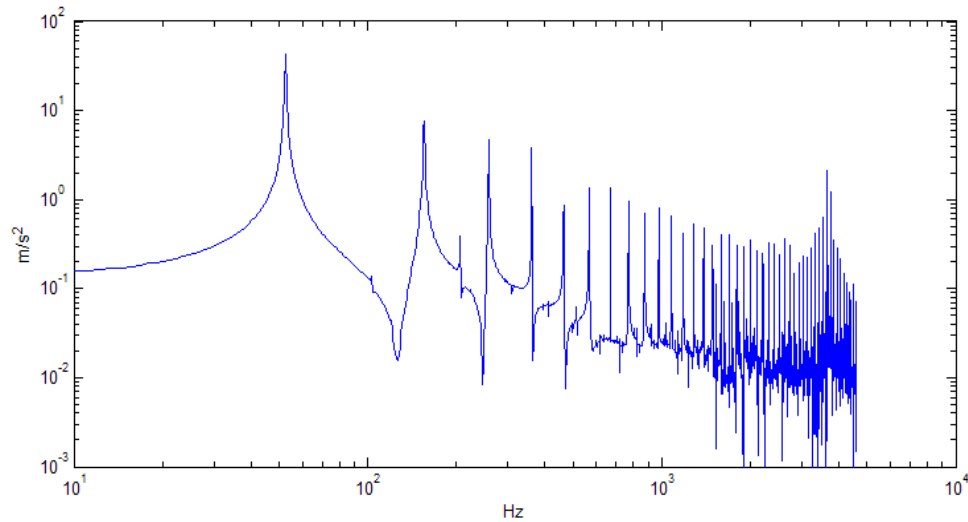


Figure 6.16: Acceleration versus frequency from the vibrometer with a 50 Hz square wave input.

The unpackaged prototype was tested on the vibrometer using the vibration input shown in Figure 6.15. The output voltage when the generator is terminated with a 130 k Ω resistor is shown in Figure 6.17. The simulated voltage is shown as a dotted line, and the measured voltage is shown as a solid line. Notice the very close match in resonant frequency. Also, the voltage magnitudes match well, although the simulated output is slightly lower. This is not unexpected as stress concentrations are not considered in the model and will result in higher than expected stress, and therefore voltage, levels.

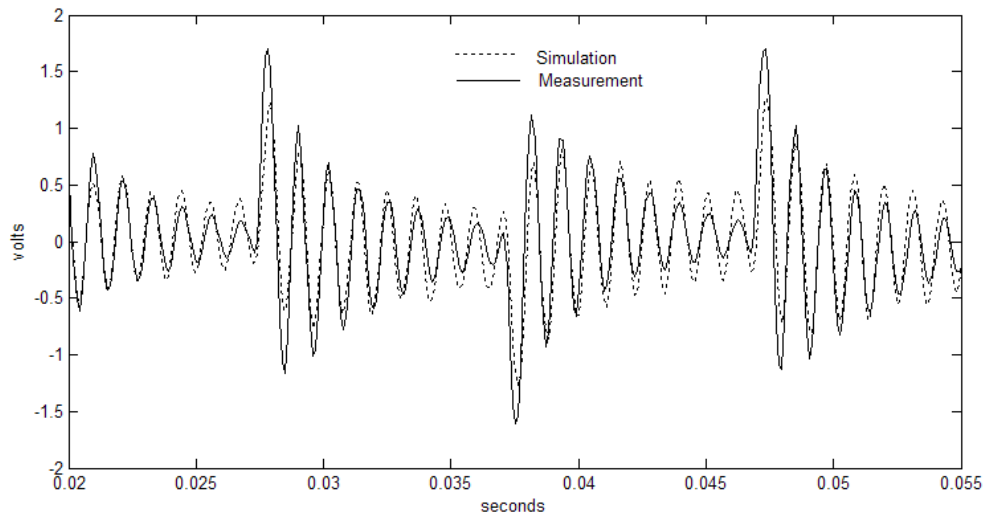


Figure 6.17: Voltage versus time for small unpackaged prototype with 130 k Ω load with a square wave input. Both simulated and measured data are shown.

The same unpackaged generator was tested with a capacitive load circuit as previously described. The vibration input was the same as shown in Figure 6.15. The voltage across the storage capacitor versus time is shown for two tests, one with a storage capacitance of 0.8 μF (Figure 6.18), and another with a storage capacitance of 3.3 μF (Figure 6.19). Again, these storage capacitances are unrealistically low, but used in order to reduce computation time for the simulations and testing time for the prototyped devices. The graphs would look exactly the same for larger storage capacitances except that the time scale would be longer.

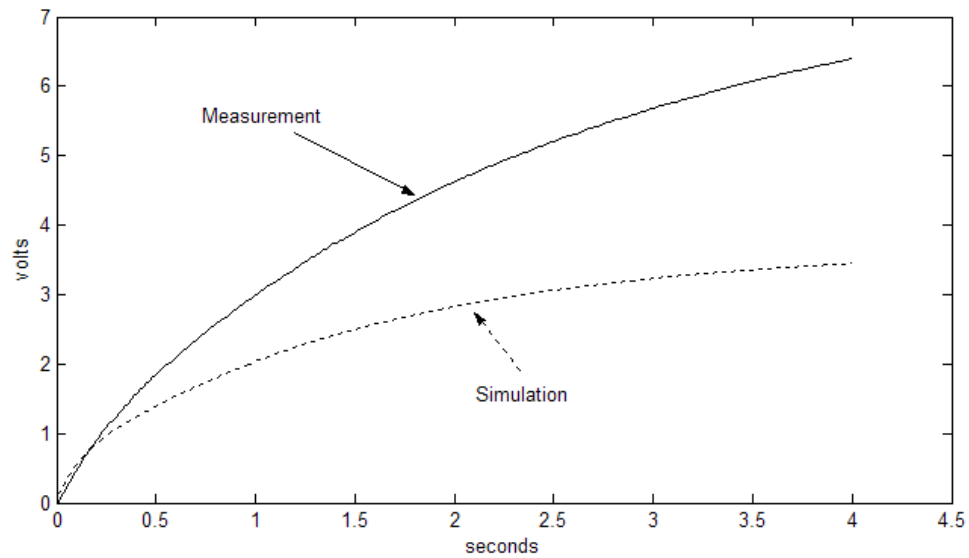


Figure 6.18: Measured and simulated voltage versus time for an unpackaged prototype with a 0.8 μF capacitive load.

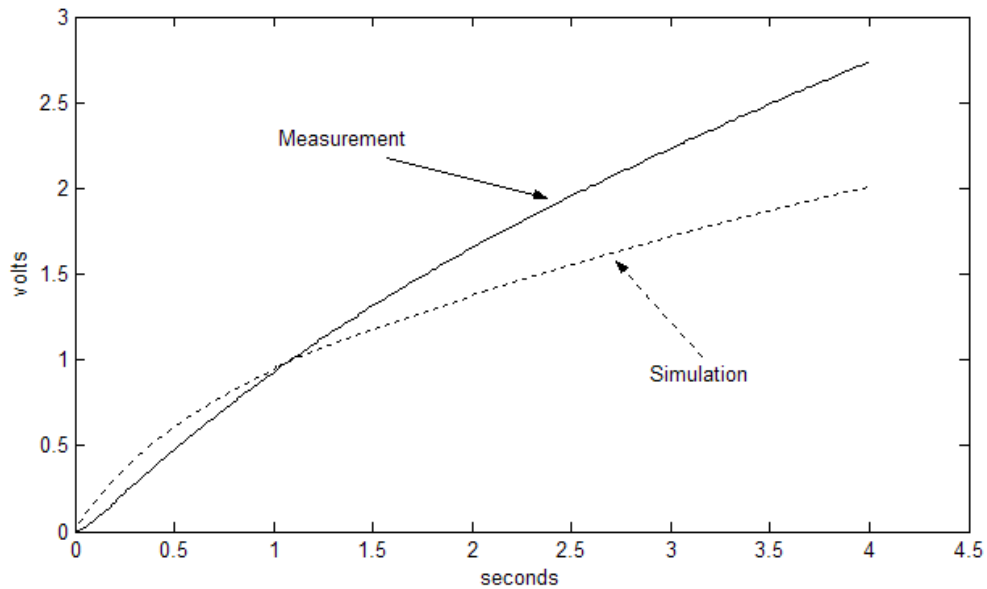


Figure 6.19: Measured and simulated voltage versus time for an unpackaged prototype with a 3.3 μF capacitive load.

In both cases the simulated voltage versus time trace is significantly lower than the measured value. This could be attributable to unmodeled stress concentrations as

mentioned before. In any case, the capacitor voltage is in the correct range to drive the input to a voltage regulator or DC-DC switching converter.

Packaged prototypes were also designed and built that could be attached to the inside of a tire and tested. Two different packages were designed. The dimensions of the bender and proof mass were the same for the packaged devices as for the unpackaged devices with the exception that the length of beam attached to the clamp was shorter (1mm versus 2.2 mm) for the packaged devices. A photograph of the first packaged device is shown in Figure 6.20, and a photograph of the second packaged prototype is shown in Figure 6.21. There are few primary differences between the two casings. The first casing is made of two acrylic parts glued together with two steel blocks acting as the clamp. The second casing uses two Delrin parts, which are stronger in impact than acrylic. The plastic clamp for the second casing is shaped in an arc in order to reduce the stress concentration at the clamp as shown in Figure 6.22. Finally, the glue joints for the second design cover entire surfaces rather than just edges, making the joints for the second design stronger. Design of the casing is ongoing, and a detailed description of the design issues is beyond the scope of this dissertation.

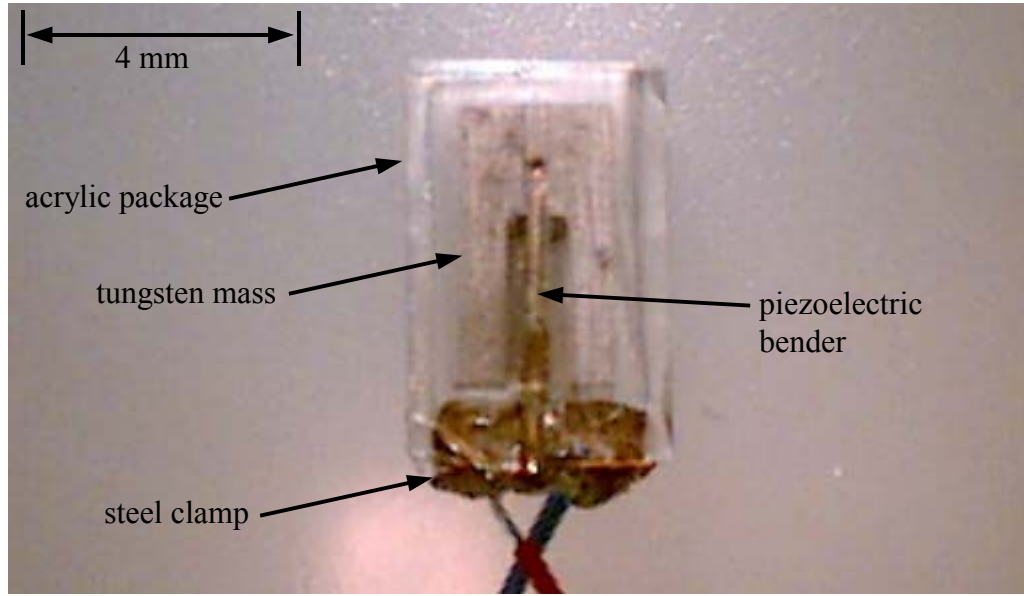
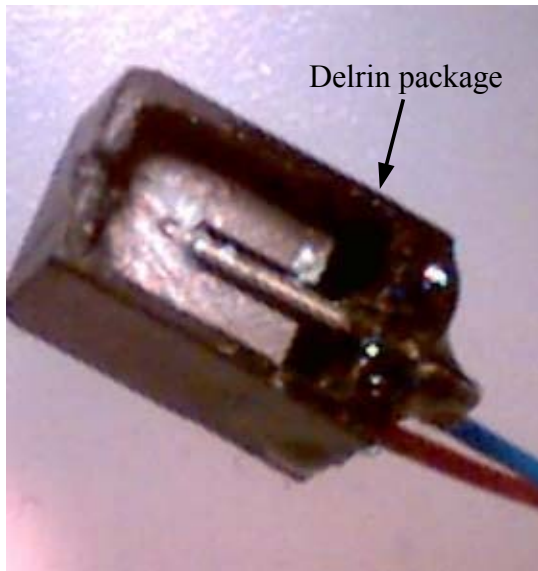
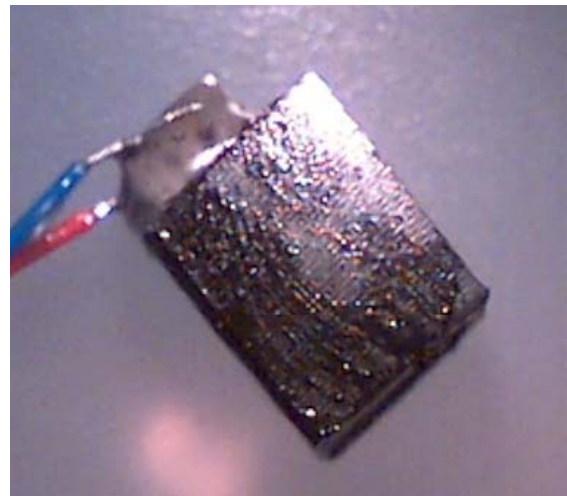


Figure 6.20: First packaged prototype for testing inside a tire. Made of clear acrylic with steel blocks acting as the clamp.

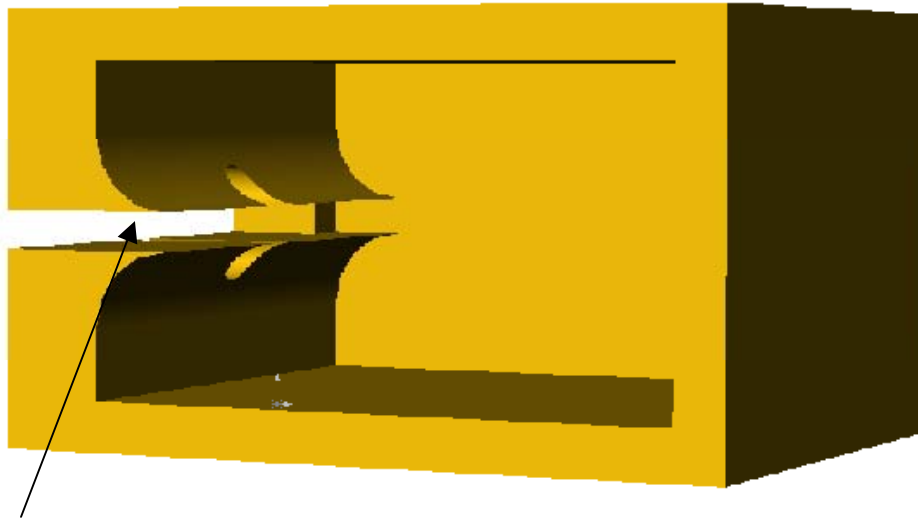


Partially assembled



Fully assembled

Figure 6.21: Second packaged prototype for testing inside a tire. Made of black Delrin. Left photograph shows assembly without the final cover. Right photograph shows the entire assembly.



Shaped clamp to reduce stress concentration.

Figure 6.22: Solid model of the primary part of the second prototype showing the shaped clamp to reduce the stress concentration.

The packaged device was tested on the vibrometer using the same square wave input and 130 k Ω load as the unpackaged device. The testing results for the first packaged casing are shown in Figure 6.23. The output exhibits significantly more damping than the unpackaged device. This is not surprising. Because the space inside the package is very restrictive, it is likely that fluid damping plays a larger role in the packaged device. Secondly, it appears that there were some impacts with the casing. These impacts would also act to damp out the oscillations more quickly. Prototypes of both casing types were shipped to the tire manufacturer for testing inside of a tire. Both casing types broke at the very high accelerations exhibited in a tire. As mentioned, work on a more robust packaging solution is ongoing, but outside the scope of the work reported here.

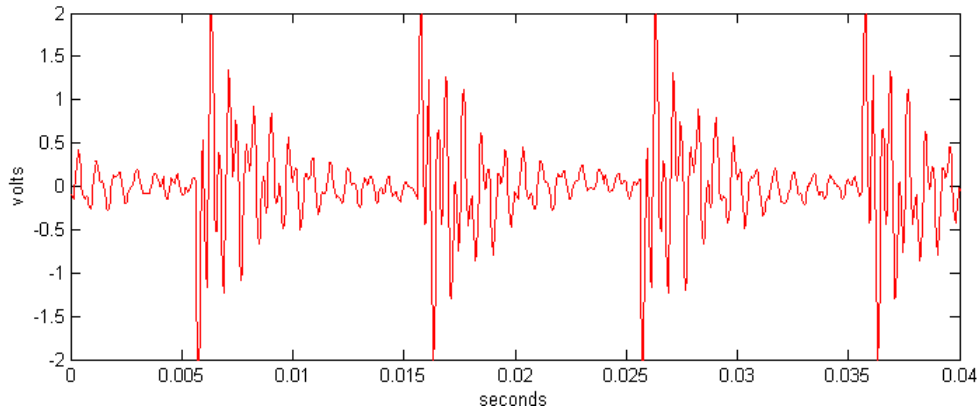


Figure 6.23: Test results for the first packaged device. Shows voltage versus time for device terminated with a 130 k Ω resistor driven by a vibrometer with a square wave input.

6.5 Conclusions

The application of the models and design principles developed in Chapter 4 have been demonstrated in the design of vibration generators for a specific application, self-powered sensors embedded inside an automobile tire. Many of the assumptions made in the development of design principles and models are not accurate for this particular application. For example, the input vibrations are not “low-level” and they are not sinusoidal in nature. However, with slight adjustments, the models developed can still effectively be used as a design tool. Additionally, many of the same design principles apply.

Good agreement between test results from an unpackaged device and simulations has been demonstrated with a resistive load. The agreement between simulation and measurement for a capacitive load is not as strong. Nevertheless, the measured voltages across the storage capacitor are in the correct range to drive the input to a DC-DC converter that would in turn drive the sensor/radio system. Simulation results using input acceleration data from actual measurements inside a tire demonstrate that from 2 $\mu\text{J}/\text{rev}$

at 20 km/hr to 6 $\mu\text{J}/\text{rev}$ at 100 km/hr can be produced. The minimum power requirements are 1.3 $\mu\text{J}/\text{rev}$, therefore, the generator appears to be able to power the target sensor/radio system.

The packaged device exhibits significantly more damping than the unpackaged device. The packaged devices have been sent to the tire manufacturer for testing inside a tire. However, testing has demonstrated that they are not capable of withstanding the very high accelerations that exist in a tire. Therefore, more work is needed on a robust casing solution. The robustness of the generator becomes a primary consideration for this example. This issue has not been explored in much detail. Work is ongoing in this area, but considered outside the scope of this dissertation.

Chapter 7: Electrostatic Converter Design

Chapters 4 through 6 have dealt with piezoelectric converters. The direction will now change to the consideration of electrostatic converters. This chapter will deal with the modeling, design, and optimization of electrostatic converters. The following chapter will discuss the processing and fabrication of electrostatic converters. And finally, Chapter 9 will cover test results.

7.1 Explanation of concept and principle of operation

Recalling the discussion of electrostatic conversion presented in chapter 3, section 3, the variable capacitor is the basis of power conversion. Mechanical vibrations driving a capacitive structure cause the capacitance, and thus the energy stored in the capacitor, to change.

Reference was made to both charge constrained and voltage constrained conversion. Again, Meninger *et al* (Meninger *et al*, 2001) give a good explanation of the merits of both charge and voltage constrained conversion. In theory, slightly more power could be produced from a voltage constrained system. This conclusion however assumes that the change in capacitance of the system is limited by a maximum allowable voltage rather than by the kinetic energy imparted by the driving vibrations. This assumption will often not be valid, and so the only advantage of a voltage constrained system is often not operative. The primary disadvantage of the voltage constrained system is that it requires two separate voltage sources for conversion to take place. The charge constrained system is much simpler in that it only requires one separate voltage source. Therefore, a charge constrained system seems the best of the two alternatives, and has

been chosen as a target system for this study. Meninger *et al* have also chosen a charge constrained system, however, no mention is made of the underlying assumption inherent in calculating the power advantage of the voltage constrained system.

A simplified circuit for an electrostatic generator using charge constrained conversion is shown in Figure 7.1. This circuit is useful for power output calculations and demonstrates the basic function of energy conversion although it is not entirely realistic. A pre-charged reservoir, which could be a capacitor or rechargeable battery, is represented as the input voltage source V_{in} . The variable capacitor C_v is the variable capacitance structure, and C_{par} is the parasitic capacitance associated with the variable capacitance structure and any interconnections. When C_v is at its maximum capacitance state (C_{max}), switch 1 (SW1) closes, and charge is transferred from the input to the variable capacitor. The capacitive structure then moves from its maximum capacitance position to the minimum capacitance position (C_{min}) with both switches open. The result is that the energy stored on C_v increases. At minimum capacitance, switch 2 (SW2) closes and the charge stored on C_v (now in a higher energy state) is transferred onto the storage capacitor C_{stor} . The mechanical vibrations have done work on the variable capacitor causing an increase in the total energy stored in the system.

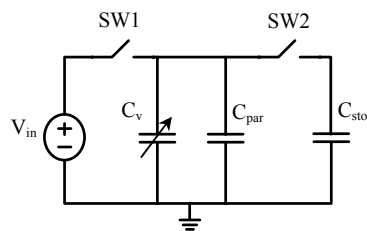


Figure 7.1: Simple circuit representation for an electrostatic converter.

In reality, the switches would either be diodes, or transistors with an inductor, and some method of returning a portion of the charge put onto the storage capacitor to the input reservoir would need to be employed. Researchers at MIT (Amirtharajah and Chandrakasan, 1998, Amirtharajah, 1999, Meninger *et al*, 1999, Amirtharajah *et al* 2000, Meninger *et al* 2001) have developed a circuit to accomplish this task. Detailed development of the power circuit is considered outside the scope of the current study. The circuit shown in Figure 7.1 is sufficient to obtain power estimates and to use as a basis for the design of the physical variable capacitance structure.

7.2 Electrostatic Conversion Model

The increase in energy stored in the variable capacitor per cycle is given by the equivalent expressions in equations 7.1a and 7.1b.

$$E = \frac{1}{2} V_{in}^2 (C_{max} - C_{min}) \left(\frac{C_{max} + C_{par}}{C_{min} + C_{par}} \right) \quad (7.1a)$$

$$E = \frac{1}{2} V_{max} V_{in} (C_{max} - C_{min}) \quad (7.1b)$$

where:

V_{max} represents the maximum allowable voltage across a switch

Depending on the specific implementation of the switches, the physical design, and the input vibrations, V_{max} may be a very limiting constraint. If it can be determined that the maximum allowable voltage will be a limiting constraint, then equation 7.1b may be the more useful of the two. Otherwise, equation 7.1a will be more useful in designing the system. The power output is, of course, just given by the energy per cycle multiplied by the frequency of operation, which will necessarily be the frequency of the input vibrations.

The energy transfer per cycle is highly dependent on the ratio of maximum to minimum capacitance. It is, therefore, important to note that actual distance of travel of the variable capacitance structure, and therefore the value of C_{\max} and C_{\min} , is determined by both the mechanical dynamics of the system and the design of the capacitive structure. A schematic of a vibrating mechanical system was shown in chapter 2 as Figure 2.4. The basic premise of the system is that there are two dampers, a mechanical damper representing pure loss, and an electrical damper representing the energy removed from the mechanical system and transferred to the electrical system. In chapter 2 it was assumed that both of these dampers were linear and proportional to velocity. Although the same schematic representation will be used to develop the dynamic model for electrostatic converters, it cannot be assumed that either damper is linear or proportional to velocity.

The equation of motion for the mechanical portion of the system, based on the schematic of Figure 2.4, is given here in equation 7.2.

$$m\ddot{z} + f_e(\dot{z}) + f_m(\dot{z}) + kz = -m\ddot{y} \quad (7.2)$$

where:

- m is the mass of the oscillating capacitive structure
- k is the stiffness of the flexures on the capacitive structure
- z is the displacement of the capacitive structure
- y is the input vibration signal
- $f_e(\dot{z})$ represents the electrically induced damping force function
- $f_m(\dot{z})$ represents the mechanical damping force function

The capacitance of the variable capacitor at a given time (t) is determined by the displacement of the structure (z) and the specifics of the design. The amount of energy per cycle that is removed from the mechanical system, and stored in the electrical system is given by equation 7.3.

$$E = \int_0^{2\pi/\omega} f_e() dz \quad (7.3)$$

where:

ω is the frequency of oscillation.

The expression for energy per cycle given by equation 7.3 is equivalent to that shown in equation 7.1a. Consider a simple example of a variable capacitor consisting of two square plates. The capacitor changes capacitance as one plate, attached to springs, oscillates between values z_{\min} and z_{\max} where z is the distance between the two plates. The form of $f_e()$ for this example is given by the following expression.

$$f_e() = \frac{Q^2}{2\epsilon_0 A} \quad (7.4)$$

where:

Q is the charge on the capacitor, which is constrained to be constant

ϵ_0 is the dielectric constant of free space

A is the area of the capacitor plates

Note that for this example, $f_e()$ is constant and not a function of z , however this is not always the case. Substituting equation 7.4 into equation 7.3 and solving yields the following expression.

$$E = \frac{Q^2}{2\epsilon_0 A} (z_{\max} - z_{\min}) \quad (7.5)$$

In deriving equation 7.5 it was assumed that all the charge is removed from the variable capacitor as it returns from the C_{\min} (or z_{\max}) state back to the C_{\max} (or z_{\min}) state. Noting that $C_{\max} = \epsilon_0 A / z_{\min}$, $C_{\min} = \epsilon_0 A / z_{\max}$, and $Q = C_{\max} * V_{in}$, equation 7.5 can be easily reduced to the following form.

$$E = \frac{1}{2} V_{in}^2 (C_{\max} - C_{\min}) \left(\frac{C_{\max}}{C_{\min}} \right) \quad (7.6)$$

Equation 7.6 is the same expression as equation 7.1a neglecting the parasitic capacitance. Note also that $(z_{\max} - z_{\min})$ is nothing more than the AC magnitude of z (the distance between plates). If it is assumed that the mechanical damping is linear viscous damping ($f_m(\dot{z}) = b_m \dot{z}$), then the AC magnitude of z is given by equation 7.7.

$$|Z| = \frac{m\omega}{b_m} |Y| \quad (7.7)$$

where:

$|Y|$ is the displacement magnitude of the input vibrations

b_m is a constant damping coefficient

ω is assumed to be equal to the natural frequency of the capacitive structure

Substituting equation 7.7 into equation 7.5 and replacing displacement magnitude with acceleration magnitude ($|A_{in}| = \omega^2 |Y|$) yields the expression in equation 7.8.

$$E = \frac{mQ^2}{2\omega b_m \epsilon_0 A} |A_{in}| \quad (7.8)$$

where:

A_{in} is the acceleration magnitude of the input vibrations, $A_{in} = Y/\omega^2$

Equation 7.8 clearly shows that the energy converted per cycle is linearly proportional to the mass of the system. This same conclusion was obtained in the development of the generic energy conversion model presented in chapter 2. Therefore, maximizing the mass of the system becomes an important design consideration. Furthermore, energy output is inversely proportional to frequency assuming that the acceleration magnitude of the input vibrations does not increase with frequency. Again, this conclusion is consistent with the generic model developed in chapter 2. However, in contrast to the generic model, equation 7.8 would imply that power output is proportional to A_{in} rather than to A_{in}^2 .

The parasitic capacitance has two effects on the system. First, the ratio of maximum voltage (V_{\max}) across C_v to the input (V_{in}) voltage, given by equation 7.9, is affected by C_{par} .

$$\frac{V_{\max}}{V_{in}} = \frac{C_{\max} + C_{par}}{C_{\min} + C_{par}} \quad (7.9)$$

This can be important in two ways. If the ratio of maximum to minimum voltage is too small, the system will not function. For example if the two switches are implemented as diodes, the $V_{\max} - V_{\min}$ must be at least large enough to overcome the forward voltage across the diode. In this case C_{par} would need to be minimized in order to maximize the V_{\max}/V_{\min} ratio. In the unlikely case that V_{\max} is too large (i.e. greater than the maximum allowable voltage for the system), a larger C_{par} would reduce V_{\max} , and therefore be desirable. Second, a larger C_{par} will result in a larger electrostatic force on the oscillating mass. In other words, it will result in more electrically induced damping. (This will be demonstrated more fully when specific designs are considered.) Meninger *et al* (Meninger *et al*, 2001) make the assertion that a large C_{par} will improve the energy conversion per cycle. This is only true if the dynamics are such that enough displacement can still be achieved with the larger C_{par} to reach the maximum allowable voltage. This is unlikely however, because a large C_{par} will increase the overall damping of the system, thus reducing the displacement of the variable capacitor. In general, it is usually best to try to reduce the parasitic capacitance, and then set the desired level of electrically induced damping with either the input voltage (V_{in}) or mechanical design parameters.

Specific power output estimates and dynamic simulations cannot be performed without first specifying the specific design concept. The choice of a design concept will

determine the forms of $f_e()$ and $f_m()$ which will complete the model presented and allow specific calculations and optimization based on the model.

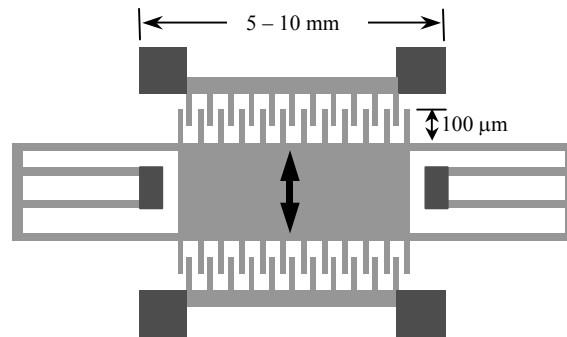
7.3 Exploration of design concepts and device specific models

As mentioned in chapter 3, the primary reason to pursue electrostatic energy conversion is the ease with which electrostatic converters can be implemented with silicon micromachining technology (or MEMS). A MEMS implementation has a few advantages. First, it has the potential to be tightly integrated with silicon based microelectronics. Second, equipment and processes to mass produce silicon micromachined devices are readily available. And third, if it ever becomes attractive to drastically reduce the size of converters, further miniaturization is readily accomplished with MEMS technology. Because the potential for MEMS implementation is the only advantage of an electrostatic converter over a piezoelectric converter, it only makes sense to consider designs that can readily be manufactured in micromachining processes.

Micromachined devices are generally planar devices (2½D) fabricated on the surface of a silicon substrate (surface micromachining). The silicon substrate can also be etched to create devices (bulk micromachining). New innovative micromachining techniques are continually being developed. A detailed discussion of micromachining is beyond the scope of this thesis. The reader is referred to Madou (Madou 1997) for a full treatment of micromachining technology applied to MEMS. For the purposes of this thesis, it will be assumed that the reader is somewhat familiar with basic micromachining processes. As demonstrated above, the maximum capacitance of the device is a key parameter to effective power conversion. It is therefore desirable to target a process that can produce devices with large capacitances. A very thick device layer, and a high aspect

ratio are therefore necessary. A process in which the devices are fabricated in the top layer of a Silicon-On-Insulator (SOI) wafer is capable of producing very thick structures (up to 500 μm or more). Furthermore, the Deep Reactive Ion Etching (DRIE) process used to create the devices is capable of producing features with aspect ratios up to 50:1. For these reasons, a SOI process will be targeted for the design of MEMS based electrostatic converters. The specific details of the fabrication process will be covered in the following section.

Three topologies for micromachined variable capacitors are shown in Figure 7.2.

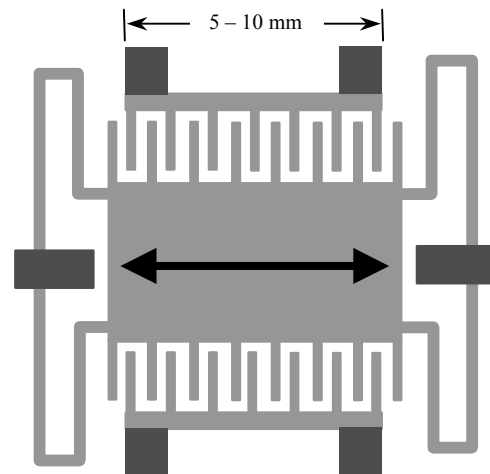


In-plane overlap type:

Capacitance changes by changing overlap area of fingers. (Not to scale)

In-plane gap closing type:

Capacitance changes by changing gap between fingers. (Not to scale)



Out-of-plane gap closing type:

Capacitance changes by changing gap between two large plates. (Not to scale)

Figure 7.2: Three possible topologies for micromachined electrostatic converters.

The dark areas are fixed by anchors to the substrate, while the light areas are released structures that are free to move. The first device at the top will be referred to as an in-plane overlap converter because the change in capacitance arises from the changing overlap area of the many interdigitated fingers. As the center plate moves in the direction shown, the overlap area, and thus the capacitance, of the fingers changes. The second device will be referred to as an in-plane gap closing converter because the capacitance changes due to the changing dielectric gap between the fingers. The third device shown will be referred to as an out-of-plane gap closing converter. Note that the figure shows a top view of the first two devices, and a side view of the third device. This third device oscillates out of the plane of the wafer, and changes its capacitance by changing the dielectric distance between two large plates. A few representative dimensions are shown in the figure.

7.3.1 Out-of-plan gap closing converter

The out-of-plane gap closing type converter will be considered first. The exact expression for the mechanical damping term is give by equation 7.10.

$$f_m () = \frac{16\mu W^3 L}{z^3} \dot{z} \quad (7.10)$$

where:

μ is the viscosity of air. Value of μ is proportional to the pressure.

W is the width of the large plate.

L is the length of the plate.

Note that the interpretation of z in this equation is slightly different than as shown in Figure 2.4 in that z represents the separation of the two plates making up the capacitor.

Thus z is the sum of the initial separation and the deflection of the flexures. The capacitance of this structure is given by the following expression.

$$C_v = \frac{\epsilon_0 WL}{z} \quad (7.11)$$

where:

ϵ_0 is the dielectric constant of free space

Finally, the expression for the electrostatic force induced is given by equation 7.12.

$$f_e() = \frac{-Q^2}{2\epsilon_0 WL} \quad (7.12)$$

where:

Q is the charge on the variable capacitor

Because the charge is held constant during the motion of the structure, the electrostatic force is constant. When the switches close, the amount of charge on the capacitor changes, but this happens very fast and can be considered to be instantaneous from the viewpoint of the mechanical subsystem.

Equations 7.10 – 7.12 demonstrate one of the problems with the out-of-plane gap closing converter. In order to obtain a large capacitance change, z must become very small, or the plates must move very close together. However, as the fluid damping force is proportional to $1/z^3$, the loss becomes very large as the plates move close together. This problem may be alleviated somewhat by packaging the device under very low pressure. However, another serious problem exists with this design concept. As the plates get close together, surface interaction forces will tend to make them stick together shorting the circuit and possibly becoming permanently attached. It is very difficult to design mechanical stops to prevent this from happening with the out-of-plane topology.

7.3.2 In-plane gap closing converter

The in-plane gap closing converter considerably improves the latter problem mentioned with the out-of-plane converter. Because the motion is now in the plane of the wafer, mechanical stops can be easily incorporated with standard fabrication processes, and therefore, the minimum dielectric gap, and thus the maximum capacitance can be precisely controlled. The expression for the fluid damping term for the in-plane gap closing type converter is given by equation 7.13.

$$f_m() = \left(\frac{\mu A}{d_0} + 16\mu N_g L_f h^3 \left(\frac{1}{(d-z)^3} + \frac{1}{(d+z)^3} \right) \right) \dot{z} \quad (7.13)$$

where:

- A is the area of the center plate
- d_0 is the vertical distance between the center plate and the substrate underneath
- N_g is the number of gaps per side formed by the interdigitated fingers
- L_f is the length of the fingers, h is the thickness of the device
- d is the initial gap between fingers

Note that z in this expression is the deflection of the flexures. The capacitance of the structure is given by the following expression:

$$C_v = N_g \epsilon_0 L_f h \left(\frac{2d}{d^2 - z^2} \right) \quad (7.14)$$

The expression for the electrostatic force induced is given by equation 7.15.

$$f_e() = \frac{Q^2 z}{2N_g d \epsilon_0 L_f h} \quad (7.15)$$

Note that the electrostatic force is proportional to the deflection of the flexure, and thus acts much like a mechanical spring except that the electrostatic force operates in the opposite direction.

While the fluid damping is still quite high for this design, large differences in capacitance can be generated and precise control of the maximum capacitance is possible if mechanical stops are included in the design.

7.3.3 In-plane overlap converter

The expression for fluid damping for the overlap in-plane converter is given by expression below.

$$f_m() = \frac{N_g \mu L_f h}{d} \dot{z} \quad (7.16)$$

where:

d is the dielectric gap between fingers

Equation 7.16 is actually in the standard form for linear viscous damping. The capacitance for the structure is given by equation 7.17.

$$C_v = \frac{N_g \epsilon_0 L_f (z + z_0)}{d} \quad (7.17)$$

where:

z_0 is the initial overlap distance of interdigitated fingers

The expression for the electrostatic force induced is given by the following expression.

$$f_e() = \frac{Q^2 d}{2 N_g \epsilon_0 h (z + z_0)^2} \quad (7.18)$$

7.4 Comparison of design concepts

A useful comparison between in-plane overlap and gap closing converters can be made without performing simulations that take into account the full dynamics of the systems. Estimates of power output per cm^3 based only on geometry and the relationship in equation 7.1a are graphed against maximum flexure (spring) deflection in Figures 7.3

– 7.5. The input voltage used for this comparison was 5 volts. Realistic assumptions were made about the minimum finger thickness and gap between fingers based on the standard fabrication technology. The distance between fingers for the in-plane overlap converters was assumed to be $1\mu\text{m}$, and the minimum dielectric gap for both types of gap closing converters was assumed to be $0.25\mu\text{m}$. A device thickness of $50\mu\text{m}$ was used for all three types of devices which is a realistic thickness based the targeted SOI process that will be described later.

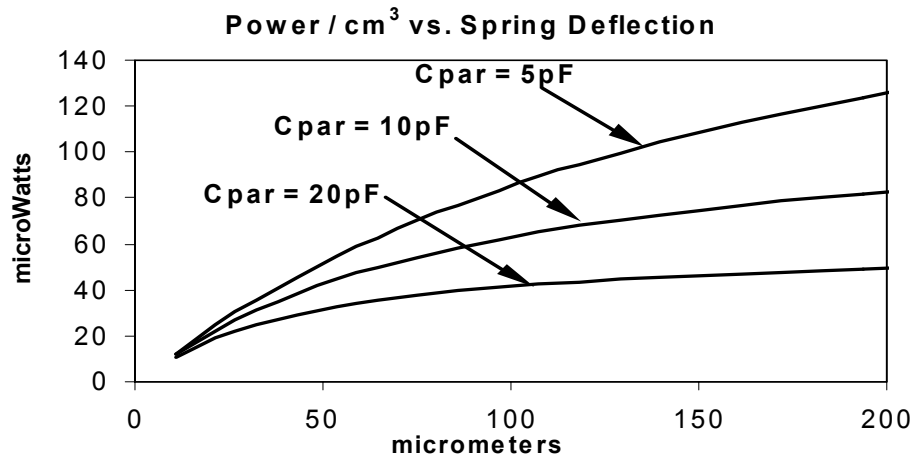


Figure 7.3: Power density vs. flexure deflection for out-of-plane gap closing converter with three different parasitic capacitances.

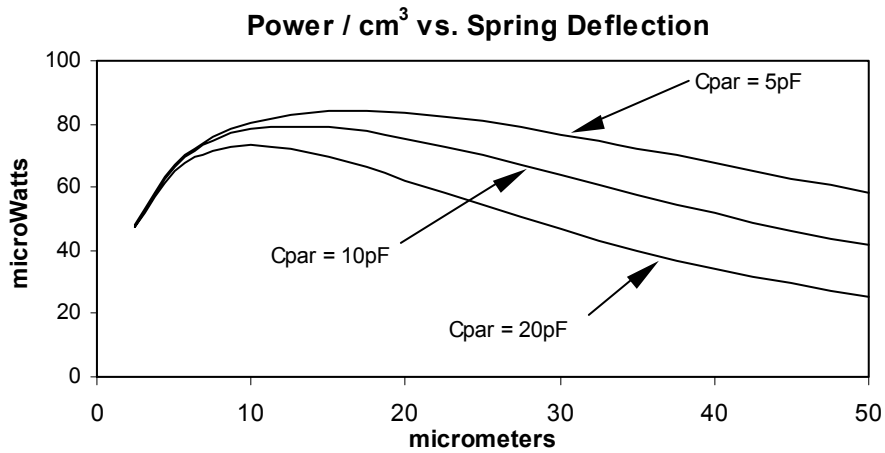


Figure 7.4: Power density vs. flexure deflection for in-plane gap closing converter with three different parasitic capacitances.

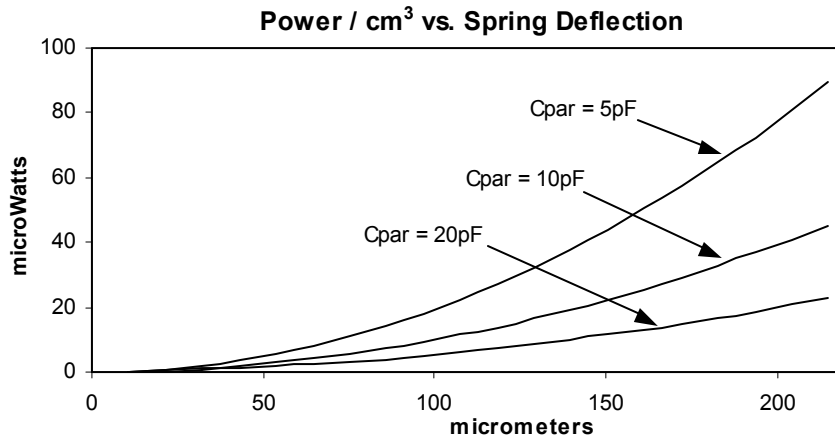


Figure 7.5: Power density vs. flexure deflection for in-plane overlap converter with three different parasitic capacitances.

It should be noted that for the in-plane gap closing converter the number of fingers that can be fabricated is a function of the maximum deflection of the flexures because the fingers must be spaced far enough apart to accommodate the displacement. Therefore a higher spring deflection results in a lower maximum (and minimum) capacitance. This is not true for in-plane overlap or out-of-plane gap closing converters. The result is that for both in-plane overlap and out-of-plane gap closing converters a larger spring deflection always results in more power out. However, there is an optimal travel distance for in-plane gap closing converters as can be seen Figure 7.4.

All three types of converters are capable of roughly the same power output. The out-of-plane gap closing converter produces the highest power output especially at low parasitic capacitances. The estimates presented here are not based on optimized designs, but on engineering judgment and the realistic constraints of the microfabrication. However, very useful trends can be seen from these estimates.

First, the maximum power output for in-plane overlap and out-of-plane gap closing converters occurs at very high spring deflections. This issue is even more acute for the overlap converter because of the upward curvature of the power traces compared with the

downward curvature for out-of-plane gap closing converters. Such large deflections raise concerns about the stability of the system. In the case of the overlap type converter, if the deflections are very large (on the order of $100\text{ }\mu\text{m}$) and the gap is very small (on the order of $1\text{ }\mu\text{m}$), only a small moment induced by out-of-axis vibrations would be necessary to cause the fingers to touch and short the circuit. This potential problem is illustrated in Figure 7.6. The optimal spring deflection for the in-plane gap closing converters is around $10\text{ to }15\text{ }\mu\text{m}$, which is very realistic and will not pose much of a stability problem.

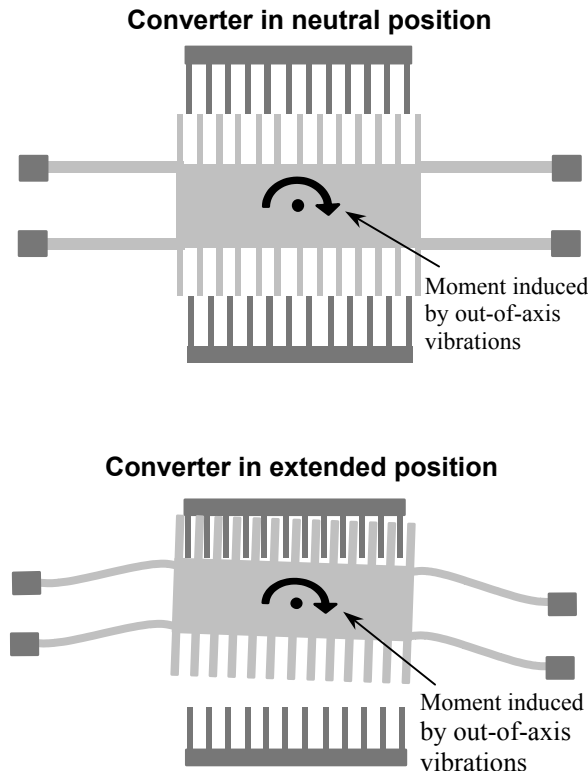


Figure 7.6: Illustration of stability problem with in-plane overlap converters.

Second, the out-of-plane gap closing converters are far less sensitive to the parasitic capacitance. A parasitic capacitance of 5 pF is very optimistic, and would likely not be possible. A parasitic on the order of tens of picoFarads is much more likely. Finally, remember that there is no guarantee that the very large spring deflections shown for in-

plane overlap and out-of-plane gap closing converters can in fact be obtained. The maximum obtainable deflections depend on the mechanics of the system, which were not included in these estimates. These preliminary estimates, however, point out the two considerations discussed better than a full dynamic simulation.

A full simulation of the three designs of Figures 7.3 – 7.5 will provide more details that can be used as a basis for comparison. Simulations were performed in Matlab using equations 7.1, 7.2, and 7.10 – 7.18. As was the case with simulations for piezoelectric converters, input vibrations of 2.25 m/s^2 at 120 Hz were used for all simulations. Figure 7.7 shows some results of a simulation of the out-of-plane gap closing converter used to generate the power estimates in Figure 7.3. Figure 7.7 shows the voltage on the storage capacitor (100 pF in this case) and the voltage on the variable capacitor, C_v , versus time. The traces clearly demonstrate the basic charge pump function of the simple simulation circuit shown in Figure 7.1. This simulation was performed with an input voltage of 5 volts, an ambient pressure of 0.01 atmospheres, and a parasitic capacitance of 20 pF. The switches are assumed to be ideal in that they turn on and off instantaneously and switching loss is neglected.

As discussed earlier, the out-of-plane topology suffers from very high squeeze film damping forces. At atmospheric pressure these damping forces dominate the system, and so most of the kinetic energy of the system is lost and very little power output is available. As various methods do exist to package MEMS structures at reduced pressures (Hsu 2000, Chang and Lin 2001), the system was simulated at a variety of different pressures. Figure 7.8 shows the output power per cm^3 vs. pressure in atmospheres. At .001 atmospheres (or 0.76 torr), the power output is $20 \text{ } \mu\text{W}/\text{cm}^3$, which may be in the

useful range. At atmospheric pressure the power output is on the order of 1 nW/cm^3 , which is far too low to be of any use.

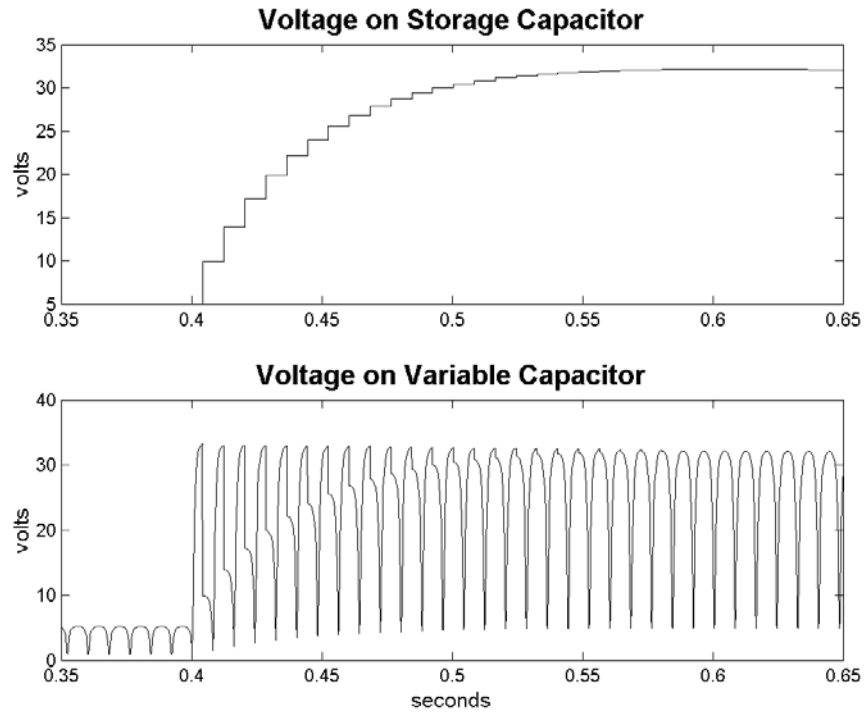


Figure 7.7: Voltage on storage capacitor and variable capacitor vs. time demonstrating the charge pump like function of the converter.

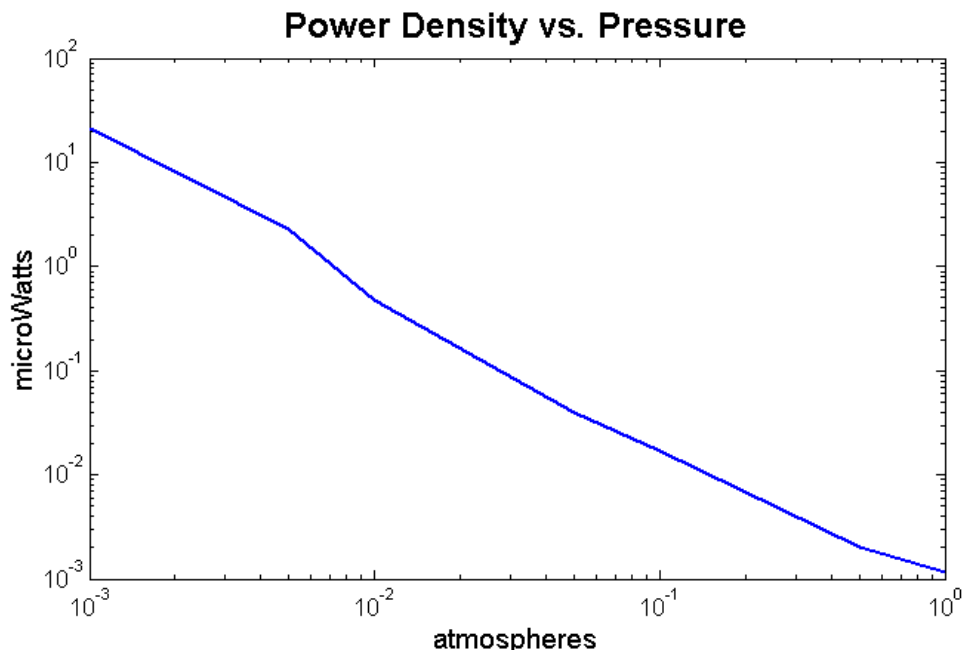


Figure 7.8: Power per cm^3 vs. pressure for an out-of-plane gap closing converter.

Figure 7.9 shows power output versus minimum dielectric gap (determined by the placement of the mechanical stops) for the in-plane gap closing converter for three different device thicknesses. As would be expected, higher power occurs for smaller minimum dielectric gaps, which produce higher maximum capacitances. A larger device thickness results in larger fluid damping forces, higher electrostatic forces, and higher maximum capacitances. It appears that the advantage of higher maximum capacitances outweighs the larger fluid damping forces in this case as the thicker devices produce more power output.

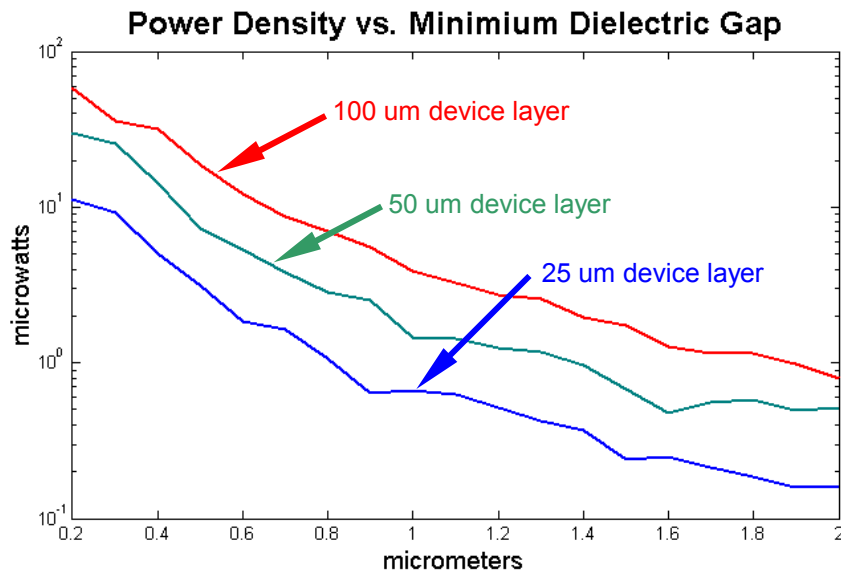


Figure 7.9: Power output vs. minimum allowable dielectric gap for an in-plane gap closing converter for three different device thicknesses.

Figure 7.10 shows results of dynamic simulations of the in-plane overlap converter used to generate the power estimates in Figure 7.5. Power output versus fabricated distance between fingers (dielectric gap) is shown for three different device thicknesses. This simulation was also performed with an input voltage of 5 volts, an ambient pressure of 0.01 atmospheres, and a parasitic capacitance of 20 pF. As expected, lower dielectric

gaps again result in higher power output. In this case the device thickness makes very little difference. The increased damping cancels the benefit of higher maximum capacitances. The most important thing to notice from the figure is that even at the very unrealistic dielectric gap of 0.2 μm the power output is only about 11 $\mu\text{W}/\text{cm}^3$, which is two to three times lower than the in-plane gap closing converter. The reason for the lower power output is that the spring deflections necessary to obtain higher output power densities are simply not achievable given the input vibrations and the simulated dynamics of the system.

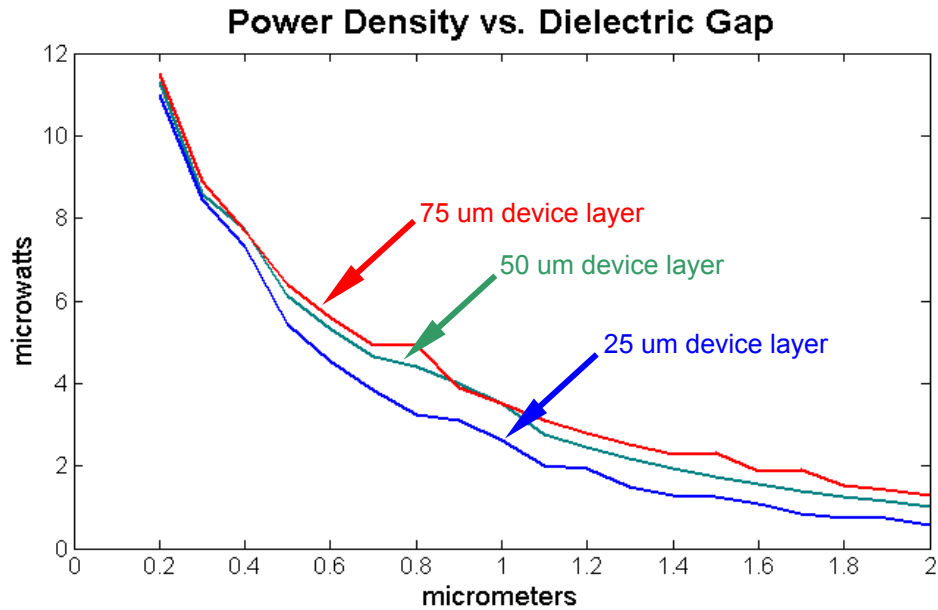


Figure 7.10: Power output vs. fabricated dielectric gap for an in-plane overlap converter for three different device thicknesses.

Given the simulations and power estimates presented above the in-plane gap closing topology seems to be the best of the three options for the following reasons: The in-plane gap closing converters are capable of equal or higher power density compared with the other two topologies. The extremely high displacements needed to make in-

plane overlap converters comparable in terms of power density are not feasible given the input vibrations under consideration and the realities of the mechanical dynamics of the system. Furthermore, because the in-plane gap closing converter will require significantly smaller displacements, it will not suffer from the potential stability problems of the overlap converter. The in-plane gap closing converter has a significantly higher power density than the out-of-plane gap closing converter at comparable pressures. At 0.01 atmospheres, simulations show less than $1 \mu\text{W}/\text{cm}^3$ for the out-of-plane converter compared to 30 to $50 \mu\text{W}/\text{cm}^3$ for in-plane gap closing converters. Finally, because limit stops can more easily be incorporated for in-plane operation, the in-plane gap closing converter does not suffer from the likely surface adhesion problems of the out-of-plane gap closing converter.

The model used in simulations for in-plane gap closing converters is developed in more detail in Appendix B. An algorithm for the simulation incorporating the limit stops is also presented in Appendix B.

7.5 Design Optimization

Using the in-plane gap closing topology as the preferred concept, a more detailed design optimization can be done. The optimization was performed in Matlab with its built in functions that use a Sequential Quadratic Programming (SQP) method. The output of a dynamic simulation was used as the “objective function” for the optimization routine. The design variables over which the device can be optimized are shown in Table 7.1.

Variables	Description
V_{in}	Input voltage
l_T	Length of the shuttle (center) mass
w_T	Width of the shuttle (center) mass
t	Device layer thickness
t_m	Proof mass thickness
l_f	Length of the interdigitated fingers
d	Nominal gap between fingers

Table 7.1: Design variables for optimization.

The width of the interdigitated fingers is determined by the combination of the device thickness (t) and the maximum aspect ratio constraint. Other parameters, such as proof mass and maximum capacitance are determined from these design parameters, design constraints, and a few assumptions.

The first constraint is that the total volume of the device must be less than 1cm^3 . As shown numerous times, the power conversion is linearly dependent on the proof mass. The mass is constrained by the total volume constraint and the material used. As silicon is a very lightweight material, it is not very desirable to use as a proof mass. Furthermore, the thickness of the device will not be more than 1mm, however, the total thickness of the device could be significantly greater given the volume constraint. The power output of the device can be greatly increased if an additional proof mass is attached to the silicon device. The resulting final device would look something like the model shown in Figure 7.11. As discussed in chapter 4, a tungsten alloy (90% tungsten, 6% nickel, 4% copper) makes a good proof mass because of its very high density (17g/cm^3). Therefore, the mass is constrained by the total volume constraint and the density

of the tungsten alloy. A second constraint is the maximum aspect ratio achievable, which is about 50.

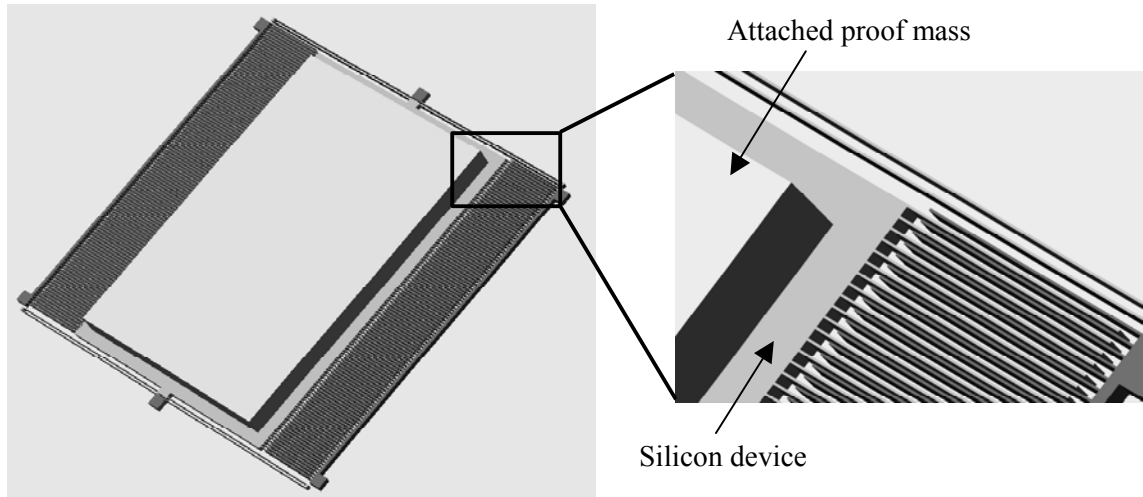


Figure 7.11: Model of an in-plane gap closing converter with proof mass.

Another assumption has been made which affects the design. Mechanical stops are designed to prevent the capacitive electrodes (the interdigitated fingers) from touching. The smaller the minimum dielectric gap (the closer the fingers are allowed to get) the higher the maximum capacitance. A realistic limit must be put on the minimum dielectric gap. Two optimizations were performed, one with a minimum dielectric gap of $0.25\ \mu\text{m}$ and another with a minimum gap of $0.5\ \mu\text{m}$.

The optimization problem can then be formulated as shown in Figure 7.12. There are two nonlinear constraints. The first is the overall volume constraint, and the second arises from the aspect ratio constraint (50 in this case) imposed by the fabrication process. Remember that the other constraint of maximum aspect ratio also comes into play in the determination of the width of the fingers.

$$\begin{aligned}
&\text{Maximize: } P = f(V_{in}, l_m, w_m, t, l_f, d) \\
&\text{Subject to: } (l_f + w_m) l_m t_m \leq 1 \text{ cm}^3 \\
&\quad \quad \quad t/d \leq \text{AspectRatio} \\
&\quad \quad \quad V_{in}, l_m, w_m, t, l_f, d \geq 0
\end{aligned}$$

Figure 7.12: Formulation of optimization problem.

An interesting difficulty arises when running this problem through the Matlab optimization routine. As might be expected, an optimal design would be one in which the mass just barely reaches the mechanical stops. If there isn't enough electrically induced damping, the mass will ram into the limit stops, which obviously is not an optimal situation. If there is too much damping, the mass will not reach the stops, reducing the maximum capacitance, which is likewise not an optimal situation. The fundamental dynamics of the system change if the mass collides with the limit stops, which causes a discontinuity in the response surface. In some areas of the design space, the mass does not collide with the limit stops, and one smooth response surface results. In other areas of the design space, the mass does collide with the stops, and a different smooth response surface results. These two response surfaces meet, but form a slope discontinuity. A visual example of this situation is shown in Figure 7.13. The simulated power output for a capacitive design is shown versus device thickness and the nominal gap between fingers. The two different surfaces are clearly evident in the figure. The light portion of the response surface results when the shuttle mass does collide with the limit stops. The dark portion results when the shuttle mass does not reach the limit stops. Along the "ridge", the shuttle mass just barely reaches the limit stops. The optimization routine cannot calculate accurate first and second derivatives at the discontinuity. Since

optimal designs will be very close the junction of these surfaces, if the optimization routine is run blindly, sub-optimal designs result. The optimization routine needs to be run in an iterative fashion with some engineering judgment. The optimization routine is run in limited design spaces where the discontinuity will not cause a problem. The output of these routines can be used with some intuition about the design space to select small areas that will be close to optimal, which would contain a discontinuity. With some judgment, the routine can be run on these smaller selected areas, and a close to optimal design can be chosen. It is very difficult to guarantee optimality with this approach, but practical designs that are nearly optimal can be generated.

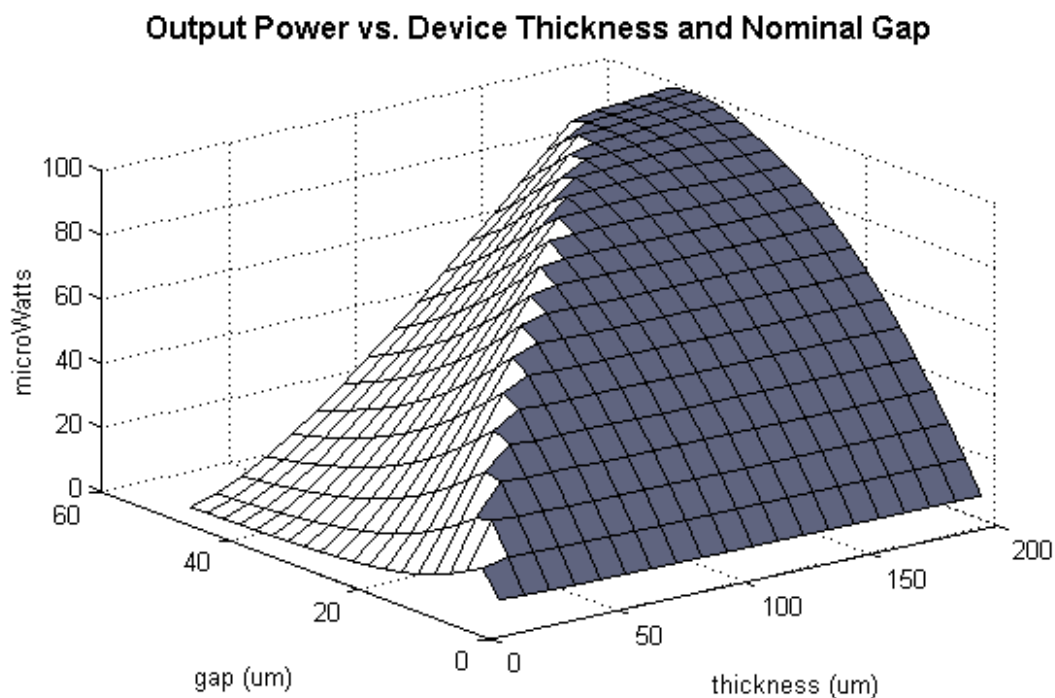


Figure 7.13: Simulated power output vs. device thickness and nominal gap between fingers. In the portion of the design space depicted by the light colored surface, the shuttle mass collides with the limit stops. In the dark portion, the shuttle mass does not reach the limit stops.

The resulting optimal design parameters, and the simulated power output, generated by the optimization routine are shown in Table 7.2. The optimal power output for a

minimum dielectric gap of 0.25 μm is 116 μW and for a minimum gap of 0.5 μm is 101 μW . While these values are higher than those predicted by designs just based on engineering intuition by a factor of about 2 or 3 (see simulation results in previous section), they are still a factor of 2 or so lower than optimal designs for piezoelectric converters.

Vars	Description of Variable	0.25 μm min gap	0.5 μm min gap
V_{in}	Input voltage	10 V	10 V
l_{T}	Length of shuttle mass	9 mm	8 mm
w_{T}	Width of shuttle mass	10 mm	10 mm
t	Device layer thickness	200 μm	200 μm
t_{m}	Proof mass thickness	5 mm	5 mm
l_{f}	Length of fingers	50 μm	50 μm
d	Nominal dielectric gap	530 μm	1.2 mm
P_{out}	Output power	116 μW	101 μW

Table 7.2: Optimal design parameters and power output for an in-plane gap closing design.

An input voltage of 10 volts may be quite high for wireless sensor applications. The output voltage could be converted down, but this would cost extra power. However, it may still be preferable to use a higher voltage for conversion, and then convert it down to power the electronics. It is not unlikely that the system would need one higher voltage source for sensors and actuators and another lower voltage source for electronics. With the load electronics and power circuitry better defined, a more limiting constraint could be put on the input voltage. The resulting optimal design would be a little lower in terms of power conversion, but may still be preferable.

It is often the case that the device layer thickness will not be a flexible design parameter. For example, if a standard foundry process is to be used, the device thickness will be set by the process. It also may be necessary for other reasons to use SOI wafers with another device layer thickness. The optimization routine could of course be run with a fixed device layer thickness. Again, the resulting maximum power output would be somewhat lower, but probably not in proportion to the decrease in device layer thickness. Designs with vastly different device layer thicknesses could, therefore, still be attractive.

7.6 Flexure design

The design of the flexures is left out of the optimization routine. The flexures must satisfy four demands:

1. The natural frequency of the device should match that of the input vibrations. Because the system mass is determined by the already obtained design parameters, the flexures must have a predetermined stiffness.
2. Given the designed range of motion along the axis of the driving vibrations, the fracture strain of the springs should not be exceeded (some factor of safety should be designed in), and the springs should ideally remain in the linear region.
3. The springs should be stiff enough that the static deflection out of the plane of the wafer should be minimal, significantly less than the space between the device and the substrate. Also, the strength of the springs should be strong

enough in the out-of-plane direction that the force of gravity on the large proof mass will not cause them to fracture.

4. The flexures should be significantly less stiff along the desired axis of motion compared with the out-of-axis directions.

The layout of a device is shown in Figure 7.14. Fairly standard folded flexures are used at each of the corners as shown in the figure. The overall lateral (in-plane) stiffness of the flexures is given by equation 7.19 and the vertical (out-of-plane) stiffness is given by equation 7.20.

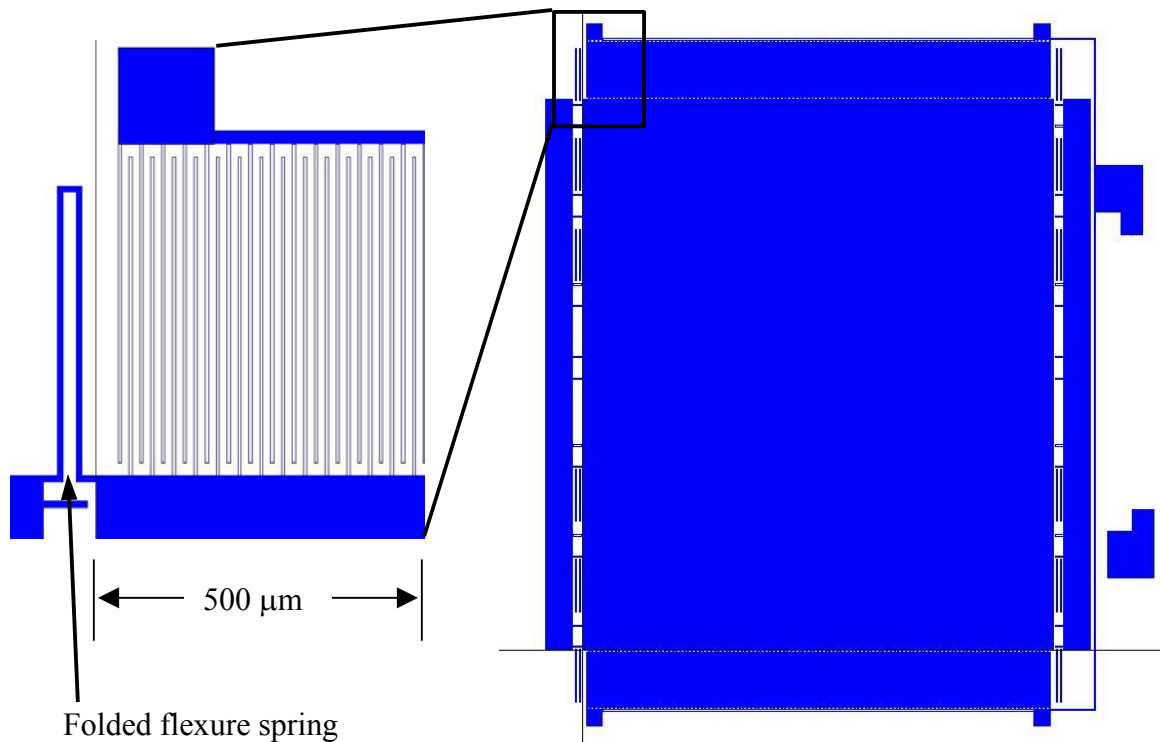


Figure 7.14: Layout of an in-plane gap closing converter with a close-up of the folded flexure spring at the corner.

$$k_l = \frac{NEtw_{sp}^3}{2l_{sp}^3} \quad (7.19)$$

$$k_v = \frac{NEw_{sp}t^3}{2l_{sp}^3} \quad (7.20)$$

where:

N is the number of folded flexures (springs)

E is the elastic (Young's) modulus of the material, silicon in this case

t is the device thickness

w_{sp} is the width of the flexure beams

l_{sp} is the length of the flexure beams

The device thickness will generally already be determined by the optimization routine, and the elastic modulus is a fixed material property. Therefore, only the spring length, width, and number of springs can be altered to achieve the desired stiffness. Incidentally, more than four folded flexures could be used. Actually, a total of twelve flexures are used on the device shown in Figure 7.14. A closer image of one side of this device, with six flexures, is shown in Figure 7.15. Note that the device has been rotated 90 degrees in this figure. It is also possible to include multiple folds in a flexure structure to make it more compliant. However, in practice this has not been necessary because of the large proof mass attached. It is important that the vertical stiffness be about 10 times the lateral stiffness to reduce out-of-axis motion. The static vertical deflection under the weight of the proof mass is also important. The static deflection is simply the gravitational force over the vertical stiffness (mg/k_v). The length and number of springs affect the vertical and lateral stiffness in exactly the same way. However, the width of the springs is linearly related to the vertical stiffness and but related to lateral stiffness by the third power. So, one can more or less set the desired vertical to lateral stiffness ratio by correctly selecting the width of the springs.

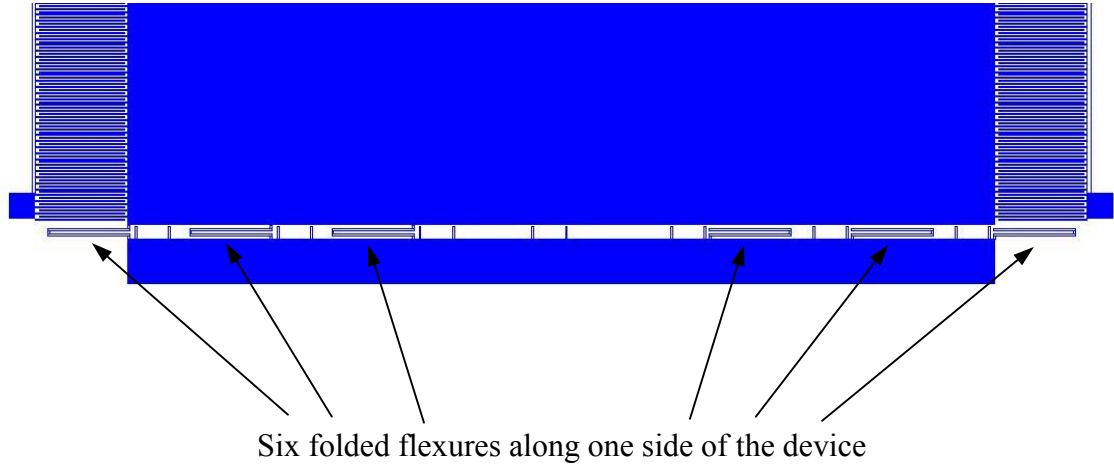


Figure 7.15: Layout of one side of a capacitive converter device showing the six flexures in parallel to increase the stiffness.

The maximum lateral deflection is determined by the nominal dielectric gap minus the minimum dielectric gap. For the design shown in Table 7.2 the maximum lateral deflection is 49.75 μm . The maximum stress due to the lateral deflection is given by equation 7.21. The fracture stress for single crystal silicon is about 70 GPa. The stress value calculated by equation 7.21 does not take into account stress concentrations. A suitable factor of safety needs to be chosen, and then the maximum stress must then remain below the yield stress divided by the factor of safety.

$$\sigma_l = \frac{3Ew_{sp}x_{\max}}{2l_{sp}^2} \quad (7.21)$$

where:

x_{\max} is the maximum lateral deflection

It is also desirable, although not absolutely necessary, that the flexures remain in the linear region under the maximum deflection. For the given type of flexures (2 link beams), a rough rule of thumb for linearity is that the maximum deflection divided by the length of the flexure (that is one link of the flexure) be 0.5 or less. Linearity depends on

the assumption that for the maximum slope or angle (θ) in the beam, $\tan(\theta)$ is approximately equal to θ . For the rule of thumb given above, $\tan(\theta)$ equals 1.013 times θ , or a 1.3% error. For the design shown in Table 7.2, the flexure of the beams needs to be less than 100 μm to remain in the linear region.

The maximum stress due to the static vertical loading of the proof mass is given by equation 7.22. As with the lateral strain, the flexures must be designed such that this stress is below the yield stress divided by a suitable factor of safety. It is likely that there will be some dynamic loading in the out-of-plane direction. Vertical limit stops of some sort would need to be incorporated in the package limiting the maximum vertical displacement to a specified value (y_{max}). The maximum stress in the flexures as a function of the maximum allowed vertical displacement is given in equation 7.23. Again, the system should be designed such that this vertical displacement will not result in a fractured flexure. If the designer needs to improve the factor of safety and/or the linearity of the flexures, the length and the number of the flexures can both be increased such that the lateral and vertical stiffness will not change, but the maximum developed stress will decrease, and the ratio of lateral deflection to spring length will decrease, thus improving the linearity.

$$\sigma_v = \frac{3mgl_{sp}}{Nw_{sp}t^2} \quad (7.22)$$

where:

m is the proof mass

g is the gravitational constant

$$\sigma_v = \frac{3Ety_{\text{max}}}{2l_{sp}^2} \quad (7.23)$$

Given the relationships presented here, the flexures should be designed to meet all four of the criteria stated above. A short example of the design of the flexures for the design shown in Table 7.2 follows. The specified device thickness is $200\text{ }\mu\text{m}$. The desired natural frequency is 120 Hz . The proof mass is calculated at 7.4 grams . The necessary lateral stiffness then becomes 4.2 kN/m . There are three parameters to specify to get the desired stiffness: beam width, beam length, and number of springs. The three must be selected in somewhat of an iterative process to make sure that acceptable factors of safety are met, and acceptable linearity is maintained. After iterating a few times and making calculations (an algorithm for this purpose is easily developed in a package like Matlab), twelve was selected as a suitable number of springs. The line shown in Figure 7.16 shows acceptable values for the width and length of the beams making up the 12 springs. A width of $20\text{ }\mu\text{m}$ and the corresponding length of $727\text{ }\mu\text{m}$ are selected as an acceptable design. Again these values were selected based on calculations of factors of safety, linearity, and static vertical deflection. Given a maximum lateral deflection of $49.75\text{ }\mu\text{m}$, the factor of safety along the axis of motion is 14.7 . Stress concentrations have not been considered which is why such a high factor of safety is desired. If it was necessary to make the beams shorter and thinner, stress concentrations could be taken into account when calculating the maximum stress, and then a much smaller factor of safety could safely be used. The ratio of maximum lateral displacement to beam length is 0.07 , which is very safely in the linear region. The vertical to lateral stiffness ratio is a very comfortable 100 . The static deflection in the vertical direction is $0.2\text{ }\mu\text{m}$, and the factor of safety based on this static deflection is a huge 423 . If a reasonable minimum factor of safety of 5 in the vertical direction is desired, then the resulting maximum

allowable vertical deflection would be 15 μm . Fabricating limit stops to limit the vertical deflection to 15 μm could be a significant challenge. These flexures are somewhat over-designed, however given the huge size of the overall device (by MEMS standards), there is plenty of physical space for them.

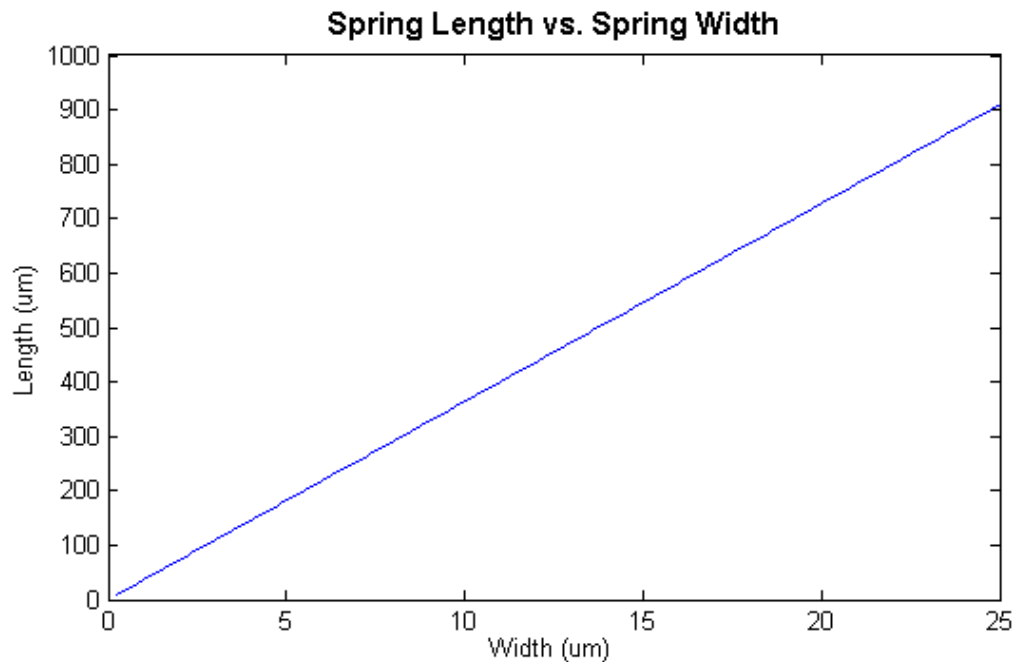


Figure 7.16: Acceptable spring flexure lengths and widths with 12 springs in parallel in order to generate a natural frequency of 120 Hz.

7.6 Discussion of design and conclusion

Perhaps the most important point to be made about this design is that the power density of an optimized design is at least a factor of 2 lower than the optimal power from a piezoelectric design. As discussed previously in chapter 3, the energy than can be converted by electrostatic transducers is inherently lower than piezoelectric converters. While there is no claim that the design topology and method used cannot be improved, it is very unlikely that any electrostatic design can be generated that can match a good piezoelectric design at the meso-scale.

The power converted is unavoidably linked to the mass of the system. Given this fact, along with an overall volume constraint of 1cm^3 , the resulting design is extremely large by MEMS standards. Also, unfortunately, in order for the electrostatic converter to generate a significant amount of power, an additional proof mass need to be attached to the device. The sheer size of the device negates one of the potential advantages of MEMS technology, which is low cost due highly parallel manufacturing methods. Additionally, given the large size, integration with microelectronics is less useful. Furthermore, the adding of such a large mass to a device with micron sized features results in a very delicate device, which would likely not be very robust.

The real advantage of a MEMS based electrostatic converter is only realized if the device is considerably scaled down in size. The dynamic models, design procedures and principles presented in this chapter will, of course, still apply to vastly smaller designs. However, the potential power conversion from the smaller designs is also much smaller because of the lower system mass. The scaling of power conversion goes down linearly with the system mass (and therefore the system volume). A converter of size 1mm^3 would then have a potential power density of about 100 nW based on the input vibrations currently under consideration. It is possible that applications with vastly higher energy vibrations, and therefore larger power output per unit volume, could make much smaller designs attractive. However, whether designs on the order of 1mm^3 will ever be very useful is an open question.

Chapter 8: Fabrication of Capacitive Converters

The design of electrostatic converters has been discussed in the previous chapter. Perhaps more than with other manufacturing technologies, the design of MEMS devices is closely tied to the target processing technology. Therefore, a very short discussion of the manufacturing process to be used has been given in chapter 7 in order to effectively produce a design. The processing that has been used will be covered in more depth in this chapter. A number of variants on the basic SOI process have been used to fabricate a string of prototypes. Each of these variants and the purpose for which the variant was used will be discussed.

8.1 Choice of process and wafer technology

As explained in chapter 7, an SOI wafer and processing technology have been selected due to the large device thickness, and therefore large capacitances that can be generated. Additionally, the Deep Reactive Ion Etching (DRIE) etching process used to create devices in the SOI wafer is capable of very high aspect ratios (up to about 50). This also improves the potential maximum capacitance. A further benefit of the very thick device layer and high aspect ratio is that the resulting devices have a very high out-of-plane stiffness compared to the in-plane stiffness. This is important in order to allow the addition of a significant amount of mass to the system after the processing is done. One potential drawback of the SOI technology is that it only provides one structural layer with which to design devices. However, only one layer is really needed for the current application. Therefore, SOI MEMS technology seems best suited for the design of electrostatic vibration-to-electricity converters.

Over the past few years, it has become increasingly common to etch MEMS structures into the device layer of SOI wafers. However, although the technology exists, at the outset of this project there was no standardized process available to the public. Within the past several months, Cronos (Cronos, 2003) has added an SOI process to their standard three-layer polysilicon process (MUMPS) and made it available to the public.

There are a couple of issues relating to the processing that will increase the complexity somewhat. First, it is essential to minimize parasitic capacitance. In typical MEMS devices, all of the electronics are on a separate die from the MEMS die. Electrical contact is usually made with wire bonds. In this case, at least two electronic devices need to be more closely integrated, the two switches that control the flow of charge into and out of the variable capacitor (see Figure 7.1). A second contributor to parasitic capacitance is the substrate beneath the device. It is therefore beneficial to etch away the substrate directly under the device. This backside etching is commonly done, but does increase the processing complexity. Finally, it is important that the single crystal silicon be highly conductive to reduce resistive losses as much as possible.

8.2 Basic process flow

Several slightly different processes have been used to create a sequence of prototype devices. These processes are all based on the same SOI MEMS technology, but differ in certain respects. This section presents a basic process flow that all of the processes more or less follow. The following section will present how each specific process used differs from the basic process flow, and why that process was used. It is assumed that the reader is familiar with micromachining processes and terminology, and so only high level explanations of the processes will be given here. The reader is referred

to Jaeger (Jaeger, 1993) and Madou (Madou, 1997) for a detailed discussion of microfabrication.

Figure 8.1 shows the basic process flow as schematics of the cross section of the wafer at sequential stages of the process. The process begins with an SOI wafer, which is a sandwich of single crystal silicon, silicon dioxide, and single crystal silicon. The cross section is not to scale. For MEMS devices, the top silicon layer (the device layer) is generally about 25 to 50 μm thick, the oxide is about 2 μm thick, and the bottom silicon layer (the substrate) is about 400 μm thick. The first step will be to apply a mask, pattern it, and etch the top layer of silicon with a DRIE process, most likely what is generally referred to as the Bosch process (Laerme *et al*, 1999). In many cases a simple UV baked photo resist mask can be used. If necessary, a hard mask made of oxide can also be used. In some of the processes used, the wafer is then covered with PSG (phosphosilicate glass) and annealed to further dope the device layer and increase conductivity. The PSG is removed before the next process. The next step is to apply metal to the top layer of the wafer. This has been done in three ways: using a thick resist process to fill in the trenches in the device layer, using a shadow mask (Cronos, 2003) to apply the metal, or refilling the device layer trenches with oxide to more or less planarize the surface and applying the metal with a standard lithographic process. The next process step, left out in some of the processes used, is to etch away portions of the substrate. Lithography is done on the backside of the wafer, and then it is etched with the same DRIE process. Finally, a timed oxide etch removes the oxide, freeing the structures. It is important to properly time this etch because unlike most surface micromachined devices, oxide remaining after the etch forms the anchors between the device layer and the substrate.

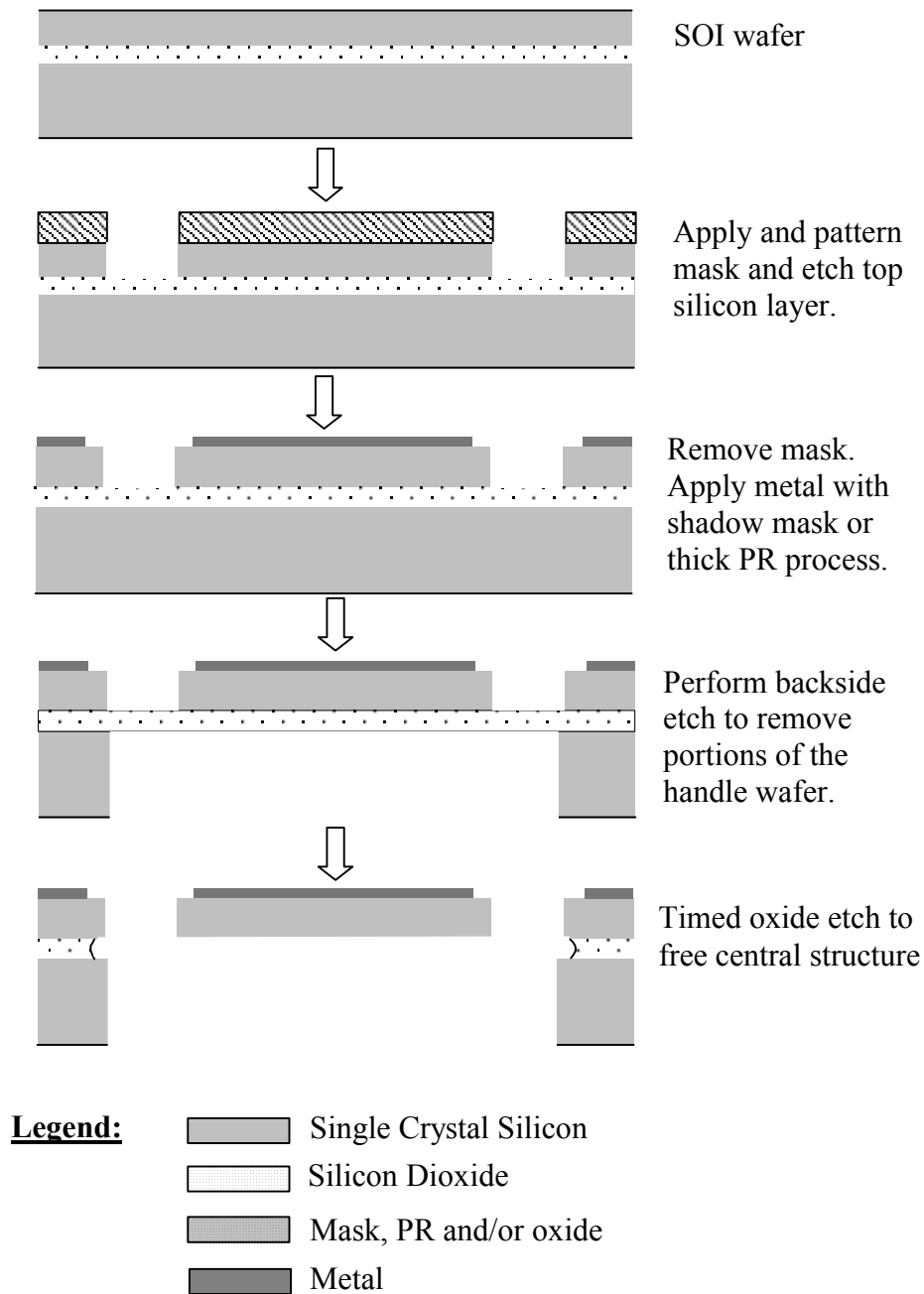


Figure 8.1: Basic process sequence used to fabricate capacitive converters.

8.3 Specific processes used

The first MEMS electrostatic vibration-to-electricity prototypes were designed for a process currently being developed in UC Berkeley's Microlab (Bellew, 2002). It is a SOI process that, in addition to single layer MEMS structures, creates solar cells, high power

MOSFETS, and diodes. The device layer is 15 μm thick. The process is very complex, but attractive because of the highly integrated electronic components. A number of smaller (on the order of 1 – 4 mm^2 in area) capacitive converter prototypes have been designed for this process. Because the space on a 1 cm^2 die needs to be shared with other designs, a full sized device has not been fabricated with this practice. The best results have been obtained with devices fabricated with this process. The disadvantage of this process is its complexity. It is actually more complex than needed for the devices currently under consideration. Nevertheless, it is the only process used in which diodes can be fully integrated with the structure, which is the primary reason for its greater success.

A second prototype device was designed for another SOI process being developed at UC Berkeley (Rhiel *et al*, 2002, Srinivasan, 2001). This process is much like the basic one shown in the previous section except that the backside etch is not performed. After the processing sequence is shown, a fluidic self-assembly process is used to assembly bare die FETS or diodes directly to the silicon die. The electronic components are not as highly integrated as in the process just described, however, this is a simpler process. Additionally, the bare die FETS assembled are of better quality than those fabricated in Bellew's process. Although the method of attachment for bare die diodes was verified, the mechanical structures fabricated were not functional. The structural layer was only 7 μm thick and so the capacitances generated by the variable capacitance structure were not very high. It seems that the parasitic capacitances dominated the system, and so the system did not function well. Additionally, no method of manually actuating the structures was included in the design. So when the structures did not work under

vibration, it was very difficult to troubleshoot the problem because the structure could not be actuated any other way.

A third set of prototypes was fabricated by the author with a simplified process identical to that shown in Figure 8.1. The device layer of the wafers used with this process was 50 μm thick. Two methods of electrically connecting to the diodes were used. First, small packaged surface mount diodes were used and wire bonds provided the connection between the MEMS die and the diodes. Second, bare die diodes were attached to the MEMS die manually with conductive epoxy. The purpose of running this process was first to simplify the process, thus increasing the chances of a successful implementation, to build devices with a thicker structural layer thus increasing the maximum capacitances, and finally to have the capability of building larger devices to which a tungsten proof mass could be attached. Tungsten proof masses were attached to the top surface of the devices manually with epoxy.

While the fabrication of the third set of prototypes was being performed, Cronos announced a new SOI MEMS process being made available to the public (Cronos, 2003). The author had the good fortune of being able to submit a design for a trial run on this process. This new process is a three mask process and is done almost exactly as is shown in Figure 8.1. The metal is applied with a shadow mask, and the device layer for the trial run was 25 μm . The intent was to manually assemble bare die diodes with conductive epoxy on the die. The prototype device submitted to this process was non-functional when it arrived. The large center plate or shuttle mass was completely broken off during processing. After the trial run, Cronos changed the thickness of the device layer to 10

μm , which limits this processes usefulness for electrostatic vibration-to-electricity converters because of the lower capacitances achieved with the thinner device layer.

While each of these processes is a little different, they are all alike in one key respect; *they all create a micromechanical device from a relatively thick device layer on an SOI wafer*. Results from prototypes fabricated with each of these processes are presented in the following chapter.

8.4 Conclusions

An attempt was made, initially, to either use standard publicly available processes or “piggy-back” on another process currently being run in UC Berkeley’s microlab for a couple of reasons. The first, and most important, is that the innovative and important contribution of this project is in the design and modeling, not in the processing, of the device. Therefore, if a suitable, available process could be found, time and money could be saved, and the likelihood of success would also be increased. A second reason for trying to find a standard process to use is that the scope of this thesis is quite broad, including the detailed modeling, design, and construction of both piezoelectric and electrostatic generators. It was felt that if a too many resources were committed to developing a process, the other portions of the project would suffer. However, suitable commercial processes could not be found. Therefore, an attempt was made to use processes currently under development in the UC Berkeley Microlab. This however, was less than completely successful. Finally, it was decided to run a custom, but simplified, process in order to be able to fabricate devices to demonstrate the electrostatic vibration-to-electricity conversion concept. More development work needs to be done on this

custom process in order for it to be a viable and reliable process for developing electrostatic vibration-to-converters.

Chapter 9: Capacitive Converter Test Results

A sequence of prototype devices has been designed and fabricated. The previous chapter explained the essential elements of the fabrication processes used. This chapter is dedicated to reporting fabrication and testing results.

9.1 Macro-scale prototype and results

A macro-scale prototype was first built using more conventional machining processes in order to verify the basic concept of operation and the test circuit before investing resources into the fabrication of MEMS devices. This device is shown in Figure 9.1. The basic device is comprised of three parts. An aluminum piece, 500 μm thick, was milled on a high spindle speed three axis machine using a milling cutter 229 μm in diameter. This piece, shown alone in Figure 9.2, serves as a flexure and an electrode. (One of the flexures is broken on the part shown in Figure 9.2.) The slots cut through the piece, which form the flexural structures, are 229 μm in width. A pocket is cut out from the backside so that there will be a dielectric gap of 250 μm in the nominal position. A printed circuit board was etched to form the other electrode of the variable capacitor and the electrical connection lines for the circuit element. This forms the bottom layer of the structure and is clearly visible in Figure 9.1. Finally, a steel mass is attached to the top of the aluminum piece. The device is an out-of-plane gap closing converter. Although this is not optimal for MEMS design, it was the most practical configuration for a macro scale test prototype. The copper electrode of on the circuit board under the aluminum piece was covered with a thin dielectric (the ink from a

Sharpie felt tip pen) in order to ensure that the two electrodes from the variable capacitor did not make electrical contact.

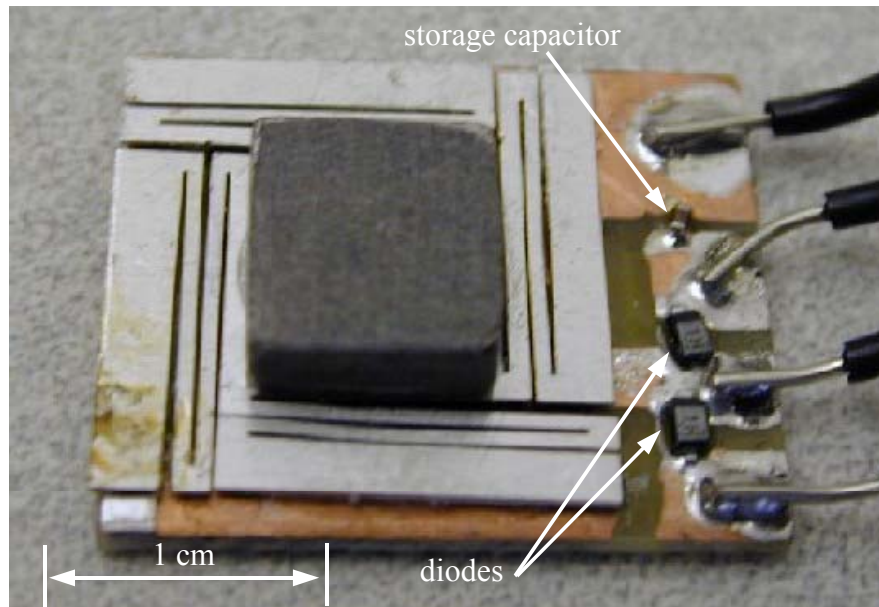


Figure 9.1: Photograph of the first macro-scale prototype built.

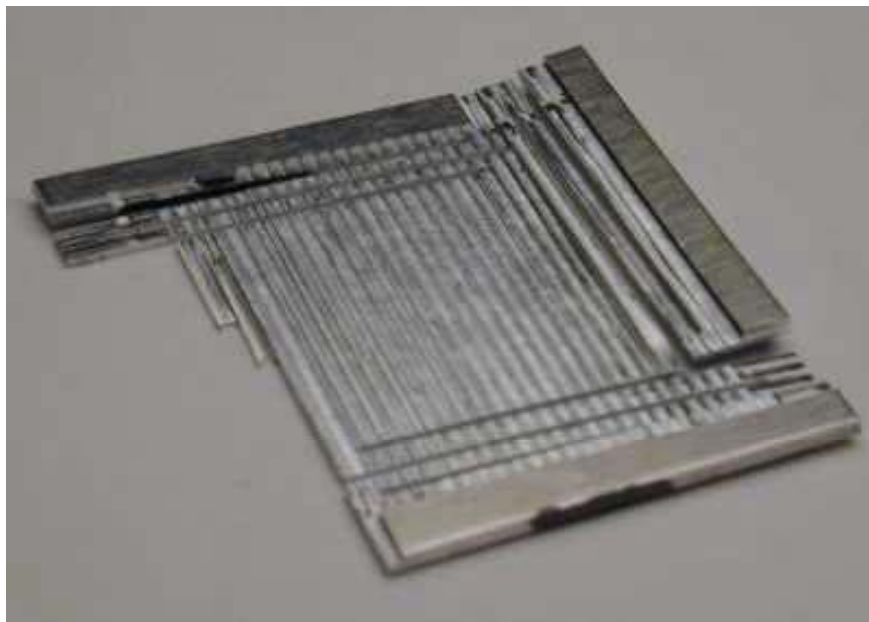


Figure 9.2: Photograph of the backside of the aluminum piece used in the macro-scale prototype.

The circuit shown in Figure 9.3 was used to measure the output of the macro-scale prototype. The op-amp in a unity gain buffer configuration was included in the circuit in order to decouple the capacitance of the storage capacitor from that of the measurement system. The output of this circuit was then measured on a standard oscilloscope.

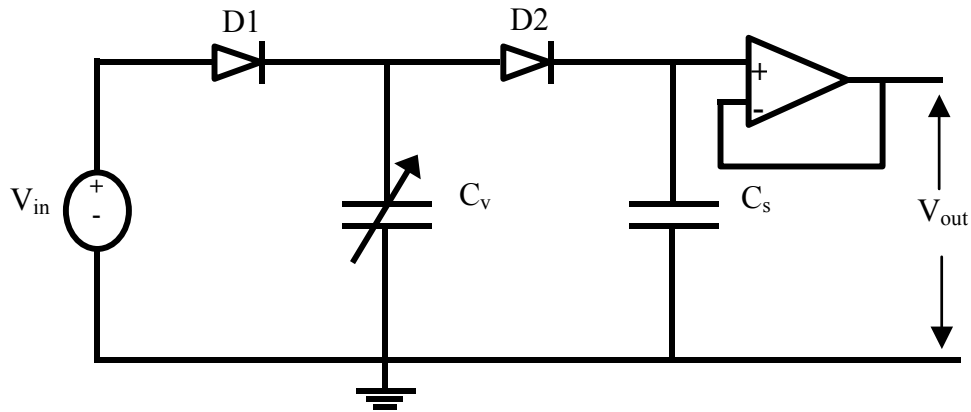


Figure 9.3: Measurement circuit for capacitive converter prototypes.

Two surface mount diodes and a very small ceramic capacitor are visible in Figure 9.1. The choice of diodes is very important. A few iterations with different diodes were performed before the system worked properly. First, the capacitance of the diodes will add to the parasitic capacitance that the variable capacitor sees. So, the capacitance of the diodes should be as small as possible. Secondly, the reverse leakage current varies considerably for different types of diodes. Reverse leakage currents generally range from about 0.1 nA to about 100 μ A. An intuitive explanation of the problem is as follows. On a capacitor of 100 pF (about the size of interest in this case), a 0.1 nA leakage will result in a voltage drop of about 1 V/s, which is OK given that the circuit is operating at about 100 Hz. However, at 1 μ A leakage, the voltage would drop at 1000 V/s, which is clearly too fast. The problem is that as the capacitance of C_v decreases (and its voltage should increase), current will be flowing back through the input diode, D1, so fast that the

voltage will never increase at the output. Furthermore, if the output voltage across C_s were to increase, the current would flow back onto C_v too fast to detect a change. Initially diodes with a low forward drop were chosen, however, these did not work well because their reverse leakage was too high. In general, diodes with a lower forward drop also have a higher reverse leakage current. It is therefore preferable to choose a diode with low leakage current and high forward drop. The diodes chosen have a leakage current of 10 nA as stated by the manufacturer.

The converter was tested by manually pushing the proof mass up and down. With a storage capacitance of 100 pF and a source voltage of 3 volts, the output voltage increased 0.25 volts per cycle. With a source voltage of 9 volts, the output voltage increased 1 volt per cycle. At an operation frequency of 100 Hz, the output power would then be less than 0.1 nW for a 3 volt source and about 1 nW for a 9 volt source. This is not very good power production, but at least the device demonstrates that the capacitive converter concept does in fact function properly.

9.2 Results from fluidic self-assembly process prototypes

Recalling the discussion of different processes used in the previous chapter, it will be remembered that a prototype device was designed for an SOI process in which bare die FETS were assembled on the MEMS die with a fluidic self-assembly process. The primary purpose of this process and these prototypes was to verify that either bare die FETS or diodes could be assembled onto the MEMS die and function effectively as switches (or diodes). A scanning electron micrograph (SEM) of the device fabricated is shown in Figure 9.4.

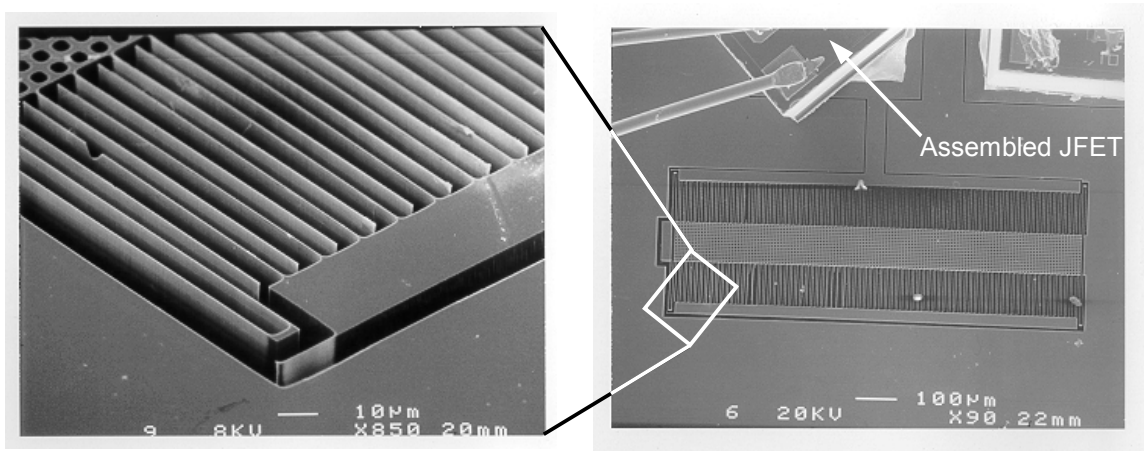


Figure 9.4: SEM of prototype device fabricated with fluidic self-assembly process.

The bare die JFETS that were assembled are clearly visible in the lower magnification picture on the right. The JFETS were wired to act as diodes as shown in Figure 9.5. Bare die JFETS were used in place of diodes primarily because of availability, but also because they tend to have low reverse leakage when wired as diodes. The JFETS were tested after assembly. One of the I-V curves from the tests is shown in Figure 9.6. Figure 9.6 shows the same data plotted on two different scales. The left graph is a linear scale. The right graph plots the absolute value of the data on a log scale. A log scale is used so that the reverse leakage current can be seen more precisely. The reverse leakage current is about 0.2 nA, which is very good compared to commercially available diodes. The forward voltage drop is about 0.75 volts, which is quite high. However, as mentioned before, there is a tradeoff between leakage current and forward voltage drop, and for this application is better to have a low leakage and a high voltage drop. Therefore, the JFETS wired as diodes seem to be a good choice for this process.

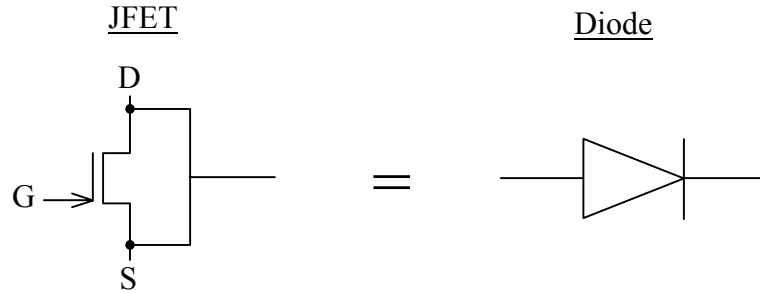


Figure 9.5: Illustration of a JFET wired to operate as a diode.

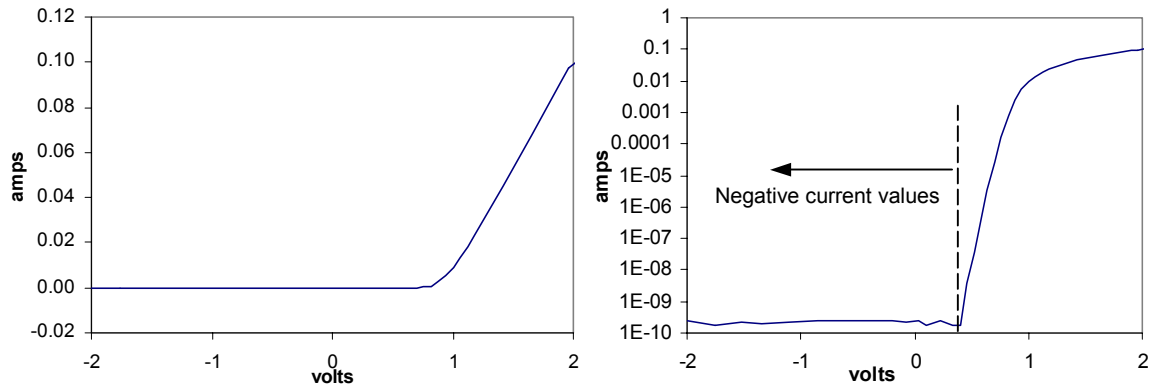


Figure 9.6: Current vs. voltage curve measured from a fluidically self assembled JFET wired as a diode. The left graph shows data on a linear scale, the right graph shows the absolute value of the data on a log scale.

The size of the variable capacitance device was only about 300 μm X 1mm due to space constraints on the die. Furthermore, the device thickness was only 7 μm . It is doubtful whether a device of this size and thickness would be able to generate a large enough capacitance to overcome the parasitics. In tests, the structure failed to increase the voltage on the output capacitor when driven by vibrations. As explained in Chapter 8, it is believed that this is because the small capacitance of the variable capacitance structure as compared to the parasitic capacitances. There was one more problem noted with the design of this device. It is useful to be able to manually move the variable capacitor back with a probe tip or by some other method in order to verify the correct operation of the system before putting it on the vibrometer. However, no probe access

points were designed in this particular device, so it was not possible to manually move the device back and forth.

9.3 Results from integrated process prototypes

A few different prototypes were designed for the integrated process in which solar cells and basic electronic components are fabricated together with SOI MEMS structures. The design of the devices for this process happened after the prototypes from the fluidic self-assembly process, so lessons learned from that prototype were incorporated in the design of devices for this process. Again, the devices designed needed to be much smaller than the optimal size because of space constraints on the die. It was therefore decided to design a number of small prototypes to verify the power conversion concept rather than a single larger (but still smaller than optimal) device that would be capable of more power output. Two small in-plane gap closing converters with thermal actuators next to them for the purpose of manually pushing the converter devices back and forth were fabricated in this process. It was thought that it would be easier to debug the converter if it could be actuated in a controlled fashion rather than just put on a vibrometer. The converter devices were identical except that the minimum dielectric gap for one device was 0.5 μm and 1.0 μm for the other device.

The thermal actuators designed to push the converter back and forth are based on the design first proposed and carried out by Cragun and Howell (Cragun and Howell, 1999). This actuator is referred to as a Thermal In-plane Microactuator or TIM. Figure 9.7 shows a schematic of a TIM and an associated converter. It should be noted that the converters in this case are fabricated such that the movable fingers are offset in the nominal position so that as voltage is put across the variable capacitor, the electrostatic

forces will cause it to naturally close, and then the TIM actuator will modulate the dielectric gap. Current is passed through the many arms, which heat up as a result of the power dissipated. As the arms heat up, they expand pushing the center yoke forward. Thermal actuators generally give a high force, low displacement output compared to electrostatic actuators. The TIMs are attractive in that they generate high force at zero displacement, which is necessary to overcome the electrostatic force pulling the converter combs together, but also can produce displacements on the order of 10 μm . Models and results have been presented for TIMs surface micromachined from polysilicon, but the author is not aware of any TIMs being implemented in an SOI process. The TIMs were carefully modeled and designed to provide both adequate force and displacement output for the associated converter. However, detailed discussion of these models and designs are beyond the scope of this thesis. The reader is referred to Lott *et al* for detailed discussion of the modeling of polysilicon TIMs (Lott 2001, Lott *et al* 2002).

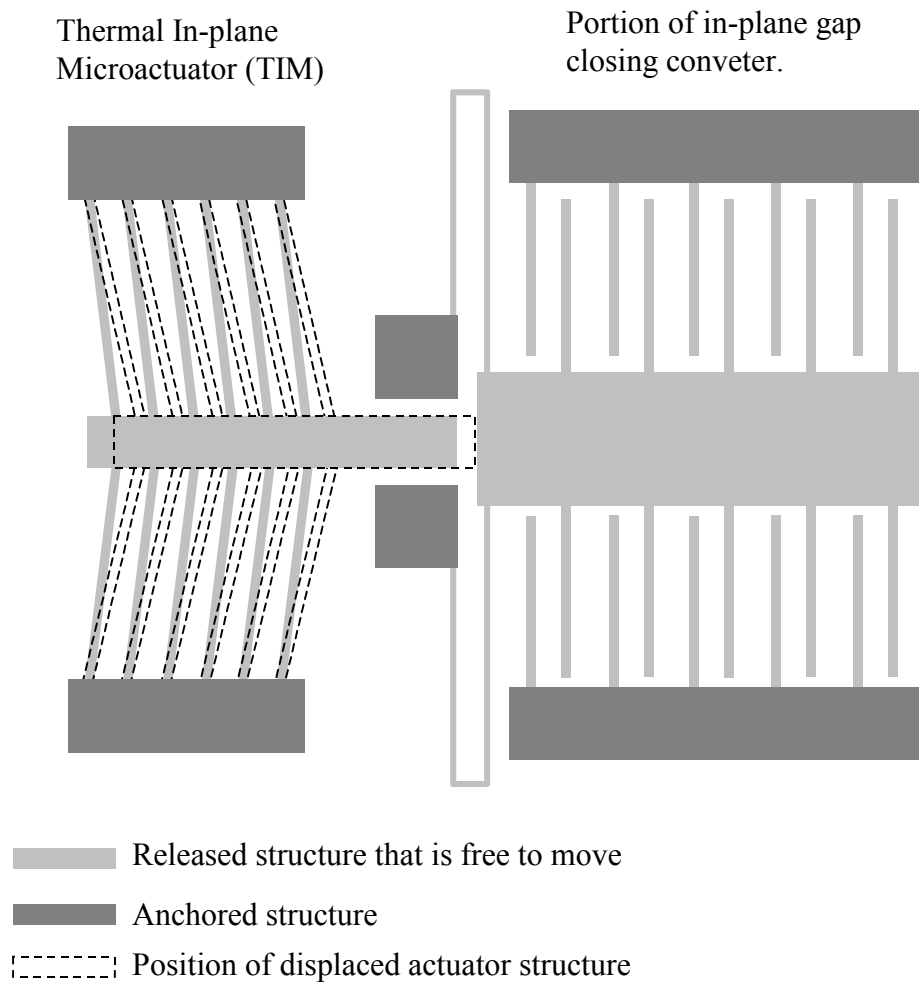


Figure 9.7: TIM actuator designed to push converter structure back and forth.

Figure 9.8 shows a Scanning Electron Micrograph (SEM) of a TIM and converter structure fabricated with this process. Figure 9.9 shows a close-up view of the interdigitated comb fingers and spring flexure. Figure 9.10 shows a sequence of images from a normal optical microscope. The sequence, going from left to right, shows the converter and TIM in their nominal positions, partly actuated or extended, and fully actuated. As the converter is pushed from its maximum capacitance position to its minimum capacitance position the voltage across the output capacitor should increase, thus verifying the correct operation of the system. Note that Figure 9.10 actually shows

the converter being pushed past its minimum capacitance position. The middle image shows the minimum capacitance position while the images on the right and left show higher capacitance positions. The image sequence shows the converter being pushed past the minimum capacitance position so that the motion can more easily be seen.

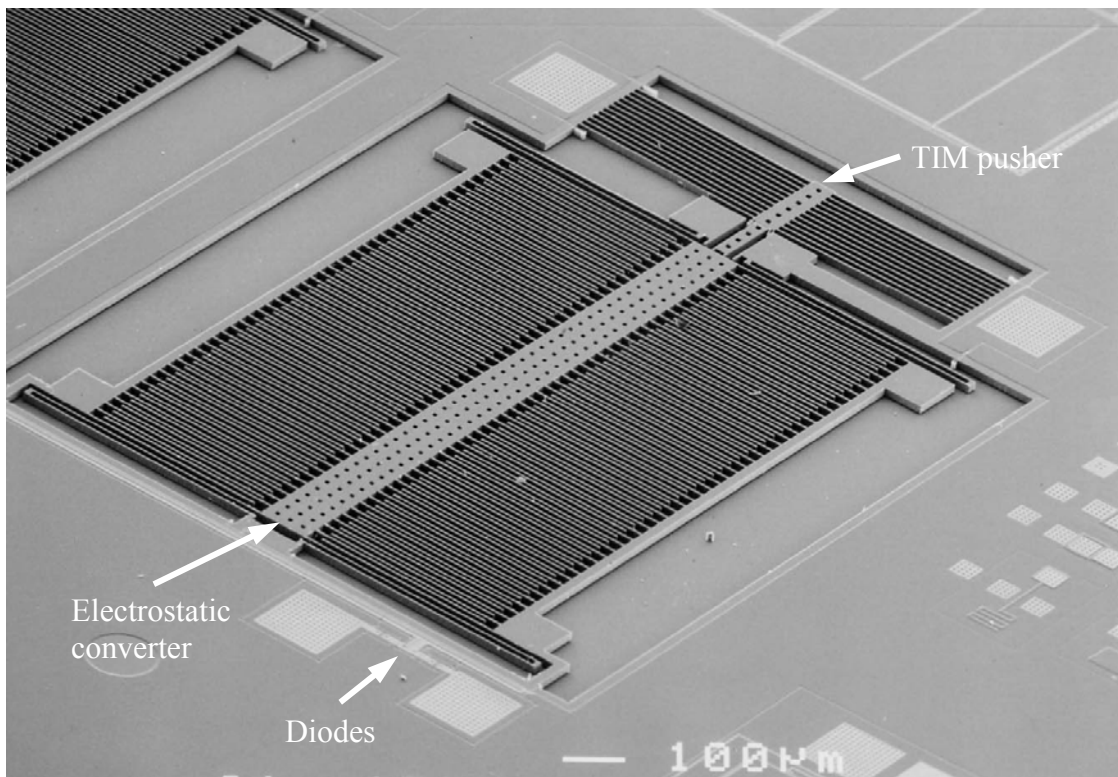


Figure 9.8: SEM of electrostatic converter with TIM pusher fabricated in the integrated process.

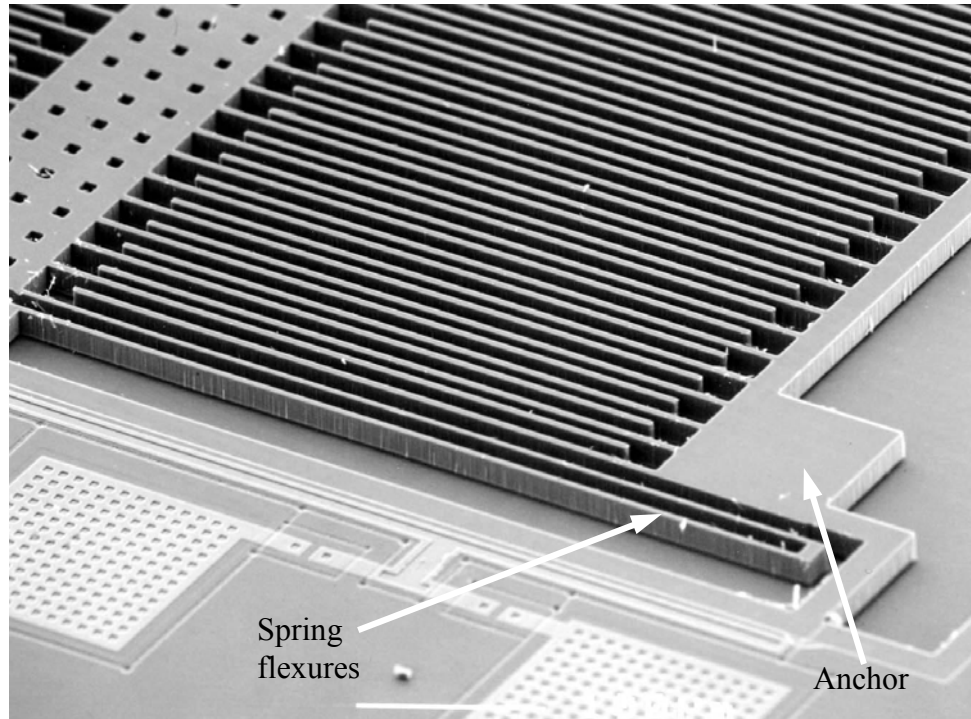


Figure 9.9: Close-up of interdigitated fingers and spring flexures.

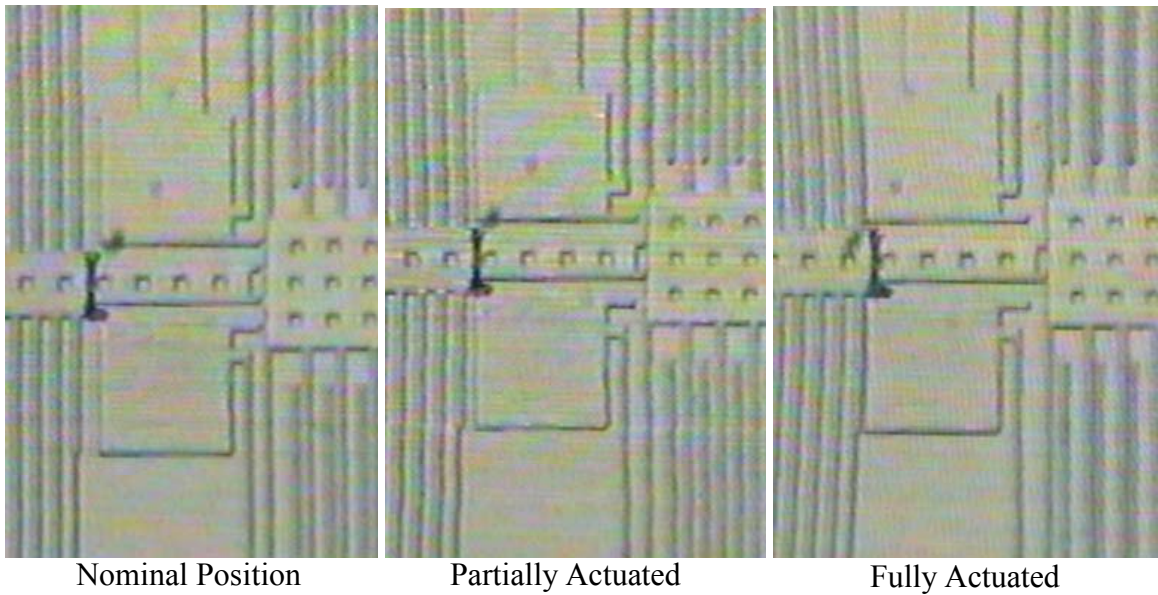


Figure 9.10: Image sequence showing the TIM actuator pushing the converter from its nominal position to a fully extended position.

Most of the devices fabricated with this process were not fully functional. The electrostatic converter structures are quite delicate, and many were broken during processing. Additionally a finite resistance across the variable capacitor (the comb

fingers) of about 2 - 5 M Ω was measured on several devices. The maximum capacitance of the converter structure is 9.6 pF. Allowing for a very large parasitic capacitance of 50 pF and the maximum measured parallel resistance of 5 M Ω , the RC time constant is still only 300 μ S. So, at frequencies below several kHz the projected increase in voltage across the variable capacitor would be effectively dissipated through the parallel resistance before it was ever detectable. It is thought that this finite resistance is due to contamination. Before the structure release the bottoms of the trenches in the silicon were filled with silicon carbide debris from processing (see Bellew 2002). The debris is removed in an ultrasonic bath during release, but it is possible that enough remains to create high resistance paths across the comb fingers. However, a couple of the devices that were successfully fabricated did not have this parallel resistance problem, and preliminary results were obtained from these devices. Both of the working devices were from the design that had a minimum dielectric gap of 0.5 μ m.

Two devices were successfully tested with an input voltage of 5 volts and an output capacitance of 100 pF. As the TIM actuator pushed the converter from a high capacitance position to a low capacitance position, the output voltage across the 100 pF capacitor increased by 0.3 volts. Based on geometry, the parasitic capacitance should be about 4.2 pF. It is, however, likely that the real parasitic capacitance is somewhat more than that. The maximum and minimum capacitances of the converter structure were calculated as 9.6 pF and 1.2 pF respectively. Using these parameters, the calculated voltage gain at the output per cycle should be 0.4 volts. The voltage across the output capacitor fed the input to an operational amplifier used in a unity gain configuration as shown above in Figure 9.3 in order to decouple that parasitic capacitance of the

measurement equipment from the output capacitor. However, some parasitic capacitance at the output still exists which may have a significant effect on the voltage gain per cycle. For example, if the output capacitance were really 125 pF, the calculated voltage gain would only be 0.32 volts. The energy gain associated with the 0.3 volt increase is 1.4 nJ. Assuming a driving frequency of 120 Hz, and remembering that this device undergoes two electrical cycles for each mechanical cycle, the power output would be 337 nW. The size of the entire converter device is about 1.2 mm X 0.9 mm X 0.5 mm (including the thickness of the substrate). Based on this volume, the power density would then be 624 $\mu\text{W}/\text{cm}^3$. However, this assumes that the input vibrations would be able to mechanically drive the structure hard enough to overcome the electrostatic forces. Given the very small mass of this system, such vibrations would be far more energetic than the standard 2.25 m/s^2 at 120 Hz. Nevertheless, the structures fabricated with this integrated process did demonstrate the basic functionality of a micromachined electrostatic vibration-to-electricity converter.

Although the design and modeling of the TIM structures has not been discussed, a few results may be of interest for future researchers. Two TIM pushers were designed. The first was capable of generating higher forces with lower displacements. This structure consisted of 32 beams (16 on each side of the yoke), which were 7.5 μm wide, 15 μm thick, and 400 μm long. The resistance of the structure was 1 k Ω . The second pusher was designed for smaller forces and higher displacements. It consisted of 24 beams (12 on each side of the yoke), which were 5 μm wide and 400 μm long. The resistance of this structure was 2 k Ω . It is this second TIM structure that is shown on the entire converter device above in Figure 9.8. A close-up view of this TIM structure is

shown below in Figure 9.11. In both cases, the beams were angled from the horizontal by $3\text{ }\mu\text{m}$. So the angle of inclination was $\sin^{-1}(3 / 400) = 0.43$ degrees. The resistivity of the silicon material can be back calculated from the resistances of the TIMS as $0.23\text{ }\Omega\text{-cm}$.

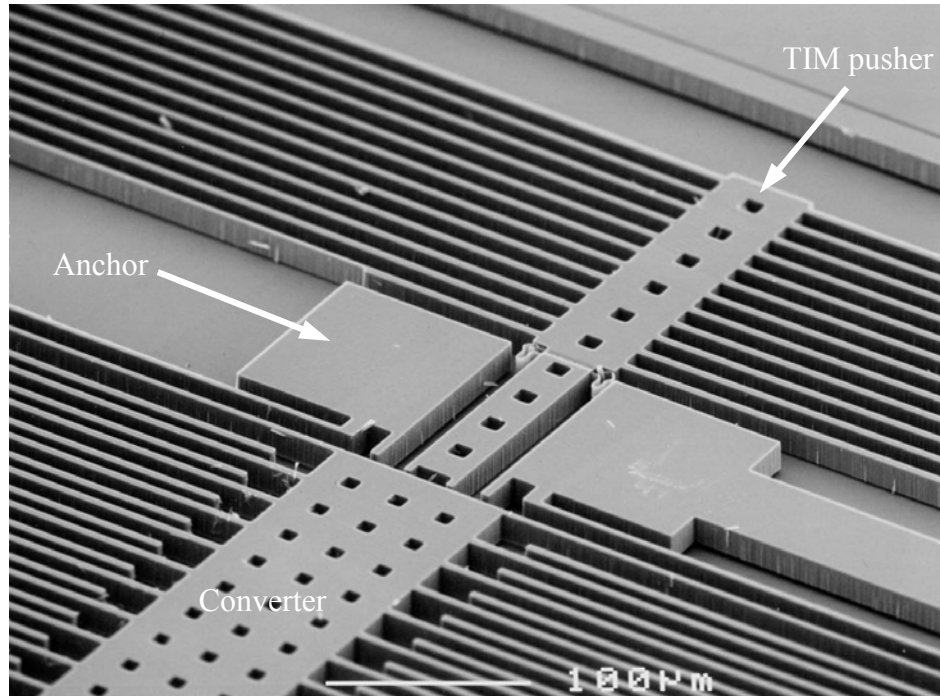


Figure 9.11: Close-up of TIM and yoke, which pushes the electrostatic converter.

Both structures were designed to reach a maximum displacement with an actuating voltage of 30 volts. The yoke began to move when the voltage across the TIM was about 7 volts, and the structure reached its maximum displacement at a voltage of about 28 volts for both structures. Additionally, in both cases, the structure broke at a voltage of about 32 volts. The second TIM, designed for less force and higher displacement, was not able to produce enough force to overcome the electrostatic attraction of the comb fingers and move the converter structure with an input of 10 volts to the electrostatic converter. Figure 9.12 shows an optical microscope image of the TIM structure pushing on the electrostatic converter with an input voltage of 10 volts. Notice that the beams on

the TIM structure are starting to buckle under the force and are still not able to move the converter structure. However, with an input of 5 volts, the TIM could easily push the converter structure. In fact, the higher displacement TIM actually pushed the converter structure well past its minimum capacitance position as shown in Figure 9.10. The higher force, lower displacement, TIM could move the converter structure with an input of 10 volts, but could not push the converter past its minimum capacitance position.

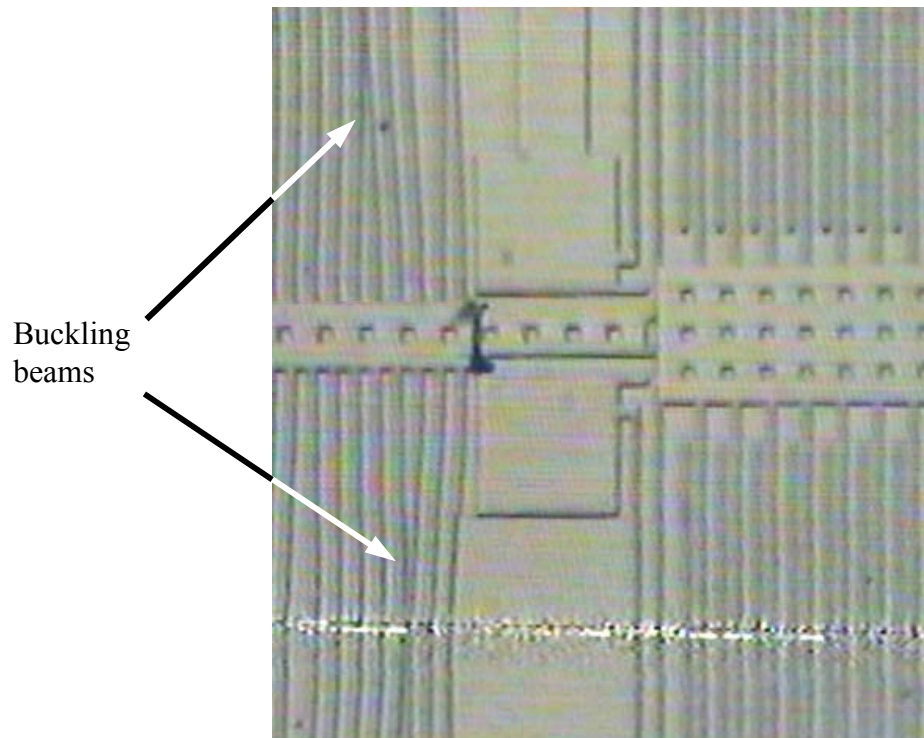


Figure 9.12: TIM structure trying to push electrostatic converter with an input of 10 volts, causing the beams on the TIM to buckle.

Another very important, perhaps even the most important, element of the integrated process designs is that the diodes acting as the input and output switches are fabricated into the wafer right next to the electrostatic converter structure. Thus, the parasitic capacitances are minimal and the characteristics of the diode can be controlled to a certain extent. Figure 9.13 shows a close-up image of the diode structures next to the converter structure. Figure 9.14 shows an I-V curve resulting from testing on one of

these diodes. As above in Figure 9.6, the values for the current are shown both on a linear scale and on a log scale (absolute values shown). As mentioned previously, the critical parameter in this case is the reverse leakage current. The average reverse leakage current as shown in Figure 9.14 for the integrated diodes is about 50 nA, which is not nearly as good as the 0.2 nA from the assembled bare die JFETs, but still adequate.

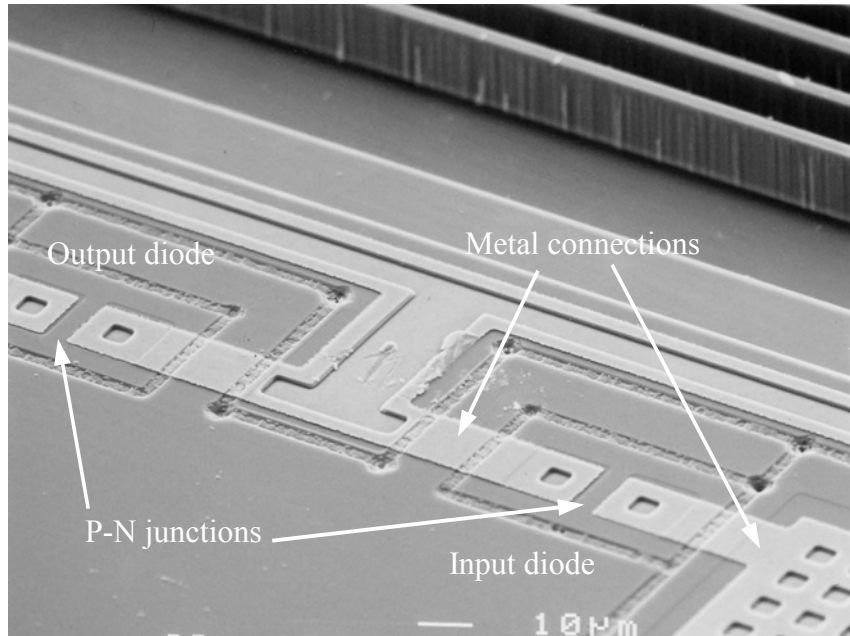


Figure 9.13: Close-up view of input and output diodes fabricated in the integrated process.

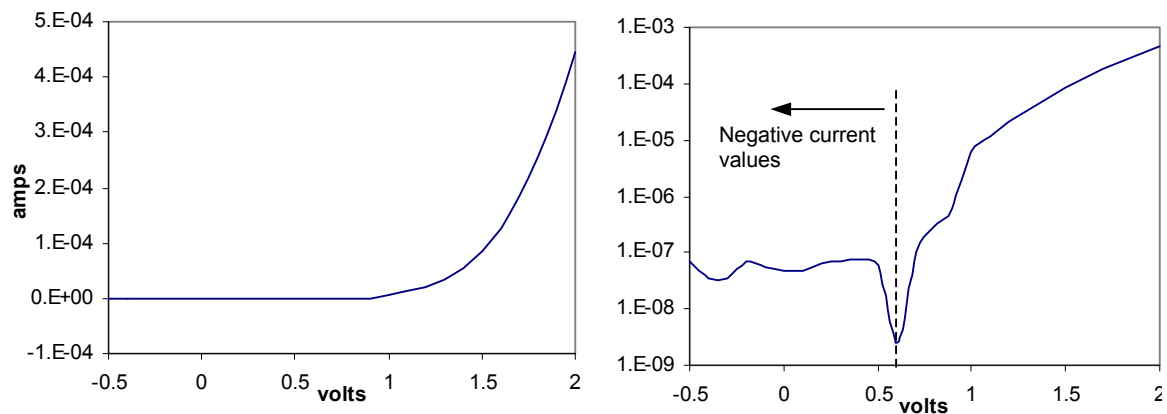


Figure 9.14: I-V curve generated from one of the diodes shown in Figure 9.13. Data is shown on a linear scale on the left graph, and the absolute value of the data is shown on a log scale on the right graph.

9.4 Results simplified custom process prototypes

As discussed in chapter 8, the author also developed and ran a simplified custom process for basically three reasons: first, in order to have enough space to design and fabricate full sized devices, second, to simplify the process, thus increasing the probability of successful implementation, and third to fabricate devices of greater thickness (50 μm) increasing the maximum capacitance of the devices. The masks for this run covered the entire wafer rather than a 1cm X 1cm die. (i.e. A stepper was not used for lithography, rather a contact lithography method was used.). Additionally, wafer space was not shared with other users. The result was that many larger designs could be accommodated. Optimal designs with a total area constraint of 1 cm^2 and 0.25 cm^2 , a thickness constraint of 50 μm , and minimum dielectric gaps of both 0.25 μm and 0.5 μm were fabricated. Additionally, test devices incorporating the TIM “pushers” were designed and fabricated.

One of the larger converters fabricated by this process is shown in Figure 9.15. The device shown is a 0.25 cm^2 device. A close-up view of the interdigitated comb fingers and a spring flexure is shown in Figure 9.16. The very large center plate is meant to accommodate additional mass to be attached after the process. More than four spring flexures (one at each corner) need to be included on this device in order to achieve the correct stiffness to produce a resonant frequency of 120 Hz with the additional mass. These extra spring flexures are barely visible, but are pointed out, in Figure 9.15. Because the oxide below the structural layer is used to anchor the structure to the substrate beneath, only about 10 μm of oxide are etched away under the structure. The anchors then must be significantly larger than 20 μm X 20 μm so that enough oxide

remains under them to act as a good anchor. However, the 10 μm oxide etch must release the enormous center plate, therefore a huge array of etch holes meant to allow the hydrofluoric acid to go beneath the center plate was etched in the silicon. There are about 40,000 etch holes on this particular device. A close-up image of these etch holes near the edge of the center plate is shown in Figure 9.17.

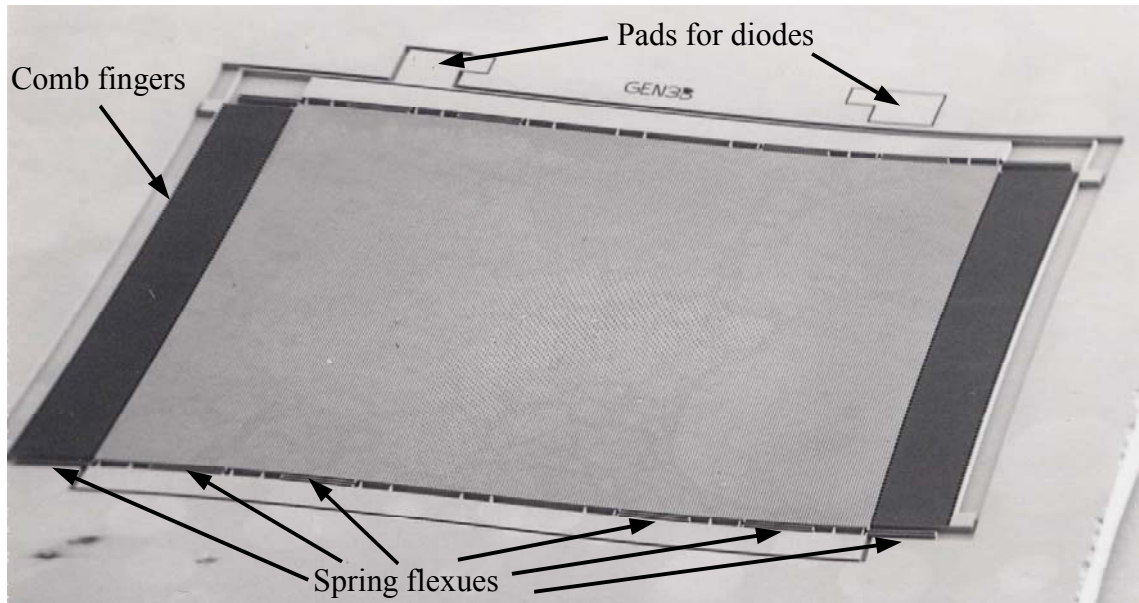


Figure 9.15: SEM image of a large (0.25 cm^2) electrostatic converter.

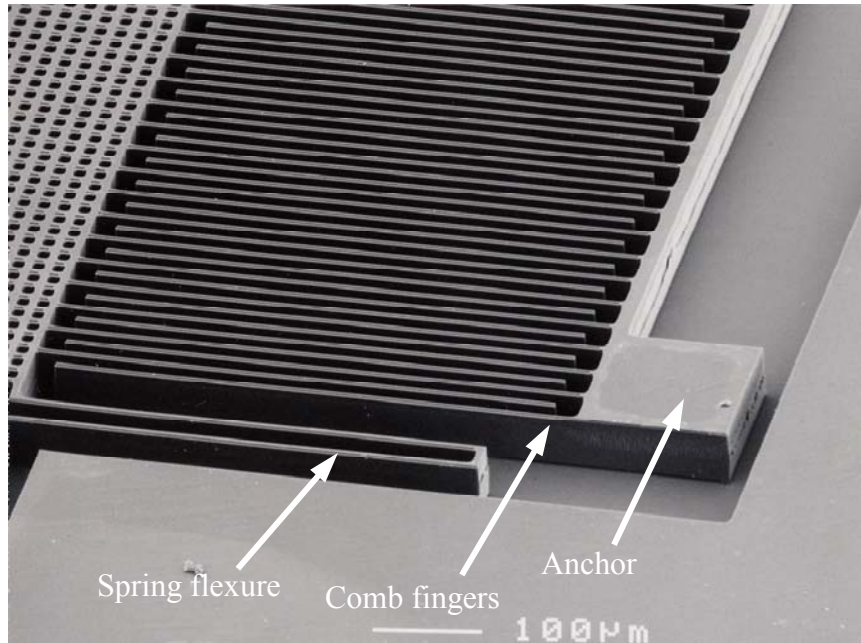


Figure 9.16: Close-up view of comb fingers and spring flexure.

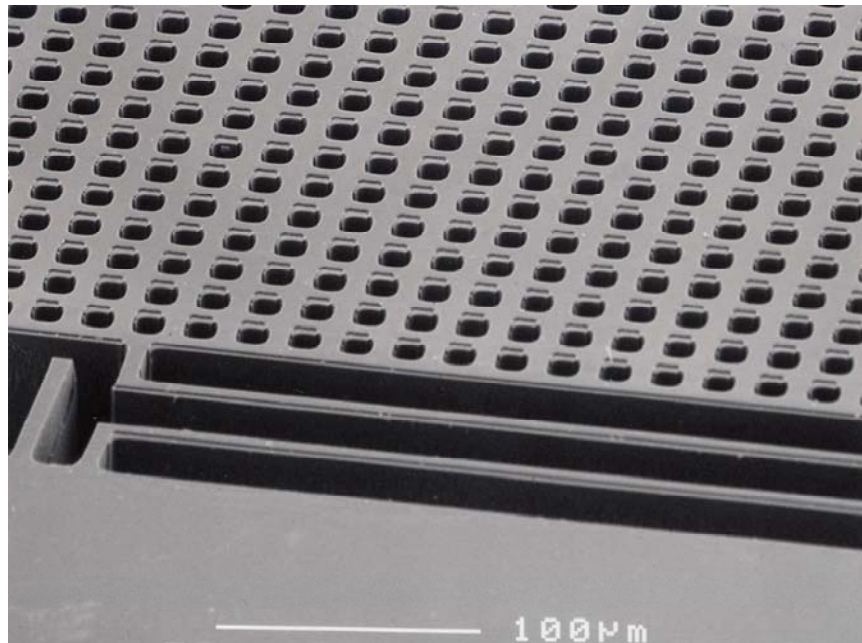


Figure 9.17: Close-up view of etch holes in the center plate on a large converter.

A large tungsten mass was manually attached to the large center plate of one of the devices fabricated. It is necessary to attach additional mass to the structure to get a useful amount of power out from the target input vibrations. The designs worked out in Chapter

7 also assume that additional mass is to be attached. An image of the device with the tungsten block attached is shown in Figure 9.18. The author has not been successful in obtaining test data from this device to demonstrate the functionality of the converter. As with other devices fabricated using this process, a combination of reverse leakage current from the diodes and high resistivity of the structure is thought to be the primary reason that the device has not functioned properly. The device is shown here to demonstrate that the mass can be effectively attached, and to show what a device with a large attached mass looks like.

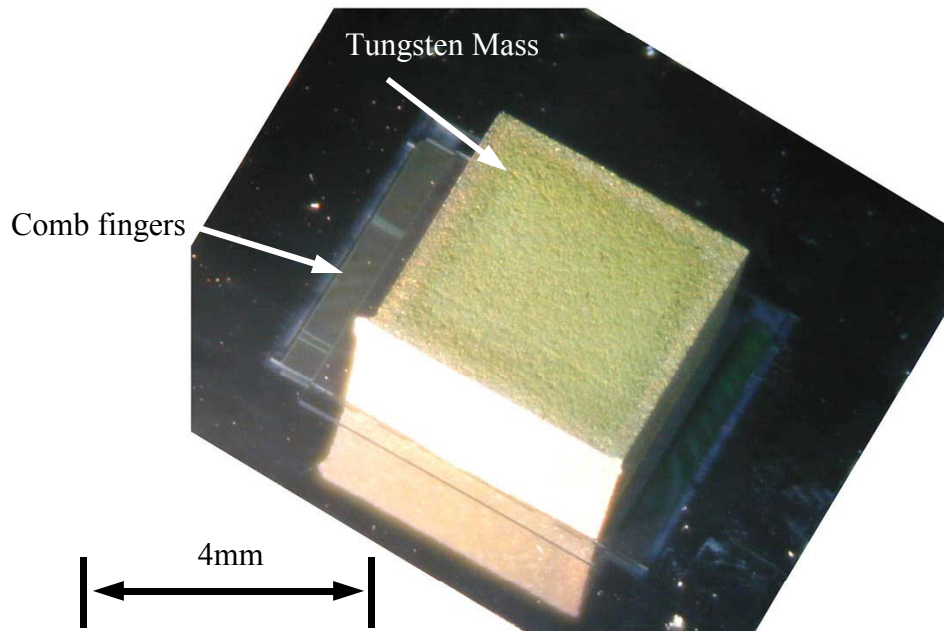


Figure 9.18: Image of electrostatic converter with attached tungsten proof mass.

Figure 9.15 shows two pads to which bare die diodes can be attached. As mentioned in Chapter 8, two methods of connecting the structure to diodes were used. First, bare die diodes were assembled on the pads shown in Figure 9.15 manually with conductive epoxy, and second the pads shown in Figure 9.15 were used as wire bond pads to connect to off chip surface mount diodes. Figure 9.19 shows a bare die diode attached to an electrostatic converter structure. One of the spring flexures is broken on

the structure shown in the image. Both conductive silver epoxy and structural epoxy were used to attach the diode. The epoxy seen around the diode is a structural epoxy applied after the silver conductive epoxy to give the bond added strength for subsequent wire bonding.

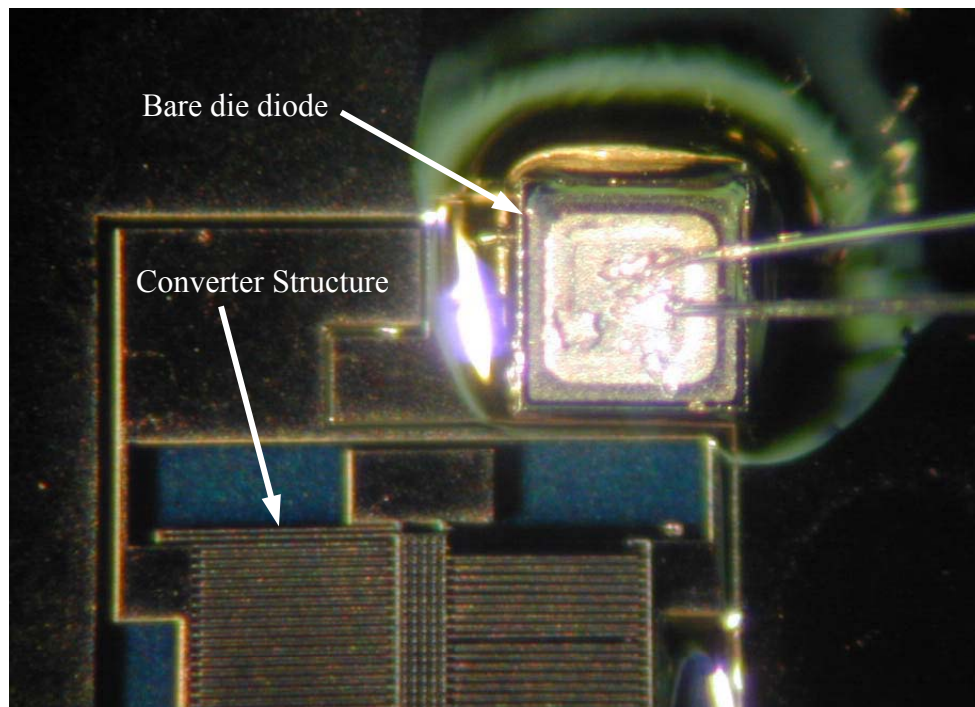


Figure 9.19: Electrostatic converter with bare die diodes attached to on-chip pads.

The reverse leakage current of the diodes is, as before, of critical importance. The manufacturer's specifications for the bare die diodes used specified that the reverse leakage current was 100 nA. Bare die diodes with lower leakage currents could not be found. However, when tested, these diodes exhibited an average reverse leakage current of 100 μ A, which is far too high for the current application. Figure 9.20 shows a measured I-V curve from one of the bare die diodes. As previously, the data is shown on both a linear and a logarithmic scale. The surface mount packaged diodes used are the same that were used for the meso-scale converter reported earlier, which have a

manufacturer's stated reverse leakage current of 10 nA. The diodes were tested, and the accuracy of the manufacturer's specification was confirmed.

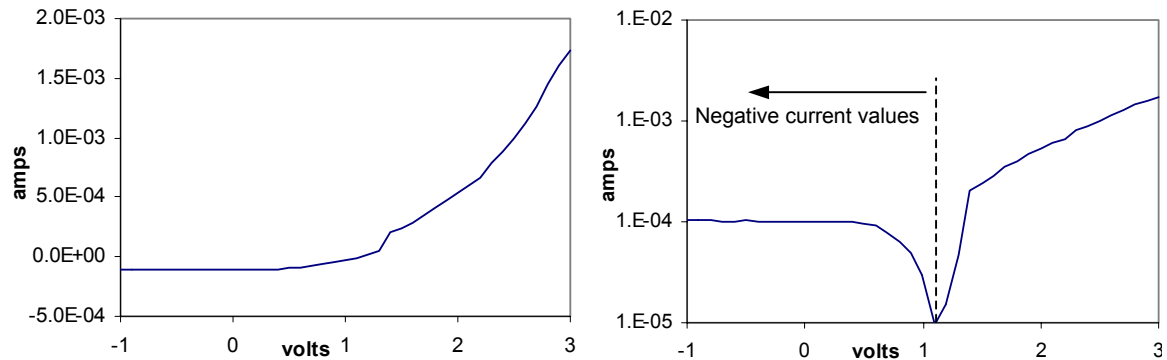


Figure 9.20: I-V curve from a bare die diode attached to electrostatic converter die. Data is shown on a linear scale on the left graph, and the absolute value of the data is shown on a log scale on the right graph.

It will be noted in the above figures that the substrate below the structures is not etched away. The initial process plan called for the substrate to be etched away, however, in each attempt to do this, the structures were broken. Therefore, the process was further simplified and the backside etch was removed in order to produce structurally sound devices. An additional processing difficulty was that the etch rate achieved in the DRIE etcher used to etch the silicon is load dependent. This means that if a large area is being etched, the etch rate is faster. The etch rate in the center of the large plate was significantly less than at the edge of the device. A number of iterations were necessary to get the etch time just right so that the etch holes in the center of the device etched all the way through and the structure could be released but the comb fingers would not be partially etched away, which happened if the etch time was too long. This situation was exacerbated by the facts that it is not possible to tell if the etch holes have completely etched through until the device is released, at which point the die cannot be etched any

further, and that the etch rates and conditions of the machine used to perform the DRIE are constantly changing a little from day to day with use.

Several structures were successfully fabricated using the author's process as shown in the above figures, however the author was not successful in building a functional electrostatic converter. The TIM devices fabricated using this process were not functional because the final resistivity of the silicon was considerably higher than planned. Therefore the required amount of power could not be dissipated in the TIM structures using reasonable voltages. However, the large structures could be manually actuated with probe tips. The devices tested were free of contamination that may have caused a parallel resistance across the variable capacitor. The measured resistance across the variable capacitor was effectively infinite, or open circuited. The reverse leakage current of the bare die diodes was clearly too high for the device to function properly. However, the reverse leakage current of the packaged surface mount diodes was low enough, 10 nA, for them to be useful. The calculated maximum and minimum capacitances of the variable capacitance structures tested were 47 pF and 7.6 pF respectively. Given these capacitances, the device should still be able to function with an effective parasitic capacitance of 300 pF in parallel with the variable capacitor. Although the packaged diodes exhibit far more parasitic capacitance than the bare die diodes, it should be far below 300 pF. So, parasitic capacitance, parallel resistance, and reverse leakage of the diodes don't appear to be the problem.

As mentioned the actual resistivity of the silicon on the wafer from which the structures were taken was considerably higher than planned. The result is that the structure itself is quite resistive. The extra resistance results in a test circuit as shown in

Figure 9.21. The effective resistances of R_1 and R_2 were measured on a structure identical to that shown in Figure 9.15 as $16.5\text{ k}\Omega$ and $760\text{ k}\Omega$ respectively. It is likely that these large resistances impede the functionality of the test device and circuit.

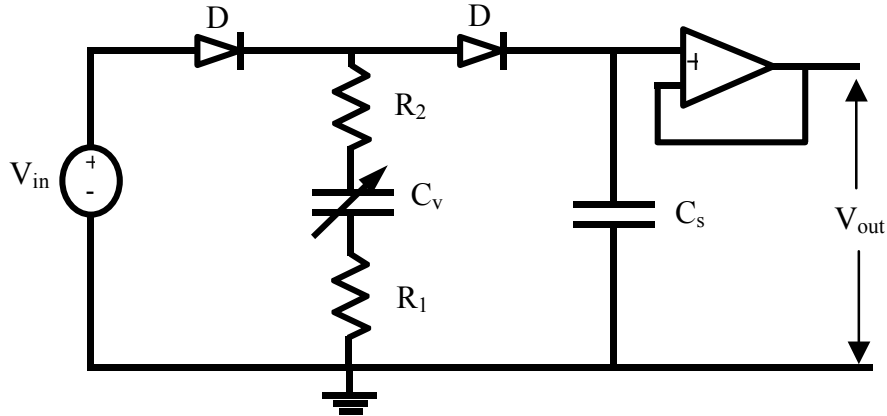


Figure 9.21: Measurement circuit for capacitive converter including parasitic resistances on capacitive structure.

9.5 Discussion of Results and Conclusions

9.5.1 Current Status

The effort to fabricate, micromachined electrostatic vibration-to-electricity converters was not completely successful. A fully functional prototype has yet to be achieved. However, models, design practices, and actual designs have been developed. Electrostatic converter structures have been fabricated on both the meso- and micro-scale. Furthermore, the fundamental voltage (and energy) step-up from mechanical actuation has been demonstrated with both meso- and micro-scale prototypes.

9.5.2 Recommendations

To achieve a fully functional electrostatic converter capable of a useful amount of power output, the following recommendations are made for future designs and processes:

- Fabricate the diodes on the MEMS chip itself. Although the JFET wired as a diode offers the best performance in terms of reverse leakage current of all the diode solutions tested, integrated diodes are still preferable because of the drastically reduced parasitic capacitance. The integrated process can be significantly simplified and still achieve integrated diodes. A new, simplified, integrated process should be developed. Ideally, the diodes will have a lower reverse leakage current than exhibited by the previously fabricated integrated diodes. The process needs to be tuned such that this is the case.
- The design should be redone in such a way as to minimize area dependent etch loading so that the DRIE process etches the silicon at a more uniform rate across the design. This means there should not be any large areas etched away on the front side of the wafer, especially near critical structures.
- It is very important that the silicon be highly doped, and that a metal conductor be deposited on the structure to further reduce parasitic resistances. The new process should include a viable method of depositing metal on the front side as the previously described integrated process does.
- Etching portions of the substrate away beneath the converter structure has the advantages of reducing the parasitic capacitance and the fluid damping. However, the likelihood of damaging structures during processing is far greater if the substrate is etched away. Therefore, ideally, the process and design could be implemented either with or without a backside etch to remove the substrate beneath converter structure.

As mentioned previously, the principle advantage of electrostatic generators is their potential for implementation in a silicon micromachining process. Implementation in a MEMS process has two advantages: first, there is more potential for monolithic integration with electronics, and second, the cost of production using highly parallel IC fabrication techniques is potentially lower. However, the power production capability of any converter is proportional to the mass of the system. A MEMS implementation, therefore, suffers because of the very low mass of planar devices made of lightweight silicon. It then becomes highly desirable, even necessary, to attach a mass to the MEMS device after fabrication. Even with the attached mass, in order to produce enough power for RF communication from the type of vibrations studied in this thesis, the area of the entire device needs to be on the order of tens to a hundred square millimeters. However, at this size, it is not cost effective to monolithically integrate the device with electronics. The price of IC's is proportional to the area of silicon they consume. Because the area consumed by electronics would be at least an order of magnitude lower than that consumed by the generator device, the cost of monolithic integration would be inordinately high. Therefore, given the current constraints and application space an electrostatic MEMS implementation of a vibration-to-electricity converter is not economically attractive. However, it is feasible that under a different set of constraints, either a much larger or higher frequency vibration source, or lower power requirements, a MEMS electrostatic converter could become attractive. It is with the understanding of this eventuality that the development of processes and designs for MEMS vibration generators must be pursued.

Chapter 10: Conclusions

10.1 Justification for focus on vibrations as a power source

Power systems represent perhaps the most challenging technological hurdle yet to be overcome in the widespread deployment of wireless sensor networks. While there is still much research to be done improving radio systems for wireless sensor networks, the technology to accomplish a wireless sensor network is currently available. However, even with the aggressive power consumption target of $100\text{ }\mu\text{W}/\text{node}$, current battery technology cannot even provide 1 year of autonomous operation per 1cm^3 of size. Although the energy density of batteries is improving with time, it is doing so very slowly compared to the improvement in size and power consumption of CMOS electronics. Wireless systems have traditionally been designed to use a battery as their power source. However, if ubiquitous wireless sensor networks are to become a reality, clearly there alternative power sources need to be employed.

Numerous potential sources for power scavenging exist. Light is routinely used as a power source using photovoltaic cells. Smart cards and RF ID tags, to which power is radiated by an energy rich reader, are also common. Myriads of other sources ranging from thermal gradients to imbalanced AC electric fields may also be imagined. It should be stated clearly that there is no single energy scavenging solution that will provide power in all potential applications. Solutions need to be tailored both to the demands of the application and to the environment in which the system will be used. Based on vibrations measured in many environments, preliminary calculations showed that power densities on the order of $100\text{ }\mu\text{W}/\text{cm}^3$ are feasible from commonly occurring vibrations.

This number compares well with other potential energy scavenging sources. For example, in common indoor lighted environments, the power density available from photovoltaic cells is only about $10 \mu\text{W}/\text{cm}^2$. Likewise, thermoelectric devices can produce about $10 \mu\text{W}$ of power from a 10°C temperature differential. Furthermore, vibrations as a power source for stand-alone wireless electronics have received very little research effort. It is believed that the research project reported herein provides an attractive power source for many environments in which low level vibrations are commonly found, and significantly contributes to the development of potentially infinite life power systems for wireless sensor nodes.

Three types of vibration to electricity converters have been considered: electromagnetic, electrostatic, and piezoelectric. After a preliminary investigation, only piezoelectric and electrostatic were pursued in detail. Both types of converters have been modeled, designed, and fabricated. While solar cell based power systems have also been developed for the target wireless sensor nodes, this has been more of a development and benchmarking effort than a research effort.

10.2 Piezoelectric vibration to electricity converters

Piezoelectric benders that exploit the 31 mode of operation were chosen as a design platform because of the higher strain and lower resonant frequencies that can be generated compared to 33 mode piezoelectric stacks. Based on input vibrations of 2.25 m/s^2 at 120 Hz, which represent an average value of the sources measured, a power generation density of $300 \mu\text{W}/\text{cm}^3$ has been demonstrated. When connected to more realistic power train circuitry, the maximum power transfer to the storage reservoir was $200 \mu\text{W}/\text{cm}^3$. Furthermore, if more control over the manufacturing process were

available (specifically, if piezoelectric layer thickness could be arbitrarily chosen for a given application), simulations of optimal designs demonstrate potential power densities approaching $700 \mu\text{W}/\text{cm}^3$ from the same vibration source.

A smaller device to be embedded inside automobile tires has also been designed, built, and tested. This device measures 4mm X 4mm X 5mm. The input vibrations used on this device were of much higher acceleration magnitude (about 50 m/s^2), and the input power was spread over the spectrum from about 10 to 100 Hz. This device produced about $80 \mu\text{W}$ of power for a power density of $1\text{mW}/\text{cm}^3$. For the given application space (i.e. devices on the order of 1cm^3 , with power generation requirements on the order of $100 \mu\text{W}$), piezoelectric converters represent the most attractive solution. Not only are they capable of higher power density, but they are more robust, and the power electronics needed are less complex than electrostatic converters.

10.3 Design considerations for piezoelectric converters

Detailed models have been developed and validated that can serve as the basis for design and optimization. Practical design relationships result from these models that can serve as guiding principles to the designer. These design principles for piezoelectric converters are summarized below.

1. The power output falls off dramatically if the resonant frequency of the converter does not match that of the driving vibrations. The converter should be designed to resonate at the frequency of the target vibrations.

2. Power output is proportional to the oscillating proof mass. Therefore, the mass should be maximized within the space constraints. The need to design for the frequency of the input vibrations, and to not exceed the yield strain of the piezoelectric material, may also limit the amount of mass that can be used.
3. The power output is inversely proportional to frequency of the driving vibrations. Therefore, the system should be designed to resonate at the lowest frequency peak in the input vibration spectrum provided that higher frequency peaks do not have a larger acceleration magnitude.
4. The energy removed from the oscillating converter can be treated as electrically induced damping. Optimal power transfer occurs when the effective electrically induced damping ratio is equal to the mechanical damping ratio. In the case of a simple resistive load, the electrically induced damping is a function of the load resistance, and so can be set by properly choosing the load resistance. In other cases, different circuit parameters can be changed which will affect the amount of electrically induced damping.
5. A storage capacitor charged up through a full wave rectifier is a fairly realistic load. Optimal power transfer to the storage capacitor occurs when the voltage across it is approximately one half the open circuit voltage of the piezoelectric converter. The load circuitry should be designed to control, or at least set limits on, the voltage range of the storage capacitor.

6. The size of the storage capacitor should be at least 10 times the capacitance of the piezoelectric device. If it is smaller than about 10 times the capacitance of the piezoelectric device, the power transfer to the storage capacitor increases with increasing capacitance. If it is greater than about 10 times the capacitance of the converter, the power transfer is largely unaffected by the size of the storage capacitor. A good rule of thumb is to design the storage capacitor to be at least 100 times the capacitance of the piezoelectric device. Additionally, the storage capacitor needs to be large enough to supply enough charge to the load during “on” cycles without its voltage dropping too far. This second consideration will probably drive the storage capacitor to be far greater than 100 times the capacitance of the piezoelectric converter.

10.4 Electrostatic vibration to electricity converters

The design of electrostatic converters was pursued primarily because they are easily implemented in silicon micromachining technology. The utilization of this fabrication technology offers the significant potential benefit of future monolithic integration with sensors and electronics. However, the fundamental conversion potential for electrostatic converters is lower than for piezoelectric converters. As explained in chapter 3, the maximum potential energy density for electrostatic transducers is lower than for piezoelectric converters. This fact is further demonstrated by the simulated power output of optimal electrostatic and piezoelectric designs. Simulations show that optimized electrostatic designs can produce about $110 \mu\text{W}/\text{cm}^3$ while optimized piezoelectric designs can potentially produce several times that value. Nevertheless, models have been

developed, designs performed, and devices fabricated. Devices have been fabricated using a SOI MEMS technique, and the basic operational principles of the converters have been demonstrated. However, power output on the same order of magnitude as that predicted by models has not yet been achieved.

In order for an electrostatic implementation to become attractive, some combination of the following would need to occur. First, in order for monolithic integration to be economically feasible, the size of the converter would need to be reduced to around 1 mm^3 rather than 1 cm^3 . Therefore, the potential power production would decrease by a factor of 1000, or to about 100 nW. If stand-alone systems that can function effectively on 100 nW of power can be implemented, then electrostatic generators could be attractive. Designing the converters to resonate at around 120 Hz in 1 mm^3 could however, be a very significant challenge. Second, in certain environments vibrations of far higher acceleration amplitudes and frequencies are available. If the vibration sources are more energetic, the same amount of power could be generated with a smaller device. If enough applications with high level vibrations arise, electrostatic generators may be the preferred implementation. At present, it is not clear that either of these two situations will exist or that electrostatic converters will become an equally attractive alternative to piezoelectric converters.

10.5 Design considerations for electrostatic converters

As with piezoelectric converters, detailed models have been developed for electrostatic in-plane gap closing generators. Based on these models, and the general model developed in Chapter 2, the following design guidelines emerge.

1. As in the case of all resonant vibration-to-electricity conversion, an electrostatic converter should be designed to resonate at the frequency of the driving vibrations. While, this consideration is perhaps less critical than it is in the case of piezoelectric converters because of the lower effective quality factor of in-plane gap closing electrostatic converters, it is nevertheless important.
2. Again, power output is proportional to mass. This consideration presents a more challenging problem in the domain of micromachined electrostatic converters because of the planar nature of most MEMS devices and the low density of silicon. Therefore, a means of attaching additional mass to the device needs to be employed.
3. The power output is related to the ratio of maximum to minimum capacitance of the converter device. Therefore, it is generally beneficial to design the converter device such that the maximum capacitance is as high as possible. As parasitic capacitance can easily swamp the device making the voltage gain across the variable capacitor negligible, it is also generally beneficial to minimize the parasitic capacitance associated with the device.
4. The range of motion of the device is determined by the nominal gap between comb fingers, the placement of mechanical limit stops, and the mechanical dynamics of the system. The level of effective electrically

induced damping is related to the range of motion of the device, and therefore an optimal nominal gap between comb fingers exists. There is strong interaction between the device geometry (such as device thickness and finger length), the mechanical dynamics, and the choice of the nominal gap. Therefore, dynamic simulations and optimization routines need to be used to properly choose the nominal gap.

10.6 Summary of conclusions

The above conclusions may be thus summarized:

1. Virtually all of the vibration sources measured in conjunction with this study have a dominant frequency in the range of 70 Hz to 125 Hz and magnitudes on the order of tenths to several m/s^2 .
2. Power densities on the order of $200 \mu\text{W}/\text{cm}^3$ are possible and have been demonstrated using piezoelectric converters from an input vibration source of 2.25 m/s^2 at 120 Hz.
3. Given the current set of design constraints, which are thought to represent most potential wireless sensor node applications, piezoelectric converters are the preferred technology because of their higher power density and simpler power electronics.

10.5 Recommendations for future work

Energy scavenging represents an ideal power solution for wireless sensor networks because of its potential to power the sensor nodes indefinitely. While the field of energy scavenging is much more broad than vibration to electricity conversion, it is this author's opinion that there is a wide variety of applications that could greatly benefit from vibration based generators. With this in mind, much more work can be done to advance the field. A few issues that have yet to be satisfactorily pursued are presented below.

As suitable applications currently exist for piezoelectric converters, it is the author's opinion that immediate research and development work should focus on piezoelectric converters until it can be shown that conditions will likely exist that would make electrostatic converters preferable. Only a very limited number of design configurations have been evaluated in this study. Other design configurations that are have better fatigue characteristics, and potentially higher power outputs should be evaluated. Although it is more difficult to fabricate piezoelectric converters on a silicon chip with a micromachining process, it is by no means impossible. It is felt that an effort to both improve thinfilm PZT (and other piezoelectric materials) processes and redesign the converter for a microfabrication process using PZT would be more justified than focusing effort on the development of an electrostatic converter.

Converters have been designed to resonate at the frequency of the driving vibrations. However, this frequency must be known for this approach to work. It is, of course, possible to actively tune the resonant frequency, however, research on space and energy efficient methods to accomplish this needs to be undertaken. Additionally, extremely low power control techniques to accomplish this tuning also need to be

investigated. An open question is whether or not the net power output will be greater with active frequency tuning.

Finally, most commercial power electronics components (i.e. voltage regulators and DC-DC converters) are optimized for systems with much higher power dissipation. Indeed, most standard designs in textbooks are not optimized for systems with average power consumptions well below 1mW. Power electronics specifically optimized for vibration to electricity conversion based on piezoelectrics could significantly improve the overall performance of the system. Furthermore, the system could significantly benefit from an extremely large inductive structure in series with the piezoelectric converter. Given the low frequency of oscillation, the size of the inductor would be too large to use traditional inductors. However, micro-mechanical structures with very large effective inductances can be fabricated and could, perhaps, improve the power transfer to the load if placed in series with the piezoelectric converter.

In a recent article in IEEE Computer, Professor Jan Rabaey states “One of the most compelling challenges of the next decade is the ‘lastmeter’ problem—extending the expanding data network into end-user data-collection and monitoring devices.” (Rabaey *et al* 2000). Indeed, it has become a widely held belief in the research and business community that the next revolution in computing technology will be the widespread deployment of low cost, low power wireless computing devices. In order for this vision to become a reality, the problem of how to power the devices in a cost effective way must be solved. Primary batteries are appropriate for a certain class of devices. However, if the wireless sensing and computing nodes are to become truly ubiquitous, the replacement of batteries is simply too costly. Energy scavenging technologies must be

developed in order to create completely self-sustaining wireless sensor nodes. The research presented in this thesis has demonstrated that low level vibrations can provide enough power to operate wireless sensor nodes in many applications. However, as stated previously, there is no single energy scavenging solution that will fit all applications and all environments. Energy scavenging solutions must, therefore, continue to be explored in order to meet the needs of an ever growing application space for wireless sensor networks.

References

- (Alessandrini *et al* 2000) Alessandrini, F., Conte, M., Passerini, S., Prosini, P.P., 2000. Overview of ENEA's projects on lithium batteries. *Journal of Power Sources*, vol.97-98, pp.768-71.
- (Amirtharajah and Chandrakasan 1998) Amirtharajah, R., Chandrakasan, A.P., 1998. Self-Powered Signal Processing Using Vibration-Based Power Generation. *IEEE Journal of Solid State Circuits*, Vol. 33, No. 5, p. 687-695.
- (Amirtharajah 1999) Amirtharajah, R., 1999. *Design of Low Power VLSI Systems Powered by Ambient Mechanical Vibration*. Ph.D Thesis, Department of Electrical Engineering, Massachusetts Institute of Technology, June 1999.
- (Amirtharajah *et al* 2000) Amirtharajah, R., Meninger, S., Mur-Miranda, J. O., Chandrakasan, A. P., Lang, J., 2000, A Micropower Programmable DSP Powered using a MEMS-based Vibration-to-Electric Energy Converter. *IEEE International Solid State Circuits Conference*, p. 362-363.
- (Bellew 2002) Bellew, C., 2002. *An SOI Process for Integrated Solar Power, Circuitry and Actuators for Autonomous Microelectromechanical Systems*, Ph.D Thesis, Department of Electrical Engineering, University of California at Berkeley, May 2002.
- (Beer and Johnston 1992) Beer, F.P., Johnston, E.R., 1992. *Mechanics of Materials*, McGraw-Hill, Inc., 1992.
- (Bomgren 2002) Bomgren, G. E., 2002. Perspectives on portable lithium ion batteries liquid and polymer electrolyte types. *Proceedings of the Seventeenth Annual Battery Conference on Applications and Advances*, 2002, p. 141-4.
- (Chandrakasan *et al* 1998) Chandrakasan, A., Amirtharajah, Goodman, R. J., Rabiner, W., 1998. Trends in low power digital signal processing. *Proceedings of the 1998 IEEE International Symposium on Circuits and Systems*, 1998, p. 604-7.
- (Chang and Lin 2001) Chang, Y.T., Lin, L. Localized Silicon Fusion and Eutectic Bonding for MEMS Fabrication and Packaging. *Journal of Microelectromechanical Systems*, vol. 9 (no. 1) (2001) 3 – 8.
- (Cragun and Howell 1999) Cragun, R., Howell, L.L., 1999. Linear thermomechanical microactuators. *Proc. ASME IMECE MEMS* (1999) pp. 181-188.
- (Cronos 2003), www.memsrus.com, Jan. 2003

- (Davis *et al* 2001) Davis, W. R., Zhang, N., Camera, K., Chen, F., Markovic, D., Chan, N., Nikolic, B., Brodersen, R. W., 2001. A design environment for high throughput, low power dedicated signal processing systems. *Proceedings of the IEEE 2001 Custom Integrated Circuits Conference*, 2001, p. 545-8.
- (Doherty *et al* 2001) Doherty, L., Warneke B.A., Boser B.E., Pister K.S.J., 2001 Energy and performance considerations for smart dust. *International Journal of Distributed Systems & Networks*, vol. 4, no.3, 2001, pp. 121-33.
- (Economist 1999) Power from the people. *The Economist*, Apr 15, 1999.
- (Evans *et al* 1996) Evans, J. G., Shober, R. A., Wilkus, S. A., Wright, G. A., 1996. A low-cost radio for an electronic price label system. *Bell Labs Technical Journal* vol. 1, Issue 2, 1996. pp. 203 –215.
- (FCC 2002) http://wireless.fcc.gov/siting/FCC_LSGAC_RF_Guide.pdf, May 2003.
- (FCC 2002) <http://ftp.fcc.gov/Bureaus/Wireless/Orders/1995/fcc95041.txt>, May 2003.
- (Flynn and Sanders 2002) Flynn, A.M.; Sanders, S.R. 2002. Fundamental limits on energy transfer and circuit considerations for piezoelectric transformers. *IEEE Transactions on Power Electronics*, vol.17, (no.1), IEEE, Jan. 2002. p.8-14.
- (Friedman *et al* 1997) Friedman, D., Heinrich, H., Duan, D-W., 1997. A Low-Power CMOS Integrated Circuit for Field-Powered Radio Frequency Identification. *Proceedings of the 1997 IEEE Solid-State Circuits Conference*, p. 294 – 295, 474.
- (Gates 2002) Gates, B., 2002. The disappearing computer. *The Economist, Special Issue: The World in 2003*, December 2002, p. 99.
- (Glynne-Jones *et al* 2001) Glynne-Jones, P., Beeby, S. P., James, E. P., White, N. M. 2001. The modelling of a piezoelectric vibration powered generator for microsystems. *Transducers 01 / Eurosensors XV*, June 10 – 14, 2001.
- (Hitachi mu-Chip 2003) Hitachi Unveils Smallest RFID Chip. *RFiD Journal*, March 14, 2003.
- (Hsu 2000) Hsu, T-R, 2000. Packaging Design of Microsystems and Meso-Scale Devices. *IEEE Transactions on Advanced Packaging*, vol. 23 (no. 4) (2000) 596 – 601.
- (Ikeda 1990) Ikeda, T., 1990. *Fundamentals of piezoelectricity*, Oxford University Press, New York, 1990.
- (Iowa Thin Film Technologies 2003) www.iowathinfilm.com , Jan. 2003.

- (Jaeger 1993) Jaeger, R. C., 1993. *Introduction to Microelectronic Fabrication*, Addison Wesley Publishing Company, Inc., 1993.
- (James *et al* 1994) James, M.L., Smith, G.M., Wolford, J.C., Whaley, P.W., 1994. *Vibration of Mechanical and Structural Systems*, Harper Collins College Publishers, New York, NY 1994.
- (Kang *et al* 2001) Kang, S., Lee, S-J. J., Prinz, F.B., 2001. Size does matter: the pros and cons of miniaturization. *ABB Review*, 2001, no.2, p.54-62.
- (Kassakian *et al* 2000) Kassakian, J.C., Schlecht, M.F., Verghese, G.C., 1992. *Principles of Power Electronics*. Addison Wesley Publishing Company, 1992.
- (Laerme *et al* 1999) Laerme F, Schilp A, Funk K, Offenbergh M., 1999. Bosch deep silicon etching: improving uniformity and etch rate for advanced MEMS applications. *Twelfth IEEE International Conference on Micro Electro Mechanical Systems* 1999, pp.211-16.
- (Lee 2001) Lee S. H. Development of high-efficiency silicon solar cells for commercialization. *Journal of the Korean Physical Society*, vol.39, no.2, Aug. 2001, pp.369-73.
- (Lee and Pisano 1993) Lee, A. P., and Pisano, A. P., Repetitive impact testing of micromechanical structures. *Sensors and Actuators A (Physical)*, A39 (1) (1993) 73-82.
- (Lee and White 1995) Lee, S.S., and White, R.M., 1995. Self-excited Piezoelectric Cantilever Oscillators. *Proc. Transducers 95/Eurosensors IX*, (1995) 41 – 45.
- (Lott 2001) Lott, C. D., 2001, *Electrothermomechanical Modeling of a Surface-Micromachined Linear Displacement Microactuator*, M.S. Thesis, Department of Mechanical Engineering, Brigham Young University, August 2001.
- (Lott *et al* 2002) Lott CD, McLain TW, Harb JN, Howell LL., 2002. Modeling the thermal behavior of a surface-micromachined linear-displacement thermomechanical microactuator. *Sensors & Actuators A-Physical*, vol.A101, no.1-2, 30 Sept. 2002, pp.239-50.
- (Madou 1997) Madou, M., 1997. *Fundamentals of Microfabrication*, CRC Press LLC, Boca Raton Florida, 1997.
- (Maluf 2000) Maluf, N., 2000. *An Introduction to Microelectromechanical Systems Engineering*, Artech House, Inc., Norwood, Massachusetts, 2000.

- (Mehra *et al* 2000) Mehra, A., Zhang, X., Ayon, A. A., Waitz, I. A., Schmidt, M. A., Spadaccini, C. M., 2000. A Six-Wafer Combustion System for a Silicon Micro Gas Turbine Engine. *Journal of Microelectromechanical Systems*, 9 (4) (2000) 517-526.
- (Meninger *et al* 1999) Meninger, S., Mur-Miranda, J. O., Amirtharajah R., Chandrakasan, A. P., Lang, J., 1999, Vibration-to-Electric Conversion, *ISPLED99* San Diego, CA, USA, p. 48 – 53.
- (Meninger *et al* 2001) Meninger, S., Mur-Miranda, J.O., Amirtharajah, R., Chandrakasan, A.P., and Lang, J.H., 2001. Vibration-to-Electric Energy Conversion. *IEEE Trans. VLSI Syst.*, 9 (2001) 64-76.
- (Moulson and Herbert 1997) Moulson, A.J., Herbert, J.M., 1997. *Electroceramics Materials Properties Applications*. Chapman and Hall, 1997.
- (National Research Council 1997) National Research Council, Rowe J.E. 1997. *Energy-Efficient Technologies for the Dismounted Soldier*, National Academy Press, 1997.
- (Nijs *et al* 2001) Nijs JF, Szlufcik J, Poortmans J, Mertens RP. Crystalline silicon based photovoltaics: technology and market trends. *Modern Physics Letters B*, vol.15, no.17-19, 20 Aug. 2001, pp.571-8.
- (Otis and Rabaey 2002) Otis, B., Rabaey, J., A 300 μ W 1.9GHz CMOS Oscillator Utilizing Micromachined Resonators., *Proceedings of the 28th European Solid State Circuits Conference*, Florence Italy, September 24 – 26, 2002.
- (Ottman *et al* 2003) Ottman G. K., Hofmann H. F., Lesieutre G. A. 2003. Optimized piezoelectric energy harvesting circuit using step-down converter in discontinuous conduction mode. *IEEE Transactions on Power Electronics*, vol.18, no.2, 2003, pp.696-703.
- (Ottman *et al* 2002) Ottman G. K., Hofmann H. F., Bhatt A. C., Lesieutre G. A. 2002. Adaptive piezoelectric energy harvesting circuit for wireless remote power supply. *IEEE Transactions on Power Electronics*, vol.17, no.5, 2002, pp.669-76.
- (Park and Shrout 1997) Park, S.E., and Shrout, T.R. 1997. Characteristics of Relaxor-Based Piezoelectric Single Crystals for Ultrasonic Transducers. *IEEE Trans. on Ultrasonics, Ferroelectric and Frequency Control Special Issue on Ultrasonic Transducers*, Vol. 44, No. 5, 1140-1147 (1997).
- (Piezo Systems Inc. 1998) Piezo Systems, Inc., 1998. *Piezoelectric Actuator/Sensor Kit Manual*, Piezo Systems, Inc., Cambridge MA., (1998).
- (Rabaey *et al* 2002) Rabaey, J., Ammer, J., Karalar, T., Li, S., Otis, B., Sheets, M., Tuan, T., 2002. PicoRadios for Wireless Sensor Networks: The Next Challenge in Ultra-

- Low-Power Design. *Proceedings of the International Solid-State Circuits Conference*, San Francisco, CA, February 3-7, 2002.
- (Rabaey *et al* 2000) Rabaey, J. M., Ammer, M. J., da Silva, J. L., Patel, D., Roundy S., 2000. PicoRadio Supports Ad Hoc Ultra-Low Power Wireless Networking. *IEEE Computer*, Vol. 33, No. 7, p. 42-48.
- (Raible and Michel 1998) Raible, C., Michel, H. 1998. Bursting with power. *Siemens Components* (English Edition), vol.33, (no.6), Siemens AG, Dec. 1998. p.28-9
- (Randall 2003) Randall, J. F. *On ambient energy sources for powering indoor electronic devices*, Ph.D Thesis, Ecole Polytechnique Federale de Lausanne, Switzerland, May 2003.
- (Riehl *et al* 2002) Riehl, P. S., Scott, K., L., Muller, R. S., Howe, R., T., 2002. High-Resolution Electrometer with Micromechanical Variable Capacitor. *Solid State Sensor, Actuator and Microsystems Workshop*, Hilton Head Island, South Carolina, June 2002, pp. 305 – 308.
- (Rosenber and Karnopp 1983) Rosenber, R. C., Karnopp, D. C. 1983. *Introduction to Physical System Dynamics*, McGraw Hill Inc., 1983.
- (Roundy *et al* 2002) Roundy S., Wright P. K., Pister K. S. J., 2002. Micro-Electrostatic Vibration-to-Electricity Converters, *ASME IMECE*, Nov. 17-22, 2002, New Orleans, Louisiana.
- (Schittowski 1985) Schittowski, K., 1985. NLQPL: A FORTRAN-Subroutine Solving Constrained Nonlinear Programming Problems. *Annals of Operations Research*, Vol. 5, pp. 485-500, 1985.
- (Schmidt 1986) Schmidt, V.H., Theoretical Electrical Power Output per Unit Volume of PVF2 and Mechanical-to-Electrical Conversion Efficiency as Functions of Frequency. *Proceedings of the Sixth IEEE International Symposium on Applications of Ferroelectrics*, (1986) 538-542.
- (Shearwood and Yates 1997) Shearwood, C., Yates, R.B., 1997, Development of an electromagnetic micro-generator, *Electronics Letters*, vol.33, (no.22), IEE, 23 Oct. 1997. p.1883-4
- (Shenck and Paradiso 2001) Shenck, N. S., Paradiso, J. A., 2001. Energy Scavenging with Shoe-Mounted Piezoelectrics, *IEEE Micro*, 21 (2001) 30-41.
- (Sim *et al* 2001) Sim, W. Y., Kim, G. Y., Yang, S. S., 2001. Fabrication of micro power source (MPS) using a micro direct methanol fuel cell (μ DMFC) for the medical application. *Technical Digest. MEMS 2001* p. 341-344.

- (Srinivasan 2001) Srinivasan, U., Liepmann, D., Howe, R.T., 2001. Microstructure to substrate self-assembly using capillary forces, *Journal of Microelectromechanical Systems*, 10-1, 17-24 (2001).
- (Starner 1996) Starner, T., 1996. Human-powered wearable computing. *IBM Systems Journal*, 35 (3) (1996) 618-629.
- (Stordeur and Stark 1997) Stordeur, M., Stark, I., 1997. Low Power Thermoelectric Generator – self-sufficient energy supply for micro systems. *16th International Conference on Thermoelectrics*, 1997, p. 575 – 577.
- (Tang *et al* 1989) Tang, W.C., Nguyen, T.-C.H., Howe, R.T., 1989. Laterally driven polysilicon resonant microstructures. *Sensors Actuators*, vol. 20, pp. 25–32, 1989.
- (TRS Ceramics 2003), www.trsceramics.com, Jan. 2003.
- (Tzou 1993) Tzou, H. S., *Piezoelectric Shells, Distributed Sensing and Control of Continua*, Kluwer Academic Publishers, Norwell, Massachusetts, 1993.
- (Verardi *et al* 1997) Verardi P, Craciun F, Dinescu M. 1997. Characterization of PZT thin film transducers obtained by pulsed laser deposition. *IEEE Ultrasonics Symposium Proceedings*. vol.1, 1997, pp.569-72.
- (Wang *et al* 2002) Wang, D. E., Arens, T. Webster, and M. Shi, 2002, How the Number and Placement of Sensors Controlling Room Air Distribution Systems Affect Energy Use and Comfort, *International Conference for Enhanced Building Operations*, Richardson, TX, October 2002.
- (Warneke *et al* 2001) Warneke, B. Atwood, B. Pister, K.S.J., 2001 Smart Dust Mote Forerunners, *Fourteenth Annual International Conference on Microelectromechanical Systems (MEMS 2001)*, Interlaken, Switzerland, Jan. 21-25, 2001.
- (Williams and Yates 1995) Williams, C.B, and Yates, R.B., 1995. Analysis of a micro-electric generator for Microsystems. *Transducers 95/Eurosensors IX*, (1995) 369 – 372.
- (Williams *et al* 2001) Williams, C.B.; Shearwood, C.; Harradine, M.A.; Mellor, P.H.; Birch, T.S.; Yates, R.B. Development of an electromagnetic micro-generator. *IEEE Proceedings-Circuits, Devices and Systems*, vol.148, (no.6), IEE, Dec. 2001. p.337-42

Appendix A, Analytical Model of Piezoelectric Generator

Chapter 4 discussed the development of an analytical model for piezoelectric generators and used this model as a basis for design. However, many of the details of the derivation of the analytical model were left out of Chapter 4 to improve the readability of the chapter. The goal of this appendix, then, is to provide the details of the derivation of the analytical model for a piezoelectric vibration-to-electricity converter.

A.1 Geometric terms for bimorph mounted as a cantilever

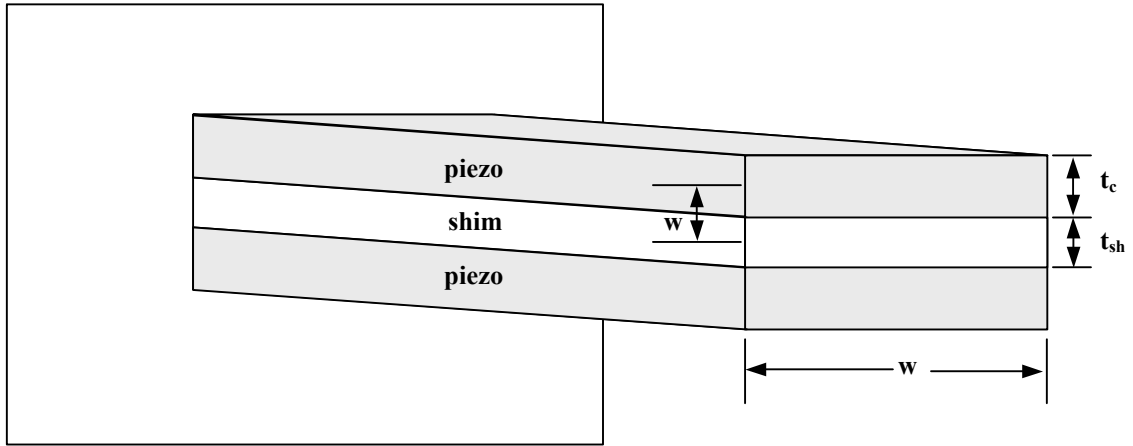


Figure A.1: Cross section of composite beam.

Because the piezoelectric bender is a composite beam, an effective moment of inertia and elastic modulus are used. The effective moment of inertia is given by equation A.1 below.

$$I = \left[\frac{wnt_c^3}{12} + wnt_c b^2 \right] + \frac{\eta_s w t_{sh}^3}{12} \quad (\text{A.1})$$

where:

w is the width of the beam.

t_c is the thickness of an individual piezoelectric ceramic layer.

n is the number of piezoelectric layers (two as shown in the figure).

b is the distance from the center of the shim to the center of the piezo layers.

t_{sh} is the thickness of the center shim.

η_s is the ratio of the piezoelectric material elastic constant to that of the center shim ($\eta_s = Y_c/Y_{sh}$ where Y_c is Young's modulus for the piezoelectric ceramic and Y_{sh} is Young's modulus for the center shim).

The elastic constant for the piezoelectric ceramic is then used in conjunction with the effective moment of inertia shown by equation A.1. The different Young's modulus of the center shim is accounted for by the term η_s in the moment of inertia (Beer and Johnston 1992).

Because the piezoelectric constitutive equations deal directly with stress and strain, it is most convenient to use them as the state equations for the dynamic system rather than force and displacement. However, in order to derive state equations in terms of stress and strain for the piezoelectric bender mounted as a cantilever beam as shown in Figure A.2, two geometric terms need to be defined. The first relates vertical force to average stress in the piezoelectric material, and the second relates tip deflection of the beam to average strain in the piezoelectric material.

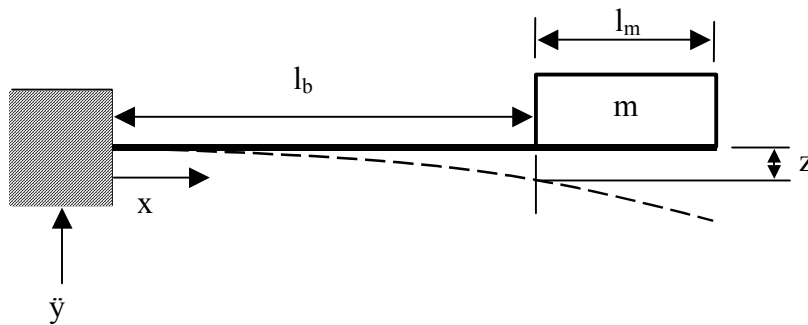


Figure A.2: Schematic of piezoelectric bender.

When purchased, the piezoelectric benders are covered with an electrode. The electrode can be easily etched away making the only the portion of the beam covered by

the electrode active as a piezoelectric element. Referring to Figure A.2, it will be assumed that the electrode length (l_e , not shown in the figure) is always equal to or less than the length of the beam (l_b in the figure). The stress and strain values of interest, and those used as state variables, are the average stress and strain in the piezoelectric material that is covered by an electrode. An expression for the average stress in the piezoelectric material covered by the electrode (hereafter referred to simply as stress) is given by equation A.2.

$$\sigma = \frac{1}{l_e} \int_0^{l_e} \frac{M(x)b}{I} dx \quad (\text{A.2})$$

where:

σ is stress.

x is the distance from the base of the beam.

$M(x)$ is the moment in the beam as a function of the distance (x) from its base.

The moment, $M(x)$, is given by equation A.3.

$$M(x) = m(\ddot{y} + \ddot{z})(l_b + \frac{1}{2}l_m - x) \quad (\text{A.3})$$

where:

l_m is the length of the mass.

\ddot{y} is the input vibration in terms of acceleration.

z is the vertical displacement of the beam at the point where the mass attaches with respect to the base of the beam.

Substituting equation A.3 in to equation A.2 yields the expression in A.4.

$$\sigma = m(\ddot{y} + \ddot{z}) \frac{b(2l_b + l_m - l_e)}{2I} \quad (\text{A.4})$$

The vertical force term in equation A.4 is simply $m(\ddot{y} + \ddot{z})$. Therefore, let us define b^{**} as shown in equation A.5.

$$b^{**} = \frac{2I}{b(2l_b + l_m - l_e)} \quad (\text{A.5})$$

b^{**} then relates vertical force to stress (σ), and $\sigma = m(\ddot{y} + \ddot{z}) / b^{**}$.

In order to derive the term relating deflection at the point where the beam meets the mass as shown in Figure A.2 to average strain in the piezoelectric material covered by the electrode (simply strain hereafter), consider the Euler beam equation shown as A.6.

$$\frac{d^2 z}{dx^2} = \frac{M(x)}{Y_c I} \quad (\text{A.6})$$

Substituting A.3 into A.6 yields equation A.7.

$$\frac{d^2 z}{dx^2} = \frac{1}{Y_c I} m(\ddot{y} + \ddot{z}) \left(l_b + \frac{1}{2} l_m - x \right) \quad (\text{A.7})$$

Integrating to obtain an expression for the deflection term (z) yields:

$$z = \frac{m(\ddot{y} + \ddot{z})}{Y_c I} \left(\left(l_b + \frac{1}{2} l_m \right) \frac{x^2}{2} - \frac{x^3}{6} \right) \quad (\text{A.8})$$

At the point where the beam meets the mass (at $x = l_b$), the expression for z becomes:

$$z = \frac{m(\ddot{y} + \ddot{z}) l_b^2}{2 Y_c I} \left(\frac{2}{3} l_b + \frac{1}{2} l_m \right) \quad (\text{A.9})$$

Finally, realizing that strain is equal to stress over the elastic constant, $\delta = \sigma/Y$, and that stress can be expressed as in equation A.4, strain can be written as shown below:

$$\delta = \frac{m(\ddot{y} + \ddot{z}) b}{2 Y_c I} (2l_b + l_m - l_e) \quad (\text{A.10})$$

Rearranging equation A.10, the force term, $m(\ddot{y} + \ddot{z})$, can be written as shown in equation A.11.

$$m(\ddot{y} + \ddot{z}) = \frac{2Y_c I}{b(2l_b + l_m - l_e)} \delta \quad (\text{A.11})$$

Substituting equation A.11 into equation A.9 yields:

$$z = \delta \frac{l_b^2}{3b} \frac{(2l_b + \frac{3}{2}l_m)}{(2l_b + l_m - l_e)} \quad (\text{A.12})$$

Let us define b^* as shown in equation A.13. b^* then relates strain to vertical displacement, or $z = \delta/b^*$.

$$b^* = \frac{3b}{l_b^2} \frac{(2l_b + l_m - l_e)}{(2l_b + \frac{3}{2}l_m)} \quad (\text{A.13})$$

A.2 Basic dynamic model of piezoelectric generator

A convenient method of modeling piezoelectric elements such that system equations can be easily developed is to model both the mechanical and electrical portions of the piezoelectric system as circuit elements. The piezoelectric coupling is then modeled as a transformer (Flynn and Sanders 2002). Figure A.3 shows the circuit model for a piezoelectric element. Note that this is the same circuit model shown in Chapter 4 as Figure 4.3. Note also that no electric load is applied to the system.

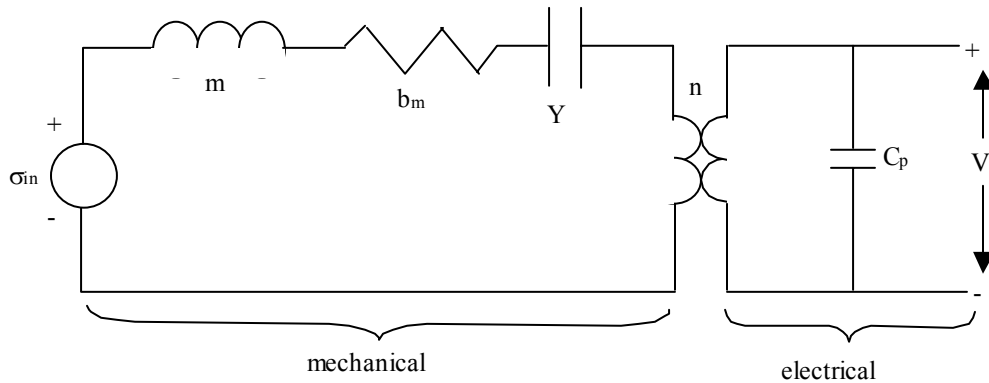


Figure A.3: Circuit Representation of Piezoelectric Bimorph

As explained in Chapter 4, the across variable (variable acting across an element) on the electrical side is voltage (V) and the through variable (variable acting through an element) is current (i) (Rosenberg and Karnopp, 1983). The across variable on the mechanical side is stress (σ) and the through variable is strain (δ). The system equations can then be obtained by simply applying Kirchoff's Voltage Law (KVL) and Kirchoff's Current Law (KCL). However, first the stress / strain relationships for circuit elements on the mechanical side need to be defined.

σ_{in} is an equivalent input stress. In other words, it is the stress developed as a result of the input vibrations. m , shown as an inductor, represents the effect of the mass, or inertial term. The stress “across” this element is the stress developed as a result of the mass flexing the beam. Equation A.4 gives the stress resulting from both the input element, σ_{in} , and the inertial element, m . Thus, the relationships for these two elements are given in equations A.14 and A.15.

$$\sigma_{in} = \frac{m}{b^{**}} \ddot{y} \quad (\text{A.14})$$

$$\sigma_m = \frac{m}{b^{**}} \ddot{z} \quad (\text{A.15})$$

However, the preferred state variable is strain, δ , rather than displacement z . Substituting strain for displacement in A.15 using the relationship from equation A.12 and A.13 yields the stress / strain relationship for the inertial element, m , in equation A.16.

$$\sigma_m = \frac{m}{b^* b^{**}} \ddot{\delta} \quad (\text{A.16})$$

The resistive element in Figure A.3 represents damping, or mechanical loss. The damping coefficient, b_m , relates stress to tip displacement, z . Therefore the units of b_m

are Ns/m^3 rather than the more conventional Ns/m . The stress / strain relationship for the damping element, b_m , becomes:

$$\sigma_{bm} = \frac{b_m}{b^*} \dot{\delta} \quad (\text{A.17})$$

Finally, the stiffness element is represented as a capacitor and labeled with the elastic constant, Y . The stress / strain relationship for this element is simply Hooke's law, shown here as equation A.18.

$$\sigma_Y = Y_c \delta \quad (\text{A.18})$$

The transformer relates stress (σ) to electric field (E) at zero strain, or electrical displacement (D) to strain (δ) at zero electric field. The piezoelectric constitutive relationships are shown again below in equations A.19 and A.20. The equations for the transformer follow directly from the piezoelectric constitutive relationships and are given in equations A.21 and A.22.

$$\delta = \sigma/Y + dE \quad (\text{A.19})$$

$$D = \epsilon E + d\sigma \quad (\text{A.20})$$

where:

d is the piezoelectric strain coefficient.

ϵ is the dielectric constant of the piezoelectric material.

$$\sigma_t = -dY_c E \quad (\text{A.21})$$

$$D_t = -dY_c \delta \quad (\text{A.22})$$

The equivalent turns ratio for the transformer is then $-dY$. The state variables, however, are current, \dot{q} , and voltage, V . Noting that $q = n\epsilon_w D$ and that $V = Et_c$, the equations for the transformer can be rewritten as:

$$\sigma_t = \frac{-dY_c}{t_c} V \quad (\text{A.23})$$

$$\dot{q}_t = -dY_c n l_e w \dot{\delta} \quad (\text{A.24})$$

Note that the expressions in equations A.23 and A.24 assume that the piezoelectric layers are all wired in parallel. If any layers that are wired in series are considered a single layer, the model will still hold. For example, if the bender is a two layer bimorph wired in series, the number of layers in the calculations should be one, and the piezoelectric thickness (t_c) used should actually be the sum of the thickness of the two layers.

Applying KVL to the circuit in Figure A.3 yields the following equation:

$$\sigma_{in} = \sigma_m + \sigma_{bm} + \sigma_t \quad (\text{A.25})$$

Substituting equations A.14, A.16 – A.18, and A.23 into A.25 and rearranging terms yields the third order equation shown as A.26, which describes the mechanical dynamics of the system with an electrical coupling term.

$$\ddot{\delta} = -\frac{Yb^*b^{**}}{m}\delta - \frac{b_m b^{**}}{m}\dot{\delta} + \frac{dY_c}{t_c} \frac{b^*b^{**}}{m}V + b^*\ddot{y} \quad (\text{A.26})$$

The combined term Yb^*b^{**} has units of force / displacement and relates vertical force to tip deflection. This is commonly referred to as the effective spring constant. Letting k_{sp} be the effective spring constant, and substituting $k_{sp} = Yb^*b^{**}$ into equation A.26 yields the simpler and more familiar expression in equation A.27.

$$\ddot{\delta} = -\frac{k_{sp}}{m}\delta - \frac{b_m b^{**}}{m}\dot{\delta} + \frac{k_{sp}d}{mt_c}V + b^*\ddot{y} \quad (\text{A.27})$$

Equation A.27 forms a portion of the complete dynamic model. Applying KCL to the electrical side of the circuit in Figure A.3 yields the rest of the model. Equation A.28 is the very simple result of applying KCL to the electrical side of the equivalent circuit.

$$\dot{q}_t = \dot{q}_{C_p} \quad (\text{A.28})$$

where:

\dot{q}_t is the current through the transformer as defined in equation A.24.

\dot{q}_{C_p} is the current through the capacitor C_p .

The capacitance of the piezoelectric device is $C_p = \frac{n\epsilon w l_e}{t_c}$. Substituting equation

A.24 into A.28, using the long expression for C_p , and rearranging terms yields the equation shown as A.29.

$$\dot{V} = \frac{-dY_c t_c}{\epsilon} \dot{\delta} \quad (\text{A.29})$$

Equations A.27 and A.29 constitute the dynamic model of the system. They can be rewritten in state space form as shown in equation A.30.

$$\begin{bmatrix} \dot{\delta} \\ \ddot{\delta} \\ \dot{V} \end{bmatrix} = \begin{bmatrix} 0 & 1 & 0 \\ -\frac{k_{sp}}{m} & -\frac{b_m b^{**}}{m} & \frac{k_{sp} d}{m t_c} \\ 0 & -\frac{dY_c t_c}{\epsilon} & 0 \end{bmatrix} \begin{bmatrix} \delta \\ \dot{\delta} \\ V \end{bmatrix} + \begin{bmatrix} 0 \\ b^* \\ 0 \end{bmatrix} \ddot{y} \quad (\text{A.30})$$

As noted previously, no electrical load has been applied to the system. The right side of Figure A.3 is an open circuit, and so no power is actually transferred in this case. Figure A.4 shows the circuit representation of the system with a simple resistive load applied.

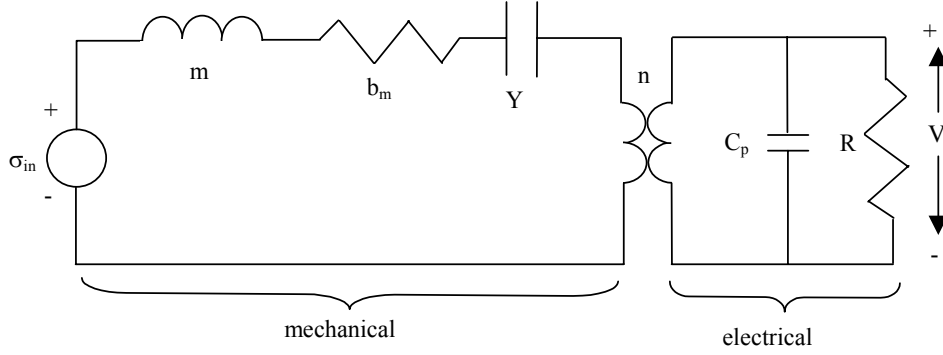


Figure A.4: Circuit model of piezoelectric bimorph with resistive load

The resulting change in the system equations is only minor. The mechanical side of the circuit, and thus equation A.27, remain unchanged. Applying KCL to the electrical side of the circuit now yields:

$$\dot{q}_t = \dot{q}_{C_p} + \dot{q}_R \quad (\text{A.31})$$

where:

\dot{q}_R is the current through resistor R.

Making the same substitutions as explained previously, and substituting V/R for the current through the resistor yields the following equation, which replaces equation A.29 in the system model.

$$\dot{V} = \frac{-Ydt_c}{\varepsilon} \dot{\delta} - \frac{1}{RC_p} V \quad (\text{A.32})$$

The new system model in state space form is given by equation A.33.

$$\begin{bmatrix} \dot{\delta} \\ \ddot{\delta} \\ \dot{V} \end{bmatrix} = \begin{bmatrix} 0 & 1 & 0 \\ -\frac{k_{sp}}{m} & -\frac{b_m b^{**}}{m} & \frac{k_{sp} d}{mt_c} \\ 0 & -\frac{dY_c t_c}{\varepsilon} & \frac{1}{RC_p} \end{bmatrix} \begin{bmatrix} \delta \\ \dot{\delta} \\ V \end{bmatrix} + \begin{bmatrix} 0 \\ b^* \\ 0 \end{bmatrix} \ddot{y} \quad (\text{A.33})$$

A.3 Expressions of interest from basic dynamic model

A few additional expressions derived from the basic model shown in equation A.33 are of interest. The first is an analytical expression for the power transferred to the resistive load. The power dissipated by the resistive load is simply V^2/R . Therefore, an analytical expression for V needs to be obtained from the equations in A.33. Taking the Laplace transform of equation A.32 and rearranging terms yields the following expression:

$$\Delta = -\frac{\varepsilon}{Y_c dt_c s} \left(s + \frac{1}{RC_p} \right) V \quad (\text{A.34})$$

where:

Δ is Laplace transform of strain (δ).

V is the voltage (the symbol V is used in both the time and frequency domain).

s is the Laplace variable.

Taking the Laplace transform of equation A.26 and rearranging terms yields:

$$\Delta \left(s^2 + \frac{b_m b^{**}}{m} s + \frac{k_{sp}}{m} \right) = \frac{k_{sp} d}{m t_c} V + b^* A_{in} \quad (\text{A.35})$$

where:

A_{in} is the Laplace transform of the input vibrations in terms of acceleration.

Substituting equation A.34 into A.35 and rearranging terms yields the following expression:

$$V \left[s^3 + \left(\frac{1}{RC_p} + \frac{b_m b^{**}}{m} \right) s^2 + \left(\frac{k_{sp}}{m} \left(1 + \frac{d^2 Y_c}{\varepsilon} \right) + \frac{b_m b^{**}}{m RC_p} \right) s + \frac{k_{sp}}{m RC_p} \right] = -\frac{Y_c dt_c b^*}{\varepsilon} A_{in} \quad (\text{A.36})$$

The expression in equation A.36 can be solved for the output voltage. The resulting expression is perhaps more meaningful with the following substitutions: $d^2 Y_c / \varepsilon$ is the square of a term commonly referred to as the piezoelectric coupling coefficient denoted by the symbol k , the Laplace variable may be substituted with $j\omega$ where j is the imaginary

number, k_{sp}/m is the natural frequency of the system represented by the symbol ω_n , and the damping term $b_m b^{**}/m$ can be rewritten in terms of the unitless damping ratio ζ as $2\zeta\omega_n$. Making these substitutions and solving for V yields:

$$V = \frac{-j\omega \frac{Y_c dt_c b^*}{\varepsilon}}{\left[\frac{1}{RC_p} \omega_n^2 - \left(\frac{1}{RC_p} + 2\zeta\omega_n \right) \omega^2 \right] + j\omega \left[\omega_n^2 (1 + k^2) + \frac{2\zeta\omega_n}{RC_p} - \omega^2 \right]} A_{in} \quad (\text{A.37})$$

If the further simplifying assumption is made that the resonant frequency ω_n matches the driving frequency ω , equation A.37 reduces to:

$$V = \frac{-j \frac{Y_c dt_c b^*}{\varepsilon}}{2\zeta\omega^2 + j \left[\omega^2 k^2 + \frac{2\zeta\omega}{RC_p} \right]} A_{in} \quad (\text{A.38})$$

As mentioned earlier, the power transferred is simply V^2/R . Therefore, using the expression in equation A.38, the resulting analytical term for the magnitude of the power transferred to the load is as follows.

$$P = \frac{1}{\omega^2} \frac{RC_p^2 \left(\frac{Y_c dt_c b^*}{\varepsilon} \right)^2}{(4\zeta^2 + k^4)(RC_p \omega)^2 + 4\zeta k^2 (RC_p \omega) + 2\zeta^2} A_{in}^2 \quad (\text{A.39})$$

The optimal load resistance can then be found by differentiating equation A.38 with respect to R , setting the result equal to zero, and solving for R . The resulting optimal load resistance is shown in equation A.40.

$$R_{opt} = \frac{1}{\omega C_p} \frac{2\zeta}{\sqrt{4\zeta^2 + k^4}} \quad (\text{A.40})$$

An equivalent electrically induced damping ratio, ζ_e , can also be derived from the analytical system model. The electrical coupling term, $\frac{k_{sp}d}{mt_c}V$, in equation A.27 can be used to find the equivalent linear damping ratio. It written in terms of an electrically induced damping ratio, ζ_e , the electrical coupling term would have the following standard form:

$$\frac{k_{sp}d}{mt_c}V = 2\zeta_e\omega\dot{\delta} \quad (\text{A.41})$$

The damping ratio, ζ_e , can then be expressed as:

$$\zeta_e = \frac{k_{sp}d}{2mt_c\omega} \frac{V}{\dot{\delta}} \quad (\text{A.42})$$

An expression, in terms of the Laplace variable s , for the voltage to strain rate ratio follows from equation A.34, and is shown below.

$$\frac{V}{\Delta s} = -\frac{Y_c dt_c}{\varepsilon(s + \frac{1}{RC_p})} \quad (\text{A.43})$$

Note that the term Δs in equation A.43 is the same term as $\dot{\delta}$ in equation A.42. Substituting A.43 into A.42, and making the substitution $k^2 = d^2Y_c/\varepsilon$ as before, the resulting expression for the electrically induced damping ratio is:

$$\zeta_e = \frac{\omega k^2}{2\left(s + \frac{1}{RC_p}\right)} \quad (\text{A.44})$$

As seen from equation A.44, the damping ratio is a function of frequency and is not necessarily real. The magnitude of damping ratio is shown below in equation A.45, which is the same as shown in Chapter 4 as equation 4.11. It should finally be noted that

if the expression for the optimal load resistance shown in equation A.40 is substituted into equation A.44, the result is that the magnitude of the electrically induced damping ratio, ζ_e , in fact is equal to the mechanical damping ratio, ζ , as expected.

$$\zeta_e = \frac{\omega k^2}{2\sqrt{\omega^2 + \frac{1}{(RC_p)^2}}} \quad (\text{A.45})$$

A.4 Alterations to the basic dynamic model

Two alterations to the basic dynamic model are of interest. First, as discussed in Chapter 4, it is useful to build a dynamic model with a rectifier and storage capacitor as a load rather than a simple resistor. Second, as discussed in Chapter 6, as the generator becomes smaller, a pin-pin mounting, rather than a strict cantilever mounting, more accurately represents the physical operation of the generator.

The changes to the basic dynamic system equations that result from a rectifier and capacitive load are discussed in sufficient detail in Chapter 4 for the reader to be able to duplicate the derivation. The new system equations are given in Chapter 4 as equations 4.15 through 4.17. Furthermore, analytical expressions for the charge and energy transferred to the storage capacitor are derived in significant detail in Chapter 4 and shown as equations 4.19 and 4.20. However, the jump from the energy transferred per half cycle in equation 4.20 and the power conversion in equation 4.21 is significant and more detail needs to be provided here.

First, the expressions for charge and energy transferred are in terms of V_1 and V_2 , which represent the voltage across the storage capacitor at the beginning and end of the half cycle respectively. However, because the value of V_2 is an unknown at the beginning of the half cycle, it must be calculated or substitutions must be made to remove

V_2 from the analytical expressions. Reconsider the expression for charge transferred per half cycle given as equation 4.19 and repeated here as equation A.46.

$$\Delta Q = \int_{t_1}^{t_2} i dt = \int_{t_1}^{t_2} C_p \frac{d(V_s - V)}{dt} dt \quad (\text{A.46})$$

This expression can be simplified and rewritten as shown in equation A.47.

$$\Delta Q = C_p \int_{t_1}^{t_2} dV_s - C_p \int_{t_1}^{t_2} dV \quad (\text{A.47})$$

Remembering that the effective source voltage, V_s , as shown in Figure 4.16 and defined by equation 4.18, can be expressed as $V_s \sin(\omega t)$, equation A.47 can be integrated and rewritten as:

$$\Delta Q = C_p (V_s \sin(\omega t_2) - V_s \sin(\omega t_1) - V(t_2) + V(t_1)) \quad (\text{A.48})$$

As in Chapter 4, $V(t_2)$ and $V(t_1)$ will hereafter be referred to as V_2 and V_1 for simplicity. t_2 is the time at which the rectification diodes turn off at the end of the half cycle. This will always occur at the top of the sinusoid that defines the effective source voltage. In other words $V_s \sin(\omega t_2) = V_s$ for any half cycle. Also, as stated in Chapter 4, ΔQ is also equal to $C_{st}(V_2 - V_1)$. t_1 is the time at which the effective source voltage, V_s , is equal to the voltage across the storage capacitor, V . In other words, the time at which the rectification diodes begin to conduct (assuming ideal diodes). At any t_1 (that is the time at which $V_s = V$ for any half cycle), the voltage across the storage capacitor, V_1 , is equal to $V_s \sin(\omega t_1)$. Substituting these three equivalencies into equation A.48 yields the expression in equation A.49.

$$V_2 - V_1 = \frac{C_p}{C_{st}} (V_s - V_1 - V_2 + V_1) \quad (\text{A.49})$$

Equation A.49 can now be solved for V_2 , which results in the following expression:

$$V_2 = \frac{C_{st}V_1 + C_pV_s}{C_{st} + C_p} \quad (\text{A.50})$$

This expression can be used in a simple calculation to generate a voltage versus time curve. Initially V_1 is zero, C_{st} and C_p are constants, and V_s is predetermined by the magnitude of the input vibrations and the beam equations. V_2 can then be calculated for the half cycle. V_2 then becomes V_1 for the next half cycle.

The analytical expression for power transferred can now be derived. The expression for energy per half cycle developed in Chapter 4 is rewritten here as equation A.51.

$$\Delta E = \frac{1}{2}C_{st}(V_2^2 - V_1^2) \quad (\text{A.51})$$

Recall that the expression for power transferred is $P = 2f\Delta E$. Equation A.50 can be substituted into A.51 and the resulting expression for energy can be placed into the above equation for power. Rearranging terms, the resulting expression for power is shown in equation A.52, which is the same expression shown in Chapter 4 as equation 4.21.

$$P = \frac{\omega C_{st}}{2\pi(C_{st} + C_p)^2} \{C_p^2V_s^2 + 2C_{st}C_pV_sV_1 - C_pV_1^2(2C_{st} + C_p)\} \quad (\text{A.52})$$

The second alteration to the basic model of interest adjusts for the compliance of the cantilever mounting. For smaller generators, a pin-pin mounting model more accurately models the physical system. A schematic of this mounting is shown in Figure A.5.

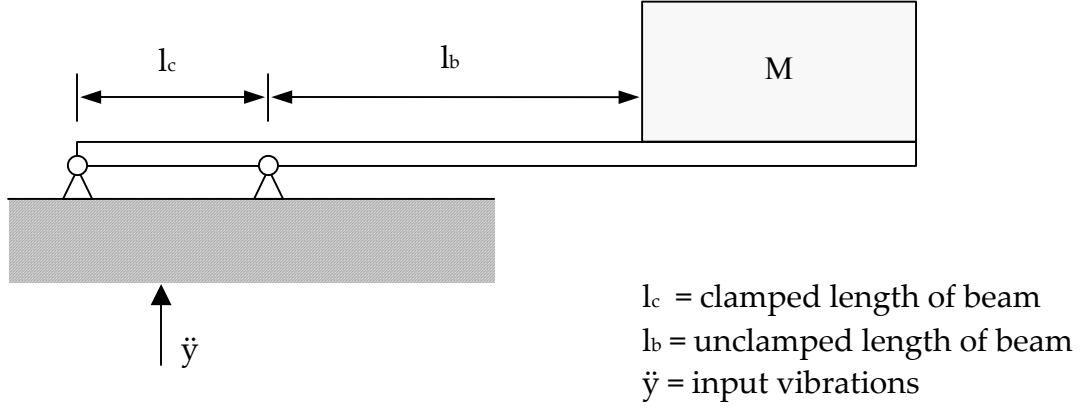


Figure A.5: Illustration of pin-pin mounting model for piezoelectric generator.

Dimensions and variables not shown in Figure A.5 are the same as shown in Figures A.1 and A.2. This adjusted mounting model does not affect the circuit representations shown in Figures A.3 and A.4, it only affects the geometric constants relating vertical force to average stress (b^{**}) and tip deflection to average strain (b^*). Therefore, only these two terms need to be re-derived. The dynamic models, as shown in equations A.30 and A.33, are unchanged, but the expressions defining b^* and b^{**} , and thus k_{sp} , are different.

In deriving an expression for the average stress in the piezoelectric material covered by the electrode, it will be assumed the length of the electrode is equal to the sum of the clamped length of the beam, l_c , and the unclamped length of the beam, l_b . The expression for the stress is then given by equation A.53.

$$\sigma = \frac{1}{l_c} \int_0^{l_c} \frac{M_1(x)b}{I} dx + \frac{1}{l_b} \int_{l_c}^{l_c+l_b} \frac{M_2(x)b}{I} dx \quad (\text{A.53})$$

where:

$M_1(x)$ is the moment function between the two pin mounts (0 and l_c).

$M_2(x)$ is the moment function between the right pin and the mass (l_c to l_b).

The functions for $M_1(x)$ and $M_2(x)$ are given in equations A.54 and A.55.

$$M_1(x) = m(\ddot{y} + \ddot{z}) \left(\frac{2l_b + l_m}{2l_c} \right) x \quad (\text{A.54})$$

$$M_2(x) = m(\ddot{y} + \ddot{z}) \left(x - a - l_b - \frac{l_m}{2} \right) \quad (\text{A.55})$$

Substituting equations A.54 and A.55 into equation A.53 yields:

$$\sigma = m(\ddot{y} + \ddot{z}) \frac{b}{4I} (4l_b + 3l_m) \quad (\text{A.56})$$

b^{**} , which relates vertical force to stress, can then be expressed as:

$$b^{**} = \frac{4I}{b(4l_b + 3l_m)} \quad (\text{A.57})$$

In considering the Euler beam equation, which will be used to derive the expression for b^* , let z_1 be the vertical deflection from $x = 0$ to l_c , and z_2 be the vertical deflection from $x = l_c$ to l_b . $M_1(x)$ then corresponds to z_1 , and $M_2(x)$ corresponds to z_2 . The Euler beam equation, as shown above in equation A.6 can be applied to each section of the beam. Substituting equations A.54 and A.55 into the two Euler beam equations, and integrating yields the expression in equation A.58 for the vertical deflection of the beam between $x = l_c$ and $x = l_c + l_b$. It should be noted that one of the boundary conditions for

z_2 is that $\frac{dz_2}{dx}(x = l_c) = \frac{dz_1}{dx}(x = l_c)$.

$$z_2 = \frac{m(\ddot{y} + \ddot{z})}{Y_c I} \left[x^2 \left(\frac{x}{6} - \frac{l_c}{2} - \frac{l_b}{2} - \frac{l_m}{4} \right) + l_c x \left(\frac{l_c}{2} + \frac{2l_b}{3} + \frac{l_m}{3} \right) - \frac{l_c^2}{12} (2l_c + 2l_b + l_m) \right] \quad (\text{A.58})$$

At the point where the mass attaches to the beam, at $x = l_c + l_b$, the expression for vertical deflection reduces to:

$$z = \frac{m(\ddot{y} + \ddot{z})l_b}{12Y_c I} (4l_b + 3l_m)(l_c + l_b) \quad (\text{A.59})$$

Strain can be expressed as $\delta = \sigma/Y$. Substituting the expression for stress from equation A.56 yields the following expression for strain.

$$\delta = m(\ddot{y} + \ddot{z}) \frac{b}{4Y_c I} (4l_b + 3l_m) \quad (\text{A.60})$$

Equation A.60 can be easily solved for the term $m(\ddot{y} + \ddot{z})$ and substituted into equation A.59. The resulting expression for vertical deflection is shown in equation A.61.

$$z = \frac{l_b}{3b} (l_c + l_b) \delta \quad (\text{A.61})$$

b^* , which relates strain to vertical displacement, or $z = \delta/b^*$, can then be expressed as:

$$b^* = \frac{3b}{l_b(l_c + l_b)} \quad (\text{A.62})$$

As previously, the effective spring constant, k_{sp} , is equal to Yb^*b^{**} . Substituting these new expressions for b^* and b^{**} into the models in equation A.30 and A.33 will yield a dynamic model incorporating a pin-pin mounting.

Appendix B, Analytical Model of In-plane Gap Closing Electrostatic Converter

Chapter 7 discussed the modeling and design of electrostatic converters. It was shown that the in-plane electrostatic converter was the topology best suited to the current application. A model was presented for all types of electrostatic converters, however the detailed derivation of the models was not presented in Chapter 7 in order to improve readability. The purpose of this appendix is to present the detailed derivation of the model for the in-plane gap closing converter. The derivation of the other two types of converters follow the exact same procedure outlined here. Additionally, an algorithm for simulation in Matlab is presented.

B.1 Derivation of electrical and geometric expressions

A schematic of the in-plane gap closing converter is shown here as Figure B.1. The simple conversion circuit used, shown previously as Figure 7.1, is repeated here as Figure B.2. The basis of conversion is the variable capacitor, C_v in Figure B.2. The capacitor is formed between the interdigitated combs shown in Figure B.1. The center shuttle moves left to right when excited by vibrations, changing the dielectric gap between the comb fingers, and thus changing the capacitance. For a more complete explanation of the process, see Chapter 7.

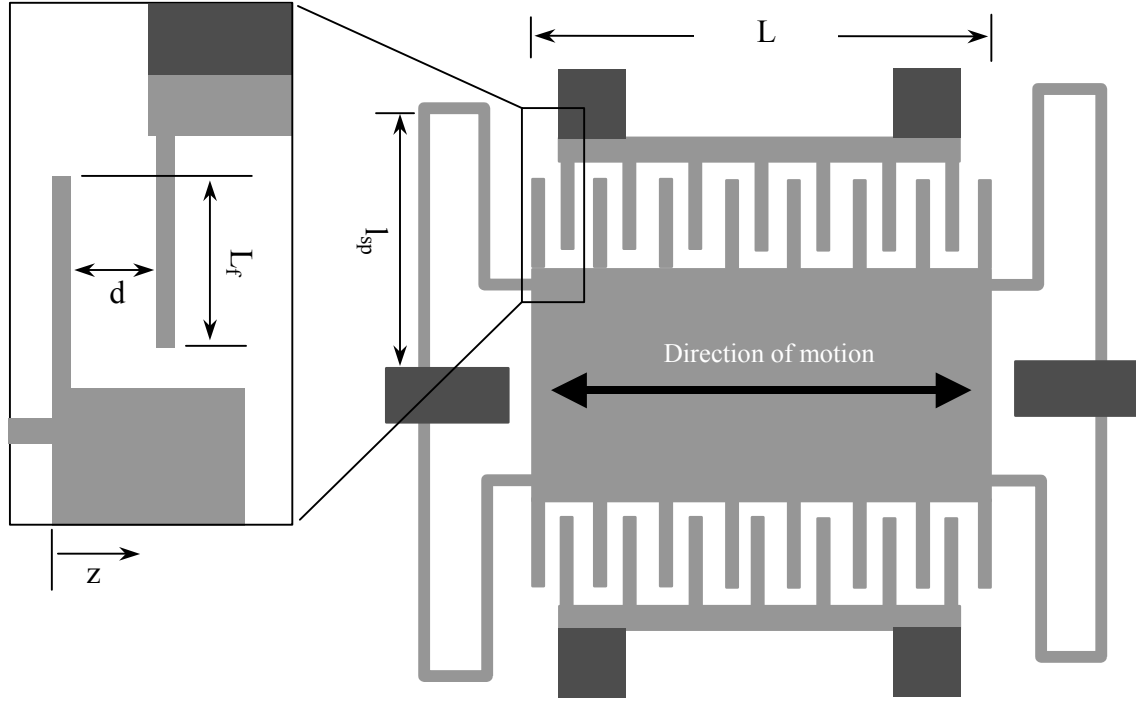


Figure B.1: Schematic of in-plane gap closing converter.

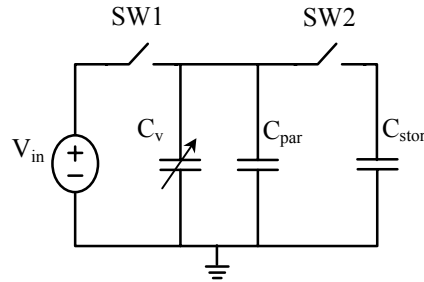


Figure B.2: Simple conversion circuit for electrostatic converters.

Let us first develop the expression for energy converted per cycle from the circuit in Figure B.2. The capacitor C_v is oscillating between a maximum value, C_{\max} , and a minimum value C_{\min} . When C_v is at C_{\max} , SW1 is closed so that the voltage, V , across C_v is V_{in} . The charge, Q , on C_v at this point is $Q = (C_{\max} + C_{\text{par}})V_{\text{in}}$ where C_{par} is a parasitic capacitance. As the center shuttle moves from the maximum capacitance position to the minimum capacitance position, both switches are open, so the charge on C_v is constant.

Therefore, at the minimum capacitance position $Q = (C_{\min} + C_{\text{par}})V_{\max}$ where V_{\max} is the voltage at that position. These expressions are summarized in equation B.1.

$$Q = (C_{\max} + C_{\text{par}})V_{\text{in}} = (C_{\min} + C_{\text{par}})V_{\max} \quad (\text{B.1})$$

Solving for V_{\max} yields:

$$V_{\max} = \frac{C_{\max} + C_{\text{par}}}{C_{\min} + C_{\text{par}}} V_{\text{in}} \quad (\text{B.2})$$

The energy stored in the variable and parasitic capacitors is greater at C_{\min} than at C_{\max} because mechanical work was done to move the C_v from the maximum to minimum position increasing the total energy stored in the capacitor. So, the energy gain per cycle is given by equation B.3.

$$E = \frac{1}{2}(C_{\min} + C_{\text{par}})V_{\max}^2 - \frac{1}{2}(C_{\max} + C_{\text{par}})V_{\text{in}}^2 \quad (\text{B.3})$$

Substituting equation B.2 in to B.3 yields:

$$E = \frac{1}{2}(C_{\min} + C_{\text{par}}) \left(\frac{C_{\max} + C_{\text{par}}}{C_{\min} + C_{\text{par}}} \right)^2 V_{\text{in}}^2 - \frac{1}{2}(C_{\max} + C_{\text{par}})V_{\text{in}}^2 \quad (\text{B.4})$$

Equation B.4 can be algebraically manipulated to yield the following expression:

$$E = \frac{1}{2}V_{\text{in}}^2 (C_{\max} + C_{\text{par}}) \left(\frac{C_{\max} + C_{\text{par}}}{C_{\min} + C_{\text{par}}} - 1 \right) \quad (\text{B.5})$$

Equation B.5 can be further reduced to yield the expression in equation B.6a, which is the same expression presented as equation 7.1a.

$$E = \frac{1}{2}V_{\text{in}}^2 (C_{\max} + C_{\text{par}}) \left(\frac{C_{\max} + C_{\min}}{C_{\min} + C_{\text{par}}} \right) \quad (\text{B.6a})$$

If V_{\max} is an important parameter because of a particular switch implementation, equation B.6a can be rewritten as equation B.6b by substitution of the expression in equation B.2. Equation B.6b is the same equation presented previously as equation 7.1b.

$$E = \frac{1}{2} V_{\max} V_{in} (C_{\max} - C_{\min}) \quad (\text{B.6b})$$

The capacitance of a structure is given by $C = \epsilon_0 A/d$ where ϵ_0 is the dielectric constant of free space, A is the overlap area of the electrodes, and d is the distance between the electrodes. The capacitance of the structure, C_v , shown in Figure B.1 is then given by equation B.7.

$$C_v = N_g \epsilon_0 L_f h \left(\frac{1}{d-z} + \frac{1}{d+z} \right) \quad (\text{B.7})$$

where:

- N_g is the number of dielectric gaps per side of the device.
- ϵ_0 is the dielectric constant of free space.
- L_f is the overlapping length of the fingers as shown in Figure B.1.
- h is the thickness of the device
- d is the nominal gap between fingers as shown in Figure B.1.
- z is the deflection of the springs as shown in Figure B.1.

Equation B.7 can be algebraically reduced to the equation for capacitance presented in Chapter 7 as equation 7.14 and shown here as equation B.8.

$$C_v = N_g \epsilon_0 L_f h \left(\frac{2d}{d^2 - z^2} \right) \quad (\text{B.8})$$

The minimum capacitance occurs at the nominal position where z equals zero. Setting z equal to zero in equation B.8 yields:

$$C_{\min} = \frac{2N_g \epsilon_0 L_f h}{d} \quad (\text{B.9})$$

If it is assumed that mechanical stops are implemented to limit the structure to a maximum displacement of z_{\max} , where z_{\max} is less than d , the minimum dielectric gap is $d - z_{\max}$. The maximum capacitance can then be written as:

$$C_{\max} = N_g \epsilon_0 L_f h \left(\frac{2d}{d^2 - z_{\max}^2} \right) \quad (\text{B.10})$$

B.2 Derivation of mechanical dynamics and electrostatic forces

A quick estimate of power generated can be derived from equations B.6a, B.9, and B.10. Note that power for this device is given by $P = 2fE$ where f is the driving frequency of the vibrations. The factor of 2 comes from the fact that the structure undergoes two electrical cycles for each mechanical cycle. Therefore power can be estimated purely from geometric design parameters, physical constants, and the input voltage. This method of estimating power was used to generate the data shown in Chapter 7 as Figure 7.4. However, there is a large assumption underlying this analysis. It is assumed that the driving vibrations do actually drive the center shuttle of the structure hard enough to physically reach the mechanical stops under the specified conditions (i.e. input voltage, nominal dielectric gap, etc.). A full and accurate analysis needs to include the mechanical dynamics of the system so that if the fluid damping and electrostatic forces are such that the shuttle mass does not reach the mechanical stops this will come out in the analysis and simulation.

Consider the general coupled dynamic equation of a general oscillating mass system given in Chapter 7 as equation 7.2 and repeated here as equation B.11.

$$m\ddot{z} + f_e() + f_m() + kz = -m\ddot{y} \quad (\text{B.11})$$

where:

m is the mass of the oscillating capacitive structure
 k is the stiffness of the flexures on the capacitive structure
 z is the displacement of the capacitive structure
 y is the input vibration signal
 $f_e()$ represents the electrically induced damping force function
 $f_m()$ represents the mechanical damping force function

The mass, m , is simply the mass of the center shuttle and any additional mass attached to the center mass. There is a folded flexure at each corner of the center shuttle. Each element of the folded flexure can be treated as a fixed – fixed beam. The effective spring constant for a fixed – fixed beam is given by equation B.12.

$$k_{fixed-fixed} = \frac{12YI}{l_{sp}^3} \quad (\text{B.12})$$

where:

Y is the elastic constant, or Young's modulus.

I is the moment of inertia of the beam.

l_{sp} is the length of the fixed-fixed beam, see Figure B.1.

The folded flexure element can be treated as two springs in series each with an effective spring constant of the fixed-fixed beam. Thus the stiffness of one flexure is half that of the fixed-fixed beam. Note that the two beams that make up the flexure appear to be quite different lengths in Figure B.1, however, the figure is not to scale and in reality the two beams are almost exactly the same length. Four folded flexures act in parallel on the center shuttle. Therefore, the aggregate spring constant, the k term in equation B.11, is four times the spring constant of a single folded flexure or 2 times the spring constant of a fixed-fixed beam. The expression for the aggregate spring constant then becomes:

$$k = \frac{24YI}{l_{sp}^3} \quad (\text{B.13})$$

Derivation of the expressions for the electrostatic force, $f_e()$, and mechanical damping force, $f_m()$, require a little more work. First consider the mechanical damping

force, $f_m()$. The dominant damping mechanism is fluid damping. The shear force of the fluid, air in this case, between two flat surfaces moving in parallel is usually referred to as Couette damping. In this case, Couette damping acts between the large center shuttle and the substrate beneath it. The expression for the force exerted on the shuttle mass is given by equation B.14.

$$F_{coute} = \frac{\mu A}{d_0} \dot{z} \quad (\text{B.14})$$

where:

μ is the viscosity of air (18 microPascal seconds)

A is the area of the of the center shuttle.

d_0 is the distance between the center shuttle and the substrate beneath it.

A second fluid damping mechanism is also active. As comb fingers move closer together, the air between them is compressed and exerts a force opposing the motion. This damping force is usually referred to as squeeze-film damping. The general expression for the force exerted on a rectangular plate moving toward or away from another plate is given by:

$$F_{fluid} = \frac{16\mu lw^3}{x^3} \dot{x} \quad (\text{B.15})$$

where:

l is the length of the rectangular plate.

w is the width of the rectangular plate.

x is the distance between the plates.

Applying equation B.15 to the in-plane gap closing converter yields the following expression for the squeeze film damping force.

$$F_{squeeze-film} = 16N_g \mu L_f h^3 \left(\frac{1}{(d-z)^3} + \frac{1}{(d+z)^3} \right) \dot{z} \quad (\text{B.16})$$

The total damping force is just $f_m() = F_{\text{coette}} + F_{\text{squeeze-film}}$, given in equation B.17, which is the same expression presented in Chapter 7 as equation 7.13.

$$f_m() = \left(\frac{\mu A}{d_0} + 16N_g \mu L_f h^3 \left(\frac{1}{(d-z)^3} + \frac{1}{(d+z)^3} \right) \right) \dot{z} \quad (\text{B.17})$$

Next consider the electrostatic force $f_e()$. The electrostatic force on a body as a function of position is given by:

$$F = - \left(\frac{\partial U}{\partial x} \right) \quad (\text{B.18})$$

where:

U is the electrostatic energy stored.

x is a general displacement variable.

The energy stored in a capacitive device is given by:

$$U = \frac{1}{2} C V^2 = \frac{Q^2}{2C} \quad (\text{B.19})$$

Either form of equation B.19 can be used with equation B.18. However, it is generally better to use the expression that will simplify the mathematics as much as possible. In this case, the charge, Q, is held constant and so is not a function of displacement whereas V is a function of displacement. Therefore, the second form of equation B.19 will be used. The energy term for the in-plane gap closing converter, using the capacitance expression in equation B.8, is as follows:

$$U = \frac{Q^2 (d^2 - z^2)}{4N_g \epsilon_0 L_f h d} \quad (\text{B.20})$$

Applying equation B.20 to equation B.18 using z as the displacement variable yields:

$$f_e() = \frac{Q^2 z}{2N_g d \epsilon_0 L_f h} \quad (\text{B.21})$$

Equation B.21 is the same expression presented as equation 7.15 in chapter 7.

B.3 Simulation of the in-plane gap closing converter

All of the equations necessary to simulate the system have now been derived. The model of the system is comprised of equations B.6a, B.9, B.10, B.11, B.13, B.17 and B.21. Making substitutions, these seven equations can be written as the following two coupled equations.

$$m\ddot{z} + \frac{Q^2}{2N_g d \epsilon_0 L_f h} z + \left(\frac{\mu A}{d_0} + 16N_g \mu L_f h^3 \left(\frac{1}{(d-z)^3} + \frac{1}{(d+z)^3} \right) \right) \dot{z} + \frac{24YI}{l_{sp}^3} z = -m\ddot{y} \quad (\text{B.22})$$

$$E = V_{in}^2 \left(N_g \epsilon_0 L_f h \left(\frac{2d}{d^2 - z_{\max}^2} \right) + C_{par} \right) \left(\frac{2d^2 - z_{\max}^2}{d^2 - z_{\max}^2} \right) \left(\frac{N_g \epsilon_0 L_f h}{C_{par} d + N_g \epsilon_0 L_f h} \right) \quad (\text{B.23})$$

Simulation of this system is not quite as straight forward as simulation of the piezoelectric converter. There are two effects that contribute to this difficulty. The first is that at certain times the switches close, instantaneously (at least compared to the mechanical system) changing some of the values that are considered to be constant for purposes of the mechanical simulation, such as the charge Q . The second is the impact of the center shuttle mass with the mechanical stops. This impact is modeled as a purely elastic impact with a coefficient of restitution of 0.5 (Lee and Pisano 1993). The Matlab differential equation solvers cannot model and solve these two effects. The following is the outline of the procedure that was used to simulate the system in Matlab.

First, the geometric dimensions, physical constants, and initial conditions are specified. A differential equation solver is then used to solve equation B.22. The Matlab function ‘ode23s’ seems to work the best. The dynamic simulation of equation B.22

needs to be stopped so that switch 1 can be closed if $C_v = C_{\max}$ and so that switch 2 can be closed if $C_v = C_{\min}$. Note that ideal switches are assumed for simulation purposes. The Matlab differential equation solvers can monitor the state variables and simple functions of the state variables for zero crossings (that is where a state variable or function of that variable crosses zero), and terminate the solver if at zero crossings. The case where $C_v = C_{\max}$ occurs when \dot{z} is zero or when the center mass hits the mechanical stops ($|z| - z_{\max_allowed} = 0$). The case where $C_v = C_{\min}$ occurs when the displacement z equals zero (i.e. the center mass is in the center position). When any of these three conditions occur, the differential equation solver stops, circuit calculations are made and stored, and the solver is restarted using the current state values and time as the initial conditions. The following list outlines specifically what is done when each of the three conditions occurs.

- Condition: $\dot{z} = 0$. C_v is at C_{\max} . Close switch 1.
 - For each time step returned by the solver (that is all time values since the last solver last stopped), calculate electrical circuit values.
 - Calculate C_v using equation B.7.
 - Both switches have been open, so Q is constant.
 - Calculate voltage on C_v as $V = Q / (C_v + C_{\text{par}})$.
 - Close switch 1 and calculate new (current) circuit values.
 - $V = V_{\text{in}}$.
 - More charge is put on variable capacitor. Re-calculate current charge as $Q = (C_v + C_{\text{par}})V_{\text{in}}$. Note the current value of C_v is C_{\max} .

- Calculate the amount of charge put in, Q_{in} , as Q minus the charge that was left on the capacitor just before the charge was re-calculated.
 - Append state variables returned by the solver and circuit values to the end of a persistent storage matrix.
 - Set initial conditions to the current state values and restart differential equation solver.
- Condition: $|z| - z_{max_allowed} = 0$. Center shuttle hit the mechanical stops. C_v is at C_{max} . Close switch 1.
 - Procedures are exactly the same as those listed above except that a new value for velocity, $\dot{z}_{new} = -0.5\dot{z}_{old}$, needs to be set as the initial condition before the solver restarts. In this way the effect of the impact is included.
- Condition: $z = 0$. C_v is at C_{min} . Close switch 2.
 - For each time step returned by the solver, calculate electrical circuit values as detailed above.
 - Close switch 2 and calculate new (current) circuit values.
 - When switch 2 closes the voltage across the variable capacitor is shorted with the output voltage. Calculate new voltages as $V = V_{stor} = (Q + Q_{stor}) / (C_v + C_{par} + C_{stor})$.
 - Calculate new value for charge on output capacitor as $Q_{stor} = C_{stor}V_{stor}$.

- Calculate amount of charge left on variable capacitor as $Q = (C_v + C_{\text{par}})V$.
- Append state variables returned by the solver and circuit values to the end of a persistent storage matrix.
- Set initial conditions to the current state values and restart differential equation solver.

After the sequence outlined above has been run for a predetermined amount of time or number of iterations, the energy gained versus time can then be calculated as the increased energy on the storage capacitor minus the amount of energy put onto the variable capacitor. This simulation can, and has, been used as the objective function for an optimization algorithm to determine design parameters such as length of fingers, nominal gap, size of center shuttle, etc. After a number of simulation iterations it will become clear that the best designs are ones in which the center shuttle mass just barely reaches the mechanical stops. If the electrostatic forces are too high, and the center shuttle does not come very close to reaching the stops, the maximum capacitance will not be as high as it could, and the resulting energy gain per cycle is not very high. If the electrostatic forces are too low the center mass will ram into mechanical stops. This is not ideal because energy is dissipated in the impact, and because higher electrostatic forces would result in more work going into the conversion of mechanical kinetic energy to electrostatic energy. Thus, the best designs are ones in which the target vibrations drive the center shuttle just hard enough to barely reach the mechanical stops.

Appendix C, Development of Solar Powered Wireless Sensor Nodes

As explained in Chapter 1, a solar cell based power system was also developed and implemented as a means of powering wireless sensor nodes. Because solar powered systems have been profitably implemented many times in the past, the primary focus of this thesis has been on the development of vibration based power systems. For this reason, the development of the solar cell based power system was discussed only very briefly in the main body of this thesis. The purpose of this appendix is to give some of the details of the solar based power systems developed to serve as a comparison to the vibration based power systems and for the reference of future researchers in this area.

C.1 Photovoltaic cell technologies

Several solar cell technologies are commercially available. They are quite similar and operate on the same basic principle, but have different characteristics and strengths. A few of the most common will be discussed here in order to understand why the particular solar cell chosen for this development project was selected. The reader is referred to the recent thesis by J. Randall (Randall 2003) for a more complete discussion of the photovoltaic effect and photovoltaic cell technologies. Many of the numbers and considerations reported here are taken from J. Randall's thesis.

Single crystal silicon (SCS) solar cells represent perhaps the highest efficiency photovoltaic technology for outdoor use that is commercially available for a reasonable price. Efficiencies range from about 15% for inexpensive commonly available cells to

over 20% (Lee 2001) for high-end research cells. SCS cells are often used in outdoor applications, but are less suitable for indoor applications. The first reason is that the spectral response of SCS cells matches that of outdoor light far better than indoor light. This causes the open circuit voltage to fall off more than with other solar cell technologies at low indoor light levels. Therefore, their efficiency is significantly lower in indoor light. A second reason that SCS cells are almost never used in indoor applications is that connecting multiple cells in series in a small area is more difficult and expensive with SCS cells than with thin film cells. Indoor applications tend to favor smaller and cheaper solar cell arrays when compared to typical outdoor applications. Finally, SCS cells are more expensive than their thin film counterparts.

Commercially available thin film polycrystalline silicon solar cells are capable of efficiencies in the range of 10% to 13% (Nijs *et al* 2001). Thin film amorphous silicon solar cells exhibit efficiencies in the range of 6% to 8%. Any thin film solar cells have the advantage that it is easier and more cost effective to connect multiple cells in series, which is almost always necessary as the open circuit voltage from a single cell is typically on 0.6 to 0.7 volts. While amorphous silicon solar cells have the lowest efficiency, they are also the least expensive to produce, and they have the further advantage that their spectral response more closely matches that of fluorescent indoor lighting, which means that their open circuit voltage is maintained better at low indoor light levels. Recently amorphous silicon solar cells on a flexible polymer substrate have become commercially available (Iowa Thin Film Technologies 2003). These offer another potential benefit where the application could make use of flexible solar cells.

Thin film polycrystalline Cadmium Telluride (CdTe) solar cell modules are also commonly available. CdTe cells have a very broad spectral response making them useful in both indoor and outdoor applications. Their efficiency range is similar to polycrystalline silicon, about 8 – 13 %. While CdTe cells are inexpensive to manufacture and exhibit relatively good efficiencies in both indoor and outdoor environments, they do contain cadmium, which is a toxic. However, it is unlikely that the small amounts of cadmium in CdTe cells offer a significant health risk (Randall 2003).

Many other photovoltaic cell technologies exist including gallium arsenide (GaAs), gallium indium phosphide (GaInP), indium phosphide (InP), titanium dioxide (TiO₂) impregnated with a photosensitive dye, and organic photovoltaics. However, these technologies are all either in the research stage, prohibitively expensive for general use, or generally not available to the public, and so have not been considered in the development project.

The decision was made to adopt a CdTe thin film solar cell for two reasons. First, it was desired to use the system indoors, and CdTe cells perform better indoors than SCS cells. Second, it is much easier to find commercially available solar cell arrays of the needed size and voltage. It is very difficult to find small arrays of SCS cells of the appropriate voltage and size. It would have therefore been necessary to have the solar cell arrays custom manufactured if SCS cells had been selected. Finally, CdTe thin film cells are relatively inexpensive, which is a significant consideration in the context of wireless sensor nodes. The specific cell chosen is a thin film solar array on a glass substrate manufactured by Panasonic (part number BP-243318). The cell measures 2.5

cm X 3.2 cm and is 0.75 mm thick. The array consists of 5 individual cells wired in series for an open circuit voltage of 3.0 volts. A photograph of the cells is shown in Figure C.1.



Figure C.1: Panasonic (BP-243318) solar cell chosen for the solar power train.

C.2 Solar Power Circuits

A solar power circuit has three primary components: a solar cell, an energy storage reservoir, and component to condition the voltage (a voltage regulator). There are two common types of energy storage reservoirs: rechargeable batteries and capacitors. Solar implementations have been developed for both types of energy reservoirs.

The advantages of using batteries are that they have higher energy density and a more stable operating voltage. The disadvantages are that they have a limited lifetime of only a few years and operate better with a more controlled charge-up profile that requires additional battery charging circuitry. Capacitors, on the other hand, have an almost limitless lifetime and do not require any specific charge-up profile.

A second decision is to be made regarding the type of voltage regulator. A linear dropout regulator, such as the TPS72501 from Texas Instruments, is the simplest type. The output voltage of linear dropout regulators is controlled by dissipating power in a

pass transistor, the effective resistance of which is carefully controlled. So, if the input is 3 volts, and the desired output is 2 volts, a third of the total energy is simply being dissipated in a resistive device. Therefore, their efficiency depends on the input to output voltage ratio and is typically lower than DC-DC switching converters. However, they are simple, small, and require very few external components. DC-DC switching converters (also called switching regulators) operate on a different principle. Rather than dissipating energy in a pass transistor, they regulate the output by quickly switching on and off a shunt element between the input and output. The average value of the output is controlled by the duty cycle of the switching, and the output voltage is smoothed to a constant value with a large inductor. See Kassakian *et al* for a more complete description of DC-DC switching converters (Kassakian *et al*, 1991). DC-DC converters typically exhibit much better overall efficiency than linear dropout regulators, however they are far more complex and require more external passive components.

Two different solutions were pursued. The first incorporated a rechargeable battery and DC-DC switching converter. The second incorporated a capacitor and linear dropout regulator. The second is less complex and smaller, but also less efficient.

A circuit diagram for the solar / battery power train is shown in Figure C.2. The operation of the circuit is straightforward. The solar cell directly charges the battery through diode D1. The DC-DC converter converts the battery voltage to the output voltage, 1.2 volts in this case. A rechargeable lithium coin battery from Panasonic (ML2020) was used in this case. The battery has a nominal operating voltage of 2.5 volts. A Texas Instruments DC-DC converter (TPS62200) was used.

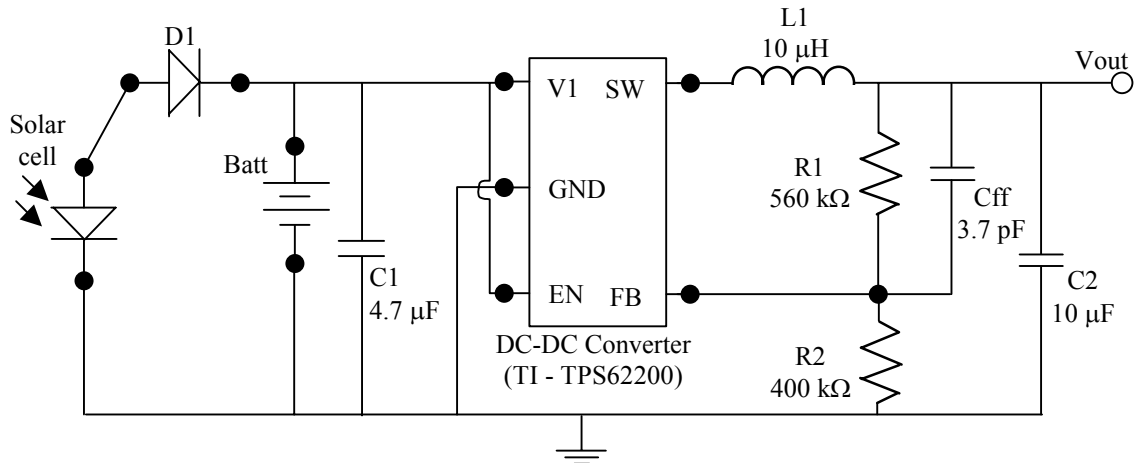


Figure C.2: Power circuit for the solar / battery power train.

One disadvantage of this circuit is that there is no charging control of the battery. Therefore, the battery lifetime will likely be shorter than it would be if a battery charging chip were included in the circuit to control the charge profile. However, such chips dissipate additional energy, and in an extremely low power application such as this, it was felt that minimization of power was more important than maximization of battery life. Likewise, there is no active control of the operating voltage of the solar cell. The operating voltage of the solar cell will simply be set by the battery voltage. Figure C.3 shows the current and power versus operating voltage of the Panasonic solar cell shown in Figure C.1 under a desktop lamp. The optimal operating point is between 2.25 and 2.5 volts. The battery and solar cell for this design were specifically chosen so that the average battery voltage is near the optimal operating voltage of the solar cell. Therefore, little is lost by not more actively controlling the operating voltage of the solar cell. It should be noted that while changing the intensity of the light source has a large effect on short circuit current of a solar cell, it has little affect on the open circuit voltage. So, even under varying light conditions, the optimal operating voltage does not change much. (Note that for single crystal silicon solar cells under low indoor conditions the open

circuit voltage does significantly drop.) If, however, a battery is used that does not match the optimal operating voltage of the solar cell well, additional circuitry can be added to allow better power transfer from the solar cell.

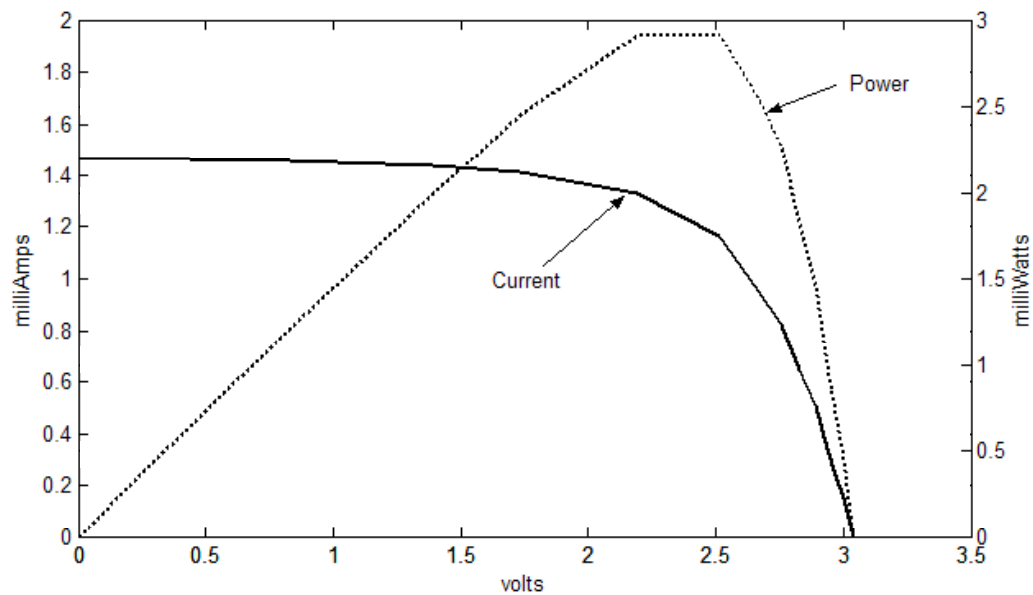


Figure C.3: Current and Power vs. Voltage for Panasonic solar cell under a lamp.

A circuit diagram for the solar / capacitor power train is shown in Figure C.2. The operation of this circuit is not quite as straightforward. The storage capacitor, C1 in Figure C.4, functions as a small energy reservoir. When the capacitor charges to a pre-specified voltage level, the supply rails to the RF circuitry are activated and the energy stored in the capacitor is consumed. Because the radio dissipates power faster than the solar cell produces it, the voltage across the storage capacitor falls when the radio is on. Once the energy is depleted and the voltage has fallen to a pre-specified low level, the supply rails are disabled and the capacitor is recharged. The high and low voltage thresholds are established by the Maxim IC (MAX6433) labeled as U2 in the figure, and the bias resistors R1, R2, and R3. Also note that the minimum period set by the Maxim IC is about 225 mSec. Therefore, if the capacitor is discharged and recharged faster than

this, the circuit waits for 225 mSec to pass before activating the voltage regulator and RF circuitry. A linear dropout regulator from Texas Instruments (TPS72051DT), labeled as U3, is used to control the output voltage to the desired 1.2 volts. In this case, the operating voltage of the solar cell is set by the voltage across capacitor C1. This voltage is controlled within a narrow range of about 1.8 to 1.9 volts by the Maxim comparator chip, U2.

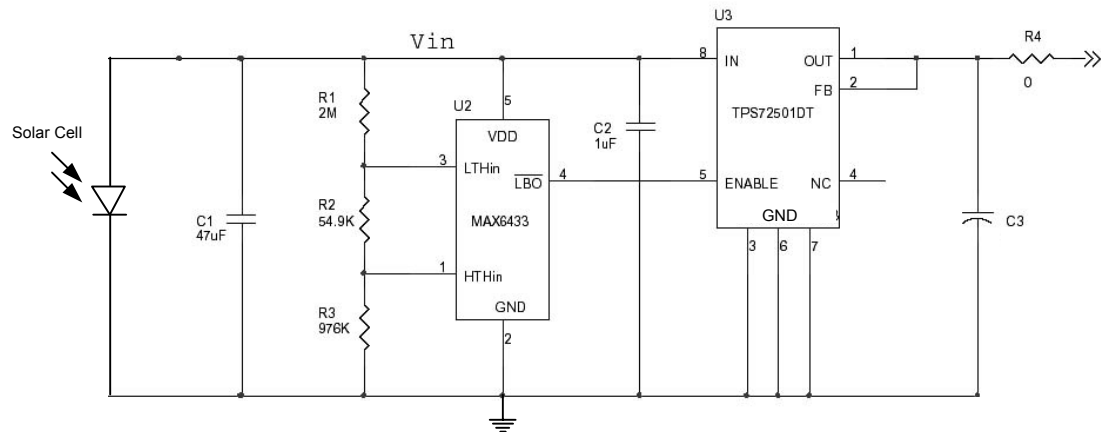


Figure C.4: Power circuit for the solar / battery power train.

C.3 Solar Power Train Results

The Panasonic solar cell has been tested in indoor environments without any power circuitry to determine its performance in low light conditions. The data from one such test are shown above in Figure C.3. Figure C.5 shows the I-V curves for four different indoor lighting conditions. A common desk lamp with a 60 watt incandescent bulb was used as a light source except in the ambient office lighting case. Table C.1 shows the maximum power, open circuit voltage, and closed circuit current from the same four light conditions. The Panasonic solar cell used is approximately 6 cm² in area.

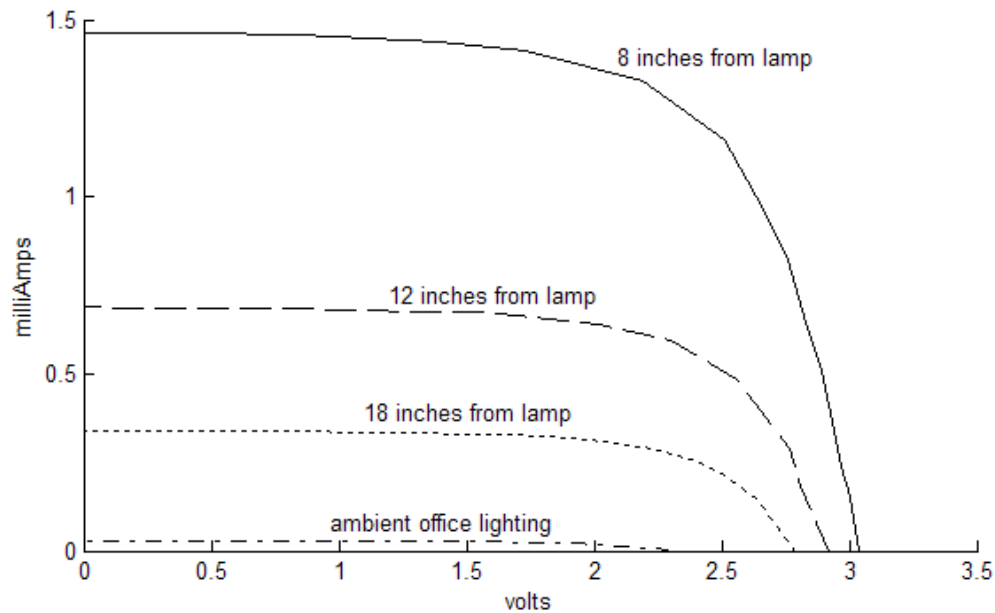


Figure C.5: I-V curves from Panasonic solar cell under 4 different light conditions.

	Max power	Open circuit voltage	Closed circuit current
8 inches from lamp	2.9 mW	3.04 V	1.46 mA
12 inches from lamp	1.4 mW	2.92 V	0.69 mA
18 inches from lamp	0.65 mW	2.79 V	0.34 mA
Ambient office light	0.042 mW	2.30 V	0.028 mA

Table C.1: Power, open circuit voltage, and closed circuit current from Panasonic solar cell under 4 different light conditions.

The solar power train incorporating a rechargeable battery and DC-DC converter as shown in Figure C.2 was implemented and tested. A photograph of the circuitry implementation is shown in Figure C.6. Two solar cells were used in parallel in this implementation in order to charge the battery up more quickly. The load connected to the output of the system was the low power radio designed by Otis and Rabaey (Otis and Rabaey 2002) described in Chapter 5. Useful test data from this system is difficult to measure. During operation the radio is continuously on and draws power from the battery. If the solar cell is providing more power than is used by the radio and power

circuitry, the battery slowly charges. Otherwise, it slowly discharges. However, because the charge and discharge curve is so flat (the voltage is constant), it is difficult to see this affect. Also, because the amount of energy that can be stored in the battery is quite large (45 mAh), the radio can operate for hours with no light at all. Figure C.7 shows the charging curve of the battery with the radio off and the two solar cells eight inches under the same desk lamp used previously. Three hours of charge time are shown here. Approximately eighteen hours of charge time are required to completely charge the battery. Figure C.8 shows the frequency spectrum of the radio signal being generated demonstrating the correct operation of the power system.

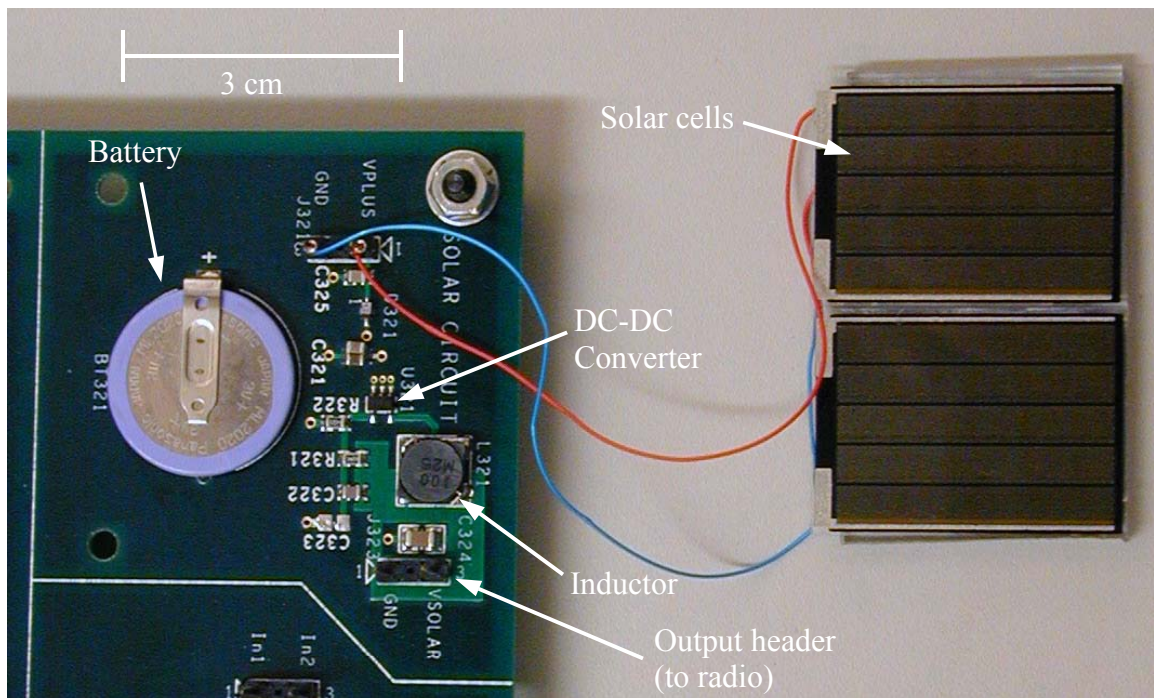


Figure C.6: Solar cells and power circuitry for solar / battery implementation.

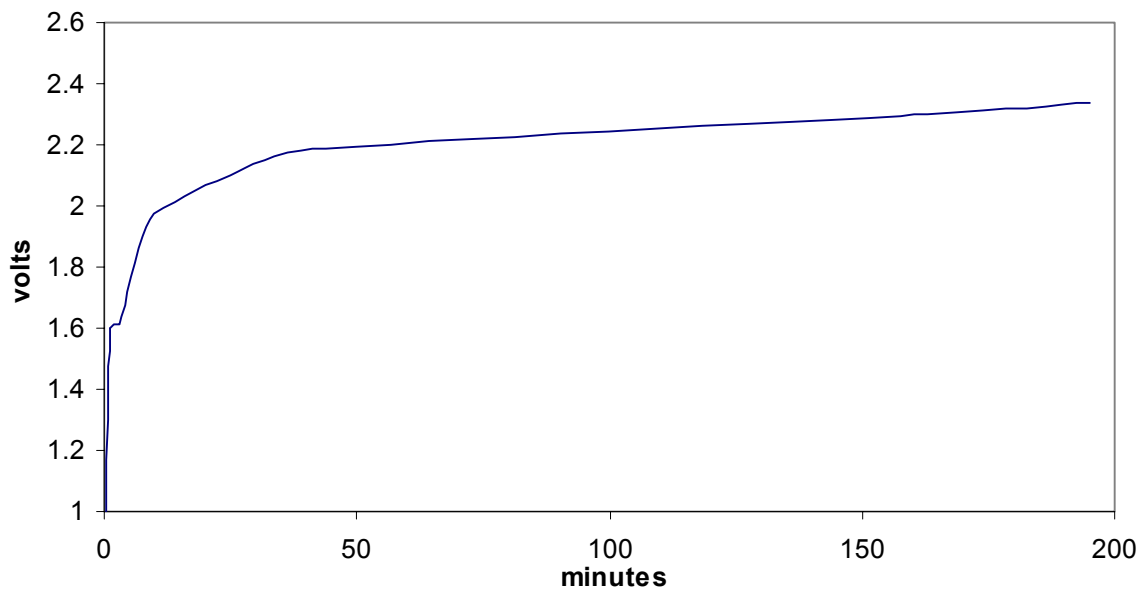


Figure C.7: Battery charge profile. Battery is being charged by 2 Panasonic solar cells in parallel.

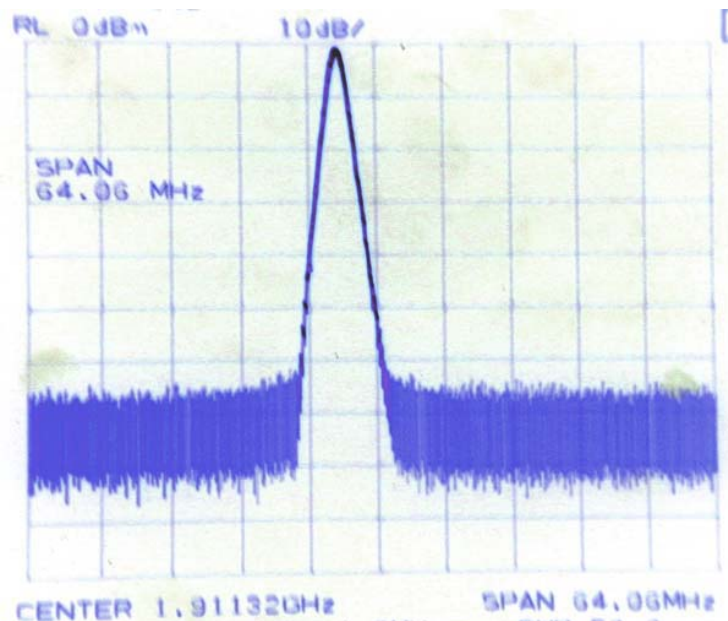


Figure C.8: Frequency spectrum of radio signal sent out antennae.

The solar power train shown above in Figure C.4, incorporating a capacitor as an energy reservoir and a linear dropout regulator, was also implemented and tested. Figure C.9 contains photographs of this implementation. Notice that the solar cell and circuitry are attached to opposite sides of the same printed circuit board. Because the energy

reservoir is smaller in this case, the radio can only turn on for short periods of time. Furthermore, the energy state of the reservoir is more clearly related to the voltage across the reservoir (capacitor). Therefore, it is a little easier to measure interesting characteristics of the circuit. Figure C.10 shows measured output for two different lighting conditions. Three traces are shown. The top trace is the voltage across the storage capacitor (or input voltage), the middle trace is the transmitted voltage signal, and the bottom trace is the voltage output of the linear regulator. The left graph shows operation under ambient office lighting. When the input reaches the specified input voltage of 1.9 volts, the regulator and radio transmitter turn on. When the voltage across the input capacitor drops to the pre-specified 1.8 volts, the regulator shuts back off and the input voltage begins to climb again. The time scale shown in the left figure is short, and so it appears that the capacitor voltage is not climbing, but it is climbing very slowly. The supportable duty cycle under these conditions is 0.36%. The right graph shows operation under a much more intense indoor light source. Again, when the regulator turns on, the capacitor voltage falls. When the input voltage reaches 1.8 volts, the regulator turns off and the capacitor recharges. In this case, the capacitor recharges quickly. However, there is an internally set minimum period of 225 milliseconds, so when the capacitor is charged back up, the circuit waits for this period to pass before turning the regulator back on. Under these conditions, the radio operates at a duty cycle of 11%.

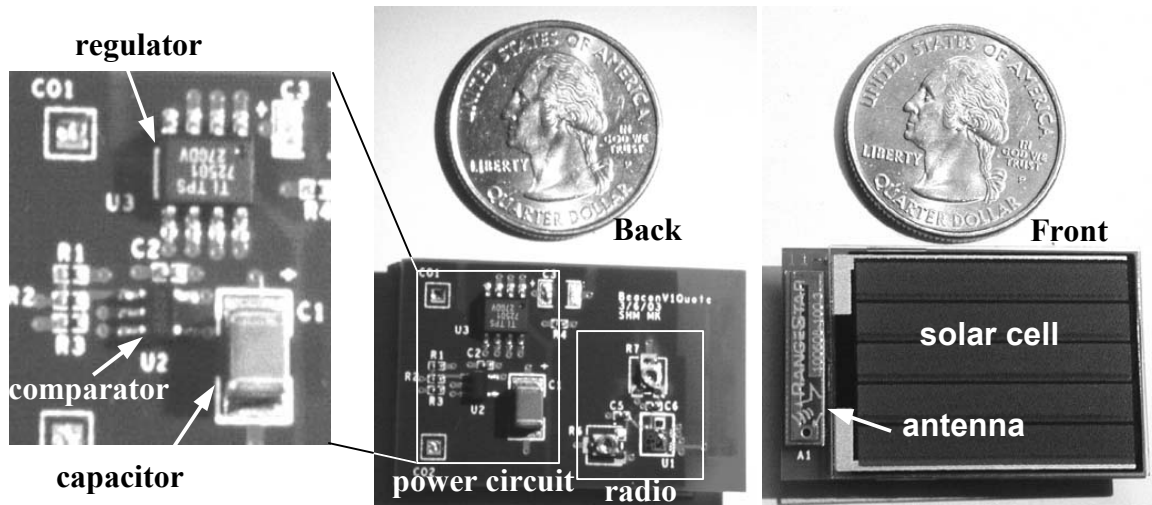


Figure C.9: Photographs of the solar / capacitor implementation.

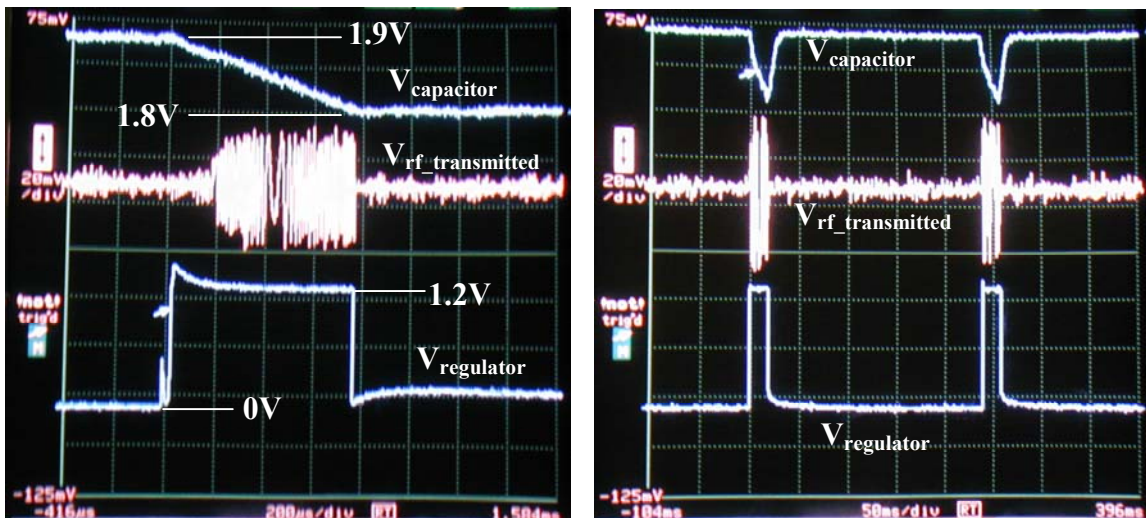


Figure C.10: Test data from solar / capacitor implementation. Three traces are shown: the voltage across the storage capacitor, the voltage signal transmitted, and the output voltage of the linear regulator. The left graph shows operation under ambient light which supports a duty cycle of 0.36% and the right graph shows operation under high indoor light conditions which supports a duty cycle of 11%.

C.4 Discussion of Results

Both circuits function correctly. One advantage of the first is that it can operate for long periods of time without a light source due to the much larger energy reservoir.

However, the disadvantage is that the battery only has a lifetime of a few years. So, the second circuit implementation has a much longer potential lifetime. A second advantage of the second implementation is that it is considerably smaller. The two largest components, other than the solar cell, in the first implementation are the battery and inductor. Both of these components are missing from the second implementation. Another basis of comparison is the efficiency of the power circuitry used. A short comparison of the efficiency of each implementation follows.

Consider the first implementation shown in Figure C.2. Assume that the radio is operating at 100% duty cycle. The quiescent current for the DC-DC converter is 20 μA . The average input voltage is 2.5 volts. So the loss due to the quiescent current is 50 μW . The DC-DC converter operates at approximately 90% efficiency. The radio dissipates 12 mW of power when on, so 1.33 mW of power is lost due to the efficiency of the DC-DC converter. The power lost through the feedback resistors is only 1.5 μW , and is therefore neglected in this analysis. Therefore, the amount of power removed from the battery is $12 + 1.33 + 0.05 = 13.4$ mW. There is a diode in between the solar cell and battery to prevent the battery from discharging through the solar cell. The forward voltage drop of this diode is about 0.3 volts. If the average voltage across the battery is 2.5 volts, then the solar cell is operating at an average voltage of 2.8 volts. Therefore, 10.7% of the power produced by the solar cell is lost in the diode. The total power produced then is $(13.4 / 0.893)$ mW, or 15 mW. The efficiency of the circuit is then $12\text{mW} / 15\text{mW}$ or 80%.

It is also useful to consider much lower duty cycles. Assume that the solar / battery circuit is now operating at 10% duty cycle. The DC-DC converter consumes only 1 μA of quiescent current in standby mode. The power lost to the quiescent current is then

only $0.1 * 20\mu\text{A} * 2.5\text{V} + 0.9 * 1\mu\text{A} * 2.5\text{V} = 7.25\text{ }\mu\text{W}$. The average power dissipated by the radio is now one tenth what it was before, or 1.2 mW . So the power lost because of the 90% efficiency is now $133\text{ }\mu\text{W}$. The total power supplied by the battery is now $1.2 + 0.133 + 0.00725 = 1.34\text{ mW}$. There is still a 10.7% power loss due to the diode. So the total power produced by the solar cell is 1.5 mW . The efficiency then is still 80%.

Consider the second implementation as shown in Figure C.4. Two components dissipate power: the linear regulator and the comparator chip. In this case the power lost through the bias resistors is well below $1\text{ }\mu\text{W}$ and so is ignored. The average current draw of the comparator chip is $1.25\text{ }\mu\text{A}$. The average input voltage is 1.85 volts , resulting in an average power dissipation of only $2.3\text{ }\mu\text{W}$. The comparator chip is operating all the time regardless of duty cycle. First consider the case where the radio is on all of the time, 100% duty cycle. The regulator draws $75\text{ }\mu\text{A}$ of quiescent current. At an average input voltage of 1.85 volts , the resulting power loss is $139\text{ }\mu\text{W}$. The power lost in the pass transistor of the regulator is $(V_{\text{in}} - V_{\text{out}}) * I_{\text{diss}}$ or $(1.85 - 1.2)\text{V} * 10\text{mA} = 6.5\text{ mW}$. The total power lost in the regulator is then $6.5 + 0.139 = 6.64\text{ mW}$. By comparison, the $2.3\text{ }\mu\text{W}$ lost in the comparator chip is negligible. Therefore, to supply 12 mW to the radio, the solar cell must produce 18.84 mW for an efficiency of 64%.

Next consider the case where the circuit of Figure C.4 is operating at 10% duty cycle. The power lost in the comparator chip is still $2.3\text{ }\mu\text{W}$. The standby current draw of the linear regulator is only $1\mu\text{A}$. Therefore, the power lost due to quiescent current in the regulator is now $0.1 * 75\text{ }\mu\text{A} * 1.85\text{ V} + 0.9 * 1\text{ }\mu\text{A} * 1.85\text{ V} = 15.7\text{ }\mu\text{W}$. The power lost in the pass transistor is now $0.1 * (1.85 - 1.2)\text{V} * 10\text{mA} = 650\text{ }\mu\text{W}$. The total power lost in the regulator is then about $666\text{ }\mu\text{W}$. The average power dissipation of the radio is

1.2 mW, so the solar cell must produce 1.87 mW of power. The resulting efficiency is still 64%.

A summary of the power and efficiency values presented above is shown below in Table C.2. As shown, the efficiency of both power circuits is constant over a wide range of duty cycles. If the duty cycle is reduced to near 1% the efficiencies will begin to drop off because the losses due to the comparator chip and the standby current become more significant. Even with the extra 10.7% loss from the diode, the solar / battery implementation is more efficient due to the use of the DC-DC converter. Perhaps the best implementation would be a cross between the two shown here incorporating a capacitor as an energy reservoir and a switching DC-DC converter. The efficiency of such an implementation could approach 90%.

	P_{radio}	$P_{\text{loss reg}}$	$P_{\text{loss diode}}$	$P_{\text{loss comp}}$	Efficiency
Solar / Batt, 100% DC	12 mW	1.38 mW	1.6 mW	NA	80%
Solar / Batt, 10% DC	1.2 mW	0.14 mW	0.16 mW	NA	80%
Solar / Cap, 100% DC	12 mW	6.64 mW	NA	2.3 μ W	64%
Solar / Cap, 10% DC	1.2 mW	0.666 mW	NA	2.3 μ W	64%

Table C.2: Power losses and efficiencies of power circuit implementations.